

Volume 65 • Number 3 • June 2017

Acta Geophysica

PAN
POLISH ACADEMY OF SCIENCES




Institute of Geophysics
Polish Academy of Sciences



Springer

Experimental study on local scouring at pile-supported piers

Mario Moreno¹  · Olga Birjukova² · Carmelo Grimaldi³ · Roberto Gaudio⁴ · António H. Cardoso²

Received: 15 January 2017 / Accepted: 10 May 2017 / Published online: 18 May 2017
© Institute of Geophysics, Polish Academy of Sciences & Polish Academy of Sciences 2017

Abstract In spite of the increasing importance of complex piers for bridges, the number of studies on these piers is comparatively small and the predictors of scour depth at complex piers are only a few, derived from limited experimental evidence. The main purpose of this paper is to share with the hydraulics community the results of 67 tests on scouring at pile-supported piers (including complex piers) aligned with the flow, under clear-water conditions close to the threshold of beginning of sediment motion, while contributing to shed some more light on the influence of the pile-cap thickness on the equilibrium scour depth, the reliability of the superposition approach, the contribution of each one of the complex pier components to the equilibrium scour depth of the ensemble, and the performance of existing predictors of local scour at complex piers.

Keywords Bridge piers · Pier scour · Laboratory studies · Movable bed · Clear water

Introduction

In the last decades, pile-supported piers have been widely used as foundation of large-span bridges across wide alluvial river valleys. The most common configuration of these piers is materialized by complex piers, which are usually composed of a column founded on a pile cap supported by several piles (*cf.* Fig. 1a). While the effects of parameters such as flow shallowness, flow intensity, sediment coarseness and gradation, pier shape, or pier alignment on the equilibrium scour depth at single-column piers have been extensively studied since the 1950s, only a limited number of comparatively recent studies on scouring at complex piers were published. They include those of Jones and Sheppard (2000), Coleman (2005), Ataie-Ash-tiani et al. (2010), Ferraro et al. (2013), Amini et al. (2014), Moreno et al. (2015, 2016a) or Amini and Mohamed (2016). These studies have focused on the influence of the complex piers geometry, including the influence of pile-cap position relative to the initial bed level, pile-group configuration, pile-cap thickness and relative column width, on the equilibrium scour depth. Still, the number of covered geometries is strikingly incomplete in view of the countless number of geometries that complex piers can configure.

The predictors of scour depth at complex bridge piers are also only a few, namely, those by Coleman (2005) (Auckland University), Sheppard and Renna (2010) (Florida Department of Transportation—FDOT), Arneson et al. (2012) (HEC-18), Moreno et al. (2016a), Amini and Mohamed (2016); they rely on little experimental evidence, and thus, their systematic assessment against new high-quality data is needed. In this context, it should be mentioned that Amini et al. (2014) performed scour tests at complex piers as well as at their respective isolated components and assessed the superposition approach adopted in

✉ Mario Moreno
mario-mo@uniandes.edu.co

¹ Departamento de Ingeniería Civil y Ambiental, Universidad de Los Andes, Bogotá, Colombia

² Departamento de Engenharia Civil, Arquitetura e Georrecursos, Instituto Superior Técnico, Universidade de Lisboa, Lisbon, Portugal

³ Setec Energie Environnement, Lyon, France

⁴ Dipartimento di Ingegneria Civile, Università della Calabria, Rende, Italy

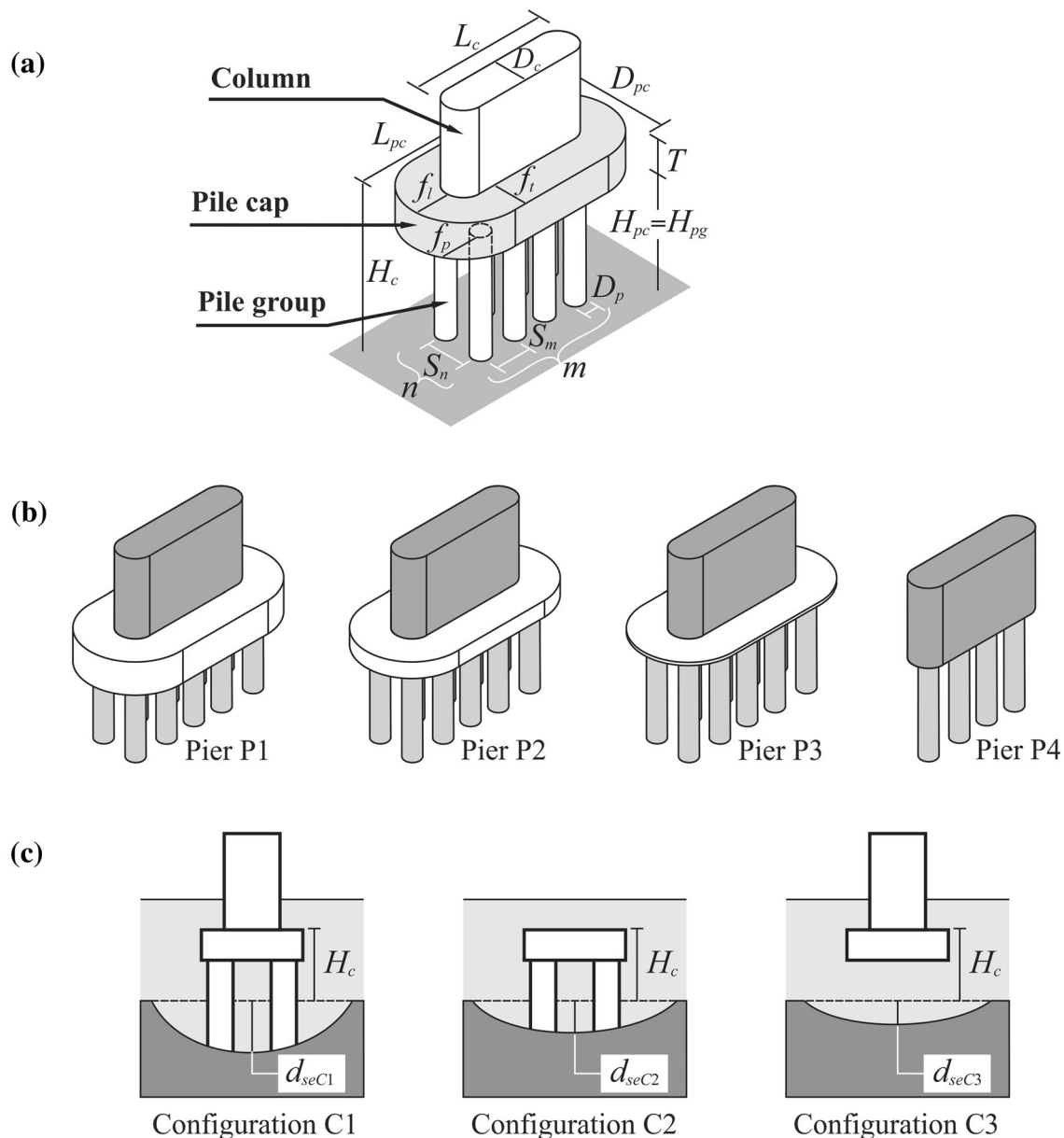


Fig. 1 a Complex piers geometry, b pile-supported piers tested, and c pier configurations

the HEC-18 method (Arneson et al. 2012). Recently, Moreno et al. (2016b) reinforced the spread idea according to which the superposition approach can disregard important interactions and joint effects of the different pier components with the flow field and the bed; therefore, they adopted a subtraction approach to experimentally assess the contribution of each component of the complex pier into the total equilibrium scour depth. According to this approach, the scour depth directly ascribable to a given pier component can be obtained by subtracting the scour depth at two contiguous pier components from the scour depth at the corresponding complete complex pier.

Some researchers (e.g., Beheshti and Ataie-Ashtiani 2010, 2016) studied the flow structure around complex bridge piers identifying the principal flow-complex-pier interactions. In contrast, Moreno et al. (2016a, b) presented their interpretation on the main flow structures thought to be present for different pile-cap positions relative to the initial bed level.

The main purpose of this paper is to share with the hydraulics community the results of 67 high-quality tests on scouring at pile-supported piers aligned with the flow, under clear-water conditions, close to the threshold of beginning of sediment motion. The consequent discussion

intends, in turn, (i) further characterize the effect of the pile-cap thickness on the equilibrium scour depth, (ii) to clarify the validity of the superposition approach, (iii) to isolate the contribution of each complex-pier component to the equilibrium scour depth, and (iv) to check the performance of existing scour predictors dedicated to complex piers. It should be noted here that except for Moreno et al. (2016a), the present study relies on tests lasting for much longer than all the others reported in the existing literature. These long duration tests led to scour depths much closer to equilibrium, constituting in itself a key contribution to the characterization of scour depth at complex piers.

Experiments

The data reported and discussed herein are the outcome of the experimental campaign initiated by Ferraro et al. (2013) on scouring at piers P1 and P3 characterized in Fig. 1b and Table 1. The 67 new experiments cover not only complete pier configurations (configuration C1 in Fig. 1c) of piers P2 and P4 and the repetition of four tests for pier P3 but, mostly, experiments on incomplete piers (configurations C2 and C3, defined according to Moreno et al. 2016b for the application of the subtraction approach, cf. Fig. 1c). Configuration C2 corresponds to piers without column, while configuration C3 corresponds to piers without the pile group. In this context, pier P4 can be viewed as an idealized complex pier, where either the pile cap or the column is absent.

Table 1 Complex pier geometry characteristics

Variable	Pier P1	Pier P2	Pier P3	Pier P4
Column shape	RRN	RRN	RRN	RRN
D_c (m)	0.049	0.049	0.049	0.049
L_c (m)	0.197	0.197	0.197	0.197
Pile-cap shape	RRN	RRN	RRN	–
D_{pc} (m)	0.148	0.148	0.148	–
L_{pc} (m)	0.298	0.298	0.298	–
T (m)	0.050	0.025	0.001	–
f_i (m)	0.050	0.050	0.050	–
f_t (m)	0.050	0.050	0.050	–
Piles shape	C	C	C	C
m	5	5	5	4
n	2	2	2	1
D_p (m)	0.025	0.025	0.025	0.025
S_m (m)	0.050	0.050	0.050	0.050
S_n (m)	0.055	0.055	0.055	–
f_p (m)	0.031	0.031	0.031	0.011

RRN rectangular round-nosed; C circular

The experiments were performed by adopting the same experimental procedure and using the same 8.0-m-long, 0.7-m-wide, and 0.7-m-deep steel flume of the Instituto Superior Técnico, Lisbon, Portugal, as described by Ferraro et al. (2013). It is worth reminding that (i) the piers were embedded in a uniform sand (median diameter: $d_{50} = 0.83$ mm; geometric standard deviation: $\sigma_g = 1.48$); (ii) the longitudinal axis of the piers was always aligned with the flow; (iii) experiments were performed under clear-water flow conditions, with constant approach flow depth, $h = 0.10$ m, and constant flow intensity $U/U_c \approx 0.92$, where $U = 0.276$ m/s was the average approach flow velocity and $U_c \approx 0.296$ m/s was the critical flow velocity for the beginning of sediment motion (value obtained experimentally by Fael et al. 2006 and Grimaldi et al. 2009 and shown to comply with the equation of Neil 1967); (iv) the aspect ratio of $B/h = 7$ was guaranteed ($B =$ flume width), this way avoiding significant wall effects in the flow field; (v) the ratio of the channel width to the equivalent pier width (calculated according to Moreno et al. 2016a) varied in the range $7.3 < B/D_e < 14$, depending on the vertical position of the column bottom relative to the initial bed level; (vi) in no experiment, measurable bed degradation was registered along the contracted flow reach; (vii) in no experiment, contraction scour was observed, since the scour holes never reached the channel walls, being completely developed in the spanwise direction. For sakes of completeness, it should still be noted that (viii) the flow discharge was measured with an electromagnetic flowmeter and the flow depth and the maximum scour depth were measured with ± 0.1 -mm-accurate points gauge; and (ix) the upstream bed reach of the channel was roughened with sparse gravel grains, to provide proper roughness and guarantee fully developed flow. The flow shallowness varied in the range $1.30 < h/D_e < 2.50$ depending on the relative position of the column bottom, and the relative sand roughness varied in the range $48 < D_e/d_{50} < 93$, close to the conditions, where the scour depth is maximal.

Excluding cases where scour depth remained null or negligible after ≈ 1 –4 days, mostly for configuration C3 of piers P3 and P4, whose pile caps were, respectively, very thin (1 mm) or inexistent, experiments lasted, on average, 13.7 days (between 6 and 41 days). These durations are generally longer than those reported in the literature and guaranteed sufficient approximation to the equilibrium stage, as it can be observed in Fig. 2. Each time evolution curve is associated with the three typical pile cap situations: above the initial bed level, partially buried in the bed and completely buried in the bed. The complete time records of the scour depth are available at <https://drive.google.com/open?id=0B7JmeEhYWblkdmhwNVRBXY14Q2c>. Longer tests corresponded to cases, where the pile cap

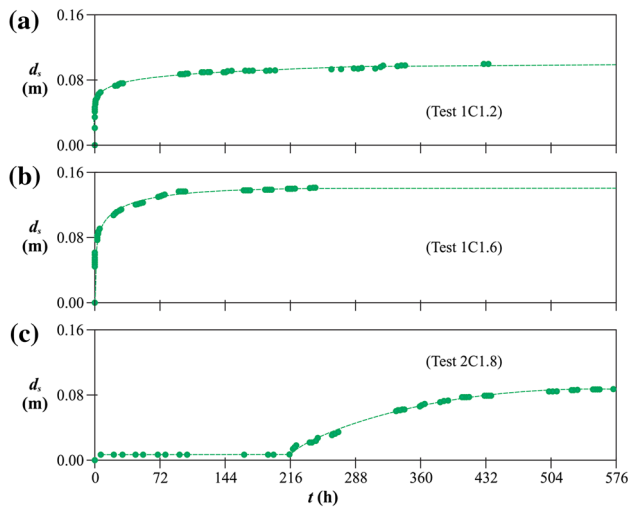


Fig. 2 Scour depth time evolution in the three typical situations: **a** pile cap above the initial bed level, **b** pile cap partially buried in the bed, and **c** pile cap completely buried in the bed

was initially buried in the bed, requiring extra work of the local flow structures to uncover the top and front surfaces of the pile caps.

Results and discussion

Data presentation

Tables 2, 3, and 4 summarize the characteristic variables of 83 tests, organized per configurations C1, C2, and C3, respectively. Table 2 also includes the variables defining 16 tests reported by Ferraro et al. (2013) for configuration C1 of piers P1 and P3. The three tables record the relative position of the column bottom, H_c/h (assumed to be positive when the top of the pile cap is above the initial bed level), the test duration, t_d , and the deepest scour depth measured at the end of each test, d_{sm} . Different vertical positions of the pile cap relative to the initial bed level were tested per pier. These positions are related to the three typical pile cap situations previously mentioned.

It is assumed herein that equilibrium scour is attained asymptotically (see Fig. 2). The records of scour-depth time evolution were extrapolated to infinite time through the six-parameter polynomial technique used by Simarro et al. (2011) as a means to estimate the most likely values of the equilibrium scour depth, d_{se} (cf. Tables 2, 3, 4).

Influence of the pile-cap thickness on the equilibrium scour depth

The influence of the pile-cap thickness on the equilibrium scour depth, d_{se} , was assessed through the results obtained

Table 2 Control variables of the tests with configuration C1 and equilibrium scour depths

Pier	Test	H_c/h	t_d (h)	d_{sm} (m)	d_{se} (m)	
P1	1C1.1	1.73	263	0.101	0.102	
	1C1.2 ^a	1.24	436	0.100	0.102	
	1C1.4 ^a	0.58	220	0.140	0.142	
	1C1.5	0.33	246	0.154	0.162	
	1C1.6 ^a	0.23	243	0.141	0.150	
	1C1.7 ^a	0.00	247	0.117	0.119	
	1C1.8 ^a	−0.07	887	0.102	0.112	
	1C1.9 ^a	−0.13	558	0.089	0.098	
	1C1.10	−0.25	746	0.071	0.080	
	1C1.11 ^a	−0.47	266	0.059	0.060	
	1C1.12 ^a	−1.10	198	0.100	0.103	
	P2	2C1.3	0.91	149	0.114	0.120
2C1.4		0.58	151	0.105	0.113	
2C1.5		0.33	146	0.116	0.123	
2C1.6		0.24	171	0.130	0.141	
2C1.7		0.00	319	0.118	0.129	
2C1.8		−0.08	582	0.088	0.104	
2C1.9		−0.12	318	0.069	0.095	
2C1.10		−0.25	526	0.061	0.073	
2C1.11		−0.50	239	0.051	0.052	
P3		3C1.3 ^a	0.89	175	0.098	0.102
		3C1.4 ^a	0.60	175	0.094	0.099
	3C1.5 ^a	0.36	173	0.089	0.098	
	3C1.6 ^{ab}	0.22	407	0.081	0.088	
	3C1.7 ^a	0.01	314	0.074	0.086	
	3C1.8 ^{ab}	−0.09	988	0.091	0.097	
	3C1.9 ^{ab}	−0.12	789	0.085	0.092	
	3C1.10 ^{ab}	−0.26	462	0.056	0.066	
	3C1.11 ^a	−0.50	214	0.050	0.050	
	P4	4C1.1	1.75	192	0.075	0.077
4C1.4		0.45	193	0.081	0.085	
4C1.6		0.24	151	0.087	0.090	
4C1.8		0.00	223	0.095	0.103	
4C1.9		−0.07	127	0.098	0.110	
4C1.10		−0.13	126	0.100	0.108	
4C1.11		−0.18	271	0.108	0.115	
4C1.12		−0.25	221	0.107	0.114	
4C1.13		−0.50	175	0.098	0.105	

^a Tests reported by Ferraro et al. (2013)

^b Tests repeated

for configuration C1 of piers P1, P2, and P3, where $T/h = [0.50, 0.25, \text{ and } 0.01]$, respectively. For these piers, only the pile-cap thickness was changed (Table 1). Ferraro et al. (2013) described extensively the influence of the column position and the pile-cap thickness on the temporal

Table 3 Control variables of the tests with configuration C2 and equilibrium scour depths

Pier	Test	H_c/h	t_d (h)	d_{sm} (m)	d_{se} (m)
P1	1C2.4	0.58	402	0.060	0.087
	1C2.5	0.37	336	0.065	0.088
	1C2.6	0.23	483	0.101	0.106
P2	2C2.3	0.91	150	0.100	0.108
	2C2.4	0.59	149	0.090	0.094
	2C2.5	0.33	199	0.104	0.110
	2C2.6	0.23	175	0.116	0.122
P3	3C2.3	0.89	162	0.100	0.102
	3C2.4	0.59	188	0.082	0.087
	3C2.5	0.33	334	0.074	0.075
	3C2.6	0.22	287	0.065	0.069
P4	4C2.2	0.90	168	0.075	0.076
	4C2.3	0.59	162	0.066	0.069
	4C2.5	0.33	162	0.061	0.063
	4C2.6	0.22	163	0.054	0.054

Table 4 Control variables of the tests with configuration C3 and equilibrium scour depths

Pier	Test	H_c/h	t_d (h)	d_{sm} (m)	d_{se} (m)	
P1	1C3.4	0.58	260	0.140	0.146	
	1C3.5	0.33	263	0.147	0.155	
	1C3.6	0.23	311	0.147	0.158	
	1C3.7	0.00	435	0.101	0.109	
	1C3.8	-0.08	724	0.101	0.113	
	1C3.9	-0.12	450	0.089	0.092	
	P2	2C3.3	0.91	167	0.008	0.012
		2C3.4	0.59	152	0.022	0.026
		2C3.5	0.33	169	0.145	0.149
		2C3.6	0.23	286	0.138	0.145
2C3.7		0.00	239	0.094	0.110	
2C3.8		-0.08	743	0.101	0.108	
2C3.9		-0.12	666	0.102	0.107	
2C3.10		-0.24	791	0.057	0.073	
P3		3C3.3	0.89	92	0.000	0.000
		3C3.4	0.59	72	0.000	0.000
		3C3.5	0.33	91	0.000	0.000
	3C3.6	0.22	162	0.005	0.006	
	3C3.7	0.00	338	0.041	0.057	
	3C3.8	-0.09	691	0.096	0.103	
	3C3.9	-0.12	664	0.093	0.100	
	P4	4C3.2	0.90	90	0.000	0.000
		4C3.3	0.59	29	0.000	0.000
		4C3.5	0.33	24	0.002	0.002
4C3.6		0.22	19	0.006	0.006	
4C3.7		0.11	122	0.069	0.072	
4C3.8		0.00	72	0.077	0.083	
4C3.9		-0.09	186	0.062	0.067	
4C3.10		-0.12	240	0.100	0.103	
4C3.11		-0.18	196	0.090	0.094	

evolution of the scour depth as well as on its final value for piers P1 and P3. Therefore, only a brief discussion is resumed herein. According to Fig. 3, (i) when the pile cap was buried below the equilibrium scour depth generated by the column (i.e., for $H_c/D_c < \approx -2.1$), without the interference of any other pier component, the scour depth was described by $d_{se}/D_c \approx 2.1$, which compares with $d_{se}/D_c \approx 2.4$ as quoted by Melville and Coleman (2000) for single cylindrical piers; (ii) when the top of the pile cap lies in the interval $-2.1 < H_c/D_c < -1.0$, the bottom of the scour hole coincides with the top of the pile cap, i.e., $d_{se} = |H_c|$, reaching the minimum of $d_{se} \approx D_c$ for $H_c/D_c = -1.0$; (iii) when the top of the pile cap lies between $H_c/D_c \approx -1.0$ and $H_c/T \approx 0.75$, the scour depth increases linearly with H_c , reaching the maxima of $\approx 2.9D_c = 0.95D_{pc}$, for $T/h = 0.25$, and $\approx 3.3D_c = 1.10D_{pc}$, for $T/h = 0.50$, at $H_c \approx 0.75T$; (iv) in the interval $\approx 0.75T \leq H_c < (h + T)$, the equilibrium scour depth decreases exponentially as the pile cap rises in the water column until it emerges out of the water, except for pier P3 in which d_{se} increases; (v) the equilibrium scour depth increases with T/h in the same zone, $\approx 0.75T \leq H_c < (h + T)$, reflecting the variation of the flow blockage with T ; (vi) for $H_c > (h + T)$, the scour depth is only dependent on the pile group and remains constant as H_c increases; and (vii) the thin pile cap of pier P3 acts as a collar when it lies in the neighborhood of the bed, reducing the scour depth (and confirming the findings of Gaudio et al. 2012 or Tafarojnoruz et al. 2012).

In accordance with Moreno et al. (2015), when the top of the pile cap is built close to the initial bed, either above or below, and the pile group is initially buried in the bed,

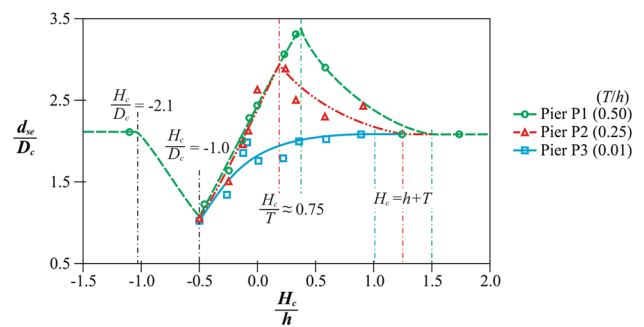


Fig. 3 Influence of the pile-cap thickness on the equilibrium scour depth

this group plays an important role in the scouring process as soon as the front faces of the upstream piles are exposed to the flow inside the scour hole. In this case, the piles tend to disrupt/break the internal boundary layer created along

the lower face of the pile cap, possibly reducing the excavating power of the resulting flow structures and inducing some scatter, as observed for piers P2 and P3.

It should be emphasized here that the variation of d_{se}/D_c with H_c/h presented in Fig. 3 for three different values of T/h only applies for rectangular round nosed piers with $D_c/D_{pc} = 0.33$ and symmetrical pile-cap overhang lengths, i.e., $f_l/f_r = 1$ (cf. Fig. 1a). A similar behavior can be postulated to occur for different values of D_c/D_{pc} , but thresholds such as $H_c/D_c = -1.0$ or $H_c/T = 0.75$ cannot be understood as universal. In fact, Moreno et al. (2016a) have suggested expressions to calculate these thresholds as a function of D_c/D_{pc} and different column and pile-cap shapes. The corresponding predictions are, respectively, $H_c/D_c = -0.71$ and $H_c/T = 0.77$. In accordance with Moreno et al. (2015), the variation of the scour depth with H_c/h presented in Fig. 3 is analogous to the other column/pile-cap shapes (e.g., circular and rectangular); however, the pile-cap positions at which the scour-depth behavior changes markedly is highly dependent on D_c/D_{pc} and T/h ratios.

Assessment of the superposition approach

The scour data obtained at pier P4 for configurations C1, C2, and C3 allows for a neat assessment of the superposition approach. According to that approach, the scour depth at a given complex pier can be obtained by adding up the scour depths registered at each pier component acting in isolation. Figure 4 compares the scour depths measured at pier P4, configuration C1, with the values resulting from adding the scour depth at the pile group, configuration C2, with the scour depth at the suspended column, configuration C3. It is clear that, except for $H_c/h = 0.11$, where the contribution of the pile group was obtained by interpolating the scour depths for $H_c/h = 0.22$ and $H_c/h = 0.00$, the superposition approach systematically under-predicts the scour depth. This under-prediction corroborates the

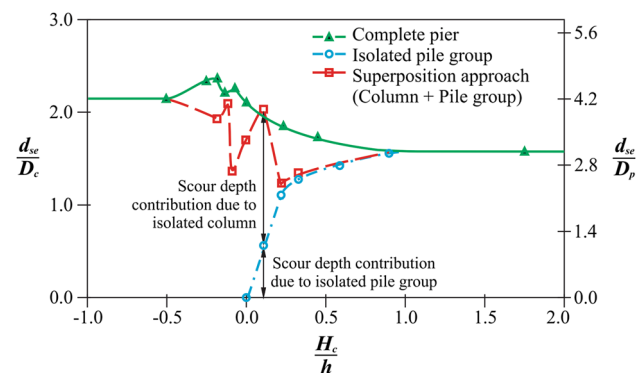


Fig. 4 Equilibrium scour depths at complete pier P4 compared with the result of the superposition approach

findings of Amini et al. (2014) and can only be ascribable to changes in the flow structure, as well as in the associated scouring mechanisms, when the pier is split into its components (see, e.g., Moreno et al. 2016b).

Figure 4 shows that the equilibrium scour depth at the pile group, composed of four piles aligned with the flow, is given by $d_{se}/D_p \approx 3.1$ when the top of the piles emerges out of the water, i.e., $H_c/h > 1$. The upper limit of $d_{se}/D_p \approx 2.4$ quoted by Melville and Coleman (2000), for isolated cylindrical piers, is exceeded by almost 30%, most likely owing to the interaction of the horseshoe and wake vortices generated at individual piles, providing extra siphoning and transport capacity to extract and move sand downstream, this way substantially increasing the scour depth (see, e.g., Lança et al. 2013b).

Contributions of complex pier components to the equilibrium scour depth

According to Moreno et al. (2016b), three factors can be used to assess the contribution of each pier component to the equilibrium scour depth of complex piers. They are

$$K_{hc} = \frac{d_{seC1} - d_{seC2}}{d_{seC1}} \quad (1)$$

$$K_{hpc} = \frac{d_{seC2} + d_{seC3} - d_{seC1}}{d_{seC1}} \quad (2)$$

$$k_{hpg} = \frac{d_{seC1} - d_{seC3}}{d_{sepgu}} \quad (3)$$

where K_{hc} is the factor accounting for the influence of the position of the column bottom, H_c (cf. Fig. 1a); d_{seC1} is the equilibrium scour depth developed at a single pier with the same geometry as the column; K_{hpc} is the factor accounting for the influence of the position of the pile-cap bottom, H_{pc} (cf. Fig. 1a); d_{sepgu} is the equilibrium scour depth developed at a single pier with the same dimensions as the pile cap; k_{hpg} is the factor accounting for the influence of the position of the pile-group top, H_{pg} (cf. Fig. 1a); d_{sepgu} is the equilibrium scour depth developed at an unsubmerged pile group; d_{seC1} , d_{seC2} , and d_{seC3} are the equilibrium scour depths at configurations C1, C2, and C3, respectively (see Fig. 1c).

To apply Eqs. (1), (2), and (3), the values of d_{seC1} , d_{seC2} , and d_{seC3} were those reported in Tables 2, 3, and 4, respectively. The values of d_{seC1} (=0.103 m) and d_{sepgu} (=0.102 m) were the equilibrium scour depths obtained in tests 1C1.12 and 1C1.1, respectively, while d_{sepgu} (=0.218 m) was obtained through the central predictor suggested by Lança et al. (2013a), whose experiments were run for the same sand, pier sizes, and flow velocity.

The variation of factors K_{hc} , K_{hpc} , and k_{hpg} with the correspondent component position relative to the initial bed

is plotted in Fig. 5a–c using the coordinates proposed by Moreno et al. (2016b). The three plots include also the data and curves suggested by these authors. Figure 5a shows that the K_{hc} values obtained in the present study follow the same trend as those reported by Moreno et al. (2016b) with two exceptions for pier P1.

The results included in Fig. 5b for pier P3 ($T/h = 0.01$), namely, the negative values of K_{hpc} when the pile cap is close to the initial bed level, unequivocally show that the pile caps induce a shielding effect on scouring by intercepting the down-flow at the upstream face of the column as well as resisting to the scouring power of the associated horseshoe vortex. This shielding effect is normally masked by the overriding scouring action of the flow structures that

develop around realistic pile caps ($T/h \gg 0.01$), namely, the down-flow and vortical structures.

Figure 5c shows that the values of K_{hpg} obtained in the present study follow the same trend as those reported by Moreno et al. (2016b) for $H_{pg}/h > 0.15$. On the contrary, for $H_{pg}/h < 0.15$, they are rather different; those of the present study are around zero and can be negative (cf. Fig. 5c). This was realized early during the experimental campaign and led to a special observation of the experiments of configurations C2 and C3 for piers P1 and P2. The results indicate that, for the present pier shapes, the piles interact with the pile cap in such a way that the former behaves as a countermeasure against scouring, particularly for small or negative values of H_{pg} . This is clearly indicated by comparing the d_{sc} values of tests 2C1.5 and 2C3.5, where $H_{pg} > 0$, or tests 2C1.6 and 2C3.6, where $H_{pg} < 0$. It is plausible that the effect of flow contraction and acceleration underneath the pile cap for configuration C3 ($d_{sc} = 145$ mm at $H_c/h = 0.23$) induced a scour capacity that is “removed” by the piles of configuration C1 ($d_{sc} = 141$ mm at $H_c/h = 0.24$), but mostly of configuration C2 as shown in Fig. 6 for $H_c/h = 0.23$. This explains the scour reduction from test 2C2.3 to test 2C2.4 and the scour invariance from test 1C2.4 to test 1C2.5, which was not observed in the corresponding tests of series C3, where the effect of flow acceleration was kept undisturbed. When the pile cap moved to even lower levels, the reduction of scour capacity induced by the piles led to the indirect inversion of the process as follows: in most experiments of configuration C2 characterized by $H_{pg} < 0$, the flow was unable to produce undercutting, and the diverted flow eroded the bed at the sides of the pile cap, creating lateral scour valleys. Thus, somehow, the sand bed underneath the pile cap acted as an extension downwards of this pier component, enhancing the scouring capacity and the scour depth as compared with the situations, where the pile cap lied higher in the flow (compare tests 1C2.6 with 1C2.5 or 2C2.6 with 2C2.5). The sand deposit underneath that the pile cap was kept stable and did not slide laterally as the conveyance subtracted by the pier and the sand deposit underneath were compensated by the scoured lateral valleys. This seems to be the reason why the values of K_{hpc} included in Fig. 5b are higher than those of Moreno et al. (2016b); this increase is easily identified by comparing data for $T/h = [0.25, 0.30]$ as well as for $T/h = [0.45, 0.50]$. The increase of K_{hpc} is also partly ascribable to the relative sediment roughness of the present study, $D_{pc}/d_{50} = 180$, as they are lower than those of Moreno et al. (2016b), but this effect is possibly minor.

In any case, there seem to be different relative scouring intensities of the local flow structures generated at the piers and pier components in both studies, deriving from their different relative sizes. It should be noticed here that the

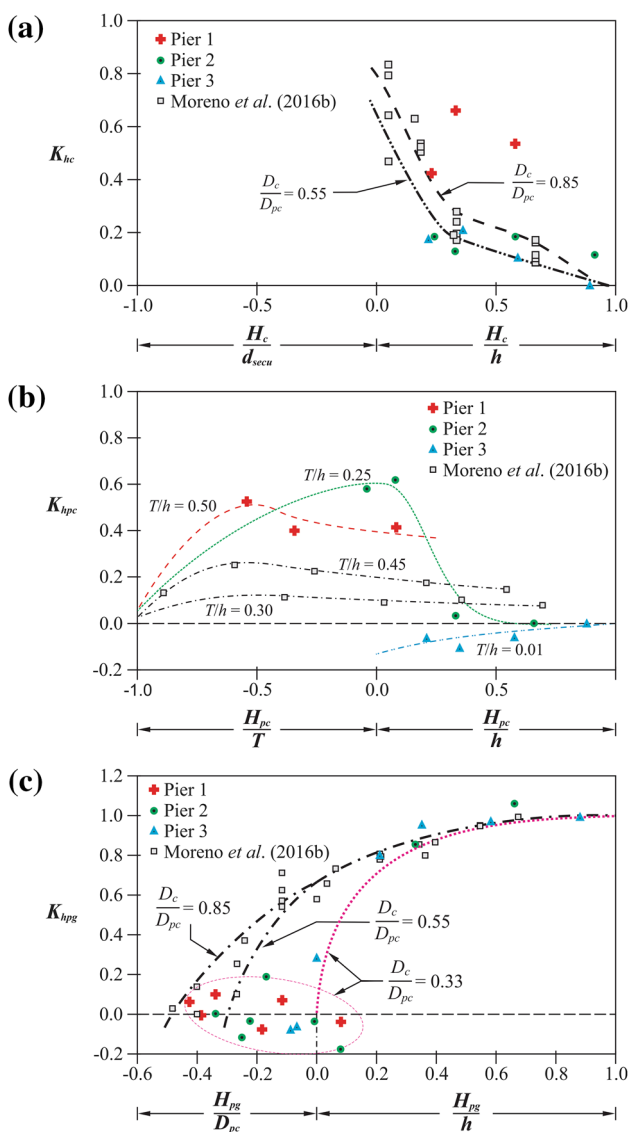
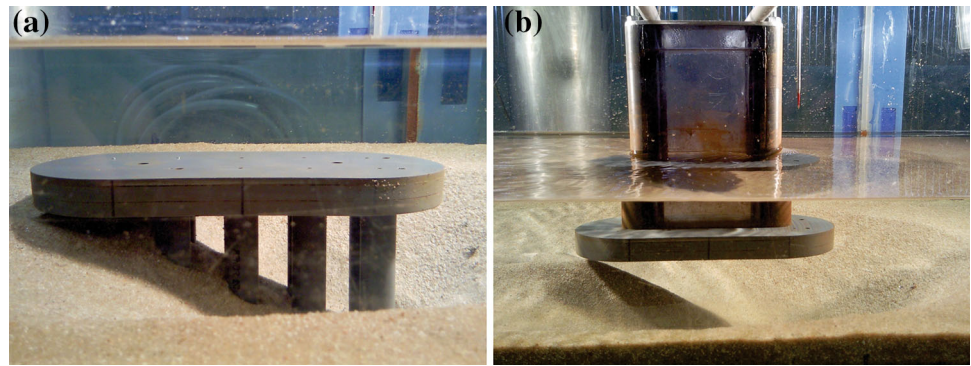


Fig. 5 Characterization of factors K_{hc} , K_{hpc} , and K_{hpg} as defined by Moreno et al. (2016b): **a** K_{hc} for the column, **b** K_{hpc} for the pile cap, and **c** K_{hpg} for the pile group

Fig. 6 Final scour hole at tests with the pile cap partially buried in the bed ($H_c/T = 0.92$): **a** test 2C2.6 and **b** test 2C3.6



present study explored a value of $D_c/D_{pc} = 0.33$, lower than those of Moreno et al. (2016b). This means that down-flow may be expected to be intercepted by the upper face of the pile cap, which may not be the case in the study of Moreno et al. (2016b), particularly for $D_c/D_{pc} = 0.85$. The present study also covers higher values of f_p/D_p (1.24, in the present study, vs. 0.60 by Moreno et al. 2016b) and lower values of T/f_p (respectively, 1.61 and 0.80 vs. 2.0, 3.0, and 4.0). This means that, in the present study, piles tend to be hidden and protected from the direct action of the horseshoe vortex generated at the upstream vertical face of the pile cap.

Applicability of available scour depth predictors

The scour data obtained for configuration C1 of piers P1 to P3 (29 experiments) were finally used to evaluate the performance of the five scour-depth predictors mentioned in the “Introduction”, i.e., the Auckland method (Coleman 2005), the FDOT method (Sheppard and Renna 2010), the HEC-18 method (Arneson et al. 2012), the method proposed by Moreno et al. (2016a), and the method suggested by Amini and Mohamed (2016). Table 5 includes the mean and the standard deviation of the ratio between the scour depths predicted by each method, d_{sep} , and the corresponding scour depths obtained in this study, d_{seo} (values of Table 2), whereas Table 6 includes the percentage of estimations of the equilibrium

scour depth of each method by considering two asymmetric bounds (+10 and –10% with respect to the line of perfect agreement). The statistics of Table 5 are organized in three groups: (1) pile cap out of the water and pile cap under water, above the initial bed level; (2) pile cap partially and completely buried in the bed; and (3) all four pile cap situations (i.e., groups 1 and 2). This analysis highlights that (i) the Auckland and FDOT methods tend to overestimate the equilibrium scour depth (i.e., at least 55% of the scour depth values above the +10% boundary), as shown in Figs. 7a, b, respectively, both methods inherently displaying highly dispersed predictions, (ii) the HEC-18 method tends to systematically underestimate the equilibrium scour depth in all four pile cap situations (i.e., 90% of the scour depth values below the –10% boundary), as shown in Fig. 7c, (iii) the method of Amini and Mohamed (2016) led to rather scattered predictions, as shown in Fig. 7d, in which 52% of the scour depth values are above the +10% boundary and 34% of the scour depth values are below the –10% boundary, and (iv) the method of Moreno et al. (2016a) produces centered predictions of the scour depth (76% of the predicted values were within the $\pm 10\%$ bound) with a rather low dispersion (see Fig. 7e). On the contrary, analysis of field data by Gaudio et al. (2010) showed that the HEC-18 method mostly overestimates the maximum scour depth at non-complex (i.e., uniform) bridge piers.

Table 5 Evaluation of equilibrium scour depth predictors

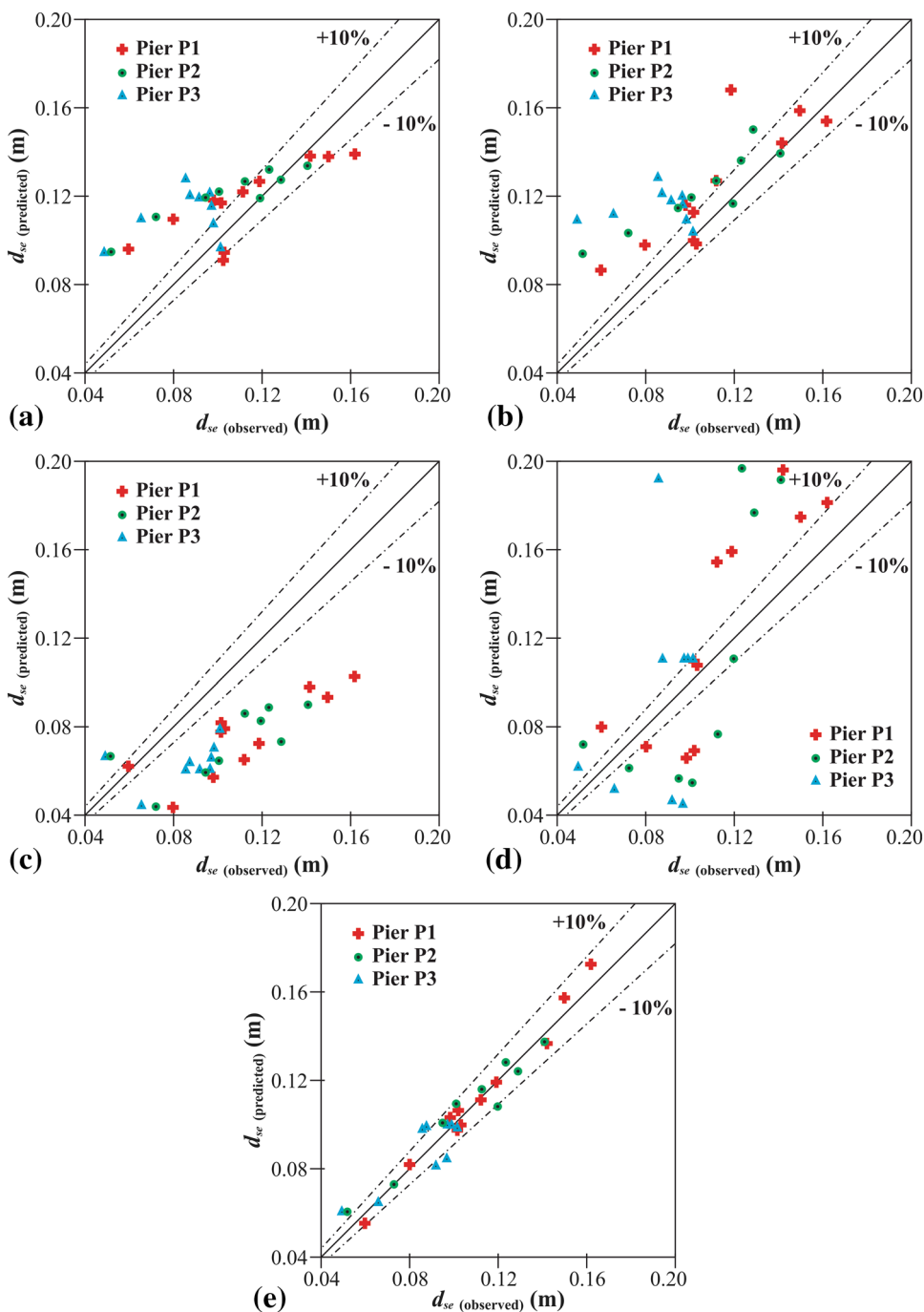
Method	Group 1	Group 2	Group 3
Auckland (Coleman 2005)	1.08 ± 0.17	1.23 ± 0.31	1.16 ± 0.27
FDOT (Sheppard and Renna 2010)	1.11 ± 0.16	1.22 ± 0.31	1.18 ± 0.27
HEC-18 (Arneson et al. 2012)	0.72 ± 0.04	0.63 ± 0.23	0.67 ± 0.18
Amini and Mohamed (2016)	1.12 ± 0.42	1.09 ± 0.33	1.12 ± 0.38
Moreno et al. (2016a)	1.02 ± 0.07	1.00 ± 0.08	1.01 ± 0.08
Mean and standard deviation of d_{sep}/d_{seo} ratio			

Table 6 Evaluation of equilibrium scour depth predictors

Method	Inside the boundaries (%)	Above the boundaries (%)	Below the boundaries (%)
Auckland (Coleman 2005)	38	55	7
FDOT (Sheppard and Renna 2010)	31	69	0
HEC-18 (Arneson et al. 2012)	3	7	90
Amini and Mohamed (2016)	14	52	34
Moreno et al. (2016a)	76	14	10

Percentage of estimations of the equilibrium scour depth

Fig. 7 Observed vs. predicted equilibrium scour depths by: **a** Auckland method, **b** FDOT method, **c** HEC-18 method, **d** Amini and Mohamed (2016), and **e** Moreno et al. (2016a)



Conclusions

The following conclusions can be drawn from the results of the extensive experimentation described above on scouring at complex piers aligned with the flow, under clear-water conditions, close to the threshold condition of beginning of sediment motion.

The effect of the pile cap on the equilibrium scour depth is null when d_{se} is such that it remains buried; for $-2.1 < H_c/D_c < -1.0$, d_{se} is limited by the presence of the pile cap and the scour depth remains equal to the pile-cap top-face depth under the initial bed level; the above-mentioned behavior reaches its minimum when H_c is equal to $-D_c$; then, the scour depth increases almost linearly with H_c , reaching the maximum value at $H_c \approx 0.75T$; in the interval $\approx 0.75T \leq H_c < (h + T)$, the equilibrium scour depth decreases exponentially as the pile cap rises in the water column until it emerges out of the water, except for pier P3 in which the thin pile cap acts as a collar; in the same range of H_c , d_{se} increases with T/h ; and for $H_c > (h + T)$, d_{se} is only dependent on the pile group and remains constant as H_c increases. The pile group plays an important role when exposed to the flow and tends to reduce the excavating power and the consequent scour depth.

The superposition approach was verified not to be valid: it almost always under-predicts the scour depth by about 30%, owing to changes in the flow structure, as well as in the associated scouring mechanisms when the pier is split into its components.

The contribution of each complex-pier component to the equilibrium scour depth was identified through the use of factors accounting for the influence of the position of the column bottom, the influence of the position of the pile-cap bottom, and the influence of the position of the pile-group top, respectively. The values of the first factor obtained in the present study follow almost always the same trend as those reported by Moreno et al. (2016b). The values of the second factor show that the pile caps induce a shielding effect on scouring by intercepting the down-flow at the upstream face of the column as well as resisting to the scouring power of the associated horseshoe vortex. The values of the third factor follow the same trend as those reported by Moreno et al. (2016b) for $H_{pg}/h > 0.15$, whereas for $H_{pg}/h < 0.15$, they are rather different, being around zero and sometimes negative: the piles interact with the pile cap in such a way that the former behaves as a countermeasure against scouring, particularly for small or negative values of H_{pg} .

The performance of five scour-depth predictors dedicated to complex piers—namely, the Auckland method (Coleman 2005), the FDOT method (Sheppard and Renna 2010), the HEC-18 method (Arneson et al. 2012), and the

methods proposed by Moreno et al. (2016a) and Amini and Mohamed (2016)—was assessed through comparison with the experimental data. It was shown that the HEC-18 method tends to underestimate the equilibrium scour depth in all pier positions, the Auckland and FDOT methods tend to overestimate the equilibrium scour depth, the method proposed by Amini and Mohamed (2016) led to rather scattered predictions, whereas the method proposed by Moreno et al. (2016a) produces centered predictions of the scour depth.

Acknowledgements The authors wish to acknowledge the master students Ricardo Calçada and Domenico Ferraro for their help in carrying out some of the present experiments. Mario Moreno would like to acknowledge the financial support of the Portuguese Foundation for Science and Technology, FCT, through the doctoral grant SFRH/BD/76396/2011. Olga Birjukova thanks the FCT, through projects PTDC/ECM/118775/2010 and RECI/ECM-HID/0371/2012, for financial support.

References

- Amini A, Mohamed TA (2016) Local scour prediction around piers with complex geometry. *Mar Georesour Geotechnol*. doi:10.1080/1064119X.2016.1256923
- Amini A, Melville BW, Ali TM (2014) Local scour at piled bridge piers including an examination of the superposition method. *Can J Civ Eng* 41(5):461–471. doi:10.1139/cjce-2011-0389
- Arneson LA, Zevenbergen LW, Lagasse PF, Clopper PE (2012) Evaluating scour at bridges (HEC-18): Technical report HIF-12-003. Federal Highway Administration, Washington, DC
- Ataie-Ashtiani B, Baratian-Ghorghi Z, Beheshti AA (2010) Experimental investigation of clear-water local scour of compound piers. *J Hydraul Eng* 136(6):343–351. doi:10.1061/(ASCE)0733-9429(2010)136:6(343)
- Beheshti AA, Ataie-Ashtiani B (2010) Experimental study of three-dimensional flow field around a complex bridge pier. *J Eng Mech* 136(2):143–154. doi:10.1061/(ASCE)EM.1943-7889.0000073
- Beheshti A, Ataie-Ashtiani B (2016) Scour hole influence on turbulent flow field around complex bridge pier. *Flow Turbul Combust* 97(2):451–474. doi:10.1007/s10494-016-9707-8
- Coleman SE (2005) Clearwater local scour at complex piers. *J Hydraul Eng* 131(4):330–334. doi:10.1061/(ASCE)0733-9429(2005)131:4(330)
- Fael CMS, Simarro-Grande G, Martín-Vide JP, Cardoso AH (2006) Local scour at vertical-wall abutments under clear-water flow conditions. *Water Resour Res* 42:W10408. doi:10.1029/2005WR004443
- Ferraro D, Tafarajnoruz A, Gaudio R, Cardoso AH (2013) Effects of pile cap thickness on the maximum scour depth at a complex pier. *J Hydraul Eng* 139(5):482–491. doi:10.1061/(ASCE)HY.1943-7900.0000704
- Gaudio R, Grimaldi C, Tafarajnoruz A and Calomino F (2010) Comparison of formulae for the prediction of scour depth at piers. In: Proc. First European IAHR congress, 4–6 May 2010, Edinburgh, UK
- Gaudio R, Tafarajnoruz A, Calomino F (2012) Combined flow-altering countermeasures against bridge pier scour. *J Hydraul Res* 50(1):35–43. doi:10.1080/00221686.2011.649548

- Grimaldi C, Gaudio R, Calomino F, Cardoso A (2009) Control of scour at bridge piers by a downstream bed sill. *J Hydraul Eng* 135(1):13–21. doi:[10.1061/\(ASCE\)0733-9429\(2009\)](https://doi.org/10.1061/(ASCE)0733-9429(2009)135(1):13-21)
- Jones JS, Sheppard DM (2000) Local scour at complex pier geometries. In: Proc. joint conference on water resource engineering and water resources planning and management, July 30–August 2 2000, Minneapolis, Minnesota, United States, doi:[10.1061/40517\(2000\)409](https://doi.org/10.1061/40517(2000)409)
- Lança R, Fael C, Maia R, Pêgo J, Cardoso A (2013a) Clear-water scour at comparatively large cylindrical piers. *J Hydraul Eng* 139(11):1117–1125. doi:[10.1061/\(ASCE\)HY.1943-7900.0000788](https://doi.org/10.1061/(ASCE)HY.1943-7900.0000788)
- Lança R, Fael C, Maia R, Pêgo J, Cardoso A (2013b) Clear-water scour at pile groups. *J Hydraul Eng* 139(10):1089–1098. doi:[10.1061/\(ASCE\)HY.1943-7900.0000770](https://doi.org/10.1061/(ASCE)HY.1943-7900.0000770)
- Melville BW, Coleman SE (2000) Bridge Scour. Highlands Ranch Water Resources, Highlands Ranch
- Moreno M, Maia R, Couto L (2015) Effects of relative column width and pile-cap elevation on local scour depth around complex piers. *J Hydraul Eng* 142(2):04015051-1–04015051-9. doi:[10.1061/\(ASCE\)HY.1943-7900.0001080](https://doi.org/10.1061/(ASCE)HY.1943-7900.0001080)
- Moreno M, Maia R, Couto L (2016a) Prediction of equilibrium local scour depth at complex bridge piers. *J Hydraul Eng* 142(11):04016045-1–04016045-13. doi:[10.1061/\(ASCE\)HY.1943-7900.0001153](https://doi.org/10.1061/(ASCE)HY.1943-7900.0001153)
- Moreno M, Maia R, Couto L, Cardoso AH (2016b) Subtraction approach to experimentally assess the contribution of the complex pier components to the local scour depth. *J Hydraul Eng* 143(4):06016030-1–06016030-7. doi:[10.1061/\(ASCE\)HY.1943-7900.0001270](https://doi.org/10.1061/(ASCE)HY.1943-7900.0001270)
- Neill CR (1967) Mean velocity criterion for scour of coarse uniform bed-material. In: Proc. of the 12th congress of the international association of hydraulics research, 11–14 September 1967, Fort Collins, Colorado, United States, 46–54
- Sheppard DM, Renna R (2010) Bridge scour manual. Florida Department of Transportation, Florida
- Simarro G, Fael C, Cardoso AH (2011) Estimating equilibrium scour depth at cylindrical piers in experimental studies. *J Hydraul Eng* 137(9):1089–1093. doi:[10.1061/\(ASCE\)HY.1943-7900.0000410](https://doi.org/10.1061/(ASCE)HY.1943-7900.0000410)
- Tafarojnoruz A, Gaudio R, Calomino F (2012) Evaluation of flow-altering countermeasures against bridge pier scour. *J Hydraul Eng* 138(3):297–305. doi:[10.1061/\(ASCE\)HY.1943-7900.0000512](https://doi.org/10.1061/(ASCE)HY.1943-7900.0000512)

Assessment of river hydromorphological quality for restoration purposes: an example of the application of RHQ method to a Polish Carpathian river

Hanna Hajdukiewicz¹ · Bartłomiej Wyźga¹ · Joanna Zawiejska² · Antoni Amirowicz¹ · Paweł Ogłęcki³ · Artur Radecki-Pawlik^{4,5}

Received: 4 January 2017 / Accepted: 28 April 2017 / Published online: 9 May 2017
© The Author(s) 2017. This article is an open access publication

Abstract Planning and implementation of effective restoration projects require appropriate assessment of a river's hydromorphological status. Two European standards on hydromorphological assessment of rivers and hydromorphological assessment methods used in Poland are reviewed in the context of their applicability for river restoration purposes. River Hydromorphological Quality assessment method is presented with a case study of the Biała River, Polish Carpathians, where this assessment was

used as basis for a restoration project aimed to establish an erodible river corridor. The results of the assessment revealed significant differences in hydromorphological quality between unmanaged and channelized river cross-sections, indicating channel regulation as a major cause of the hydromorphological degradation of the Biała and confirming the choice of the erodible river corridor as an appropriate method of its restoration. The assessment indicated hydromorphological features of the river that were severely modified within the channelized reaches and which are likely to improve the most with the removal of bank protection and allowing free channel migration.

✉ Bartłomiej Wyźga
wyzga@iop.krakow.pl

Hanna Hajdukiewicz
hanahaj@gmail.com

Joanna Zawiejska
zawiejsk@up.krakow.pl

Antoni Amirowicz
amirowicz@iop.krakow.pl

Paweł Ogłęcki
oglecki@poczta.onet.pl

Artur Radecki-Pawlik
rmradeck@cyf-kr.edu.pl

Keywords Hydromorphological quality · Hydromorphological assessment · European standard · River restoration · Erodible river corridor

Introduction

Human activity affects the state of riverine ecosystems through direct impacts on river biocoenoses (e.g. introduction of alien and invasive species), changes in water quality or physical state of habitats. Negative effects of deteriorated water quality on river ecosystems resulting from increased input of biogenic substances and pollution from sewage, agriculture or industry (Meybeck 2003) have been extensively described in the literature. Over the last decades, methods of assessment of the physicochemical water parameters were standardized (EPA 2001) and attempts to improve the quality of river water were commonly undertaken. Despite the widespread occurrence of practices leading to river change (e.g. channelization, gravel mining, disruption of river continuity by dams and flow regulation by dam reservoirs), their negative effects

¹ Institute of Nature Conservation, Polish Academy of Sciences, al. Mickiewicza 33, 31-120 Kraków, Poland

² Institute of Geography, Pedagogical University of Cracow, ul. Podchorążych 2, 30-084 Kraków, Poland

³ Department of Environmental Engineering, Warsaw University of Life Sciences, ul. Nowoursynowska 159, 02-787 Warsaw, Poland

⁴ Department of Hydraulics Engineering and Geotechnique, University of Agriculture, al. Mickiewicza 24/28, 30-059 Kraków, Poland

⁵ Faculty of Civil Engineering, Cracow University of Technology, ul. Warszawska 24, 31-155 Kraków, Poland

on the physical state of habitats and river biocoenoses were recognized relatively late (Muhar and Jungwirth 1998). In many countries, the necessity to improve the quality of river habitats only recently started to be noticed by water management authorities.

The term hydromorphology was introduced to describe physical river characteristics and processes as they determine the condition of river ecosystem. Hydrological regime, river continuity and morphological conditions were indicated in the Water Framework Directive as the three key elements of hydromorphological river quality (European Commission 2000).

According to the Water Framework Directive, the assessment of hydromorphological conditions supports the assessment of biological components of river ecosystems (European Commission 2000) which play a decisive role in the evaluation of river status. However, this assumption only reflects the feasibility of diagnosing the state of river biocoenosis rather than the conditioning factors. In reality, hydromorphological conditions are the primary control on the biotic elements of river ecosystems (Vaughan et al. 2009; Elozegi et al. 2010) as they influence the species richness of river communities (Elozegi et al. 2010) and many ecosystem functions such as nutrient and organic matter storage, rates of decomposition of organic matter, primary production and ecosystem respiration (Elozegi and Sabater 2013).

Proper functioning of river ecosystem requires its three-dimensional connectivity: undisturbed migration of biota and sediment transfer along the river, at least seasonal connectivity between river water and water bodies in the floodplain area, and vertical connectivity between river and hyporheic zone (Kondolf et al. 2006). Furthermore, the key controls on river hydromorphological quality are the spatial complexity of habitats and dynamism of hydrological and morphological processes (Elozegi et al. 2010). Even with the lack of human intervention in river channels and floodplains, hydromorphological conditions are not static but undergo constant changes as the rivers adjust to changing environmental conditions in the catchments and valley floors (Dufour and Piégay 2009). This creates the need to determine the dynamically changing reference conditions that relate to the contemporary environmental conditions in the catchments (Wyźga et al. 2012b).

With the degradation of river ecosystems, in several countries actions were undertaken to improve their state or re-establish natural features of river hydromorphology (Habersack and Piégay 2008; Rinaldi et al. 2013c). In Europe, restoration efforts were supported by the regulations of the Water Framework Directive that obliged the member states to re-establish good ecological status of rivers by 2015 (European Commission 2000). Consequently, a number of assessment methods were developed in particular countries to enable systematic evaluation of

river hydromorphological quality (Rinaldi et al. 2013a). Attempts at the standardization of these procedures brought about reviews (Belletti et al. 2015) and comparisons of the methods used in different countries (Raven et al. 2002; Scheifhacken et al. 2012), and the European Committee for Standardization published two standards with the nomenclature and framework for hydromorphological evaluation of rivers (Boon et al. 2010). However, many of the applied methods have one or more limitations: (1) they had been developed before the introduction of the Water Framework Directive and even though they provided the basis for its hydromorphological guidelines, they are not fully adjusted to its regulations; (2) they consist in static inventory of river habitat features and as such do not allow recognition of the ongoing hydrological and geomorphological processes; (3) they are general and involve little or no field surveys. As a consequence of the two latter limitations, these methods of assessment are of very limited use for the purposes of river restoration. The adequate assessment method should be based on detailed recognition of the extent and causes of degradation of river's hydromorphological conditions and allow the analysis of this state not only in the context of past human intervention in the river channel and corridor but also in the context of river adjustment to environmental changes (Wyźga et al. 2012b; Rinaldi et al. 2013b).

In Poland, significant degradation of many rivers calls for restoration measures that would allow improvement of river integrity. Hydromorphological evaluation of rivers in the country has been performed with a few methods (Lewandowski 2012). The lack of a versatile, suitable method of assessment led to the development of River Hydromorphological Quality (RHQ) method (Wyźga et al. 2009, 2010b) designed also for the purpose of planning and evaluation of restoration measures.

This paper aims to provide:

- a critical review of European standards on the assessment of river hydromorphology;
- an overview of the methods of river quality assessment most widely used in Poland;
- a presentation of the RHQ method and its use with a case study of the Biała River as well as the discussion of applicability of this method for river restoration purposes.

European standards of hydromorphological assessment

Studies focused on developing methods of hydromorphological assessment of rivers started in European countries long before the introduction of the Water Framework

Directive; and in Poland in the early 1990s (Lewandowski 2012). The directive created the need for unification of the methods of hydromorphological assessment of rivers, resulting in the publication of two guidance standards by the European Committee for Standardization (Boon et al. 2010). European Standard EN 14614 (CEN 2004) indicated guidelines for hydromorphological assessment of river features. It indicated 10 assessment categories, six of which related to the assessment of channel, two to banks and riparian zone, and two to floodplain/river corridor (Table 1). For particular categories, the standard identified hydromorphological features that should be assessed (Table 1).

European Standard EN 15843 (CEN 2010) provided guidelines to the assessment of anthropogenic modifications of river hydromorphology. Among the assessment categories listed in EN 14614 standard, those crucial for the evaluation of anthropogenic modification to river hydromorphology (so-called core categories) were now distinguished from the remaining group of subsidiary

categories of features that may exert a positive influence on the quality of river habitats (Table 1). The standard asserts that categories from the first group do not require definition of reference conditions and the degree of modification in each category is considered proportional to the share of the modified part of assessed reach in its total length. Only the evaluation of the second group of categories requires comparison of the observed river state to the reference conditions defined for the relevant river type.

This second European standard contains both valuable elements and ones that make this methodology of hydro-morphological river assessment of little or no use for river restoration purposes. Undoubtedly, the advantage of the standard is that it uses a degree of deviation from natural conditions, and not the abundance of morphological conditions considered beneficial for river biota, to assess river hydromorphological quality (Boon et al. 2010).

The method of assessment presented in the standard is largely simplified; this can be advantageous if rapid evaluation of numerous rivers is to be performed to comply

Table 1 Assessment categories and features of the channel, banks, riparian zone and floodplain of the Biała assessed to evaluate the hydromorphological quality of the river according to the European

Standard EN 14614 (CEN 2004) and classification of assessment features as core or subsidiary in the European Standard EN 15843 (CEN 2010)

No.	Assessment category	Assessed feature	Core/subsidiary feature
Channel			
1	Channel geometry	Channel planform	Core
		Channel cross-section and longitudinal profile	Core
2	Substrate	Artificial/natural bed substrate	Core
		Degree of modification of substrate material	Subsidiary
3	In-river vegetation and organic debris	Aquatic vegetation and island vegetation within the river's active zone ^a	Subsidiary
		Organic material (leaves, woody debris)	Subsidiary
4	Erosion/deposition features	Presence of erosional and depositional channel forms	Subsidiary
5	Flow	Modification of natural flow hydraulics by engineering works and structures	Core
		Modification of natural flow regime	Core
		Degree of connectivity between river channel and hyporheic zone ^a	Not considered in EN 15843
6	Longitudinal river continuity	Impact of engineering structures on longitudinal river continuity—sediment transport and biota migration	Core
Banks and riparian zone			
7	Bank structure	Modification of river banks (material, profile, height)	Core
8	Riparian zone	Vegetation and land use in the riparian zone	Core
Floodplain			
9	Land use and associated features in the river corridor	Land use in the river corridor/floodplain	Core
		Presence of remnant channels, oxbows and mires within the floodplain	Core
10	Lateral connectivity and channel migration	Degree of lateral connectivity of river and floodplain, and continuity of floodplain along the river	Core
		Constraint on lateral channel movement	Core

^a Feature modified or added to the list indicated in European Standard EN 14614

with the requirements of the Water Framework Directive. However, it will be entirely unusable for river restoration that must be based on adequate and credible recognition of the degree and causes of degradation of the river in question. A serious flaw of this methodology is the lack of relating the state of the assessed river to relevant reference conditions and the assessment of several categories of features on the basis of the percentage of river length in which they have been modified, without considering the degree of the modification.

This opinion can be illustrated with the following example. Planform geometry of a wide river with multi-thread channel may be variously modified by human activity. In the most extreme case, channelization of the multi-thread channel will result in the formation of a significantly narrower, single-thread channel. Transformation of the channel planform can also consist in its partial constriction with groynes and a reduction in the number of low-flow channels, while the multi-thread channel pattern is maintained. If both such changes occur along a similar length of assessed river reaches, according to the EN 15843 methodology the degree of channel modification should be considered equal in either case. At the same time, it is evident that the degree of deviation from natural conditions for both cases is different. This example can be related to the Italian river Tagliamento which is considered a model ecosystem of an Alpine river with undisturbed, braided channel pattern (Tockner et al. 2003). Over the past century, the width and the braiding index of the Tagliamento decreased by half (Surian and Rinaldi 2004), partially as a result of the river adjustment to decreasing bedload supply and partially because of engineering works carried out along the entire reach length. According to the EN 15843 standard, the current channel planform should then be considered extremely modified, which contradicts the wide recognition of the state of this river as nearly natural. Similar paradoxical results are obtained when EN 15843 methodology is applied to assess other categories of river hydromorphological quality.

Hydromorphological assessment methods and their utility for river restoration purposes

Attributes of assessment methodology useful for river restoration purposes

To be applicable for the purposes of river restoration, a method of hydromorphological assessment must fulfill the following criteria:

- the assessment should aim to determine the degree of deviation from typical undisturbed conditions for a

given river rather than the abundance of habitat features beneficial for river biota (CEN 2010) that may vary between different types of watercourses;

- degree of modification of river hydromorphology is determined in relation to reference conditions that define the best attainable river state under contemporary environmental conditions in the catchment (Wyżga et al. 2012b);
- the assessment is largely based on field surveys to allow adequate recognition of the type, location and extent of the modification to river hydromorphology;
- the methodology allows to recognize hydrological and geomorphological processes that control the state of the river ecosystem, including the processes of river adjustment to changing environmental conditions (Rinaldi et al. 2013b).

Methods of hydromorphological assessment and their suitability for river restoration purposes

Below we review the general groups of methods of hydromorphological assessment in the context of their applicability for the purposes of river restoration. Methods evaluating the quality of physical river habitats, such as the German LAWA-FS (LAWA 2000) or the British River Habitat Survey, RHS (Raven et al. 1997), are most common worldwide and have been in use the longest (Rinaldi et al. 2013a; Belletti et al. 2015). This category encompasses methods for the survey and characterization of physical habitat elements, which can be classified as river habitat surveys or physical habitat assessments (Belletti et al. 2015). Although these methods are based on field surveys, they do have certain limitations which put in question their applicability for hydromorphological assessment in river restoration projects. With the large number of parameters to be assessed, these methods are time-consuming but yield a static image of a river unrelated to ongoing geomorphological processes, especially the existence or lack of geomorphic dynamic equilibrium and the processes of river adjustment to changing environmental conditions (Rinaldi et al. 2013a, c). Of this group, the RHS is rather popular in Poland (Szozkiewicz et al. 2007).

In Europe, several methods of hydromorphological assessment have been developed for the purposes of monitoring required by the regulations of the Water Framework Directive (Rinaldi et al. 2013a). Some of these methods are relatively new: e.g. HEM in the Czech Republic (Langhammer 2007) or Polish MHR (Ilnicki et al. 2010a). The main aim of these methods is to provide a fast assessment of many rivers to determine their hydromorphological state and report on it to the European

Table 2 Comparison of hydromorphological assessment methods used in Poland and their applicability for river restoration

Method	Reference conditions	Criteria used in hydromorphological evaluation	Field data collection	Consideration of physical processes	Applicability for river restoration ^a
River habitat survey (RHS)	Combination of near-natural habitat conditions with habitat quality score within the 20% highest ranked sites	Degree of habitat modification and habitat quality (based on the diversity and richness of habitat features beneficial for river biota)	All evaluated features	Not included	Limited
Hydromorphological monitoring of rivers (MHR)	River state in the mid-20th century, prior to intensification of agriculture	Degree of deviation from undisturbed (reference) conditions	Some features surveyed along 10% of the length of evaluated river	Not included	No
River hydromorphological quality (RHQ)	Best attainable river state under current environmental conditions in the catchment but without human impact on the river	Degree of deviation from undisturbed (reference) conditions	All evaluated features	Included	Yes

^a Refers to the method sensitivity to identify features that would need to be restored and will probably be improved by restoration measures

Commission. Their general approach is thus in agreement with the expected outcomes. These methods are based on the analysis of maps, aerial photos and orthophotos as well as information in existing relevant databases, with very little data collected in field surveys, which severely limits the use of these methods for detailed planning and monitoring of restoration projects.

The third group of methods used in many countries is these based on field inventory of the river condition but in which evaluation is also based on the assessment of the ongoing processes, such as existence or lack of three-dimensional connectivity of river ecosystem, stability, erosion or accretion of river banks and channel adjustment to environmental conditions. These methods involve evaluation of the entire river corridor and both present and recent river change analysed on maps, aerial photos and orthophotos (Rinaldi et al. 2013a; Belletti et al. 2015). This group of methods includes, among others, the Australian River Styles Framework (Brierley and Fryirs 2005); IHG method in Spain (Ollero et al. 2011), MQI in Italy (Rinaldi et al. 2013b) and Polish method of river hydromorphological quality assessment RHQ (Wyźga et al. 2009, 2010b, 2012b). Consideration of ongoing processes and field recognition of the river state make these methods most suitable for river restoration purposes.

Methods of hydromorphological assessment used in Poland

Below we briefly describe principal methods of hydromorphological assessment used in Poland. River Habitat Survey method, developed in the UK, belongs to the

methods assessing physical river habitat and is frequently used in Poland where its application is facilitated by a country-specific manual (Szozzkiewicz et al. 2007). This method does not account for ongoing geomorphological processes and some other deficiencies related to its use are specified below (Table 2). The method determines the degree of anthropogenic modification of the river habitat and its quality reflected in the presence and richness of the features considered beneficial for river biota (Raven et al. 1997). The set of hydromorphological parameters existing under undisturbed conditions may differ considerably between rivers in different physiographic settings (Kujanová et al. 2016) and, thus, hydromorphological evaluation based on habitat quality index does not seem appropriate as in many rivers low richness or diversity of habitat features is natural and reflects naturally low morphological diversity of these rivers (Wyźga et al. 2012b). Although the users of the RHS method notice various degrees of diversity of particular river habitat features in different regions (Szozzkiewicz et al. 2006), they persist in using the index of habitat quality. The RHS method also uses habitat quality as one of the components in defining reference conditions for a particular river type. High-quality (reference) hydromorphological conditions are here associated with the sites in which the low degree of anthropogenic modification allows them to be classified as near-natural and the habitat quality score falls within the 20% highest ranked sites (Raven et al. 2002).

The Polish MHR method was developed for the rapid assessment of rivers for the purposes of the Water Framework Directive. As a result, only few analysed parameters are determined in a field survey along 10% of

the length of an assessed river (Ilnicki et al. 2010a). The method evaluates an almost full range of river features indicated in the EN 14614 standard (Ilnicki et al. 2010a); however, it also has a few serious flaws indicated below (Table 2). Descriptive/qualitative evaluation of some parameters prohibits their inclusion in the quantitative indices of hydromorphological quality. Bed substrate that cannot be assessed with use of cartographic data is excluded from evaluation. Reference conditions were defined as those existing in the mid-20th century, prior to the intensification of agriculture in the catchments (Ilnicki et al. 2010b). This manner of defining reference conditions is hardly acceptable; although cultivation may significantly impact river water quality, especially the content of biogenic substances, its influence on hydromorphology is negligible, particularly in comparison with channelization works. In mountain catchments, agricultural practices may increase the supply of fine sediment to the rivers, but in Europe, including Poland, the culmination of agricultural and pastoral pressure in mountain areas occurred in the 19th century and has since progressively decreased (Kondolf et al. 2002; Wyzga et al. 2012b). Finally, in the case of some parameters such as channel slope, width and depth or bank inclination, their higher variability is associated with a better state of the river (Ilnicki et al. 2010a). This resembles the manner of evaluation typical of RHS method, based on the diversity of habitat features rather than on the degree of deviation from the conditions that would be natural for a particular river (surface water body).

With a lack of relevant assessment procedure that would provide insight into both river state and active fluvial processes in Poland, a new method of assessment—River Hydromorphological Quality, RHQ, was developed (Wyzga et al. 2009, 2010b) to enable evaluation of hydromorphological river conditions in the context of its contemporary dynamics. This method is described in detail below.

Hydromorphological assessment of river quality with RHQ method

Hydromorphological evaluation can be carried out for parts of a river course with similar hydrology and morphology (surface water bodies), for segments of water bodies (survey units) or for river cross-sections (CEN 2004). Evaluation with RHQ method can also be performed for these spatial units of rivers. This paper presents evaluation of 20 cross-sections of the Biała River located in its upper and middle course that was performed with this method.

Hydromorphological assessment of the river in the analysed cross-sections involved scoring of 10 groups of features of the channel, banks and riparian zone as well as

floodplain/river corridor (Table 1) specified in the European Standard EN 14614 (CEN 2004; Wyzga et al. 2010b). Two features were added to the ones listed in the European Standard EN 14614: river island vegetation and the degree of connectivity between river channel and hyporheic zone. As a result, assessment of aquatic vegetation was replaced with the assessment of both aquatic and terrestrial vegetation in the active zone of the river. This better reflected the role of island vegetation in the formation of the ecosystem of multi-thread rivers (Mikuś et al. 2013) and the differences in the naturalness of vegetation on islands and in the riparian zone of mountain rivers (Kaczka et al. 2008). In the evaluation of modifications to river flow, the assessment of runoff regime and flow hydraulics was supplemented with the assessment of the degree of connectivity between river channel and hyporheic zone. Unrestricted water exchange between river channel and the alluvium is important for river biota (Brunke and Gonsler 1997), and its anthropogenic disturbances such as clogging of interstices in the gravel framework with fines (Wood and Armitage 1997) or significant channel incision and transformation of alluvial boundary conditions into bedrock ones (Rinaldi et al. 2013c) limit or prevent such exchange. This feature should be evaluated for almost all river types with the exception of watercourses that naturally flow in bedrock channels. By contrast, naturalness of river island vegetation can be evaluated only for island-braided (multi-thread), wandering and anastomosing rivers.

Hydromorphological assessment of the river is preceded by field inspection and the presentation and analysis of extensive data on the river to achieve congruent understanding of the evaluation procedure and river state. First, for each assessed hydromorphological feature, near-natural and extremely modified conditions are defined. Near-natural conditions correspond to the development of a given feature under reference conditions for the particular river, whereas similar extremely modified state (e.g. paved floodplain) may be relevant for a range of river types. For example, near-natural conditions in the floodplain area/river corridor were described as a mosaic of various successional stages of vegetation, including tamarisk (*Myricaria germanica*) and willow shrubs and mature willow or alder forest (Fig. 1a). Extremely modified conditions were represented here by a parking area with impermeable surface and typified by very low hydrodynamic roughness (Fig. 1b). In turn, near-natural conditions of lateral connectivity and channel migration accompanied unprotected alluvial channel banks with the height typical of the vertically stable river (Fig. 2a). Extremely modified conditions were represented by the presence of bank reinforcement and significant channel incision, precluding lateral channel migration and inundation of riparian areas by floodwaters (Fig. 2b). With near-natural and extremely



Fig. 1 Examples of near-natural (a) and extremely modified conditions (b) for land use in the river corridor. Under near-natural conditions, various successional stages of vegetation occur in the floodplain area, from tamarisk (*Myricaria germanica*) and willow shrubs to mature willow or alder forest. The asphalt-paved parking place adjacent to the river bank represents extremely modified conditions

modified states of a given feature identified, particular experts evaluate the spectrum of conditions between these extreme states in terms of their impact on the quality of the river ecosystem.

Second, hydromorphological reference conditions are indicated as those representing the best attainable river state. Significant environmental changes that occurred in the Polish Carpathian catchments during the 20th century, especially a decline in high-intensity farming and grazing and subsequent hillslope afforestation (Lach and Wyżga 2002; Kozak et al. 2007), preclude use of the historical state of the rivers, presented on 19th-century maps, as hydromorphological reference conditions (Wyżga et al. 2012b). Instead, the conditions should be defined as the river state that exists or would exist under contemporary environmental conditions in the catchment but with no human modifications to channel, riparian areas and floodplain of a river (Wyżga et al. 2012b).

Third, the current state of the river is characterized with diagrams of channel morphology in the assessed cross-

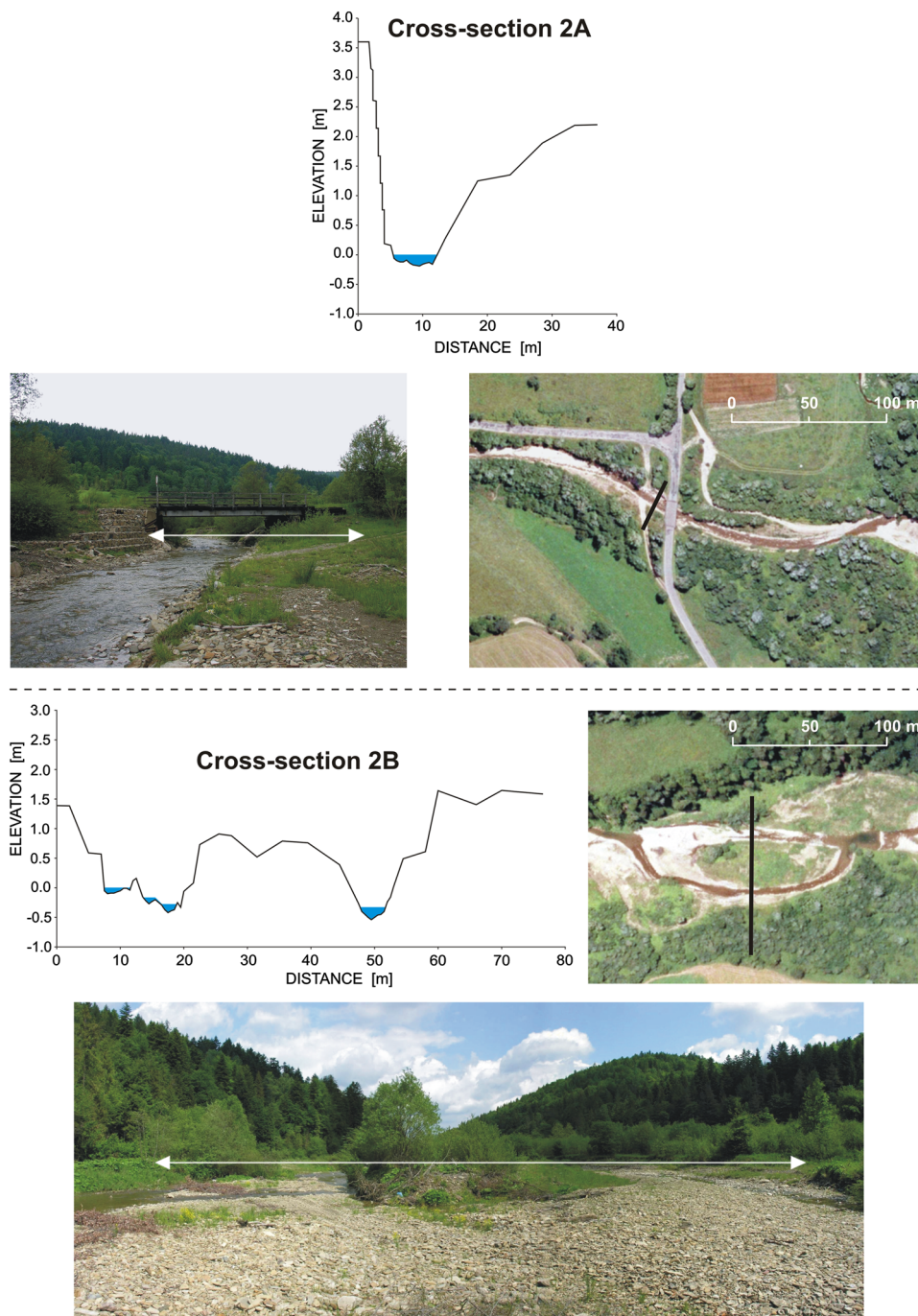


Fig. 2 Examples of near-natural (a) and extremely modified conditions (b) for lateral connectivity of the river ecosystem and channel migration. The unmanaged, sinuous channel can freely migrate on the floodplain. The mode of river channelization presented in the lower photo results not only in the lateral stability of the channel but also in the loss of lateral connectivity of the river ecosystem

sections, photographs of the cross-sections and position of the river on the orthophoto (Fig. 3). Finally, changes that occurred in the river sections adjacent to the assessed cross-sections over the last few decades are presented using historical maps as well as archival aerial and ground photographs from the second half of the 20th century (Fig. 4). From this period, good cartographic and photographic documentation of river changes is available and it provides information on both human-induced modification of the river and trends in channel adjustment to changing environmental conditions (Wyżga et al. 2010b), especially important as some of these changes could have been very fast (Fig. 4). The analysed river sections should extend upstream and downstream of the evaluated cross-sections on the length of at least 2 channel widths from the beginning of the period considered; their absolute length is thus variable depending on the river size in a given valley reach and the degree of change in channel width over the last few decades.

Hydromorphological evaluation of the river was performed by five experts in fluvial geomorphology, river engineering and freshwater ecology. Each river feature

Fig. 3 Examples of the sources of information used to evaluate hydromorphological quality of the Biała in the surveyed cross-sections from the upper course of the river, shown for *cross-section 2A* with single-thread, regulated channel and *cross-section 2B* with multi-thread channel



was scored on a scale from 1 (near-natural conditions) to 5 (extremely modified conditions). For categories consisting of two or three evaluated features (Table 1), the score was averaged. Final evaluation of the hydromorphological quality in a cross-section was expressed by the average of scores in the assessed categories, given by the five experts. Based on this final score, particular cross-sections were associated with one of the five classes of hydromorphological quality (high, good, moderate, poor and bad).

Hydromorphological assessment of the Biała river

Study area

The Biała is a gravel-bed river draining a catchment with an area of 983 km² in the Polish Carpathians (Fig. 5). The river rises at about 730 m a.s.l. and has relatively gentle channel slope that decreases from 0.017 to 0.003 on the length of the studied sections. With such channel slope, the river is typified by a riffle and pool channel pattern



Fig. 4 Incision of the Biała River and transformation of its alluvial channel into a bedrock one that occurred between 2004 and 2009 in the vicinity of site 1 as a result of upstream-progressing bed degradation induced by the gravel exploitation carried out 1 km downstream. The photos are examples of the data used to present changes of the river having occurred over the few past decades in the vicinity of the evaluated cross-sections

according to the classification of Montgomery and Buffington (1997). In its upper course, the river flows through low mountains of Beskid Niski where it is supplied with coarse and medium-sized sandstone material. Very high flow variability in this part of the Biała and the delivery of coarse, non-cohesive sediment to the unmanaged river result in the formation of a wide, multi-thread channel (cf. Wyźga et al. 2016b). In the middle course within the Ciężkowice Foothills, the Biała flows across alternating sandstone and shale complexes that are the source of cobble to pebble material along with large volumes of fines. As a result, the Biała remains a gravel-bed river but under undisturbed conditions it forms a sinuous channel.

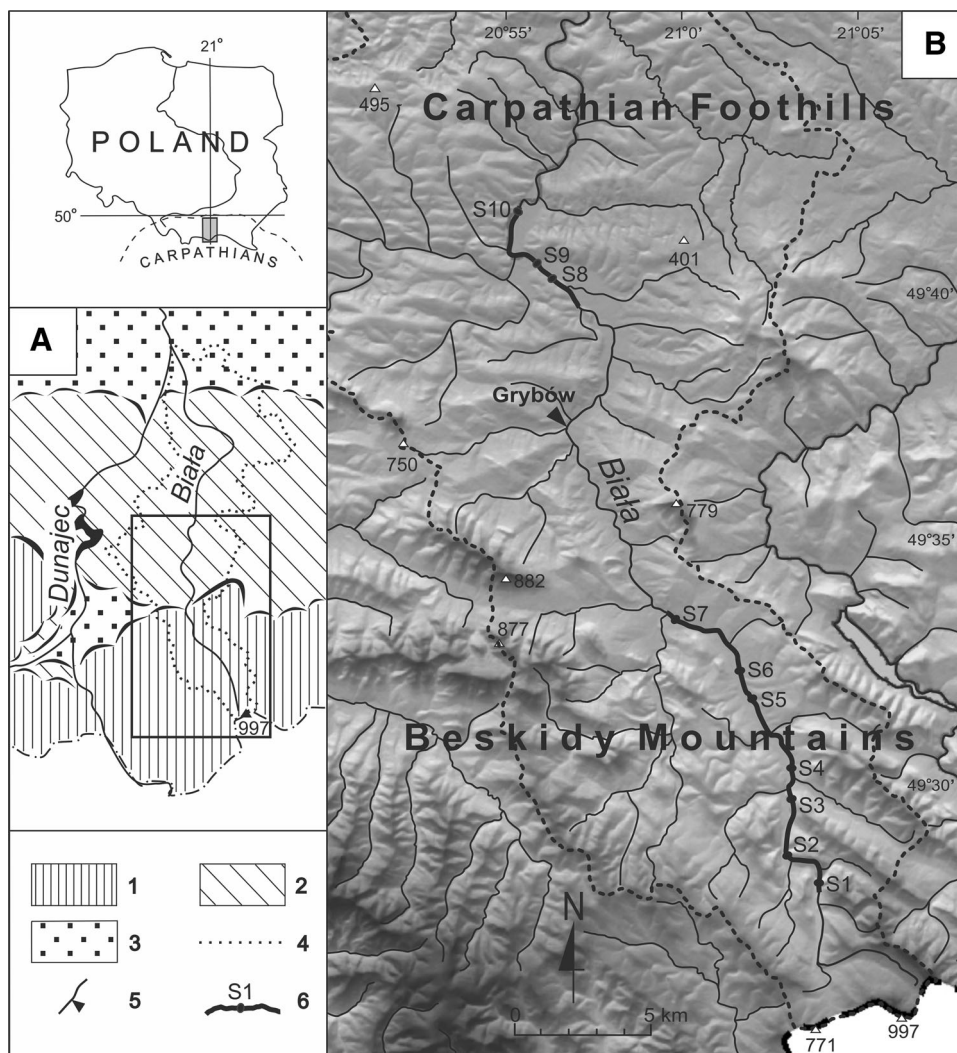
In the 20th century, the Biała was subjected to severe modification resulting from human activity. In the lower part of its upper course and along the entire middle course, channel width decreased significantly (to a quarter or a sixth of the initial value) and the river incised by as much as 2.5 m. The principal cause of these changes was river channelization leading to the formation of a narrow and

straight channel (cf. Wyźga 2001, 2008). These changes were strengthened by widespread, uncontrolled in-channel gravel mining (cf. Rinaldi et al. 2005). The tendency to channel narrowing and incision could have also been reinforced by a reduction in sediment supply to the river (cf. Lach and Wyźga 2002) resulting from a considerable increase in forest cover in the mountain part of the catchment after the World War II (Kozak et al. 2007). Some human impacts such as illegal in-channel gravel mining (Wyźga et al. 2010a) and the removal of large wood from the river have continued also in recent years.

Channel changes presented above are known to incur a range of negative effects, such as decreased storage of floodwater in floodplain areas and the resultant increase in peak flows of flood waves in downstream river reaches (Wyźga 1997; Kundzewicz et al. 2014; Wyźga et al. 2016a) or deterioration of the state of river biocoenosis (Wyźga et al. 2013). To limit the negative consequences of the channel changes and improve hydromorphological quality of the Biała, an erodible river corridor was established in the mountain and foothill river sections (14.5 and 5.9 km in length, respectively) (Fig. 5). Both parts of the corridor consist of alternating river reaches with a given type of channel management: longer (1–3 km) unmanaged reaches and shorter (0.1–0.3 km) channelized ones adjacent to bridges. Following establishment of the corridor, the river is allowed to develop its channel freely in the unmanaged reaches, whereas it remains channelized in the vicinity of bridges. Future improvement of hydromorphological state of the river, resulting from unrestricted formation of the Biała channel within the corridor, is thus expected to occur in the unmanaged reaches, whereas the state of the channelized reaches will most likely remain unchanged.

Prior to the start of the restoration project on the Biała, hydromorphological quality assessment was performed for 10 sites, with each site consisting of a pair of cross-sections located in neighbouring unmanaged and channelized river reaches. These pairs of cross-sections were selected to determine differences in hydromorphological quality of the river between its channelized and freely developing reaches at the beginning of the restoration project. Hydromorphological assessment will be repeated at the end of the project to demonstrate its effectiveness in improving the river status in the unmanaged reaches. The average distance between unmanaged and channelized cross-sections at the sites equals 780 m and is 22 times greater than the average channel width in the twenty studied cross-sections. It is considered sufficiently large to ensure that fluvial processes in the unmanaged cross-sections are not influenced by hydraulic conditions in the channelized cross-sections. The chosen pairs of cross-sections are located between major tributaries (Fig. 5) and carry similar

Fig. 5 *a* Location of the Biała River in relation to physiogeographic regions of southern Poland. *b* Upper and middle parts of the Biała catchment and detailed setting of the studied sites. 1 mountains of intermediate and low height; 2 foothills; 3 intramontane and submontane depressions; 4 boundary of the Biała catchment; 5 flow-gauging stations; 6 study sites (S1 to S10) and river sections proposed for erodible river corridor. In the figure, sites are indicated in half distance between the unmanaged and the channelized cross-section from a given site



flow. With such location of the cross-sections, the Wilcoxon signed rank test was used to determine statistical significance of the differences in the scores of hydromorphological river quality between the evaluated unmanaged and channelized cross-sections.

Hydromorphological reference conditions

The most obvious and direct approach to determine reference conditions in the RHQ method is to use characteristics of a river reach that remains in a near-natural state (Wyźga et al. 2012b). However, in the case of the Biała even those reaches which are currently devoid of regulation structures have been affected by earlier (channel training and incision) and recent human activities (uncontrolled gravel extraction or the removal of large wood), and as such they cannot provide information on a reference state of the river. Therefore, reference conditions were determined based on analogue but undisturbed river reaches draining catchments

with similar size and environmental conditions (in terms of relief and land use).

Under undisturbed channel conditions, environmental controls on the upper course of the Biała should lead to the formation of a multi-thread channel (cf. Wyźga et al. 2016b). Very few multi-thread river reaches have been preserved in the Polish Carpathians and an unmanaged reach in the middle course of the Czarny Dunajec is the closest analogue of the environmental conditions in the Biała. Using the Czarny Dunajec River as an analogue, reference conditions for the upper Biała can be defined as the occurrence of alluvial, island-braided channel. In its unmanaged reach, the Czarny Dunajec forms a heavily island-braided channel (Wyźga et al. 2010b, 2012b). Because the Biała exhibits significantly higher flow variability, the resultant high lateral mobility of its channel would most likely reduce the development of islands in the river's active zone, typical of the Czarny Dunajec. The latter river typically supports a few low-flow channels, but

at low to medium water stage only some of them convey a significant proportion of the total flow and have fast water current, whereas the other channels, mostly fed by groundwater, carry low discharges and exhibit slow velocity. Particular channels may differ in depth, width, slope and bed-material grain size (from cobbles to sand or mud). Braids are separated by gravel bars or wooded islands. Riparian zone, floodplain and islands are overgrown with natural, diverse plant communities including herbal communities, tamarisk (*Myricaria germanica*) and willow shrubs, and mature willow or alder forest. Large wood deposition is common within the river, with a significant proportion of wood deposits represented by whole trees and shrubs (Wyźga and Zawiejska 2010; Wyźga et al. 2015). The river channel has remained vertically stable (no long-term trend in its vertical position has occurred despite the occurrence of short-term fluctuations) at least during the so-called engineering time, i.e. over several decades. For upper sites of the Biała, the analogue reference height of the river banks equals a few tens of centimetres, whereas for sites 6–7 it is 1.2–1.5 m. Dry palaeochannels and oxbows are present on the floodplain.

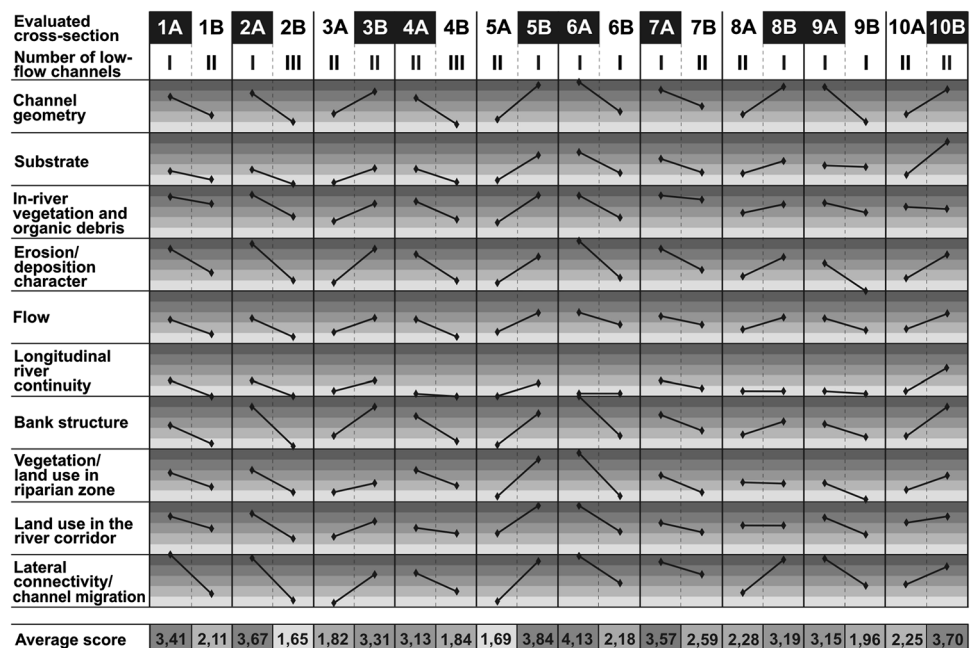
Under undisturbed channel conditions, Carpathian rivers draining catchments with similar environmental conditions to the middle Biała catchment form sinuous gravel-bed channels with a distinct tendency to meander (Wyźga 2001), and such reference conditions were indicated for the Biała in the lower section of the planned erodible river corridor (sites 8–10). Such rivers normally carry flow in a

single channel; however, occasionally mid-channel bars form within a riffle area leading to the division of flow, and chutes may form inside channel bends that at low to medium water stage are fed by groundwater. Gravel point bars are large. River banks are asymmetric: concave banks are steep and eroding, while convex ones are gentle and aggrading. In vertically stable rivers, a third to a half of the bank profile consists of overbank sands and muds. Convex sides of channel bends are gradually colonized by vegetation, from pioneer herbal communities encroaching on bar tops, to willow shrubs and mature willow and poplar forest. Oxbows and dry, crescent-shaped palaeochannels are common on the floodplain.

Hydromorphological quality of the river at the assessed sites

Results of the evaluation of particular categories of hydromorphological quality of the Biała and aggregated scores for the paired cross-sections are presented in Fig. 6. The assessment scores ranged from 1.65 (high quality) to 4.13 (poor quality). Scores for the unmanaged cross-sections ranged from 1.65 to 2.59 (Figs. 6, 7a), allowing to associate two of the cross-sections with class 1 of hydromorphological quality and eight cross-sections with class 2 (Fig. 7b). Scores for channelized cross-sections ranged from 3.13 to 4.13 (Figs. 6, 7a), with four such cross-sections falling into class 3 and six into class 4 of hydromorphological quality (Fig. 7b). The average score for the

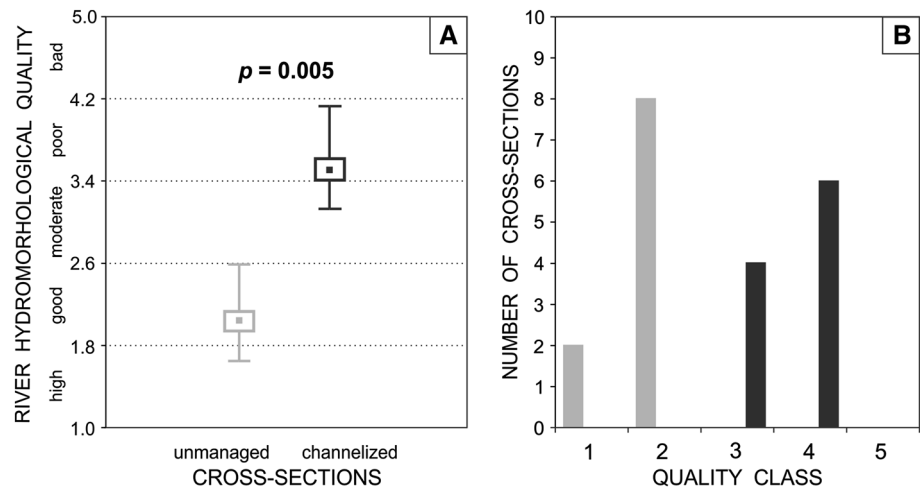
Fig. 6 Averages of the scores given by five expert evaluators for particular assessment categories and average scores of the hydromorphological river quality in the 10 surveyed pairs of channelized and unmanaged cross-sections of the Biała. Numbers of unmanaged cross-sections are shown on white background and those of channelized cross-sections on black background. All scores are shown against hydromorphological quality classes. The vertical scale for each assessed category ranges between 1 (for near-natural conditions) and 5 (for extremely modified conditions)



KEY FOR HYDROMORPHOLOGICAL QUALITY CLASSIFICATION:

1,00-1,79 - High 1,80-2,59 - Good 2,60-3,39 - Moderate 3,40-4,19 - Poor 4,20-5,00 - Bad

Fig. 7 Average scores (a) and histograms of the classes (b) of hydromorphological river quality in 10 unmanaged (grey diagrams) and 10 channelized (black diagrams) cross-sections of the Biała. The result of a Wilcoxon test for significance of the difference between average scores of hydromorphological river quality in the unmanaged and channelized cross-sections is indicated



unmanaged cross-sections was 2.04 (class 2) and 3.51 (class 4) for the channelized ones and this difference was statistically significant (Wilcoxon test, $p = 0.005$) (Fig. 7a).

Differences in hydromorphological quality were also apparent between the mountain and foothill sections of the Biała, with greater range of scores given to the cross-sections located in the mountain river course. Here, unmanaged cross-sections were associated with classes 1 and 2 (two and five cross-sections, respectively), with scores varying between 1.65 and 2.59. The class 1 cross-sections supported three low-flow channels and had diverse morphology, the presence of erosional and depositional forms and considerable cross-sectional variability of flow velocity and bed-material grain size. The cross-sections associated with hydromorphological quality class 2 lacked wooded islands and supported few wood deposits; they were also typified by modified channel geometry, decreased lateral mobility and connectivity resulting from river incision as well as cultivation of the floodplain areas (Fig. 6). Scores for channelized cross-sections ranged from 3.13 to 4.13, placing two cross-sections in class 3 and five cross-sections in class 4 (Fig. 6). Apart from longitudinal river continuity and bed material in the upstream sites, most components of the river's hydromorphological quality have been modified in these cross-sections. Despite radical changes of flow hydraulics, the overall modification of river flow in channelized cross-sections was usually assessed as moderate due to little or no modification to the runoff regime of the Biała (Fig. 6).

Variation in hydromorphological quality of the Biała in its foothill course was less pronounced but also here the two types of cross-sections received distinctly different scores. Unmanaged cross-sections represented class 2, with scores ranging from 1.96 to 2.28 (Fig. 6). A lack of wood deposits in the channel and changes to vegetation in floodplain areas associated with farming lowered the total

score (Fig. 6). Scores for the channelized cross-sections ranged between 3.15 and 3.70, with two of them associated with class 3 and one with class 4 of hydromorphological quality (Fig. 6). With fairly low degree of modification to riparian vegetation and only one of the river banks artificially reinforced, these cross-sections were considered less modified than channelized cross-sections in the upper course of the Biała. A distinctly worse score for the channelized cross-section at site 10 resulted from the disruption of river continuity by a concrete weir located about 100 m downstream from the cross-section (Fig. 6).

Variation in ten assessment categories of hydromorphological river quality

Figure 8 compares the range and average scores in particular assessment categories of hydromorphological river quality between unmanaged and channelized cross-sections of the Biała, and indicates statistical significance of the difference between the two types of cross-sections. Channelized cross-sections were scored significantly worse in all assessment categories, although the difference between scores for both types of cross-sections varied. Channel geometry was among the categories with the remarkably large difference in naturalness between the two types of river cross-sections: average scores for channelized and unmanaged cross-sections differed by two classes of hydromorphological quality (Fig. 8). Channel geometry in unmanaged cross-sections was considered near-natural or only slightly modified; the latter reflected the effect of river incision on channel geometry. In turn, channelized cross-sections have a radically changed geometry with single-thread, deep and flat-bottomed channel about three times narrower than in unmanaged cross-sections.

Average scores for bed material differed between both types of cross-sections by 1.5 quality classes (Fig. 8). Unmanaged cross-sections at sites 1–5 were typified by

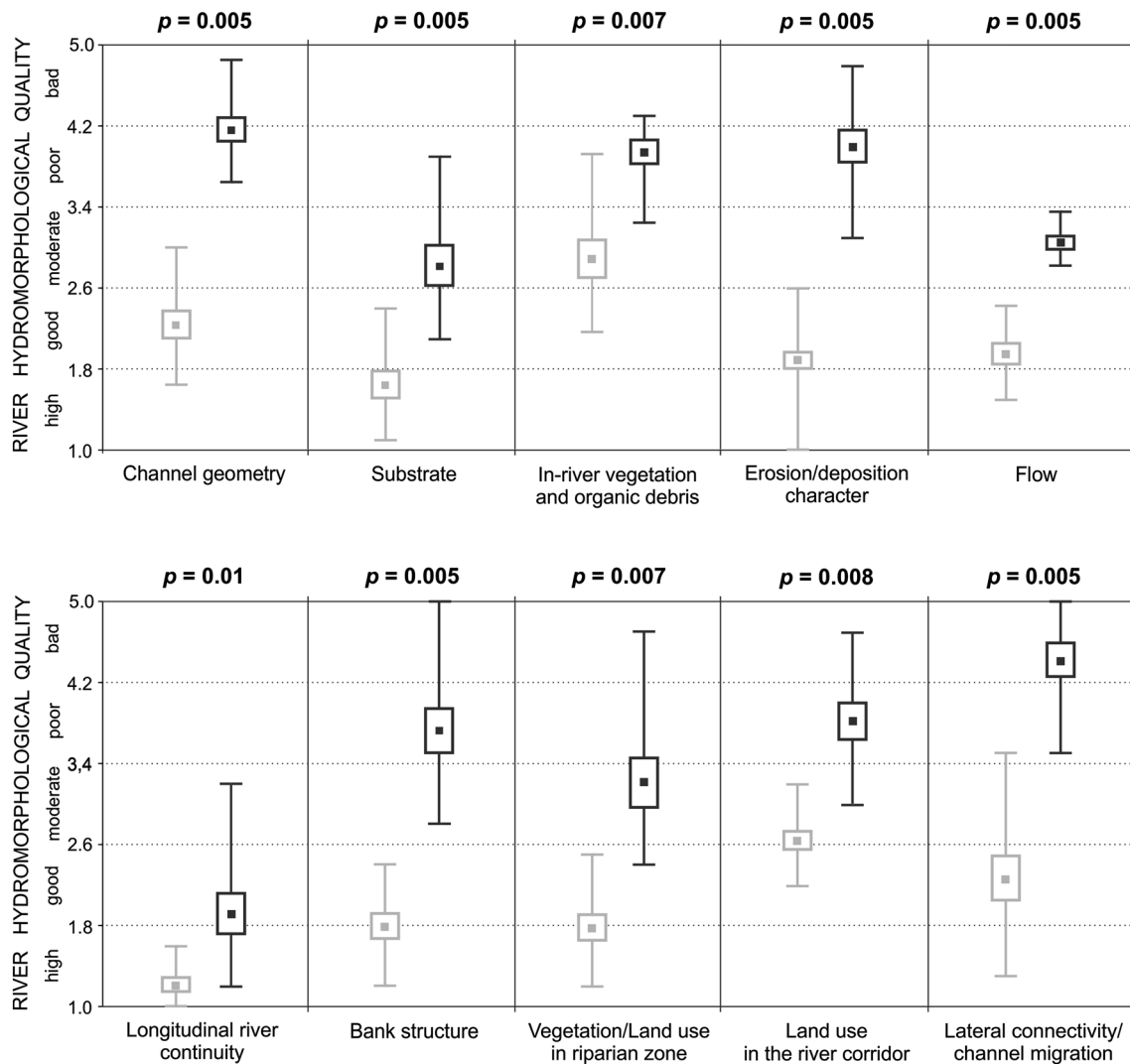


Fig. 8 Range and mean value of the average scores given in particular assessment categories of hydromorphological river quality to 10 surveyed unmanaged cross-sections (*grey diagrams*) and 10 channelized cross-sections (*black diagrams*) of the Biała. Range plots show mean value (*squares*), standard error of the mean (*boxes*) and

extreme values (*whiskers*) of the average scores. For each assessment category, statistical significance of the difference between scores given to both cross-section types, determined by a Wilcoxon test, is indicated; *p* values <0.05 are indicated in **bold**

high variability in bed-material grain size (cobbles to mud), that was considered natural, while less spatially variable bed material in the downstream unmanaged cross-sections was regarded as only slightly modified. Gravelly channel bed with well-developed armouring in channelized cross-sections was considered moderately modified. The only exception was a concrete channel bed of the channelized cross-section at site 10 that was classified as extremely modified (Fig. 6).

Scores for in-river vegetation and woody debris in channelized and unmanaged cross-sections differed by 1 quality class (Fig. 8). In both cross-section types, aquatic vegetation consisted of algal communities typical of mountain gravel-bed rivers. Wooded islands were present in only two out of seven unmanaged cross-sections in the upstream river

section where their occurrence was indicated as typical under undisturbed (reference) conditions. Wood deposits were scarce in unmanaged cross-sections and nearly lacking in channelized ones. All these features were reflected in moderate and poor quality score in this category for the unmanaged and channelized cross-sections.

Average scores for the occurrence of erosional and depositional forms differed between the two types of cross-sections by 2.5 quality classes (Fig. 8). The morphological complexity of the river bed was considered natural in a half of unmanaged cross-sections and slightly modified in the other half. With little morphological complexity of the channel bed in channelized cross-sections, the occurrence of erosional and depositional forms was considered highly modified.

Scores for the river flow in both cross-section types differed by 1.5 quality classes (Fig. 8), which reflected a radical change to flow hydraulics and constraints on the water exchange between river channel and alluvium, caused by bank reinforcements, in channelized cross-sections, but also similar runoff regime in closely located channelized and unmanaged cross-sections.

River continuity was given high-quality score in unmanaged cross-sections and good in channelized ones (Fig. 8). The latter score reflected the presence of a 2-m-high weir downstream of the channelized cross-section at site 10 (Fig. 6) and disturbances to bedload transport caused by a few narrow-span bridges in channelized river reaches.

Average scores given to river banks in the two types of cross-sections differed by 2.5 quality classes (Fig. 8). Only the river banks in unmanaged cross-sections at the upstream-located sites received very good scores. In the unmanaged cross-sections at sites 6–10, the relatively high banks partially cut in bedrock received good score. Markedly worse scores for the banks in channelized cross-sections reflected bank reinforcement with gabions or riprap on one or both channel sides.

On average, the scores for vegetation/land use in the riparian zone differed between the two types of cross-sections by nearly 2 quality classes (Fig. 8). Riparian vegetation was considered natural in the majority of unmanaged cross-sections and slightly modified in the remaining ones. Bulldozed gravelly surface along the banks in channelized cross-sections was mostly overgrown with ruderal species or grasses. In recently channelized river reaches (cross-sections at sites 5 and 6), the riparian area was entirely devoid of vegetation (Fig. 6).

River corridor in the two types of cross-sections obtained scores differing by 1.5 quality classes (Fig. 8). Half of the unmanaged cross-sections had slightly changed floodplain area and in the remaining ones modification was classified as moderate. River corridor adjacent to channelized cross-sections can hardly be inundated and is used either for grazing or housing and infrastructure; the degree of its modification was considered moderate to very high.

Channel mobility and lateral connectivity of the river and floodplain were features with the highest difference in naturalness (2.5 quality classes) between unmanaged and channelized cross-sections (Fig. 8). Bank reinforcement severely limits lateral channel mobility, while the formation of high-capacity channel in the course of river training and channel incision greatly reduces the potential for floodplain inundation and leads to the loss of lateral connectivity of the river ecosystem.

Discussion

Utility of European standards and assessment methods for river restoration purposes

Out of the two CEN standards which specified the methodology for hydromorphological assessment of rivers, the earlier EN 14614 standard (CEN 2004) is useful for planning and monitoring of restoration projects. This standard indicates the major features of the channel, river banks, riparian zone and floodplain that are key to the river hydromorphological quality. In contrast, the methodology for the assessment of anthropogenic modification to river hydromorphology proposed in the EN 15843 standard is so simplified that the resultant evaluation can only be useful for creating reports on hydromorphological monitoring of river state required by the Water Framework Directive. The lack of wider utility of the standard was reflected by the voting results during its resolution: out of 30 representatives of the member states, only 21 voted for the acceptance of the standard, while 9 abstained (Boon et al. 2010).

The methods developed for monitoring river hydromorphology, including Polish MHR method (Ilnicki et al. 2010a), aim to provide fast evaluation of many rivers to identify the degree of accomplishment of the environmental objectives of the Water Framework Directive in particular countries. That is why the methods are general and produce results that are not useful for planning and assessment of particular restoration activities. The Polish MHR method was developed to evaluate whole water bodies (rivers) and thus it cannot be used for the assessment of river reaches or particular cross-sections as it was done in the present study with the RHQ method.

In turn, a fundamental flaw of the methods of river habitat assessment is that they do not involve recognition of geomorphological processes influencing the present and the future hydromorphological state of rivers (Rinaldi et al. 2013a, c; Belletti et al. 2015), and this considerably limits their applicability for river restoration purposes. The RHS method belonging to this group involves the assessment of the richness of habitat features beneficial for river biota and includes the richness-based habitat quality in the definition of reference conditions. Consequently, the results of such assessment are incomparable to those based on the degree of deviation from the near-natural/undisturbed conditions. Moreover, the average number of sites evaluated with this method for a given abiotic river type in Poland is low, reflecting a substantially lower total number of evaluated sites (ca. 950; Szoszkiewicz and Gebler 2011) than in the UK (ca. 20,000 sites; Szoszkiewicz et al. 2006) and 26 river types distinguished in the country. This seriously reduces reliability of establishing reference conditions

(defined by the conditions at the 20% of highest ranked sites; Raven et al. 2002) and, consequently, also of calibration of hydromorphological conditions at particular sites against type-specific reference conditions.

The criteria for the applicability of a method for planning and monitoring of river restoration, indicated in the earlier part of the paper, are fulfilled by the third of the identified groups of methods, including Polish RHQ method. The set of features analysed in the RHQ method complies with that indicated in the EN 14614 standard and the assessment determines their deviation from reference (undisturbed) state. The method is applicable to any river in Poland (and elsewhere), provided that the assessment is preceded by identification of reference conditions for that river type. Reference conditions are defined taking into account their dynamic character and river adjustment to changing environmental conditions in the catchment (Wyźga et al. 2012b). This is particularly important in the context of land use changes that occurred in southern Poland during the 20th century (e.g. Lach and Wyźga 2002; Kozak et al. 2007), as well as the ongoing and future climate change predicted for the 21st century (e.g. Romanowicz et al. 2016). The method is based on field surveys that allow recognition of the development of all assessed features of the channel, banks and riparian zone as well as floodplain/river corridor. Together with the analysis of cartographic and photographic documentation, this allows the evaluators to recognize adequately the type, location and extent of modifications to river hydromorphology. Considered in the method is the degree of longitudinal, lateral and vertical connectivity of river ecosystem, river adjustment (e.g. bed armouring represents the adjustment of bed substrate resulting from the deficit of bed material in relation to river transport capacity; cf. Wyźga 2012) to environmental changes in the catchment and direct human intervention in the river channel, as well as the impact of the river change on the stability of river banks or the rate of their retreat and the potential for lateral migration of the channel. This allows to analyse the hydromorphological state of assessed river in the context of controlling hydrological and geomorphological processes. As the evaluation is performed by experts from different disciplines of river science, it reflects the opinions expressed from different perspectives and their averaged assessment gives a more objective result than evaluation performed by a specialist from a single discipline of river science (Wyźga et al. 2010b).

Hydromorphological state of the Biała and a measure for its restoration

Evaluation of the hydromorphological state of the Biała River with RHQ method showed channelized river cross-

sections to be in class 4 of hydromorphological quality, and unmanaged cross-sections in class 2, on average. This points to channel regulation as a major cause of the degradation of hydromorphological state of this river in its upper and middle course. This conclusion was in agreement with the results of a study on benthic macroinvertebrates in the river that identified channelization-induced habitat degradation as the main cause of the deterioration of the river's ecological state (Wyźga et al. 2013). Notably, the difference in scores given to both types of river cross-sections was greater at the sites where no channel incision is observed in unmanaged river reaches, but smaller where the Biała is deeply incised in such reaches. A similar pattern of hydromorphological quality was found with the RHQ method for the Czarny Dunajec River, in which channelized cross-sections differed by three quality classes from cross-sections in the unmanaged reach with a multi-thread, vertically stable channel and by two classes from those in the unmanaged reach with a single-thread, deeply incised channel (Wyźga et al. 2009, 2010b). Also in this river, the spectacular disparity in hydromorphological quality scores between different types of cross-sections was reflected in marked differences in the richness of riverine communities: fish (Wyźga et al. 2009) and benthic macroinvertebrates (Wyźga et al. 2012a).

Establishing the erodible corridor in which the river is allowed to develop its channel freely will promote improvement of the hydromorphological conditions degraded as a consequence of the river channelization and the simultaneous adjustment of fluvial forms and processes to ongoing environmental changes in the catchment. This method of restoration of the Biała will be also cost-effective in the unmanaged river reaches in which most of the riparian areas is a state property and the potential impacts of free channel migration on private lands as well as settlements and infrastructure on the valley floor are minimal (Wyźga et al. 2014). A recent occurrence of a large flood on the Biała initiated self-recovery of the river in the unmanaged reaches within the erodible corridor. The flood increased the river width in these reaches by half, on average, although the degree of river widening was smaller in the deeply incised river sections and greater in its less incised sections (Hajdukiewicz et al. 2016). After the flood, unmanaged reaches of the Biała are typified by markedly smaller values of unit stream power and bed shear stress than channelized reaches (Czech et al. 2016) and this, together with the delivery of coarse material from eroded channel banks and tributaries, will likely promote the cessation and reversal of the tendency to channel incision.

The largest differences (by two classes) in hydromorphological quality between channelized and unmanaged cross-sections were associated with channel geometry, the presence of erosional and depositional channel forms, bank

structure, channel mobility and lateral connectivity of the river and its floodplain. This enables identification of those features that will likely improve the most with the removal of bank protection and allowing free channel migration. The smallest difference in hydromorphological quality was found with regard to longitudinal river continuity which reflects the lack of transversal engineering structures (with only one exception) in the studied sections of the Biała.

The evaluation of the Biała also showed that despite significantly better hydromorphological quality of the river in the unmanaged cross-sections, in most of them and in most assessed categories this quality is still below the high category, typical of rivers with undisturbed fluvial processes. However, considering the long-term human pressure on the river over the past century, the results of the evaluation are hardly surprising. Unrestricted functioning of the river within the delimited corridor may significantly improve several elements of its hydromorphological quality, also those most modified such as in-river vegetation and woody debris or floodplain land use. A marked improvement of some hydromorphological features, such as channel planform or the presence of erosional and depositional channel forms, may be attained over several years as a result of the passage of a few flood waves. However, a few tens of years will be necessary for the incised river to form new, low-lying floodplains and for these areas to be vegetated by spontaneous succession of riparian plant communities which will next supply wood debris to the river. A direct effect of the establishment of the erodible river corridor is the onset of free channel mobility, but the expected improvement of the river's hydromorphological state may be achieved after a period markedly longer than the duration of the restoration project itself.

Conclusions

Assessment of river hydromorphological state for river restoration purposes should not only determine its current quality but also diagnose reasons for its degradation and pinpoint features that need improvement so that the planned restoration measures will be accurate and lead to an increase in river integrity. Out of the three methods of hydromorphological assessment used in Poland, only the RHQ method fulfills all the criteria for methods useful for planning and monitoring of river restoration projects. The assessment of the Biała with the RHQ method indicated two unmanaged cross-sections to fall in class 1 of hydromorphological quality and eight such cross-sections in class 2. In turn, four channelized cross-sections were classified to represent class 3 and six class 4. With the average scores of 2.04 (class 2) and 3.51 (class 4), the two

types of river cross-sections significantly differed in hydromorphological quality. Although unmanaged and channelized cross-sections differed in each assessment category of hydromorphological quality, channel geometry, the presence of erosional and depositional channel forms, bank structure, channel mobility and lateral connectivity of the river and its floodplain were identified to be most severely modified as a result of the river channelization. These river features are thus likely to be improved the most with allowing free channel migration within the erodible river corridor. Differences in hydromorphological quality between the two types of cross-sections were somewhat less pronounced at the sites where the river is deeply incised in unmanaged and channelized reaches.

Acknowledgements This study has been supported by the statutory funds of the Institute of Nature Conservation, Polish Academy of Sciences. The final manuscript benefited from the efforts of three anonymous reviewers.

Open Access This article is distributed under the terms of the Creative Commons Attribution 4.0 International License (<http://creativecommons.org/licenses/by/4.0/>), which permits unrestricted use, distribution, and reproduction in any medium, provided you give appropriate credit to the original author(s) and the source, provide a link to the Creative Commons license, and indicate if changes were made.

References

- Belletti B, Rinaldi M, Buijse AD, Gurnell AM, Mosselman E (2015) A review of assessment methods for river hydromorphology. *Environ Earth Sci* 73:2078–2100. doi:[10.1007/s12665-014-3558-1](https://doi.org/10.1007/s12665-014-3558-1)
- Boon PJ, Holmes NTH, Raven PJ (2010) Developing standard approaches for recording and assessing river hydromorphology: the role of the European Committee for Standardization (CEN). *Aquat Conserv Mar Freshw Ecosyst* 20:55–61. doi:[10.1002/aqc.1097](https://doi.org/10.1002/aqc.1097)
- Brierley GJ, Fryirs K (2005) *Geomorphology and river management: applications of the River Styles Framework*. Blackwell, Oxford, p 416
- Brunke M, Gonser T (1997) The ecological significance of exchange processes between rivers and groundwater. *Freshw Biol* 37:1–33. doi:[10.1046/j.1365-2427.1997.00143.x](https://doi.org/10.1046/j.1365-2427.1997.00143.x)
- CEN (2004) Water quality—guidance standard for assessing the hydromorphological features of rivers, EN 14614. CEN, Brussels, p 21
- CEN (2010) Water quality—guidance standard on determining the degree of modification of river hydromorphology, EN 15843. CEN, Brussels, p 24
- Czech W, Radecki-Pawlik A, Wyźga B, Hajdukiewicz H (2016) Modelling the flooding capacity of a Polish Carpathian river: a comparison of constrained and free channel conditions. *Geomorphology* 272:32–42. doi:[10.1016/j.geomorph.2015.09.025](https://doi.org/10.1016/j.geomorph.2015.09.025)
- Dufour S, Piégay H (2009) From the myth of a lost paradise to targeted river restoration: forget natural references and focus on human benefits. *River Res Appl* 25:568–581. doi:[10.1002/rra.1239](https://doi.org/10.1002/rra.1239)
- Elosegi A, Sabater S (2013) Effects of hydromorphological impacts on river ecosystem functioning: a review and suggestions for

- assessing ecological impacts. *Hydrobiologia* 712:129–143. doi:[10.1007/s10750-012-1226-6](https://doi.org/10.1007/s10750-012-1226-6)
- Elosegi A, Díez J, Mutz M (2010) Effects of hydromorphological integrity on biodiversity and functioning of river ecosystems. *Hydrobiologia* 657:199–215. doi:[10.1007/s10750-009-0083-4](https://doi.org/10.1007/s10750-009-0083-4)
- EPA (2001) Parameters of water quality. Interpretation and standards. Environmental Protection Agency, Wexford, p 132
- European Commission (2000) Directive 2000/60/EC of the European Parliament and of the Council of 23 October 2000 establishing a framework for Community action in the field of water policy. *Off J Eur Commun L* 324(43):1–72
- Habersack H, Piégay H (2008) River restoration in the Alps and their surroundings: past experience and future challenges. In: Habersack H, Piégay H, Rinaldi M (eds) Gravel-bed rivers VI: from process understanding to river restoration. Developments in earth surface processes 11. Elsevier, Amsterdam, pp 703–737. doi:[10.1016/S0928-2025\(07\)11161-5](https://doi.org/10.1016/S0928-2025(07)11161-5)
- Hajdukiewicz H, Wyźga B, Mikuś P, Zawiejska J, Radecki-Pawlik A (2016) Impact of a large flood on mountain river habitats, channel morphology and valley infrastructure. *Geomorphology* 272:55–67. doi:[10.1016/j.geomorph.2015.09.003](https://doi.org/10.1016/j.geomorph.2015.09.003)
- Ilnicki P, Górecki K, Grzybowski M, Krzemińska A, Lewandowski P, Sojka M (2010a) Principles of hydromorphological surveys of Polish rivers. *J Water Land Develop* 14:3–13. doi:[10.2478/v10025-011-0001-9](https://doi.org/10.2478/v10025-011-0001-9)
- Ilnicki P, Górecki K, Grzybowski M, Krzemińska A, Lewandowski P, Sojka M (2010b) Ecological quality classes of river hydromorphology. *J Water Land Develop* 14:15–27. doi:[10.2478/v10025-011-0002-8](https://doi.org/10.2478/v10025-011-0002-8)
- Kaczka RJ, Wyźga B, Zawiejska J (2008) Tree ring study of the island formation and riparian forest along a gravel-bed river in the Polish Carpathians. In: Elferts D, Brumelis G, Gärtner H, Helle G, Schleser G (eds) Tree rings in archaeology, climatology and ecology 6, Proceedings of the Dendrosymposium 2007, 3–6 May 2007, Riga, Latvia. Association for Tree Ring Research, Potsdam, 106–110
- Kondolf GM, Piégay H, Landon N (2002) Channel response to increased and decreased bedload supply from land use change: contrasts between two catchments. *Geomorphology* 45:35–51. doi:[10.1016/S0169-555X\(01\)00188-X](https://doi.org/10.1016/S0169-555X(01)00188-X)
- Kondolf GM, Boulton AJ, O’Daniel S, Poole GC, Rahel FJ, Stanley EH, Wohl E, Bång A, Carlstrom J, Cristoni C, Huber H, Koljonen S, Louhi P, Nakamura K (2006) Process-based ecological river restoration: visualizing three-dimensional connectivity and dynamic vectors to recover lost linkages. *Ecol Soc* 11:5. doi:[10.5751/ES-01747-110205](https://doi.org/10.5751/ES-01747-110205)
- Kozak J, Estreguil C, Troll M (2007) Forest cover changes in the northern Carpathians in the 20th century: a slow transition. *J Land Use Sci* 2:127–146. doi:[10.1080/17474230701218244](https://doi.org/10.1080/17474230701218244)
- Kujanová K, Matoušková M, Kliment Z (2016) Hydromorphological parameters of natural channel behavior in conditions of the Hercynian System and the flysch belt of the Western Carpathians on the territory of the Czech Republic. *Geomorphology* 258:69–81. doi:[10.1016/j.geomorph.2016.01.016](https://doi.org/10.1016/j.geomorph.2016.01.016)
- Kundzewicz ZW, Stoffel M, Kaczka RJ, Wyźga B, Niedźwiedz T, Pińskwar I, Ruiz-Villanueva V, Łupikasza E, Czajka B, Ballesteros-Canovas JA, Małarzewski Ł, Choryński A, Janecka K, Mikuś P (2014) Floods at the northern foothills of the Tatra Mountains—a Polish-Swiss research project. *Acta Geophys* 62:620–641. doi:[10.2478/s11600-013-0192-3](https://doi.org/10.2478/s11600-013-0192-3)
- Lach J, Wyźga B (2002) Channel incision and flow increase of the upper Wisłoka River, southern Poland, subsequent to the reforestation of its catchment. *Earth Surf Process Landforms* 27:445–462. doi:[10.1002/esp.329](https://doi.org/10.1002/esp.329)
- Langhammer J (2007) HEM Hydroekologicky monitoring. Metodika pro monitoring hydromorfologických ukazatelů ekologické kvality vodních toků. PiF UK, Praha, p 66
- LAWA (2000) Gewässerstrukturgütebewertung in der Bundesrepublik Deutschland, Verfahren für kleine und mittelgroße Fließgewässer. Landerarbeitsgemeinschaft Wasser, Schwerin
- Lewandowski P (2012) Polish investigations on river hydromorphology. *Polish J Environ Stud* 21:957–965
- Meybeck M (2003) Global analysis of river systems: from Earth system controls to Anthropocene syndromes. *Phil Trans R Soc Lond B* 1379:1–21. doi:[10.1098/rstb.2003.1379](https://doi.org/10.1098/rstb.2003.1379)
- Mikuś P, Wyźga B, Kaczka RJ, Walusiak E, Zawiejska J (2013) Islands in a European mountain river: linkages with large wood deposition, flood flows and plant diversity. *Geomorphology* 202:115–127. doi:[10.1016/j.geomorph.2012.09.016](https://doi.org/10.1016/j.geomorph.2012.09.016)
- Montgomery DR, Buffington JM (1997) Channel-reach morphology in mountain drainage basins. *Geol Soc Am Bull* 109:596–611
- Muhar S, Jungwirth M (1998) Habitat integrity of running waters—assessment criteria and their biological relevance. *Hydrobiologia* 386:195–202
- Ollero A, Ibisate A, Gonsalo LE, Acín V, Ballarín D, Draz E, Domenech S, Gimeno M, Granado D, Horacio J, Mora D, Sánchez M (2011) The IHG index for hydromorphological quality assessment of rivers and streams: updated version. *Limnetica* 30:255–261
- Raven PJ, Fox P, Everard M, Holmes NTH, Dawson FH (1997) River habitat survey: a new system for classifying rivers according to their habitat quality. In: Boon PJ, Howell DL (eds) Freshwater quality: defining the indefinable? The Stationery Office, Edinburgh, pp 215–234
- Raven PJ, Holmes NTH, Charrier P, Dawson FH, Naura M, Boon PJ (2002) Towards a harmonized approach for hydromorphological assessment of rivers in Europe: a qualitative comparison of three survey methods. *Aquat Conserv Mar Freshw Ecosyst* 12:405–424. doi:[10.1002/aqc.536](https://doi.org/10.1002/aqc.536)
- Rinaldi M, Wyźga B, Surian N (2005) Sediment mining in alluvial channels: physical effects and management perspectives. *River Res Appl* 21:805–828. doi:[10.1002/rra.884](https://doi.org/10.1002/rra.884)
- Rinaldi M, Belletti B, Van de Bund W, Bertoldi W, Gurnell A, Buijse T, Mosselman E (2013a) Review on hydromorphological methods. Report of FP7 REFORM Project, p 202
- Rinaldi M, Surian N, Comiti F, Bussetini M (2013b) A method for the assessment and analysis of the hydromorphological condition of Italian streams: the morphological quality index (MQI). *Geomorphology* 180:96–108. doi:[10.1016/j.geomorph.2012.09.009](https://doi.org/10.1016/j.geomorph.2012.09.009)
- Rinaldi M, Wyźga B, Dufour S, Bertoldi W, Gurnell A (2013c) River processes and implications for fluvial ecogeomorphology: a European perspective. In: Shroder J, Butler DR, Hupp CR (eds) Treatise on Geomorphology. Vol. 12. Ecogeomorphology. Academic Press, San Diego, 37–52. doi:[10.1016/B978-0-12-374739-6.00321-3](https://doi.org/10.1016/B978-0-12-374739-6.00321-3)
- Romanowicz RJ, Bogdanowicz E, Debele SE, Doroszkiewicz J, Hisdal H, Lawrence D, Meresa HK, Napiórkowski JJ, Osuch M, Strupczewski WG, Wilson D, Wong WK (2016) Climate change impact on hydrological extremes: preliminary results from the Polish-Norwegian project. *Acta Geophys* 64:477–509. doi:[10.1515/acgeo-2016-0009](https://doi.org/10.1515/acgeo-2016-0009)
- Scheiffhacken N, Haase U, Gram-Radu L, Kozovyi R, Berendonk TU (2012) How to assess hydromorphology? A comparison of Ukrainian and German approaches. *Environ Earth Sci* 65:1483–1499. doi:[10.1007/s12665-011-1218-2](https://doi.org/10.1007/s12665-011-1218-2)
- Surian N, Rinaldi M (2004) Channel adjustments in response to human alterations of sediment fluxes: examples from Italian rivers. In: Golosov V, Belyaev V, Walling DE (eds) Sediment

- transfer through the fluvial system. *Intern Ass Hydrol Sci Publ* 288, 276–282
- Szoszkiewicz K, Gebler D (2011) Ocena warunków hydromorfologicznych rzek w Polsce metodą River Habitat Survey (Assessment of hydromorphological conditions in Polish rivers based on the River Habitat Survey). *Ochr Środ Zas Natur* 47, 70–81 (in Polish, with English summary)
- Szoszkiewicz K, Buffagni A, Davy-Bowker J, Lesny J, Chojnicki BH, Zbierska J, Staniszewski R, Zgola T (2006) Occurrence and variability of River Habitat Survey features across Europe and the consequences for data collection and evaluation. *Hydrobiologia* 566:267–280. doi:10.1007/s10750-006-0090-7
- Szoszkiewicz K, Zgola T, Jusik S, Hryc-Jusik B, Raven P, Dawson FH (2007) Ocena hydromorfologiczna wód płynących. Podręcznik do badań terenowych według metody River Habitat Survey. Bogucki Wydawnictwo Naukowe, Poznań, p 163
- Tockner K, Ward JV, Arscott DB, Edwards PJ, Kollmann J, Gurnell AM, Petts GE, Maiolini B (2003) The Tagliamento River: a model ecosystem of European importance. *Aquat Sci* 65:239–253. doi:10.1007/s00027-003-0699-9
- Vaughan IP, Diamond M, Gurnell AM, Hall KA, Jenkins A, Milner NJ, Naylor LA, Sear DA, Woodward G, Ormerod S (2009) Integrating ecology with hydromorphology: a priority for river science and management. *Aquat Conserv Mar Freshw Ecosyst* 19:113–125. doi:10.1002/aqc.895
- Wood PJ, Armitage PD (1997) Biological effects of fine sediment in the lotic environment. *Environ Manage* 21:203–217
- Wyźga B (1997) Methods for studying the response of flood flows to channel change. *J Hydrol* 198:271–288. doi:10.1016/S0022-1694(96)03289-1
- Wyźga B (2001) A geomorphologist's criticism of the engineering approach to channelization of gravel-bed rivers: case study of the Raba River, Polish Carpathians. *Environ Manage* 28:341–358. doi:10.1007/s002670010228
- Wyźga B (2008) A review on channel incision in the Polish Carpathian rivers during the 20th century. In: Habersack H, Piegay H, Rinaldi M (eds) Gravel-bed rivers VI: from process understanding to river restoration. *Developments in earth surface processes* 11. Elsevier, Amsterdam, pp 525–555. doi:10.1016/S0928-2025(07)11142-1
- Wyźga B (2012) Cechy teksturalne zwirowych osadów korytowych jako odzwierciedlenie dynamiki przepływu wody i transportu rumowiska w ciekach z różnych stref klimatycznych (Textural patterns of river gravels as a reflection of water and sediment dynamics in watercourses from various climatic zones). In: Łajczak A et al (eds) Antropopresja w wybranych strefach morfoklimatycznych—zapis zmian w rzeźbie i osadach. Uniwersytet Śląski, Sosnowiec, pp 461–469
- Wyźga B, Zawiejska J (2010) Large wood storage in channelized and unmanaged sections of the Czarny Dunajec River, Polish Carpathians: Implications for the restoration of mountain rivers. *Folia Geogr Ser Geogr Phys* 41:5–34
- Wyźga B, Amirowicz A, Radecki-Pawlik A, Zawiejska J (2009) Hydromorphological conditions, potential fish habitats, and the fish community in a mountain river subjected to variable human impacts, the Czarny Dunajec, Polish Carpathians. *River Res Appl* 25:517–536. doi:10.1002/rra.1237
- Wyźga B, Hajdukiewicz H, Radecki-Pawlik A, Zawiejska J (2010a) Eksploatacja osadów z koryt rzek górskich—skutki środowiskowe i procedury oceny (Exploitation of sediments from mountain river beds—environmental impact and evaluation procedures). *Gosp Wodna* 6:243–249 (in Polish, with English summary)
- Wyźga B, Zawiejska J, Radecki-Pawlik A, Amirowicz A (2010b) A method for the assessment of hydromorphological river quality and its application to the Czarny Dunajec, Polish Carpathians. In: Radecki-Pawlik A, Hernik J (eds) *Cultural Landscapes of River Valleys*. Agricultural University in Kraków, Kraków, pp 145–164
- Wyźga B, Oglecki P, Radecki-Pawlik A, Skalski T, Zawiejska J (2012a) Hydromorphological complexity as a driver of the diversity of benthic invertebrate communities in the Czarny Dunajec River, Polish Carpathians. *Hydrobiologia* 696:29–46. doi:10.1007/s10750-012-1180-3
- Wyźga B, Zawiejska J, Radecki-Pawlik A, Hajdukiewicz H (2012b) Environmental change, hydromorphological reference conditions and the restoration of Polish Carpathian rivers. *Earth Surf Process Landforms* 37:1213–1226. doi:10.1002/esp.3273
- Wyźga B, Oglecki P, Hajdukiewicz H, Zawiejska J, Radecki-Pawlik A, Skalski T, Mikuś P (2013) Interpretation of the invertebrate-based BMWP-PL index in a gravel-bed river: insight from the Polish Carpathians. *Hydrobiologia* 712:71–88. doi:10.1007/s10750-012-1280-0
- Wyźga B, Amirowicz A, Oglecki P, Hajdukiewicz H, Radecki-Pawlik A, Zawiejska J, Mikuś P (2014) Response of fish and benthic invertebrate communities to constrained channel conditions in a mountain river: case study of the Biała, Polish Carpathians. *Limnologica* 46:58–69. doi:10.1016/j.limno.2013.12.002
- Wyźga B, Zawiejska J, Mikuś P, Kaczka RJ (2015) Contrasting patterns of wood storage in mountain watercourses narrower and wider than the height of riparian trees. *Geomorphology* 228:275–285. doi:10.1016/j.geomorph.2014.09.014
- Wyźga B, Kundzewicz ZW, Ruiz-Villanueva V, Zawiejska J (2016a) Flood generation mechanisms and changes in principal drivers. In: Kundzewicz ZW, Stoffel M, Niedzwiedz T, Wyźga B (eds) *Flood risk in the upper vistula basin*. Springer, Cham, pp 55–75. doi:10.1007/978-3-319-41923-7_4
- Wyźga B, Zawiejska J, Hajdukiewicz H (2016b) Multi-thread rivers in the Polish Carpathians: occurrence, decline and possibilities of restoration. *Quatern Intern* 415:344–356. doi:10.1016/j.quaint.2015.05.015

Well-log based rock physics template of the Vienna Basin and the underlying Calcereous Alps

Nebojsa Tucovic¹ · Nina Gegenhuber¹

Received: 30 December 2016 / Accepted: 30 March 2017 / Published online: 13 April 2017
© The Author(s) 2017. This article is an open access publication

Abstract In this study, the ratio of compressional and shear wave velocity versus acoustic impedance as rock physics template for northern part of the Vienna Basin has been derived for siliciclastic rocks based on formation evaluation of well-log data. The results have been verified through wells in different areas drilled in various depths. Additionally, depositional sequences like prograding deltas and braided rivers have been plotted onto the rock physics template to illustrate the effect of changing shale volume. Carbonates below the basin have been included into the study and results from previous projects, based on laboratory data and petrophysical models on certain lithologies in the Vienna Basin, have been used to compare the outcome. The result is a rock physics template which includes important properties such as porosity, true vertical depth and fluid type from log data and which is considered useable throughout different areas and various lithologies of the Vienna Basin.

Keywords Rock physics template · Formation evaluation · Vienna Basin · Depositional sequences

Introduction

Seismic measurements are the most frequently used methods in exploration activities in the oil and gas industry. More advanced and complex tools to get more qualitative as well as quantitative information out of a seismic

cube have been developed through the last decades. Ødegaard and Avseth (2009) published the so-called rock physics template (RPT). Their idea was to create basin and lithology-dependent templates mainly with elastic properties of rocks (most commonly the ratio of compressional and shear wave velocity (v_p/v_s) and acoustic impedance (AI)) of rocks. These templates, which are able to indicate fluid and lithology trends, can then be used for interpretation of seismic data from the corresponding basin or lithology. In further consequence rock physics templates have been widely used in the exploration activities within the industry. Numerous studies have been conducted. Most of the studies used elastic properties in siliciclastic rocks to construct the templates with petrophysical models (Avseth et al. 2009; Chi and Han 2009; Gupta et al. 2012).

Rock physics templates for carbonate reservoirs have been created too. Ba et al. (2013) created multiscale rock physics templates for carbonates and validated them with laboratory, well and seismic data. Gegenhuber and Pupos (2015) determined elastic properties with Hashin and Shtrikman (1962) bounds and derived v_p/v_s -acoustic impedance-based rock physics templates from laboratory data for three different carbonate types from Austria under dry and wet conditions, applied additionally on log and seismic data (Pupos 2015).

Avseth and Veggeland (2015) introduced additional rock stiffness/rock impedance (PEIL) and fluid softness/fluid impedance (CPEI) attributes which honour fundamental rock physics from v_p/v_s -AI rock physics templates. The combined use of these two attributes can help differentiate between fluid and lithology anomalies in the rock physics template. Additionally, Avseth and Carcione (2015) used rock physics templates to get an understanding of complex kerogen-rich Jurassic source rocks from the Norwegian Shelf. v_p/v_s -acoustic impedance behaviour

✉ Nina Gegenhuber
nina.gegenhuber@unileoben.ac.at

¹ Chair of Applied Geophysics, Montanuniversitaet, Leoben, Austria

throughout the different processes in the compaction and hydrocarbon generation of source rocks helps to determine the maturity of the rock and generation of hydrogen.

Hermana et al. (2016) derived rock physics templates from attenuation parameters (SQp and SQs) and applied it to a real dataset from Malay Basin. They concluded that their attenuation-based rock physics templates derive better lithology and fluid separation results than conventional v_p/v_s -acoustic impedance rock physics templates on the considered dataset. Tucovic et al. (2016) created resistivity-acoustic impedance rock physics templates based on deep reading logging while drilling data as a foundation for further work of real-time template-based logging while drilling interpretation for enhanced geosteering operations.

Although all these rock physics templates are able to distinguish between gas and water and different lithologies, they are still not suitable for determining oil saturation within seismic data and are mainly usable just for one lithology with certain properties throughout the basin.

As pointed out, RPTs are a valuable tool in seismic exploration industry. The goal of this paper is to create a rock physics template which is applicable in the whole pull-apart basin in Lower Austria and the underlying Calcareous Alps with well-log based formation evaluation. Parts are evaluated with derived RPTs out of laboratory data. Depth-related trends are considered as well as different lithologies with their evaluated properties from formation evaluation of the logs. Depositional sequences like prograding deltas or braided rivers are visualized on the created template to validate it.

Geology of the Vienna Basin

Vienna Basin is a 200-km-long and 60-km-wide rhombic pull-apart basin located in the northeast part of Austria. It is a mature basin operated by OMV since the 1930s. The basement of the Vienna Basin is the Bohemian Massif overlain by the autochthonous sedimentary cover which is Jurassic to Cretaceous age (Ladwein 1988). This sedimentary cover is followed by the Flysch Zone (Lower Cretaceous–Eocene) and finally the Northern Calcareous Alps (Permian–Cretaceous), which have been overthrust during the northwest-directed transportation in lower Cretaceous–Oligocene age with piggy back basins on their back. After the thrusting in the middle Miocene (Badenian), north south compression with associated compensation movement of the nappes to northeast occurred. This resulted in separation of the Northern Calcareous Alps and Carpathians associated to extension and pull-apart effects (Wessely 2006). During this time, main subsidence and sedimentation of clastic sediments as a result of transgressive/regressive cycles due to sea level changes took

place (Kreutzer 1992). Thus, the sediments of the Vienna Basin are of Neogene age and reach 5–6 km at some locations (Ladwein 1988).

Early stages of basin development in Otnangian and Karpatian are dominated by lacustrine to fluvial environment while in Badenian (Middle Miocene) transgressive/regressive cycles with prograding deltas in marine environment are dominating (Sauer et al. 1992). Here the most reservoirs in the Vienna Basin are saturated and the sand horizons are numbered. An example is 16th TH (Tortonian horizon) which consists of many on-lapping layers, which are composed of prograding delta front sequences and separated by flooding events. By the side, already more than 400 wells have been drilled into this 16th TH, also called the Matzen sand and the associated Matzen giant field which has been discovered in 1949 and is one of the largest multi-pool oil and gas field onshore Europe (Kienberger and Fuchs 2006). In the following Sarmatian, marine environment evolved to brackish water conditions and lead to lacustrine and fluvial deposits in the Pannonian (Sauer et al. 1992). Up to 20 sand horizons have been deposited and numbered here throughout the basin. After the Sarmatian, during the Pannonian sedimentation continued in lacustrine environment with deposition of fluvial clastic sediments.

Besides the huge number of reservoirs within the Neogene part of the succession, commercial pay zones have been found within the Triassic dolomites underneath the Basin in the allochthonous nappes (Ladwein 1988). This dolomite called the “main dolomite” is formed in shallow lagoon areas and shallow water zones with very low porosity (Gegenhuber and Pupos 2015). Main source rocks in the basin are the Upper Jurassic (Malmian) marls in the autochthonous part of the section (Hamilton et al. 1999), which are generated below the basin in depths of 3–6 km (Ladwein 1988). Sachsenhofer (2001) identified a geothermal gradient of the basin of 30 °C/km.

Data and methodology

Data

Data used are wireline log data from the northern part of Vienna Basin. Most of data are available from Field A, which is situated on a structural high. Thus, wells which have been used for creation of rock physics templates from this field have reached true vertical depths (TVD) of about 2.3 km. Other fields are located in deeper areas of the basin, mainly on structural low, but still in the northern part. One well per field have been used in Field B (true vertical depth of about 4.1 km), Field C and D (true vertical depths of about 3 km). A simple sketch to illustrate

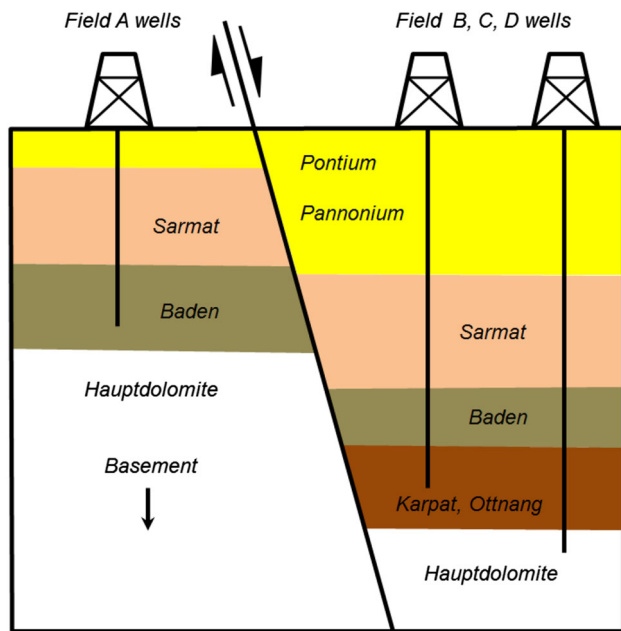


Fig. 1 Simple sketch illustrating the shallow Field A wells on structural highs and Field B–D wells on structural lows

the wells from different fields is shown in Fig. 1. The three wells in other areas of the basin (Field B, C and D) have been mainly used to evaluate the rock physics templates created with detail-evaluated wells from shallower areas from Field A because they encountered the same and similar siliciclastic rocks in much greater depths.

Table 1 shows the encountered formations and their horizons within the wells with the corresponding ages. Ages in the second column are from Central Paratethys nomenclature. Third column indicates the availability of hydrocarbons within the corresponding formations throughout the basin. In the last column the four fields are indicated which have the necessary data (shear velocity was the limiting factor) to create a rock physics template. As visible, “the main dolomite” from the Calcareous Alps beneath the basin has been drilled in the deep well in Field D too.

Methodology

Formation evaluation of Field A wells

To create a rock physics template from log data alone, it is necessary to complete a full formation evaluation of the investigated wells. This has been done with well measurement data from Field A. Formation tops, lithology discrimination, reservoir identification and fluid type and saturation have been fully determined within the Field A. The next step was to pick out shale and sand intervals to create model rock physics template shale and sand lines. These have been picked after the criteria defined in

Table 2. Additionally, sand has been differentiated after the various fluid contents (gas, oil, water).

In Fig. 2, an example of log representation of a hydrocarbon reservoir with surrounding shale deposited in early Miocene is shown. The first track shows picked lithology and fluid intervals for the rock physics template. This reservoir sand has gas- and oil-bearing zones and is over- and underlain by shale layers.

With data from shale and sand (water–oil–gas) horizons from Field A, a scatter plot with four variables (resistivity, acoustic impedance, density and v_p/v_s) and two-dimensional combinations are determined. It was used to see where the best fluid and lithology separation can be achieved. As used by numerous studies in the past, v_p/v_s –acoustic impedance crossplot has shown best results for fluid and lithology discrimination.

Choosing the right two-dimensional crossplot for differentiation

Figure 3 shows scatter plot with resistivity, acoustic impedance, v_p/v_s ratio and density of the picked fluid-discriminated sand horizons and shale layers. It is clearly visible that green (oil reservoirs) and red (gas reservoirs) points are plotting always in areas of higher formation resistivity. Blue data points, which represent water-bearing sand horizons are slightly separated from shales coloured in brown. Note the significant oil/gas separation in density-included crossplots. Resistivity-included crossplots separate well between hydrocarbon and water. Thus, density–resistivity and acoustic impedance–resistivity crossplots (indicated with a red dashed circle) are very good fluid discriminators. On the other side, lithology (shale–sand) is not sufficiently separated in these crossplots. From first look onto the crossplots best results regarding lithology discrimination are reached at acoustic impedance– v_p/v_s and density– v_p/v_s crossplots (marked with the blue dashed circle). Thus, for this study standard acoustic impedance– v_p/v_s crossplot is chosen.

Modelling the rock physics template with well data from Field A

In the next step, elastic data from the picked horizons from formation evaluation in wells from Field A is plotted onto a v_p/v_s –AI crossplot. Figure 4 shows lithology-discriminated data points from these wells including shale and sand. Shale and sand lines have been fitted to the data. Shale line is modelled above the shale data points (brown) because below this line the shale is getting mixed with silt and sand. Sand line on the other side has been modelled below the water-saturated sand points because above the sand is getting mixed with clay.

Table 1 Encountered and evaluated formations within the study which have been used for creation of rock physics templates

Age	Age (Tethys)	Reservoir	Subage/formation	Horizons	Elastic data available
<i>Miocene</i>	<i>Pontian</i>	–	Pontian	–	–
		G	Middle Pannonian	Middle Pannonian horizon	Field A
	<i>Sarmatian</i>	G	Lower Pannonian	Lower Pannonian horizon	Field A
		O & G	Upper Sarmatian	Sarmatian horizon	Field A
		O & G	Lower Sarmatian	Sarmatian horizon	Field A
		O	Buliminen Rotalien zone	–	Field A, B (deep), C (deep)
	<i>Badenian</i>	O & G	Sandschaler zone	Tortonian horizons	Field A, B (deep), C (deep)
		O & G	Upper Lageniden	Lower Tortonian horizon	Field A, B (deep), C (deep)
		–	Aderklaa Conglomerate	–	Field A, B (deep), C (deep)
	<i>Karpatian</i>	–	Aderklaa formation	–	Field C (deep), D (deep)
		G	Gaenserndorf formation	–	Field C (deep), D (deep)
	<i>Ottmangian</i>	O	Bockflies formation	–	Field D (deep)
	<i>Eggenburgian</i>	–	Missing in study area	–	–
<i>Trias.</i>	<i>N. Calc. Alps</i>	O & G	Main dolomite	–	Field D (deep)

All used formations in this study except the Triassic “main dolomite” have been deposited during the Miocene. Most reservoirs have been deposited in mid-Miocene during Badenian time

G gas, O oil

Table 2 Lithology and fluid discrimination criteria within the logs

Shale	>60% Vsh
Sand _{water-bearing}	<20% Vsh & Sw >80%
Sand _{gas-bearing}	<20% Vsh & Sw <50% and logs indicate gas
Sand _{oil-bearing}	<20% Vsh & Sw <50% and logs indicate oil

Thus, between these two lines on the crossplot the lithology is a mixture between sand and shale. The scattering of the sand–shale data points results from the fact that sand and shale lithologies are hardly clean in the field data (100% sand/clay content). As shown in Table 2, shale horizons have been picked, if shale volume is bigger than 60%. Red line represents 100% gas saturation in sands and is modelled below the picked gas-bearing reservoir intervals because they are not 100% gas-saturated. Note the green points slightly below the 100% water saturation sand line which represent picked oil-bearing reservoirs, most of them in Badenian ages.

After the curve fitting and determination of corresponding shale, sand (water and gas) lines for the Field A lithologies in the Vienna Basin, additional information of well-log interpretation have been used to model other relevant properties onto the template. Unlike Fig. 4 which shows just picked sand and shale lithologies, the four crossplots in Figs. 5 and 6 show all data points from wells within the Field A with modelled shale and gas/water sand lines.

In each crossplot different colour scales have been used which have been delivered from formation evaluation of the Field A wells. Left crossplot in Fig. 5 has total porosity

as colour scale with determined porosity isolines. The crossplot on the right in Fig. 5 shows the same data points from wells from Field A with true vertical depth as colour scale. Here it is more difficult to distinguish between different TVD trends resulting in higher uncertainty of the true vertical depth trendlines. Isolines are directly drawn in the plot, using the colour code from the porosity and depth.

In the two crossplots in Fig. 6, same data from Field A as in Fig. 5 is plotted with shale volume (left) and water saturation (right) as colour scale. As expected the shale volume and the water saturation values show the predicted plotting behaviour. Water-saturated formations (shales and water-saturated sands) plot above the blue water line and below the shale line while hydrocarbon-saturated reservoirs plot below. Low shale volume (where clean sand can be assumed) fits the sand line (and the gas-bearing direction) quite well. Exception is some shallow low shale areas which are indicated in the crossplot. Here it is assumed that the compressional velocity measurements are not valid anymore because of the low compaction and high porosity of the formation.

Validating the rock physics template with deeper wells from Field B, C and D

In the next step, the determined shale and sand lines from wells in Field A have been validated with wells, which drilled the same and similar siliciclastic formations in bigger depths. Each crossplot in Fig. 7 shows data from one well drilled in different fields and in different area of the northern part of the Vienna Basin. As described in the data chapter before, these

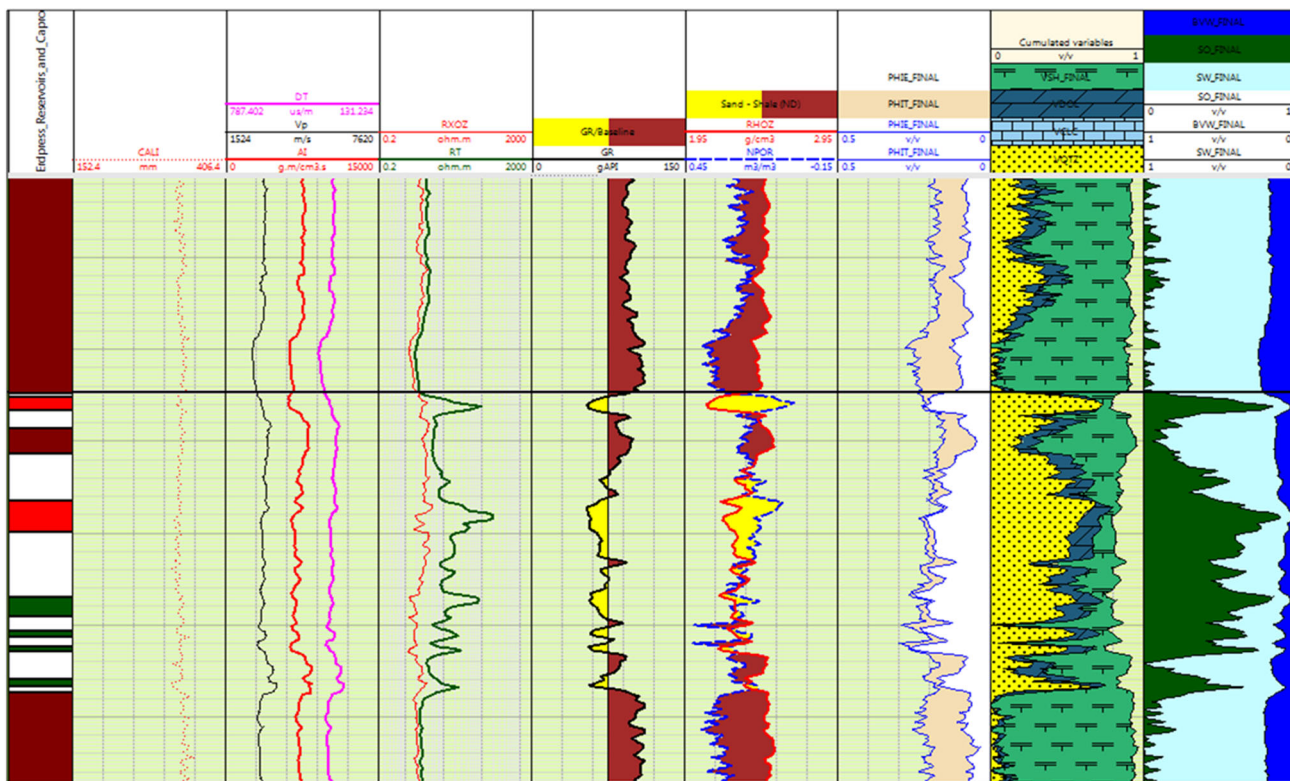


Fig. 2 Lithology interpretation example from one of the sand horizons in the Sarmatian section of the Vienna Basin. The zonation from the first track (red gas; green oil; brown shale) have been used for the creation of the rock physics templates

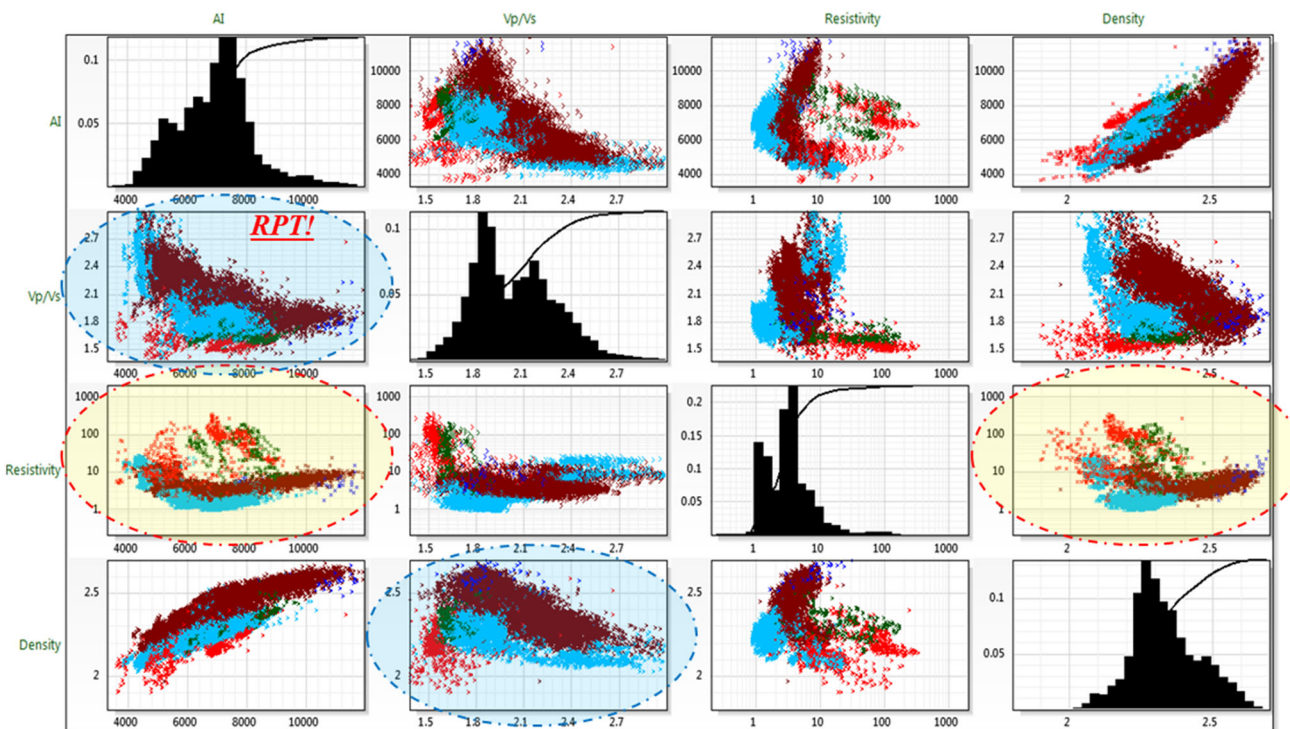


Fig. 3 Scatter plot matrix of AI, v_p/v_s ratio, resistivity and density for Field A data of the picked sand and shale packages within the Field A wells. Colour scale is lithology–fluid based. Red gas; green oil; blue water; brown shales. Interesting combinations are highlighted

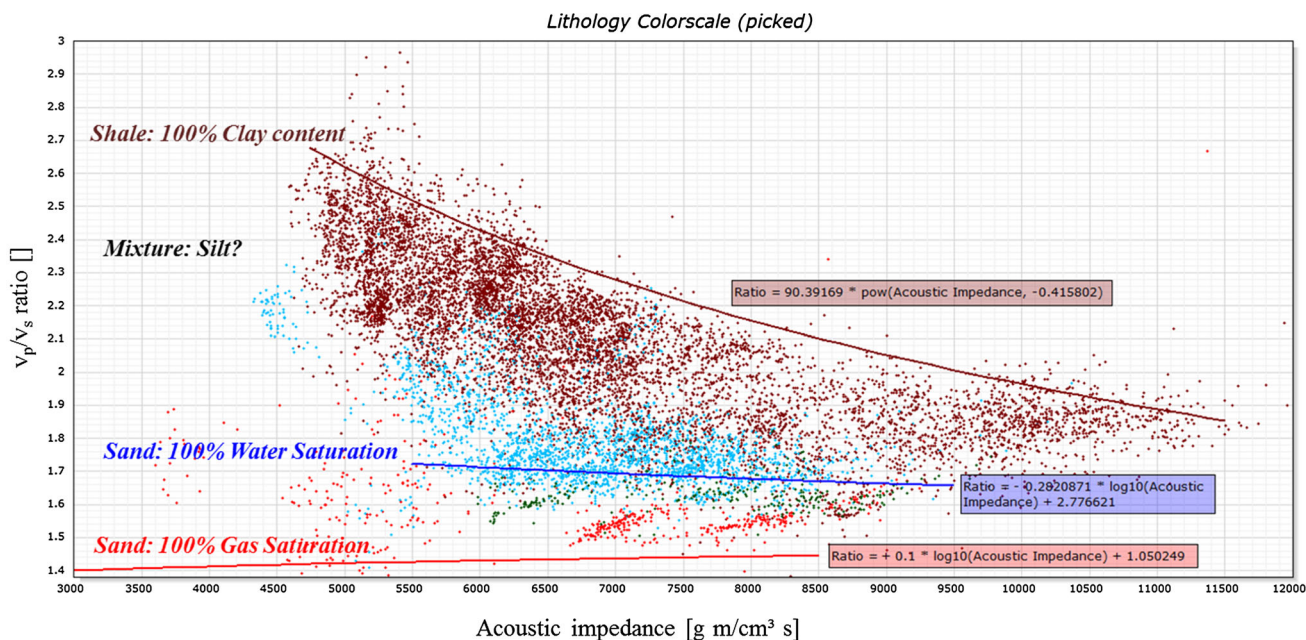


Fig. 4 v_p/v_s versus AI rock physics template with the shale (brown) and sand (red gas; green oil; blue water) zonation from the Field A wells. Modelled shale, water sand and gas sand lines with their equations are displayed too

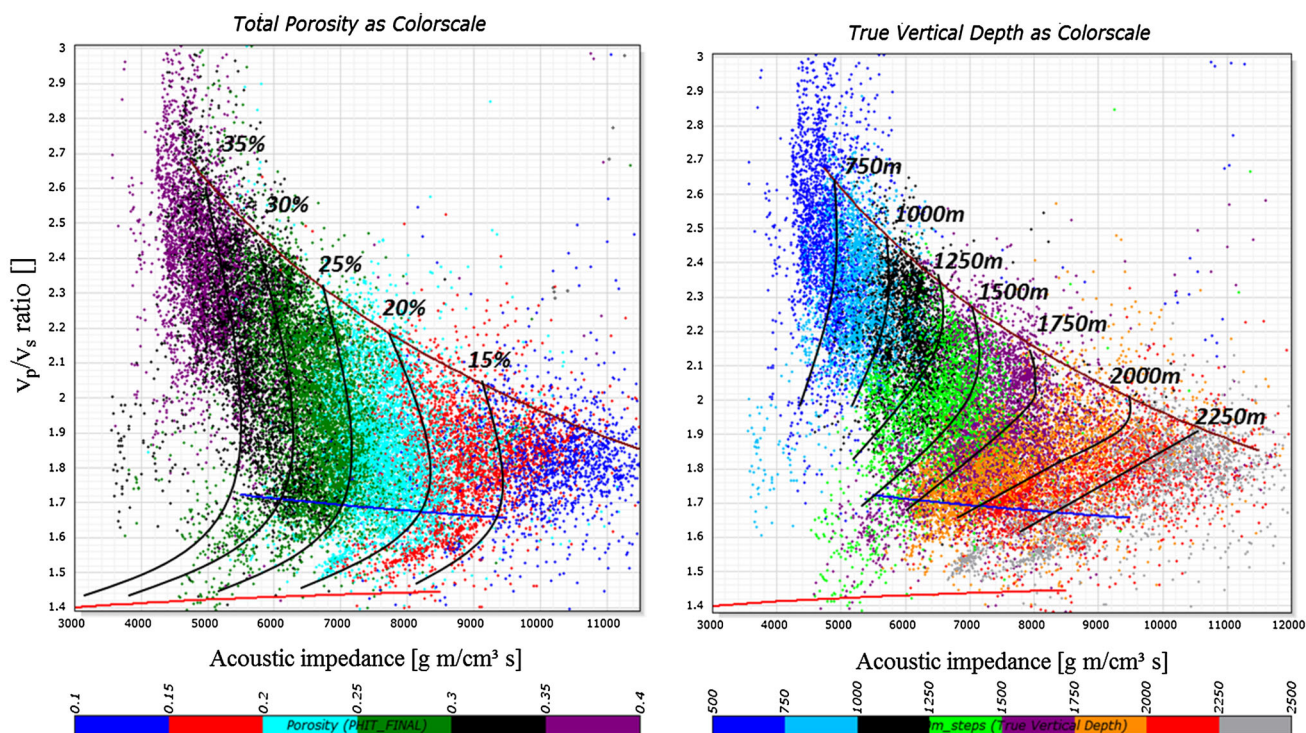


Fig. 5 v_p/v_s –AI crossplots from all wells (Field A) with modelled shale, water–sand and gas–sand lines. On the left total porosity is used as colour scale and on the right TVD is used as colour scale. Some porosity and TVD isolines are indicated on each crossplot

wells are mainly located in structural lows with the same formations encountered approximately 1.5 km deeper than the wells from Field A.

Thus, note the different x-axes from previous v_p/v_s –AI crossplots (starting at AI = 7000 g m/cm³ s). As visible in the

crossplot, the encountered lithologies, consisting mainly of shales and sands from Badenian, Karpatian and Ottngian ages of the Field B, C and D wells are fitting very well between the sand and shale line derived from Field A. Ottngian (first crossplot, brown data points), which consists mainly of shales,

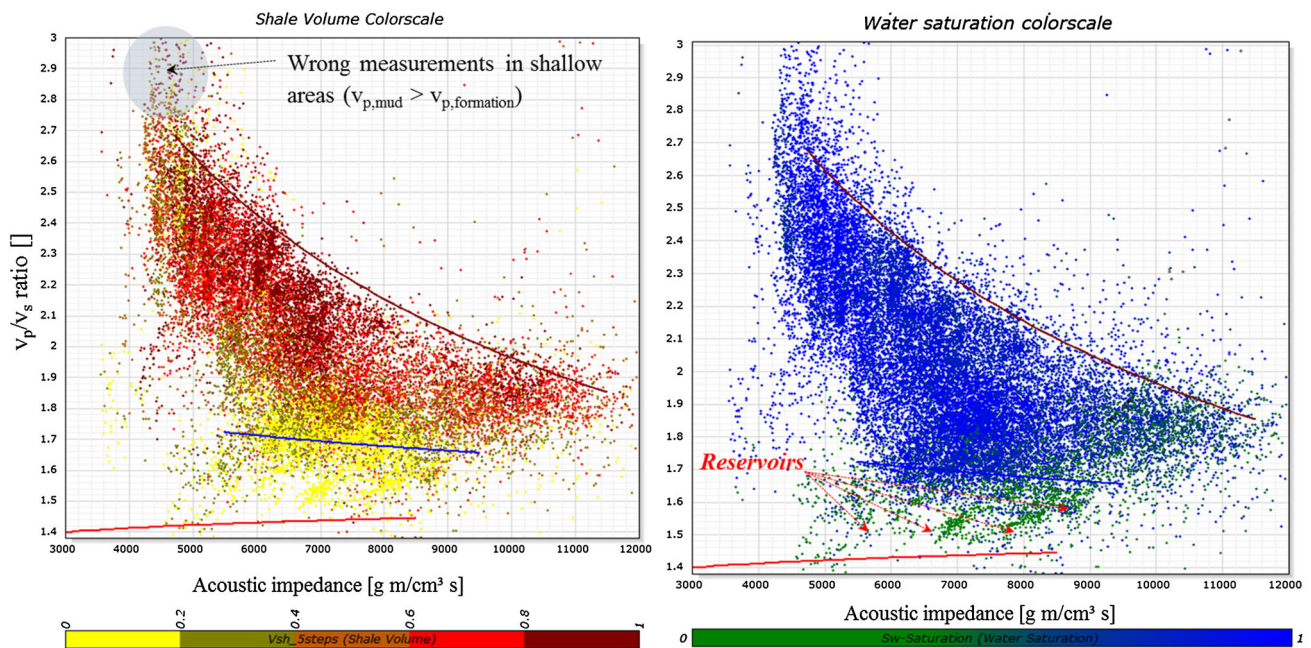


Fig. 6 v_p/v_s –AI crossplots from wells (Field A) with modelled shale, water–sand and gas–sand lines. On the *left* calculated shale volume is used as colour scale and on the *right* calculated water saturation has been used as colour scale

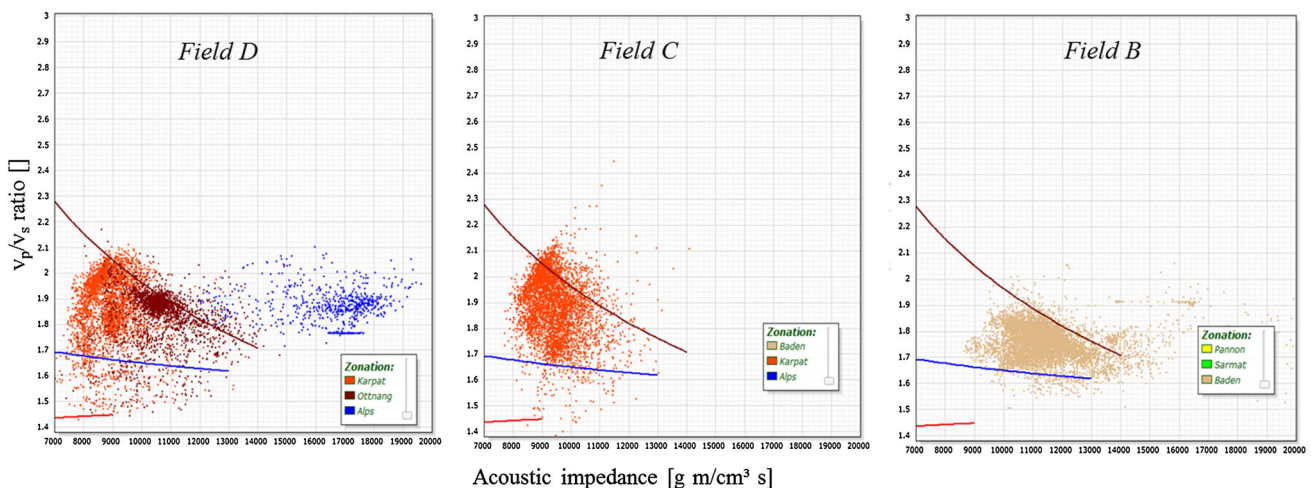


Fig. 7 All available data from the remaining wells (v_s limiting factor) plotted on a v_p/v_s –AI crossplot with shale and sand (water and gas) lines derived from Field A wells. Note that the starting point of

plots slightly below the modelled shale line. “The main dolomite” below the basin, which has been drilled by a well in Field D plots in area slightly below v_p/v_s ratio of 2 and acoustic impedance of above 15000 $\text{g m/cm}^3 \text{ s}$.

Results and interpretation

In the following section, lithology and fluid effects and the influence of different depositional sequences within the Vienna Basin on the plotting behaviour and the derived shale

the x -axes is different from the previous crossplots ($7000 \text{ g m/cm}^3 \text{ s}$) due to the deeper depth of investigated formations

and sand lines within the Neogene sequence of the Vienna Basin, as well as “the main dolomite” beneath will be interpreted and discussed. Additionally, data will be compared to already existing rock physics templates derived by laboratory measurements and petrophysical models.

The created rock physics template follows the trends which has already been shown in numerous studies and discussed and summarized, e.g. by Avseth et al. (2005) or Schön (2015):

- Gas saturation decreases v_p/v_s ratios and acoustic impedance.

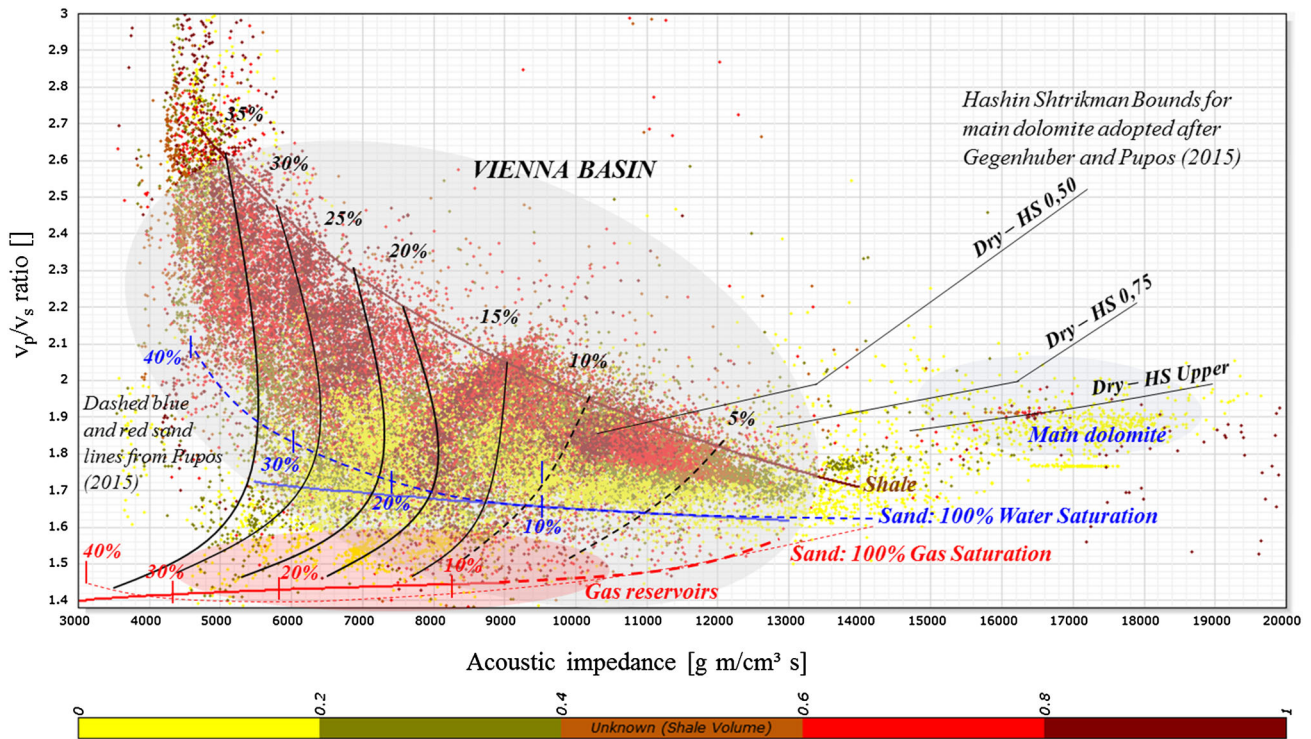


Fig. 8 v_p/v_s -AI crossplot with determined sand and shale lines; shale volume as colour scale. Porosity isolines from Fig. 5 are indicated too. Two more isolines (10 and 5% porosity) are estimated.

- Shale content increases v_p/v_s ratios and decreases acoustic impedance.
- Compaction decreases v_p/v_s ratios and increases acoustic impedance.
- Porosity slightly increases v_p/v_s ratios and decreases acoustic impedance.
- Oil–water contrasts are hardly recognized with elastic measurements.

The last point, which states out that oil–water contrasts are hardly recognized with elastic measurements due to similar oil and water densities, is true, but as visible in Fig. 3 the green points (oil-bearing reservoirs) have significantly different plotting areas compared to the blue water-saturated sands. Thus, in Vienna Basin it could be possible to define oil-bearing sand area and to try to read them out of seismic. Gas-bearing horizons are clearly separated from water and oil-bearing sands due to the different elastic properties of the fluids.

The porosity trend shown in Fig. 4 indicates a good correlation with the elastic parameters and the above statement from previous studies is given. However, when looking at different lines (water/gas sand and shale) at same acoustic impedance on the x -axis, porosity of gas-bearing sand is the lowest followed by shale and last but not least water-bearing sand. This is the same trend shown

in previous studies (e.g. Avseth et al. 2005). In true vertical depth colour-scaled crossplot in the same figure, the true vertical depth gradients show similar behaviour although there are some uncertainties in these isolines as stated out before and visible on the crossplot. Reasons for the uncertainty of true vertical depth trendlines could be the faulting of the basin and the related different compaction rate depending on the, e.g. hanging or footwall side of the fault and the timing of the fault. Another reason for the uncertainty of the true vertical depth lines could be the deviation of the drilled wells and the tool during the measurements. Anisotropic shale formations will result in higher velocity measurements when measured under deviated conditions than when the well is fully vertical at the same true vertical depth and compaction behaviour. Nevertheless, the modelled true vertical depth trend lines still are showing predicted behaviour and can be used for further investigations.

In Fig. 8, all available data from Field A and remaining wells in Vienna Basin are plotted onto v_p/v_s -acoustic impedance crossplot with the determined sand and shale lines and porosity trend lines. Colour scale shale volume has been chosen. Porosity isolines from Fig. 5 are indicated too. Two more isolines (10 and 5% porosity) are estimated (dashed because of uncertainty).

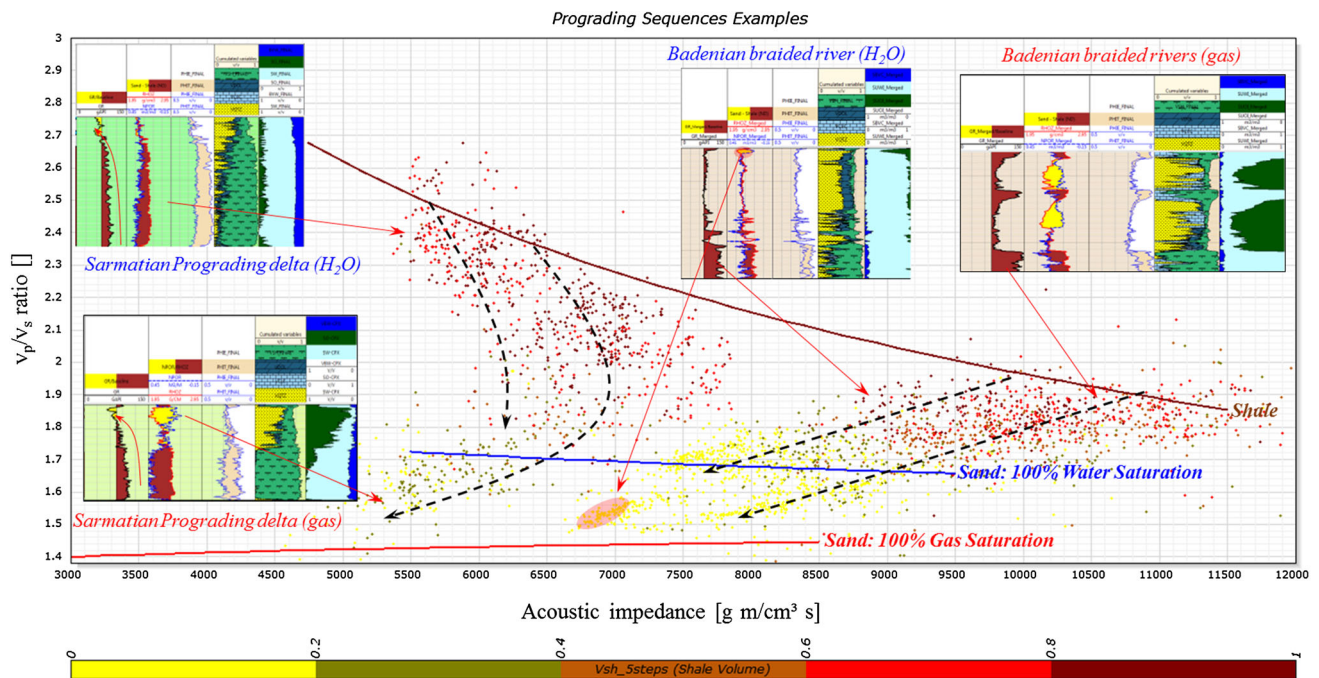


Fig. 9 v_p/v_s -AI crossplot with determined sand and shale lines. Some selected prograding (and non-prograding) sequences from shallower and deeper areas of the wells are plotted to present their behaviour on

the rock physics template. Log view from plotted data is displayed to get a better understanding

Hashin–Shtrikman bounds from previous work from Gegenhuber and Pupos (2015) on dry (black) carbonate samples (including “main dolomite”) are plotted on the right side of the template. Within that study saturated bounds have been derived too, but due to the fact that dolomite here is dry only dry bounds are shown in the crossplot.

Additionally, for comparison reasons data derived from laboratory measurements on plugs (siliciclastic lithology water-bearing and gas-bearing sand) are indicated in dashed thin blue and red lines with the derived porosity. These plugs are from Badenian age sand reservoirs from Vienna Basin and modelled with petrophysical models (Cement models (Dvorkin and Nur 1996 and Avseth et al. 2000), Hashin–Shtrikman bounds (1962), and Gassmann fluid substitution (Gassmann 1951)). The lines are results of an unpublished master thesis related to rock physics templates in Vienna Basin (Pupos 2015).

As visible, there are two main areas of the crossplot. Data points from the Neogene (Miocene) siliciclastic lithology of the Vienna Basin itself are on the left side with lower acoustic impedance values and data points from the northern Calcareous Alps, i.e. the dense and low-porosity “main dolomite” are on the right side in areas of higher acoustic impedance values. Therefore, a kind of petrographic code (=influence of mineralogy/lithology) is visible. When considering the shale volume colour scale of all

available data, the shale and sand lines fit very well to the data. Below the blue 100% water saturation line most of the data are taken from hydrocarbon-bearing reservoirs, above the sand is less clean.

Equations 1–3 below represent the sand and shale regression lines which have been derived through the curve fitting on the well data as described in the methodology chapter.

$$\text{Shale: } \frac{V_p}{V_s} = 90.4 \cdot \text{AI}^{-0.416} \quad (1)$$

$$\text{Sand (water): } \frac{V_p}{V_s} = -0.2821 \cdot \log_{10}(\text{AI}) + 2.777 \quad (2)$$

$$\text{Sand (gas): } \frac{V_p}{V_s} = 0.1 \cdot \log_{10}(\text{AI}) + 1.0503 \quad (3)$$

When comparing the sand lines to the laboratory and model equation-derived sand lines from Pupos (2015), the log-derived data fit very well the laboratory-derived data in areas of higher acoustic impedance. There are some misfits (including resistivity) especially in areas of lower acoustic impedance with the water-saturated sand line. These deviation results from the fact that the model-based lines are calculated and extrapolated from data from an exact lithology and certain reservoir in Badenian time. Thus, homogenous lithology is presupposed throughout the whole well. The data derived from logs take different

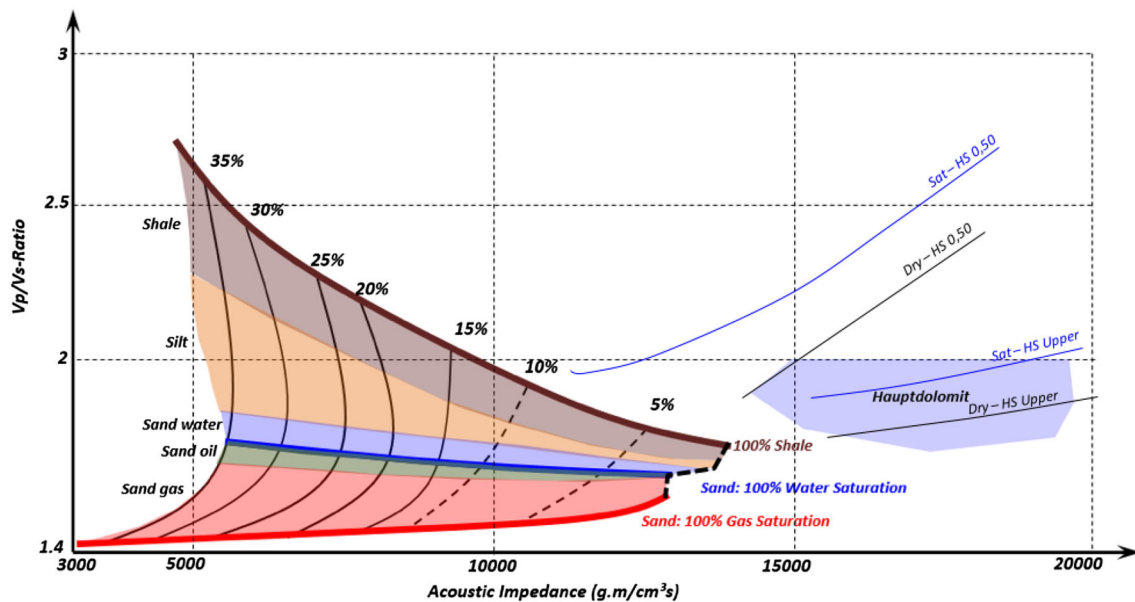


Fig. 10 Final rock physics template applicable for Vienna Basin with indicated lithologies and fluids as well as porosity trend lines. Additionally, HS bounds for carbonates (Gegenhuber and Pupos 2015) are included

lithologies into account and can be used more generally throughout the basin.

Gegenhuber and Pupos (2015) measurements and the derived upper bounds for carbonate (including “the main dolomite”) samples fit well to the data points from well measurements in Field D where “the main dolomite” has been reached. Formation evaluation indicates a dense and low-porosity dolomite, which explains that the upper HS bounds fit to the data.

Regarding the “mixture lithology” between the water-saturated sand line and shale line, a closer look is taken with some examples of depositional sequences. Figure 9 below shows depositional trends within the rock physics template with the aid of some selected reservoir examples from Sarmatian and Badenian ages. Two coarsening upward trends (due to delta deposition in Sarmatian) are presented on the left side of the plot. In general, the fine (clay) part of the delta plots near the predicted shale line as it should be. When the grains become coarser and the sand takes over, the data points shift into the direction of higher AI and lower v_p/v_s ratios towards the sand line. In further consequence, there are two possibilities of plotting behaviour: if the sand is filled with gas the trend reverses again into the direction of gas or if the sand on the top of the depositional sequence is filled with water or oil the data points stays near the water line.

On the right side of the crossplot two Badenian reservoirs deposited within braided rivers are shown as example. The left reservoir is a shallower Badenian horizon which is water-bearing in the shown example; while the

right reservoir is around 50 m deeper Badenian horizon which has two gas-bearing very clean sand packages. They are both shifting in the direction of the water- and gas-saturated sand lines when the sand fraction amount is increasing, but they do not follow the reversal trend (from shale to sand) like the shallower Sarmatian prograding delta reservoirs in the left part of the crossplot.

Shales plot in higher AI areas and sands plot in lower AI areas. Reason for this behaviour could be the faster compaction of shales with depth and the reversal of the trend as we have encountered within the Sarmatian reservoirs. Another explanation for the missing of the reversal trend could be the deviation of the wells and the anisotropic behaviour of the shales. As already mentioned, with increasing tool deviation within the borehole, velocity measurements (which are included in the acoustic impedance calculation) are apparently increasing because of the anisotropic shale layers. At the same time, they remain stable in sands independent of deviation. Because most of the wells used are deviated after a certain depth (most of the cases from 1.5 km), this could play a major role here.

Conclusion and outlook

A general rock physics template for Vienna Basin derived fully from log data is created throughout the study. This final template including the carbonate bounds (saturated and dry) from Gegenhuber and Pupos (2015) is shown in Fig. 10.

It is shown that the template created with formation evaluation data honours lithological heterogeneity throughout the basin. Additionally, it is shown that laboratory-derived templates with petrophysical models fit the well data very well in greater depths, but in shallower areas there are misfits because of the assumed homogeneity of the lithology in experimentally derived data and limited cores. Examples of depositional sequences with shale and sand parts (braided rivers and prograding deltas) behave as predicted within the rock physics template. Concluding, the template from well-log data represents the general basin lithology very well even in different areas of the basin. Fluid discrimination in the reservoir sands is given on the template too. Even oil-bearing sands show some significant discrimination from water-bearing sands. Thus, in further consequence inversion results from seismic data sets from different parts of the Vienna Basin will be used to screen the basin for commercial reservoirs. Additionally, further work will include true vertical depth into next templates as part of the axis, due to the fact, that this property correlates with elastic properties and is derivable from seismic data.

Acknowledgements Open access funding provided by Montanuniversität Leoben. The authors would like to thank OMV for the permission to publish data.

Open Access This article is distributed under the terms of the Creative Commons Attribution 4.0 International License (<http://creativecommons.org/licenses/by/4.0/>), which permits unrestricted use, distribution, and reproduction in any medium, provided you give appropriate credit to the original author(s) and the source, provide a link to the Creative Commons license, and indicate if changes were made.

References

- Avseth P, Carcione J (2015) Rock physics template analysis of Norwegian shelf clay-rich source rocks. Third EAGE workshop on rock physics, extended abstracts: RP23
- Avseth P, Veggeland T (2015) Seismic screening of rock stiffness and fluid softening using rock physics attributes. *Interpretation* 3:85–93. doi:10.1190/INT-2015-0054.1
- Avseth P, Dvorkin J, Mavko G, Rykkje J (2000) Rock physics diagnostic of North Sea sands: link between microstructure and seismic properties. *Geophys Res Lett* 27:2761–2764. doi:10.1029/1999GL008468
- Avseth P, Mukerji T, Mavko G (2005) Quantitative seismic interpretation: applying rock physics tools to reduce interpretation risk. Cambridge University Press, Cambridge
- Avseth P, van Wijngaarden AJ, Mavko G (2009) Rock physics estimation of cement volume, sorting, and net-to-gross in North Sea sandstones. *Lead Edge* 28:98–108. doi:10.1190/1.3064154
- Ba J, Cao H, Carcione J, Tang G, Yan XF, Sun WT, Nie JX (2013) Multiscale rock physics templates for gas detection in carbonate reservoirs. *J Appl Geophys* 93:77–82. doi:10.1016/j.jappgeo.2013.03.011
- Chi XG, Han DH (2009) Lithology and fluid differentiation using rock physics template. *Lead Edge* 28:1424–1428. doi:10.1190/1.3064147
- Dvorkin J, Nur A (1996) Elasticity of high-porosity sandstones: theory for two North Sea datasets. *Geophysics* 61:1363–1370. doi:10.1190/1.1444059
- Gassmann F (1951) Elastic waves through a packing of spheres. *Geophysics* 16:673–685
- Gegenhuber N, Pupos J (2015) Rock physics template from laboratory data for carbonates. *J Appl Geophys* 114:12–18. doi:10.1016/j.jappgeo.2015.01.005
- Gupta S, Chatterjee R, Farooqui M (2012) Rock physics template (RPT) analysis of well logs and seismic data for lithology and fluid classification in Cambay Basin. *Int J Earth Sci* 101:1407–1426. doi:10.1007/s00531-011-0736-1
- Hamilton W, Wagner L, Wessely G (1999) Oil and gas in Austria. *Mitt Österr Geol Ges* 92:235–262
- Hashin Z, Shtrikman S (1962) A variational approach to the theory of effective magnetic permeability of multiphase materials. *J Appl Phys* 33:3125–3131
- Hermana M, Lubis LA, Ghosh PD, Sum CW (2016) New rock physics template for better hydrocarbon prediction. Offshore technology conference Asia, OTC-26538-MS
- Kienberger G, Fuchs R (2006) Case history of the Matzen Field/Matzen Sand (16th TH): a Story of success! Where is the end? SPE Europec/EAGE annual conference and exhibition, SPE 100329
- Kreutzer N (1992) Matzen Field, Austria (Vienna Basin). AAPG treatise of petroleum geology. Atlas of Oil and Gas Fields, Structural Traps VII, pp 57–98
- Ladwein HW (1988) Organic geochemistry of Vienna Basin: model for hydrocarbon generation in overthrust belts. *AAPG Bulletin* 72:586–599
- Ødegaard E, Avseth P (2004) Well log and seismic data analysis using rock physics templates. *First Break* 22:37–43. doi:10.3997/1365-2397.2004017
- Pupos J (2015) „Rock physics template“—application on different rocks and different scales. Unpublished Master Thesis, Montanuniversität Leoben, Austria
- Sachsenhofer RF (2001) Syn- and post-collisional heat flow in the Cenozoic Eastern Alps. *Int J Earth Sci* 90:579–592
- Sauer R, Seifert P, Wessely G (1992) Guidebook to excursions in the Vienna Basin and the adjacent Alpine-Carpathian thrustbelt in Austria. *Mitt Oesterr Geol Ges* 85:1–264
- Schön JH (2015) Physical properties of rocks: fundamentals and principles of petrophysics. Elsevier, Amsterdam
- Tucovic N, Bartetzko A, Wessling S, Schön J, Gegenhuber N (2016) Resistivity and acoustic impedance based rock physics templates for enhanced well placement and reservoir understanding. 78th EAGE conference and exhibition, extended abstracts, We STZ013
- Wessely G (2006) Geologie der Österreichischen Bundesländer, Niederösterreich. Geologische Bundesanstalt, Wien, pp 189–226

The magnetic susceptibility of soils in Krakow, southern Poland

Anna Wojas¹ 

Received: 11 April 2017 / Accepted: 18 April 2017 / Published online: 3 May 2017
© Institute of Geophysics, Polish Academy of Sciences & Polish Academy of Sciences 2017

Abstract Studies into the magnetic susceptibility have been used to assess the soils contamination in the Krakow area. The results of topsoil (over a 2×2 km grid), subsoil (37 shallow holes) and soil samples (112) measurements were presented as maps of soil magnetic susceptibility (both volume and mass) illustrating the distribution of parameters in topsoil horizon (0–10 cm) and differential magnetic susceptibility maps between topsoil horizon and subsoil (40–60 cm). All evidence leads to the finding that the highest values of magnetic susceptibility of soil are found exclusively in industrial areas. Taking into consideration the type of land use, the high median value ($89.8 \times 10^{-8} \text{ m}^3 \text{ kg}^{-1}$) was obtained for samples of cultivated soils and is likely to be connected with occurrence of fertile soil (chernozem). Moreover, enrichment of soils with Pb and Zn accompanies magnetic susceptibility anomalies in the vicinity of the high roads and in the steelworks area, respectively.

Keywords Magnetic susceptibility · Soil pollution · Krakow

Introduction

The soils of Krakow (Poland's historic second city) located in southern Poland, have been a subject of magnetic susceptibility (MS) investigations during the last decade to determine its pollution. The first data concerning MS of soils in Krakow area come from the publication by Magiera et al. (2002). Until now, reconnaissance investigations have been done in selected parts of the city, namely in the close vicinity of the steelworks (Magiera 2004; Rosowiecka and Nawrocki 2010) and in Nowa Huta, local district (Hasso-Agopsowicz et al. 2004; Wojas 2009).

Urban soils have been recently the subject of MS investigations in other countries, e.g. Turkey (Canbay et al. 2010; Kucer et al. 2012), Jordan (El-Hasan et al. 2009; El-Hasan and Lataifeh 2013), Iran (Karimi et al. 2011, Dankoub et al. 2012), Mexico (Morton-Bermeaa et al. 2009), Romania (Gârbacea and Ioane, 2010), etc.

It should be emphasised that natural conditions (especially topography, climate and meteorological features) of Krakow have a negative impact on the circulation of air mass which in turn manifest the smog formation which we see today. Krakow is situated in an exceptionally narrow part of the Vistula valley following an east-westerly direction. Additionally, the land elevation in the western part of the city makes the flow of air mass difficult. The strength of wind is often very poor in the city and windless days are a common occurrence. For the previous reasons stated, the majority of pollutants released into the atmosphere within the city area are usually present in soil over a short distance from their original point of emission.

Geochemical studies of soil samples collected in the 1990s throughout the whole area of Poland (Pasiczna 2003) have proven that permissible levels of heavy metals, the most common of which are Pb, Zn, Cu and the

✉ Anna Wojas
awojas@agh.edu.pl

¹ Department of Geophysics, Faculty of Geology, Geophysics and Environmental Protection, AGH University of Science and Technology, 30 Mickiewicza Av., 30-059 Krakow, Poland

following Ni, Cd, Hg are less commonly observed, were exceeded in the surrounding sites within Krakow. Geochemical anomalies have occurred mainly in the city centre and in the surroundings of the former Lenin Steelworks (currently ArcelorMittal Poland SA industrial plant, see Fig. 1), situated in the eastern part of Krakow. The steelworks, in operation since 1954, is the largest contributor of dust, ash, gaseous pollution and all airborne matter present in the atmosphere (Regional Inspectorate for Environmental Protection in Krakow 2013). Mineralogical studies of atmospheric particulate matter (PM) released by the steelworks have revealed that it contains mostly heavy metals such as Fe, Zn, Mn, as well as minor amounts of Pb, Cu, Ni, and sometimes Cd (Lis and Pasieczna 1995 and references therein). It has also indicated that the emission of gaseous particles, PM and heavy metals from “EC Kraków” heat and power plant (Fig. 1), located to east from the city centre, constitutes an important source of soil pollution. Lis and Pasieczna (1995) have suggested that soil pollution in Krakow is also associated with the functioning of local boilers and household hearths as well as increasing road traffic.

This paper concerns a magnetic susceptibility survey of soils in Krakow and laboratory studies of samples, examined in 2008–2012. The objectives of this study were as follows:

- investigations of topsoil magnetic properties (determination of MS of soils, identification of MS anomalies),
- indication of increased values of soils MS correlated with heavy metals concentrations,
- analysis of the relationship between soil type (Skiba et al. 2013) and soil MS.

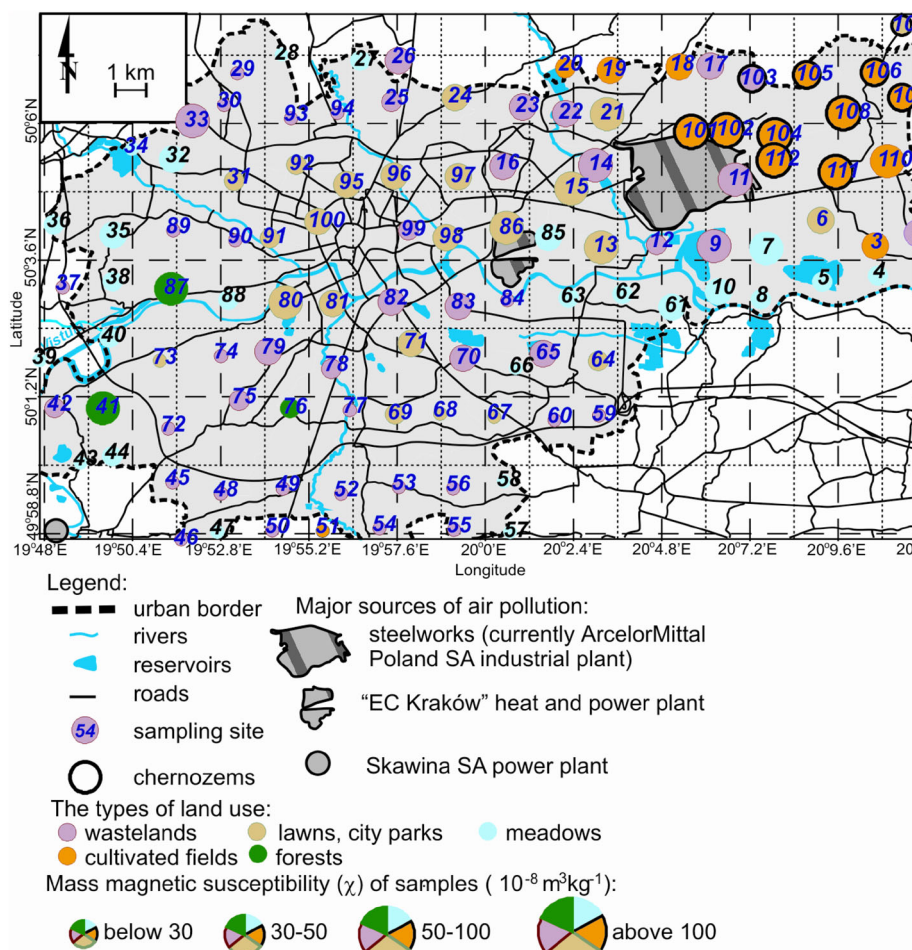
Materials and methods

Measurements of topsoil MS were carried out at 112 locations over a 2×2 km grid throughout the entire area of Krakow (Fig. 1).

The measurement sites respected specific criteria, namely:

- minimum distance from a road—20 m,

Fig. 1 Distribution of 112 measurement sites over the area of Krakow. The map includes such aspects as type of land use, mass magnetic susceptibility ($\chi \times 10^{-8} \text{ m}^3 \text{ kg}^{-1}$) of soils and the occurrence of chernozem soil



- existing vegetation allows for a proper contact of field survey sensor with the studied soil,
- with the exception of forest areas, measurements were not performed in close vicinity of the tree trunks, i.e., the measurement sites were placed in uncovered areas with no barriers preventing the direct fall of air pollutants on the soil surface. In less urbanised areas, measurement sites were located mainly in wastelands, meadows and forests, whereas in strongly urbanised areas, they were situated in parks, housing estate greens, urban greens and former fortifications (Fig. 1).

Surveys of MS were carried out using MS2 meter supplied with MS2D sensor produced by Bartington Company, with approximately 6 cm measurement range. Depth of response is 50% at 1.5 cm and 10% at 6 cm (Bartington Instruments Ltd. 2002). Apparent volume magnetic susceptibility κ_a (Sharma 1997) of soils was measured in situ, in 112 locations with minimum 5 repetitions in accordance with the applicable procedure (Bartington Instruments Ltd. 2002; Schibler et al. 2002). In some places the vegetation was removed to ensure a proper contact of the sensor with soil. In the case of MS exceeding 50.0×10^{-5} [SI], additionally the author drilled to a depth of approximately 100 cm and took measurements of MS in the excavated area with the use of down-hole MS2H sensor. Furthermore, an extensive soil material [112 soil samples from the depth (0–10) cm] was collected at each measurement site during fieldwork for laboratory measurements, including MS measurements and geochemical analysis. The soil material, collected from the depth of (0–10) cm, was dried at room temperature, crushed and placed in 10 cm^3 plastic containers.

In the next stage, the laboratory magnetometric studies involved study of low-frequency (465 Hz) volume magnetic susceptibility (κ). Volume MS of total of topsoil samples was measured using the MS2 meter with MS2B sensor working in the magnetic field of 80 A/m (Bartington Instruments Ltd. 2002). Subsequently, after weighing the soil samples, their mass magnetic susceptibility (χ) was calculated according to the formula:

$$\chi = \frac{\kappa}{\rho} [\text{m}^3\text{kg}^{-1}], \quad (1)$$

where: κ volume MS [–], ρ volume density [kg/m^3].

Values of χ are density-independent, hence the comparison of magnetic properties of material coming from different environments is possible.

Geochemical analysis, including pH value and content of heavy metals (Pb, Zn, Cu, Cd, Ni, Fe) was carried out for soil samples (37) with κ above 30.0×10^{-5} [SI]. Soil reaction (pH) was determined by potentiometric method, whereas the content of heavy metals in soil was measured with atomic absorption spectrometry (AAS). The study

included the heavy metals that can contaminate soils in Krakow (Pasiczna 2003).

On the basis of the results of surveys and laboratory studies, maps of MS of soils in Krakow have been constructed, namely:

1. map of the apparent volume magnetic susceptibility of topsoil (at the depth of 0–10 cm) (Fig. 2),
2. map of the mass magnetic susceptibility of topsoil (Fig. 3),
3. map of the volume magnetic susceptibility of subsoil (at the depth of 40–60 cm) for areas subjected to high anthropogenic factors (Figs. 5b, 6b), namely urbanised surroundings of industrial areas,
4. maps of differential magnetic susceptibility between topsoil (0–10 cm) and subsoil at the depth of (40–60) cm for areas subjected to high anthropogenic factors (Figs. 5c, 6c).

The magnetic susceptibility maps were prepared using ‘Surfer Surface Mapping System’ software provided by Golden Software.

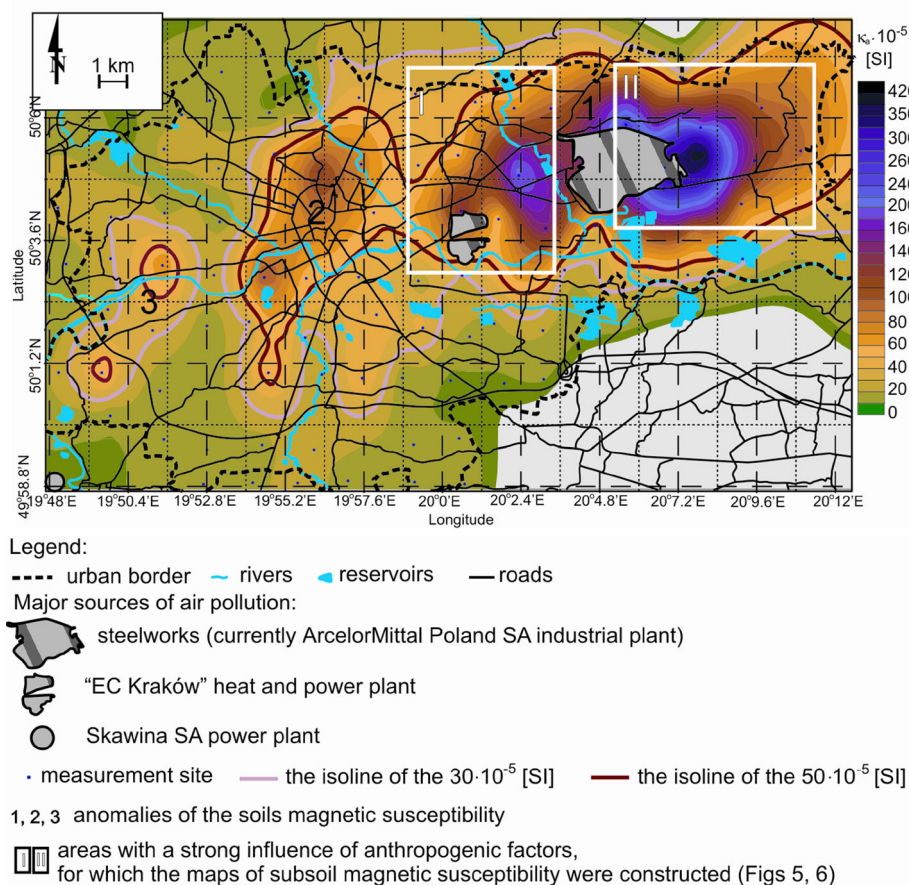
The maps (Figs. 2, 5, 6) contain two thick isolines with values 30.0×10^{-5} [SI] and 50.0×10^{-5} [SI]. In Upper Silesia (strongly industrialised region of Poland), the values of κ_a of soil in the range of $(30.0\text{--}50.0) \times 10^{-5}$ [SI] indicate a considerable risk of soil contamination with heavy metals, while the values exceeding 50.0×10^{-5} [SI] imply the absolute necessity of geochemical studies (Magiera 2004, Strzyszc et al. 2006). On the other hand, soils in the unpolluted region of the Carpathians are characterised by low MS values, usually below 30.0×10^{-5} [SI] (Magiera et al. 2002; Gonet and Wojas 2016). It should be mentioned that topsoil MS depends on magnetic mineralogy, concentration and grain-size of magnetic particles in soil. The parent material on which the soil is formed and pedogenesis intensity cannot be omitted. For these reasons, each finding and the data received therein is case specific and independent of each of other.

Results and discussion

Apparent volume magnetic susceptibility of topsoil (0–10 cm)

Topsoil (0–10 cm) κ_a in the whole area of Krakow varies in a very wide range, i.e. $(11.8\text{--}434.6) \times 10^{-5}$ [SI]. The high average value of the all measurements (53.0×10^{-5} [SI]) points to the significant influence of anthropogenic factors on top layer of soil. On the map of topsoil magnetic susceptibility (Fig. 2), three major MS anomalies (positive, with increased values of MS) can be distinguished. These

Fig. 2 Map of apparent volume magnetic susceptibility ($\kappa_a \times 10^{-5}$ [SI]) of topsoil (0–10 cm) in Krakow (Wojas 2012)



anomalies occur in different parts of Krakow: eastern (1), central (2) and south-western (3).

Anomaly 1 is the biggest one. An extension of the anomaly and its approx. W-E orientation are in clear relation (Magiera et al. 2016) with west winds prevailing in Krakow. The anomaly is marked by two peaks. The first one is situated in the centre of Nowa Huta district, to the west of the steelworks (Fig. 2). High MS (220.0×10^{-5} [SI]) is probably caused by soil pollution with magnetic particles originating from high traffic in this region. The second, much larger peak of the anomaly is situated in close proximity to the steelworks, on the eastern side. It should be noted that it corresponds to increased heavy metals contents in soil, especially Zn, Pb, Cu and Cd (Pasieczna 2003). Very high values of topsoil MS in the close vicinity of the steelworks, reaching 434.6×10^{-5} [SI] (Jarzyna et al. 2012), are mainly associated with technogenic magnetic particles (TMP) (Magiera et al. 2011, 2015) arising from industrial emission and comprising iron compounds (oxides, sulphides, etc.). The industrial pollutions emitted by ArcelorMittal Poland SA consist of iron minerals such as: magnetite $\text{Fe}^{2+} \text{Fe}^{3+}_2\text{O}_4$, hematite $\alpha\text{-Fe}_2\text{O}_3$, siderite FeCO_3 , wüstite Fe^{2+}O , olivine (Fe, Mg silicate), melanterite $\text{Fe}^{2+}[\text{SO}_4] \cdot 7\text{H}_2\text{O}$, illesite (Mn,

Zn, Fe) $\text{SO}_4 \cdot 4\text{H}_2\text{O}$ (Maneck and Marszałek 1993). This is reflected in the strong correlation between MS and Fe (see "Geochemical studies of topsoil (0–10 cm)" section). The increase of topsoil MS in this part of the city can be additionally caused by other anthropogenic factors, such as:

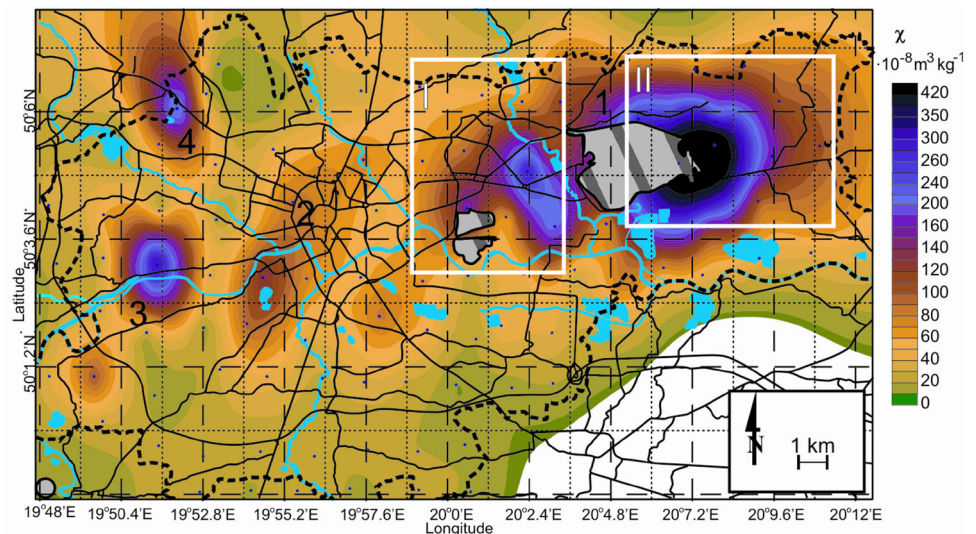
- thermal transformations of magnetic minerals in soil caused by a consequence of burning grass (currently prohibited by law, although still taking place),
- the corrosion and rubbing of metal railway elements,
- the usage of chemical fertilisers (containing ash) in agricultural areas (Hasso-Agopsowicz et al. 2004),

which cause the enrichment of soil with iron compounds.

Furthermore, no assurance can be given to the fact that geogenic factors have no influence on the soil MS due to the weathering of magnetic minerals present in rocks creating the foundation of railway track and, moreover, the occurrence of chernozem soil (Fig. 1) characterised by stronger magnetic properties (Jeleńska et al. 2004) compared with other soil types.

In summary, topsoil κ_a measured in the vicinity of the steelworks are:

Fig. 3 Map of mass magnetic susceptibility ($\chi \times 10^{-8} \text{ m}^3 \text{ kg}^{-1}$) of topsoil (0–10 cm) in Krakow




Legend:

--- urban border — rivers ▲ reservoirs — roads • sampling site


Major sources of air pollution:

 steelworks (currently ArcelorMittal Poland SA industrial plant)

 "EC Kraków" heat and power plant

 Skawina SA power plant

1, 2, 3, 4 anomalies of the soils magnetic susceptibility

 areas with a strong influence of anthropogenic factors, for which the volume susceptibility maps of subsoil were constructed (Figs 5, 6)

- lower in confrontation with MS of soils exposed to strong human impact, e.g. in the strongly industrialised Upper Silesia region (Magiera et al. 2002), as well as in the areas in the proximity of power plants, e.g. Chrzanów and Jaworzno (Heller et al. 1998),
- higher in comparison to MS of soils near others ironworks in southern Poland (Rosowiecka and Nawrocki 2010).

The topsoil in western part of the anomaly 1, situated within the area of "EC Kraków" heat and power plant (Fig. 2), is strongly magnetic with MS varying in the range of $(50.0\text{--}145.0) \times 10^{-5}$ [SI]. The anomaly may be caused by magnetic particles released with ash from the heat and power plant as well as particles accompanying road traffic pollution. Moreover, in these soils the limit values of Cu and Pb content are exceeded (Pasieczna 2003).

Magnetic susceptibility anomaly 2 (Fig. 2) in the Krakow city centre is less extensive. This anomaly has a visibly elongated shape and its intensity is about four times lower (maximum κ_a is 119.4×10^{-5} [SI]) in comparison to anomaly 1. It is almost certainly associated with soil pollution by magnetic particles released by road transport. The influence of traffic on the soil magnetic properties is clearly visible on the map along the main roads. A

localization and an extension of the anomaly is strictly connected with a position on the map of dual carriageway road which is the only road running through the city centre, in the N–S direction, connecting nearby cities in the south part of Poland. In the effect, a very high intensity of road traffic and road congestion are often observed in this region. The anomaly is connected also with coal burning in local boilers and coal stoves in households.

A moderate in size, magnetic susceptibility anomaly 3 is located in S–W part of the city (Fig. 2). Its extension is similar to the anomaly 2. In this case, a maximum value of topsoil MS occurs on the hillside in a forest and amounts to 73.0×10^{-5} [SI]. Sources of increased values of MS may be an accumulation of dust and fly ashes in soil, emitted by Skawina SA power plant (located near the south-western border of Krakow, Fig. 2) and air pollutions from strongly industrialised region of Upper Silesia. A lithogenic origin (occurrence of calcareous soils in this region) can be also influential because of enhancement content of Fe and Pb (Dankoub et al. 2012) in soils.

The presented anomalies of topsoil magnetic susceptibility cover the most of the Krakow area. In the other places, MS of topsoil is distinctly lower and ranges between $(10.0\text{--}30.0) \times 10^{-5}$ [SI].

Mass magnetic susceptibility of topsoil (0–10 cm)

Weighing of 112 soil samples allowed the author to determine volume density (ρ) of sample collection and afterwards establish mass MS (i.e. χ). Median value of soil χ , as the most representative value, was calculated for five groups of samples collected in areas of different land development (Table 1). The results show that forest soils and cultivated soils (mostly located close to the steelworks) have the highest median values (106.9×10^{-8} and $89.8 \times 10^{-8} \text{ m}^3\text{kg}^{-1}$, respectively). Lower value is observed in the case of soils of lawns and city parks ($62.8 \times 10^{-8} \text{ m}^3\text{kg}^{-1}$). Similar, lower χ median values have been noted in areas of meadows ($35.4 \times 10^{-8} \text{ m}^3\text{kg}^{-1}$) and wastelands ($27.9 \times 10^{-8} \text{ m}^3\text{kg}^{-1}$).

The results of χ have been compared (Table 1) with χ of soils in Poland (Magiera et al. 2002). It can be concluded that soils in Krakow vs. Poland display:

- conspicuously lower maximum values of χ (in each of the considered type of land use),
- higher median values of χ in meadows, forest areas, cultivated fields as well as, lawns and parks,
- lower median value of χ in wastelands.

Afterwards, a map of χ of topsoil in Krakow was constructed on the basis of 112 values (Fig. 3). Anomaly 1, prevalent in the eastern part of Krakow, is clearly visible (Fig. 3). The second peak of the anomaly, observed in the centre of Nowa Huta district, is also prominent. Anomaly 2 has a lower intensity specifically in the city centre. The most attention is paid to the western part of Krakow. Anomaly 3 in the south-western region of the city is considerably stronger because of a much higher value of χ for sample 87 (Fig. 1). High χ values for sample 87 as well as 41 can be related with uninterrupted accumulation of magnetic particles for many years taking into account the type of land use (forests) (Magiera et al. 2006).

Contrary to the map of κ_a (Fig. 2), fourth positive anomaly has appeared on the map of mass MS (Fig. 3). It is situated in the north-western part of the city and has no equivalent on the previous map. It is caused probably by

impeded contact of MS2D sensor with soil (due to dense and high grass). Nevertheless, additional MS measurements, in a denser measurement and sampling network, should be taken in the future to take a deeper insight into this discrepancy.

What is more, an attempt to find a connection between χ and type of soil was made. The types of soil in Krakow area were taken from publication by Skiba et al. (2013). Unfortunately, the study has revealed the lack of clear relationship between topsoil MS and the soil type. This fact can be caused by considerable pollution of soil in Krakow.

Geochemical studies of topsoil (0–10 cm)

Geochemical studies of soil samples have concerned the determination of pH and content of six heavy metals (Pb, Zn, Cu, Cd, Ni and Fe). The results are shown in Table 2 (exceeded values are in bold).

The studies have indicated that the soils are predominantly alkaline (pH > 7.5) (Polish Standard PN-ISO 10390: 1997) and confirmed the previous geochemical studies (Pasiczna 2003). Soils with the strongest (7.7–9.0) alkaline reaction were noted in the vicinity of the steelworks. The Pearson correlation coefficient between MS and Fe, calculated for alkaline soils collected in the eastern part of Krakow is >0.83 (statistical significance level $p = 0.05$). The alkaline reaction of soils is chiefly associated with the natural calcareousness of loess occurring in this area (Gradziński 1972). Furthermore, possible alkaline character (Magiera et al. 2011) of TMP settled on the ground surface can also affect soil reaction. The exception is low pH value (5.25, an acidic reaction) of soil sample 108 (Fig. 1) from agricultural area (to the east of the steelworks). Due to increased value of MS and acidic reaction of soil, the soil liming procedure is recommended in order to limit the absorption of heavy metals by plants which are cultivated in this area (Hołubowicz-Kliza 2006).

Conversely, pH of soils in areas without strong influence of human factor (i.e., forest areas) are strongly acidic or acidic [<5.0 or (5.1–6.0), respectively].

Geochemical analysis of heavy metals concentration in soils has demonstrated that high content of Zn accompanies

Table 1 Mass magnetic susceptibility ($\chi \times 10^{-8} \text{ m}^3\text{kg}^{-1}$) of soil samples according to the type of land use at sampling site

Land use	<i>n</i>		Min.		Max.		Mean		Median	
	Krakow	Poland*	Krakow	Poland*	Krakow	Poland*	Krakow	Poland*	Krakow	Poland*
Wastelands	46	284	11.7	1.4	588.2	1157.6	58.8	124.5	27.9	52.4
Lawns, city parks	24	744	8.4	0.8	302.4	1768.1	80.5	108.5	62.8	59.0
Meadows	24	1900	12.3	0.1	129.6	1660.4	42.9	30.8	35.4	14.8
Cultivated fields	15	4892	29.5	0.2	651.4	747.9	157.2	23.9	89.8	16.2
Forests	3	2422	46.8	−0.4	342.4	697.0	165.4	22.4	106.9	12.7

* Literature data (Magiera et al. 2002), *n* number of soil samples

Table 2 Soil reaction (pH), heavy metal contents and mass magnetic susceptibility for soil samples (37) with κ above 30.0×10^{-5} [SI]

Sampling site no.	Geographical coordinates		The type of land use	Mass magnetic susceptibility $\chi \times 10^{-8} \text{ m}^3 \text{ kg}^{-1}$	pH	Content (mg kg ⁻¹)					Fe (%)
	N	E				Pb	Zn	Cu	Cd	Ni	
6	50°4'0.1"	20°9'7.8"	Lawn/city park	95.8	6.87	33	127	14	1	21	2.92
7	50°3'30.4"	20°7'38.9"	Meadow	129.6	6.69	32	133	19	2	25	2.81
9	50°3'33.0"	20°6'13.4"	Wasteland	228.8	7.29	58	243	24	2	50	4.54
11	50°4'42.9"	20°6'47.9"	Wasteland	588.2	8.99	36	158	14	1	15	3.37
13	50°3'31.6"	20°3'9.4"	Lawn/city park	224.5	6.33	63	256	32	1	40	3.65
14	50°4'58.0"	20°2'59.6"	Wasteland	101.2	8.85	22	128	11	0	14	1.69
15	50°4'33.4"	20°2'20.4"	Lawn/city park	302.4	6.54	37	274	14	1	13	2.26
16	50°4'57.0"	20°0'28.9"	Wasteland	88.0	6.63	33	207	15	3	16	1.71
18	50°6'41.6"	20°5'16.5"	Cultivated field	57.5	7.96	15	57	8	0	11	1.23
19	50°6'37.8"	20°3'24.1"	Cultivated field	83.3	5.95	30	108	14	1	13	1.79
21	50°5'51.9"	20°3'18.9"	Lawn/city park	114.4	8.66	23	119	13	0	17	2.20
22	50°5'52.3"	20°2'11.2"	Wasteland	61.6	8.54	22	111	15	0	17	1.95
23	50°5'59.8"	20°1'0.4"	Wasteland	53.4	8.17	17	78	11	0	16	1.90
41	50°0'42.0"	19°49'35.6"	Forest	106.9	4.84	70	66	8	1	9	0.83
63	50°2'38.2"	20°2'14.0"	Meadow	47.1	8.05	25	111	21	0	34	3.02
69	50°0'35.7"	19°57'32.8"	Lawn/city park	37.5	8.14	23	100	24	0	26	2.39
76	50°0'42.0"	19°54'41.3"	Forest	46.8	5.25	21	39	17	0	6	0.37
80	50°2'33.8"	19°54'33.8"	Lawn/city park	137.9	8.20	79	293	34	1	16	2.36
81	50°2'32.6"	19°55'50.8"	Lawn/city park	72.3	7.86	35	154	19	0	16	1.54
86	50°3'51.7"	20°0'34.5"	Lawn/city park	167.9	6.94	60	263	17	1	19	2.02
87	50°2'48.0"	19°51'27.1"	Forest	342.4	5.11	139	238	14	3	10	1.98
92	50°4'58.5"	19°54'51.9"	Lawn/city park	44.6	6.41	33	97	16	0	13	1.41
95	50°4'37.6"	19°56'13.8"	Lawn/city park	72.3	7.22	43	145	19	0	16	1.72
96	50°4'46.8"	19°57'31.2"	Lawn/city park	75.9	8.44	26	108	13	0	14	1.69
98	50°3'41.9"	19°58'56.2"	Lawn/city park	62.6	8.30	28	142	17	1	23	2.30
99	50°3'49.6"	19°57'54.3"	Lawn/city park	45.3	8.13	19	79	11	0	13	1.33
100	50°3'58.8"	19°55'26.7"	Wasteland	86.4	7.99	80	150	29	1	12	1.59
101	50°5'33.2"	20°5'36.5"	Lawn/city park	271.5	8.23	53	1494	23	1	18	2.56
102	50°5'34.9"	20°6'33.5"	Cultivated field	264.3	6.82	37	920	13	1	13	2.33
104	50°5'29.6"	20°7'52.9"	Wasteland	255.7	7.78	29	424	14	1	14	2.52
105	50°6'32.8"	20°8'44.5"	Cultivated field	89.8	8.08	17	91	11	0	16	1.96
106	50°6'35.7"	20°10'35.6"	Cultivated field	82.1	8.11	24	97	11	0	14	1.72
108	50°5'52.7"	20°9'44.9"	Lawn/city park	104.6	5.25	21	126	12	0	15	1.89
109	50°6'9.2"	20°11'20.4"	Cultivated field	85.7	7.71	22	114	14	0	17	1.70
110	50°5'2.3"	20°10'56.4"	Cultivated field	103.6	8.63	31	137	15	1	18	2.26
111	50°4'50.8"	20°9'32.4"	Cultivated field	164.8	8.46	27	131	14	1	14	2.15
112	50°5'3.3"	20°7'51.5"	Cultivated field	651.4	8.51	45	378	19	1	14	4.01
						100	300	150	4	100	
						The limit values*					

* According to Regulation of the Minister of Environment of 9 September 2012

the increased value of MS only in the close vicinity of the steelworks. In this case the highest concentration of Zn in soil amounts to 1494 ppm (anomaly 1, sampling site 101, see Fig. 1).

There is an increased content of Zn (293 ppm, the limit value is 300 ppm) and Pb (80 ppm, the limit value is 100

ppm) in the soils of the city centre (anomaly 2, sampling site 100, see Fig. 1). Furthermore, in the forest area of anomaly 3 (sampling site 87, see Fig. 1), the Zn content is enhanced (238 ppm) and, what is more, the limit value of Pb content is exceeded (139 ppm). It should be mentioned that previous geochemical studies of soils from this region

(Pasiczna 2003) showed low content of heavy metals (Pb, Zn, Cd, Cu and Hg).

It is worth emphasising that permissible contents of Cu, Cd, Ni in soils are not exceeded in any of the areas with increased values of soil MS ($>30.0 \times 10^{-5}$ [SI]).

Geochemical analyses were supplemented with the correlation between the mass MS and concentrations of heavy metals expressed by pollution load index (PLI) (Tomlinson et al. 1980):

$$PLI = \sqrt[n]{CF_1 \cdot CF_2 \cdot \dots \cdot CF_n} \quad (2)$$

where:

CF_n —contamination factor, the ratio of the metal's concentration (F_n element) to its background value (the lowest concentration value for this element),

n —number of elements.

The Pearson's correlation coefficient is $R = 0.75$ (Fig. 4) for group of samples (closed circles) with the exception of two samples (11 and 112, closed triangles) from the nearest distance from the industrial plant.

Magnetic susceptibility of subsoil (40–60 cm) and differential magnetic susceptibility maps between topsoil horizon and subsoil

An average value of subsoil MS in strongly industrialised regions of Krakow (near the steelworks and the heat and power plant) amounts to the level of 40.0×10^{-5} [SI] and is slightly higher than topsoil MS ($(10.0\text{--}30.0) \times 10^{-5}$ [SI]) in areas with a weak impact of anthropogenic factors.

Subsoil MS in the vicinity of the heat and power plant (Fig. 5b) ranges from 18.2 to 62.8×10^{-5} [SI]. The enhanced MS values (above 50×10^{-5} [SI]) may be connected with magnetic properties of alluvia of Vistula river (Skiba et al. 2013) and easier migration of magnetic minerals in the soil profile because of looser and better permeable alluvial soil.

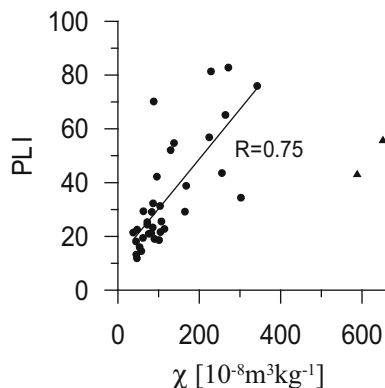


Fig. 4 Plot of the correlation between the mass MS and concentrations of heavy metals expressed by pollution load index (PLI)

In the centre of Nowa Huta district (Fig. 5b), lower values of subsoil MS (below 50×10^{-5} [SI]) have been noted (Fig. 5b). It is probably the effect of a lower content of magnetic particles occurring in the soil at the depth of (40–60) cm and confirms the accumulation of heavy metals mainly in upper horizons of soil profile.

In addition, maps of differential κ_a have been prepared in order to gain a better insight into a level of soil pollution in areas strongly affected by the human activity. The maps, representing the difference between κ_a of topsoil (0–10 cm) and subsoil (40–60 cm), reflect topsoil pollution.

Anomaly in differential MS map (Fig. 5c) is observed in the centre of Nowa Huta district. Increased MS values (up to 180.0×10^{-5} [SI]) are the evidence of highly urbanised area with heavy traffic.

The subsoil MS to the west and north-east of the steelworks suggests a possible relationship with soil type (comp. Figs. 1, 6b), i.e., chernozem soil (Skiba et al. 2013) which exhibits naturally stronger magnetic properties (Hanesch and Scholger 2005). In the chernozem soil areas, MS values reach 80.0×10^{-5} [SI] (Fig. 6b). On the other hand, in the areas covered with soil of different type (situated S and SE of the steelworks), the subsoil MS is lower ($<40.0 \times 10^{-5}$ [SI]).

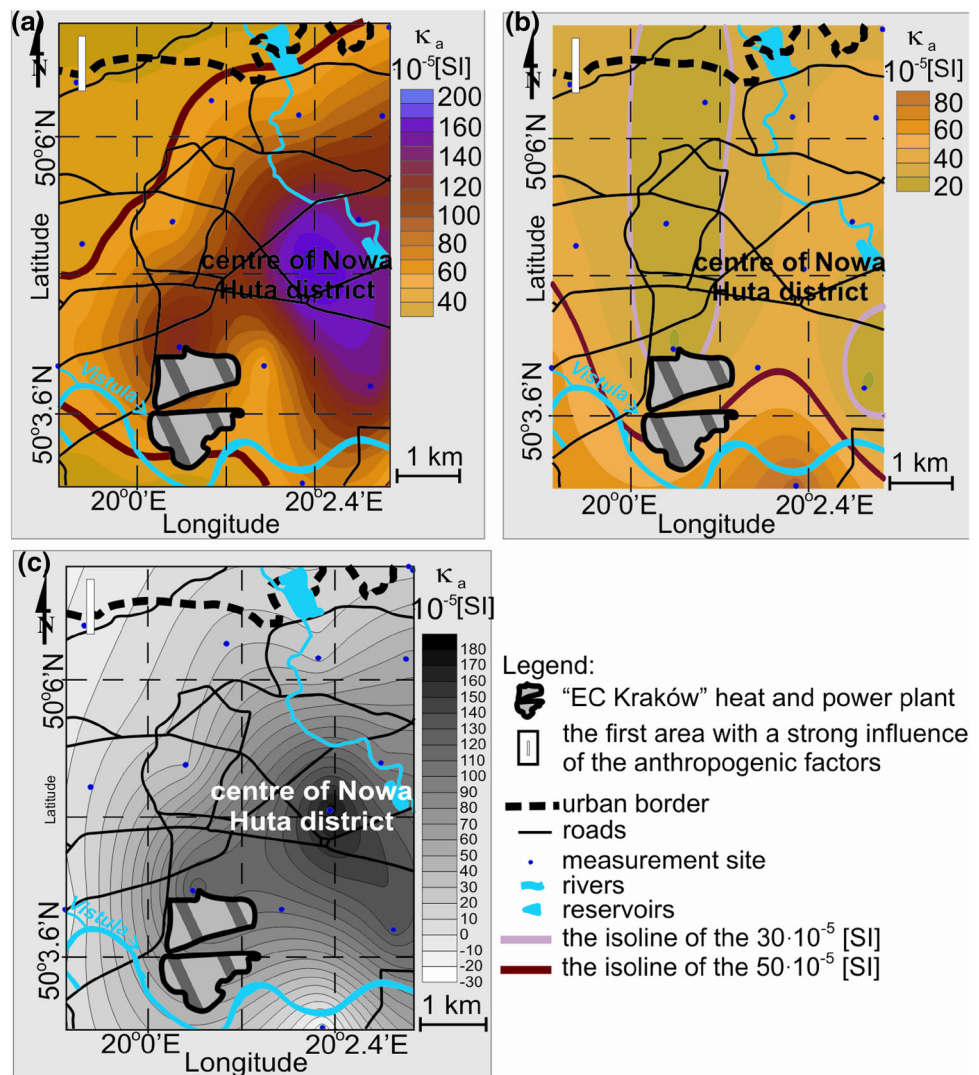
A high differential MS of soils in close proximity of the steelworks reaches 340.0×10^{-5} [SI] (Fig. 6c) and is determined by distinctly higher (up to 420.0×10^{-5} [SI]) MS of topsoil (Fig. 6a) compared to subsoil MS (Fig. 6b). This fact indicates topsoil pollution and in consequence very serious danger for pollution of plants cultivated in this region.

Conclusions

In this study area, which includes urbanised, industrialised and agricultural regions, anthropogenic factors play a key role in the creation of soil magnetic properties (especially MS) and soil pollution. This study allows the author to locate with accuracy four key areas which represent high risk of soil pollution. The research confirms that industrial emissions have the strongest influence on the level of topsoil pollution in Krakow.

The magnetic susceptibility anomaly 1 (maximum value of $651.4 \times 10^{-8} \text{ m}^3 \text{ kg}^{-1}$) is clearly visible on the map in the vicinity of the steelworks region. Geochemical studies of samples show that Zn and Pb content in soil exceeds the permissible values, in this area. Dangerous components of the particulate matter in the atmospheric air (heavy metals, toxic substances, etc.) deposited in the soil throughout the last century pose a severe threat for the quality of crops growing in this area. For this reason both monitoring and

Fig. 5 Apparent volume magnetic susceptibility maps of a) topsoil (0–10 cm), b) subsoil (40–60 cm) and c) map of differential magnetic susceptibility between topsoil and subsoil from the region of “EC Kraków” heat and power plant (area I in Figs. 2, 3)



protection of the environment are of paramount importance reference the area in close proximity of the steelworks.

In addition, subsoil MS may be connected with geogenic (natural) factors associated with occurrence of chernozem soil. Natural enhancement MS (over 40.0×10^{-5} [SI]) at the depth of (40–60) cm confirms the stronger magnetic properties of chernozem soil.

Topsoil in Krakow yields lower values of MS in comparison to soils in strongly industrialised areas in Poland (e.g. Upper Silesia). Nevertheless, only MS of soils in wastelands ($27.9 \times 10^{-8} \text{ m}^3\text{kg}^{-1}$) is lower in comparison, than those found in Poland. MS of soil in cultivated fields ($89.8 \times 10^{-8} \text{ m}^3\text{kg}^{-1}$) is significantly higher due to the adjacent steelworks area. Furthermore, high κ_a values obtained in the forest areas can be related with uninterrupted accumulation of magnetic particles for many years.

The factor of wind direction is especially important in the case of MS anomaly 1 caused by pollution from ArcelorMittal Poland SA industrial plant. Consequently

other sources of soil pollution for example, traffic and low emissions are unaffected by wind direction.

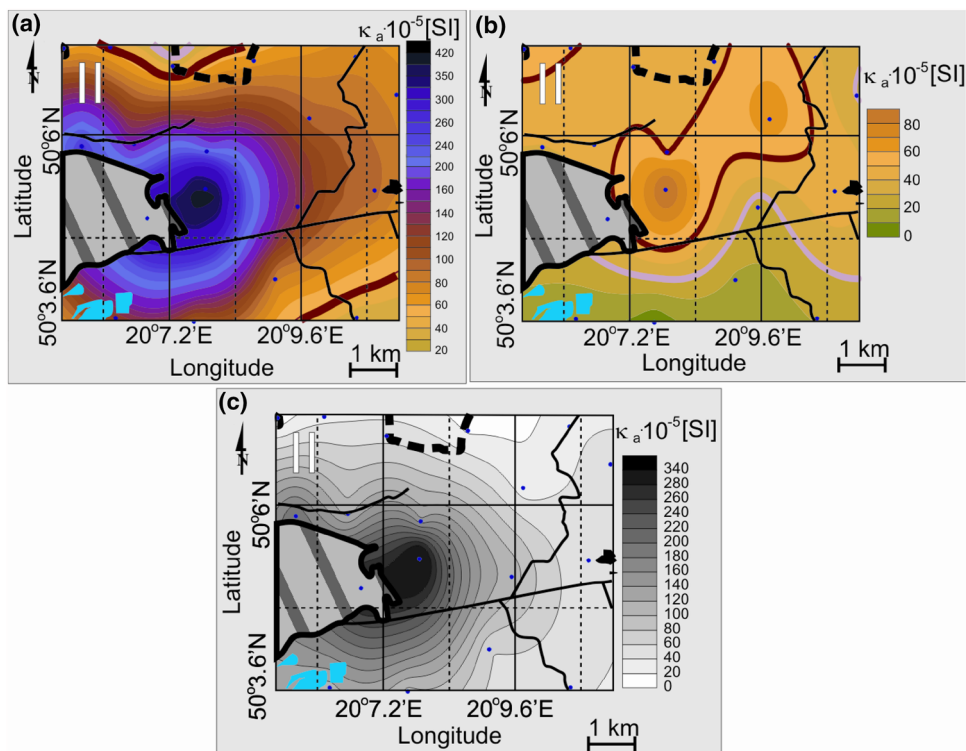
The influence of road traffic on soil magnetic properties is recognised in the vicinity of the high roads in the centre of Krakow (anomaly 2), and in the centre of Nowa Huta district (anomaly 1). Enrichment of soils with Pb accompanies MS anomalies in the central part of Krakow.

The anomalies on the maps of κ_a and mass MS of soils are qualitatively matching.









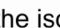
Considerable topsoil (0–10 cm) pollution has not allowed the author to determine a relationship between soil MS and soil type.

Additional study (hysteresis loops, anhysteresis magnetic susceptibility, etc.) of soil samples collected in the MS anomalies areas should be carried out in order to describe magnetic minerals in detail. Furthermore, the origin of anomaly 4, near the Krakow boarder, has not been completely investigated and more detailed survey (denser measurement network) will be planned.

Fig. 6 Apparent volume magnetic susceptibility maps of **a** topsoil (0–10 cm), **b** subsoil (at the depth of 40–60 cm) and **c** map of differential magnetic susceptibility between topsoil and subsoil from the region of the steelworks (currently ArcelorMittal Poland SA industrial plant) (area II in Figs. 2, 3)



Legend:

-  steelworks (currently ArcelorMittal Poland SA industrial plant)
-  the second area with a strong influence of the anthropogenic factors
-  urban border
-  rivers
-  reservoirs
-  roads
-  measurement site
-  the isoline of the $30 \cdot 10^{-5}$ [SI]
-  the isoline of the $50 \cdot 10^{-5}$ [SI]

In the end, magnetic susceptibility mapping could be a useful tool in assessment of soil pollution in Krakow and could be used in soil monitoring.

Acknowledgements The author would like to thank Reviewers for their important suggestions.

The study was conducted under Dean's Grant No. 15.11.140.077 entitled "Measurements and initial processing of measurement data concerning the magnetic susceptibility of soils in the Krakow region", AGH University of Science and Technology, Faculty of Geology, Geophysics and Environmental Protection.

References

- Bartington Instruments Ltd. (2002) Operation manual for MS2 magnetic susceptibility system, OM0408, Issue 27, Oxford, UK, ISBN: 0 9523409 0 9
- Canbay M, Aydin A, Kurtulus C (2010) Magnetic susceptibility and heavy-metal contamination in topsoils along the Izmit Gulf coastal area and IZAYTAS (Turkey). *J Appl Geophys*. 70(1):46–57. doi:10.1016/j.jappgeo.2009.11.002
- Dankoub Z, Ayoubi S, Khademi H, Lu SG (2012) Spatial distribution of magnetic properties and selected heavy metals in calcareous soils as affected by land use in the Isfahan region, Central Iran. *Pedosphere* 22(1):33–47. doi:10.1016/S1002-0160(11)60189-6
- El-Hasan T, Lataifeh M (2013) Field and dual magnetic susceptibility proxies for heavy metal pollution assessment in the urban soil of Al-Karak City, South Jordan. *Environ. Earth Sci*. 69:2299–2310. doi:10.1007/s12665-012-2058-4
- El-Hasan T, Al-Nawiseh AJ, Lataifeh MS (2009) Environmental magnetism: heavy metal concentrations in soils as a function of magnetic materials content. *Jordan J Earth Environ Sci* 2(Sp. Publ. No. 1):38–49 ISSN: 1995-6681
- Gârbacea GF, Ioane D (2010) Geophysical mapping of soils. *New data on Romanian soils based on magnetic susceptibility*. Rom J Geophys 54:83–95. București, ISSN: 1220-5680
- Gonet T, Wojas A (2016), Investigations of magnetic properties of soils in the Cisna—Wetlina Landscape Park. *Geol Geophys Environ* 42(1):7–19. ISSN: 299-8004
- Gradziński R (1972) Przewodnik geologiczny po okolicach Krakowa, Wydawnictwa Geologiczne, Warsaw, UKD 55(026)(438.311-194,2) (in Polish)
- Hanesch M, Scholger R (2005) The influence of soil type on the magnetic susceptibility measured throughout soil profiles. *Geophys J Int* 161(1):50–56. doi:10.1111/j.1365-246X.2005.02577.x
- Hasso-Agopsowicz A, Jeleńska M, Wicik B (2004) Magnetic susceptibility of chernozems. *MGRSD* 11:57–61. e-ISSN: 2084-6118
- Heller F, Strzyszczyk Z, Magiera T (1998) Magnetic record of industrial pollution in forest soils of Upper Silesia, Poland. *J Geophys Res* 103(B8):17767–17774. Paper No. 98JB01667, 0148-0227/98/98JB-01667509.00

- Hołubowicz-Kliza G (2006) Wapnowanie gleb w Polsce, Instrukcja upowszechnieniowa, No. 128, IUNG-PIB Publisher, Puławy, ISBN: 83-89576-31-7 **(in Polish)**
- Jarzyńska JA, Dec J, Karczewski J, Porzucek S, Tomecka-Suchoń S, Wojas A, Ziętek J (2012) Geophysics in near-surface investigations. In: Hwee-San L (ed) *New achievements in geoscience*. ISBN: 978-953-51-0263-2, InTech. 46–80. doi:[10.5772/37067](https://doi.org/10.5772/37067)
- Jeleńska M, Hasso-Agopsowicz A, Kopcewicz B, Sukhorada A, Tyamina K, Kądziałko-Hofmokl M, Matviishina Z (2004) Magnetic properties of the profiles of polluted and non-polluted soils. A case study from Ukraine. *Geophys J Int* 159:104–116. doi:[10.1111/j.1365-246X.2004.02370.x](https://doi.org/10.1111/j.1365-246X.2004.02370.x)
- Karimi R, Ayoubi S, Jalalian A, Sheikh-Hosseini AR, Afyuni M (2011) Relationships between magnetic susceptibility and heavy metals in urban topsoils in the arid region of Isfahan. *Central Iran. J Appl Geophys*. 74:1–7. doi:[10.1016/j.jappgeo.2011.02.009](https://doi.org/10.1016/j.jappgeo.2011.02.009)
- Kucer N, Sabikoglu I, Can N (2012) Measurements of environmental pollution in industrial area using magnetic susceptibility method. *Acta Physica Polonica A* 121(1):20–22. PACS: 91.25.fd, 91.62.Rt
- Lis J, Pasieczna A (1995) *Geochemical atlas of Cracow and environs: 1:100 000*. Polish Geological Institute, Warsaw **(in Polish)**. ISBN 83-7372-852-X
- Magiera T (2004) Wykorzystanie magnetometrii do oceny zanieczyszczenia gleb i osadów jeziornych, Works and Studies: No. 59, Institute of Environmental Engineering Polish Academy of Sciences in Zabrze, ISBN: 8391382486 **(in Polish)**
- Magiera T, Lis J, Nawrocki J, Strzyszczyk Z (2002) Magnetic susceptibility of soils in Poland. Institute of Environmental Engineering Polish Academy of Sciences in Zabrze, Poland **(in Polish)**. ISBN 83-86986-64-6
- Magiera T, Strzyszczyk Z, Kapička A, Petrovsky E, Team Magprox (2006) Discrimination of lithogenic and anthropogenic influences on topsoil magnetic susceptibility in Central Europe. *Geoderma* 130:299–311. doi:[10.1016/j.geoderma.2005.02.002](https://doi.org/10.1016/j.geoderma.2005.02.002)
- Magiera T, Jabłońska M, Strzyszczyk Z, Rachwał M (2011) Morphological and mineralogical forms of technogenic magnetic particles in industrial dusts. *Atmos Environ*. 45(25):4281–4290. doi:[10.1016/j.atmosenv.2011.04.076](https://doi.org/10.1016/j.atmosenv.2011.04.076)
- Magiera T, Parzenty H, Róg L, Chybiorz R, Wawer M (2015) Spatial variation of soil magnetic susceptibility in relation to different emission sources in southern Poland. *Geoderma* 255–256:94–103. doi:[10.1016/j.geoderma.2015.04.028](https://doi.org/10.1016/j.geoderma.2015.04.028)
- Magiera T, Parzenty H, Łukasik A (2016) The influence of the wind direction and plants on the variability of topsoil magnetic susceptibility in industrial and urban areas of southern Poland. *Environ Earth Sci*. 75:213. doi:[10.1007/s12665-015-4846-0](https://doi.org/10.1007/s12665-015-4846-0)
- Manecki M, Marszałek M (1993) Zanieczyszczenie atmosfery w Krakowie, *Cykl: Problemy ekologiczne Krakowa*, Nr 16
- Globalne, kontynentalne i lokalne zanieczyszczenia atmosfery. Wydawnictwa AGH, Kraków **(in Polish)**
- Morton-Bermeaa O, Hernandez E, Martinez-Pichardoa E, Soler-Arechaldea AM, Lozano Santa-Cruz R, Gonzalez-Hernandez G, Beramendi-Orosco L, Urrutia-Fucugauchia J (2009) Mexico City topsoils: heavy metals vs. magnetic susceptibility. *Geoderma* 151(3–4):121–125. doi:[10.1016/j.geoderma.2009.03.019](https://doi.org/10.1016/j.geoderma.2009.03.019)
- Pasieczna A (2003) *Atlas of urban soils contamination in Poland*. Polish Geological Institute, Warsaw **(in Polish)**. ISBN 83-7372-636-5
- Polish Standard PN-ISO 10390 (1997) Jakość gleby. Oznaczanie pH **(in Polish)**. <http://sklep.pkn.pl/pn-iso-10390-1997p.html>. Accessed 24 Apr 2017
- Regional Inspectorate for Environmental Protection in Krakow (2013) *Raport o stanie środowiska w województwie małopolskim w 2012 roku*, Cracow, ISBN: 978-83-63638-05-4 **(in Polish)**
- Regulation of the Minister of Environment of 9 September 2012 (2012) w sprawie standardów jakości gleby oraz standardów jakości ziemi. *Journal of Laws (in Polish)*. <http://isap.sejm.gov.pl/DetailsServlet?id=WDU20021651359>. Accessed 24 Apr 2017
- Rosowiecka O, Nawrocki J (2010) Assessment of soils pollution extent in surroundings of ironworks based on magnetic analysis. *Stud Geophys Geod*. 54:185–194. doi:[10.1007/s11200-010-0009-7](https://doi.org/10.1007/s11200-010-0009-7)
- Schibler L, Boyko T, Ferdyn M, Gajda B, Holl S, Jordanova N, Rfslar W, Team MAGPROX (2002) Topsoil magnetic susceptibility mapping: data reproducibility and compatibility, measurement strategy. *Stud Geophys Geod* 46:43–57. doi:[10.1023/A:1019885532390](https://doi.org/10.1023/A:1019885532390)
- Sharma PV (1997) *Environmental and engineering geophysics*. Cambridge University Press, UK. ISBN 9781139171168
- Skiba S, Drewnik M, Szymański W, Żyła M (2013) Chapter. 6. Gleby. In: Degórska B, Baścik M (eds) *Środowisko przyrodnicze Krakowa*, Cracow. ISBN: 978-83-88424-89-2 **(in Polish)**
- Strzyszczyk Z, Magiera T, Rachwał M (2006) Application of Soil magnetometry for identification of technogenic anomalies in trace metal and iron contents: a case study in the Katowice Forest district. *Polish J Environ Stud* 15(2a):176–184. doi:[10.2478/v10239-012-0039-7](https://doi.org/10.2478/v10239-012-0039-7)
- Tomlinson DL, Wilson JG, Harris CR, Jeffrey DW (1980) Problems in the assessment of heavy-metal levels in estuaries and the formation of a pollution index. *Helgolander Meeresunt*. 33(1–4):566–575. doi:[10.1007/BF02414780](https://doi.org/10.1007/BF02414780)
- Wojas A (2009) *Badania podatności magnetycznej gleb miejskich w Krakowie*. Geologia, kwartalnik AGH 35(z. 2/1):489–496 **(in Polish)**
- Wojas A (2012) *Badanie podatności magnetycznej gleb na obszarze Krakowa jako wskaźnika ich zanieczyszczenia*. *Górnictwo i Geologia, kwartalnik Politechniki Śląskiej* 7:287–299. ISSN: 1896-3145 **(in Polish)**

Gravimetric surveys for assessing rock mass condition around a mine shaft

Janusz Madej¹

Received: 19 April 2017 / Accepted: 26 April 2017 / Published online: 18 May 2017
© The Author(s) 2017. This article is an open access publication

Abstract The fundamentals of use of vertical gravimetric surveying method in mine shafts are presented in the paper. The methods of gravimetric measurements and calculation of interval and complex density are discussed in detail. The density calculations are based on an original method accounting for the gravity influence of the mine shaft thus guaranteeing closeness of calculated and real values of density of rocks beyond the shaft lining. The results of many gravimetric surveys performed in shafts are presented and interpreted. As a result, information about the location of heterogeneous zones of work beyond the shaft lining is obtained. In many cases, these zones used to threaten the safe operation of machines and utilities in the shaft.

Keywords Gravity profiling PGr · Mining corrections of gravity · Interval and complex density

Introduction

Vertical gravimetric measurements performed in a borehole require specialist equipment, i.e., a borehole gravimeter. The results obtained with this tool are very useful for the interpretation of geophysical surveys associated with the results of other geophysical methods.

The gravimetric measurements can also be performed in mine shafts. First such works (Fajkiewicz 1956; Fajkiewicz and Zespołem 1984; Fajkiewicz et al. 1986, 1988) were based on a field gravimeter for measuring relative gravity.

Thanks to the use of a special measuring bridge (Fajkiewicz et al. 1988), the gravimetric observations were realized in a mining cage. Thanks to the bridge, the gravimeter could be disposed in a system completely independent of the cage, its vibrations and movements. In such conditions, when the vibrations of the skips and shaft equipment were not transmitted on the bridge, the gravimetric observations could be safely realized. For this reason, the gravimetric surveys in a shaft may play an important role in recognizing geotechnical conditions of the rock mass beyond the shaft lining (Łój 2012).

Basic methods

Gravimetric profilings in a shaft lie in measuring the vertical distribution of gravity. This distribution creates bases for calculating the Bouguer anomaly, i.e., a difference determined with the following formula (Fajkiewicz 1980; Snyder 1976):

$$\Delta g_B = \Delta g'_p - \Delta g_N, \quad (1)$$

where $\Delta g'_p$ measured gravity with corrections and Δg_N average change of gravity with depth.

In a horizontally laminated geological medium, the measured gravity is expressed by the formula (Łukawczenko 1948):

$$\Delta g_p = \frac{\partial g}{\partial z} \sum_{i=0}^n h_i - 4\pi G \sum_{i=0}^n \rho_i h_i + \delta g_i, \quad (2)$$

where $\frac{\partial g}{\partial z} \sum_{i=0}^n h_i$ change of gravity with depth, $4\pi G \sum_{i=0}^n \rho_i h_i$ sum of attraction of layers of density ρ_i and thickness h_i , δg_i component corresponding to gravitational effect of existing heterogeneities beyond the shaft lining of limited horizontal size.

✉ Janusz Madej
madej@geol.agh.edu.pl

¹ AGH University of Science and Technology, Kraków, Poland

Component (3) (Fig. 1) corresponds to a change of gravity in a layer between its roof and the bottom. Graphically, this change (Fig. 1) is represented by inclined sections of (3) distribution. The inclination changes on the boundaries of the layer, which is connected with the density of the layer. Therefore, by measuring the vertical change of gravity between the roof and the bottom of an unlimited horizontal layer, one may determine the density of the layer, provided that suitable corrections accounting for the place of observation are introduced.

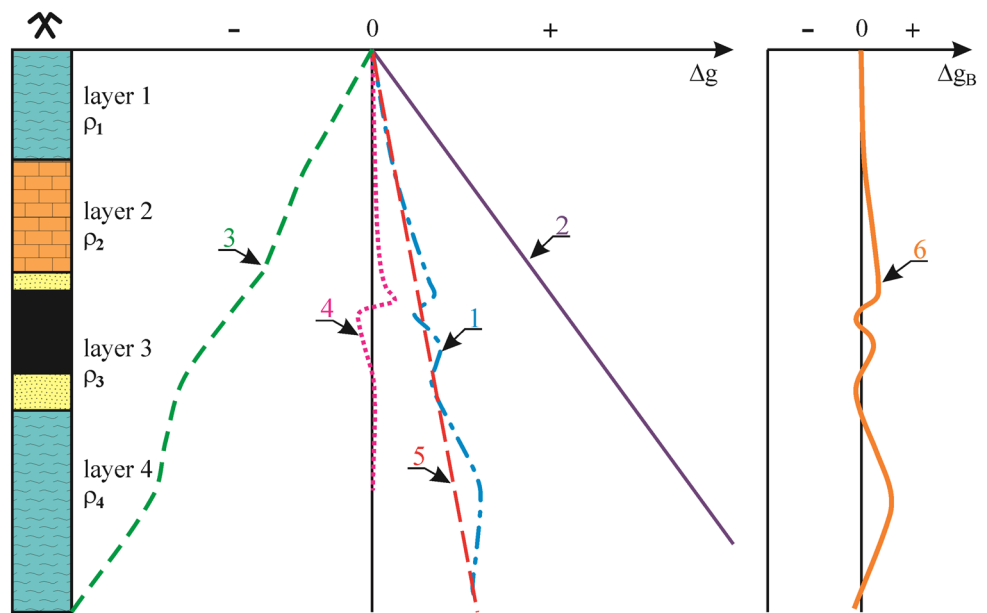
The location of measuring points with respect to the boundaries of the layer is presented in Fig. 2. The calculation of density can be performed between the positions of the successive point. Only in the case of points located in the thickness interval of a layer, the density can be determined correctly, i.e., between points 2 and 3.

The gravimetric survey in a shaft can also be realized in such depth intervals which correspond to the location of the shaft girders. Frequently, the difference of gravity at points corresponding to the boundaries of the layers cannot be established. Therefore, the difference of gravity defined on the basis of gravimetric measurements is called interval density.

It is calculated from the formula:

$$\rho_i = \frac{1}{4\pi G} \left(\frac{\partial g}{\partial h} - \frac{\Delta g_p''}{h_i} \right), \quad (3)$$

Fig. 1 Character of gravity changes with depth



- 1 measured gravity
- 2 vertical change of gravity with depth
- 3 gravitational attraction of plane-parallel surfaces
- 4 gravity distribution vs. heterogeneity of layers
- 5 average change of gravity with depth
- 6 distribution of vertical Bouguer anomaly

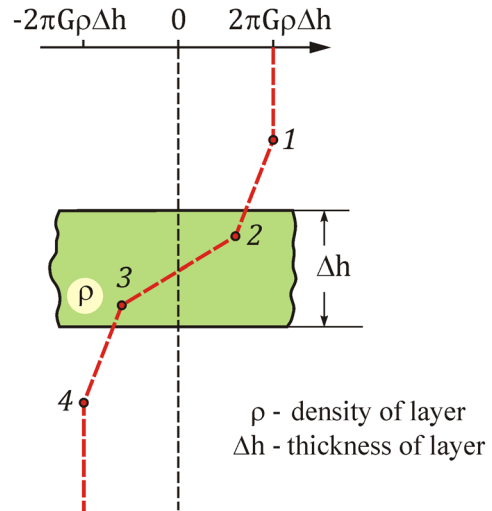


Fig. 2 Unlimited horizontal layer in vertical gravimetric survey

where $\Delta g_p''$ difference of gravity measured in the bottom and in the roof of a layer, taking into account suitable gravity correction (it look “Gravity corrections”). $\frac{\partial g}{\partial h}$ vertical gradient of gravity.

Apart from interval density, also average density can be calculated, on base of formula (3). For doing so, an average change of gravity Δg_N in interval h equal to a vertical distance between two extreme measuring points in the shaft

is introduced to the formula. The average density is then calculated with a very high accuracy $\pm 0.001 \text{ Mg m}^{-3}$. The calculation error for interval density is much higher due to the small distances between measuring points $\Delta h \ll h$.

It can be calculated for the formula:

$$\delta\rho_i = \left| \frac{1}{4\pi G} \frac{\delta(\Delta g)}{\Delta h} \right|, \quad (4)$$

where $\delta(\Delta g)$ is a mean squared error of a single measurement of gravity.

The influence of the measuring error and distances between measuring points on the accuracy of determining the interval density is presented in Fig. 3. If the gravimetric measurements in a shaft were made with an accuracy of, e.g., $\pm 0.02 \text{ mGal}$, the determined interval density of a layer 5 m thick is burdened with an error $\pm 0.05 \text{ Mg m}^{-3}$, which constitutes about 2% of average density of rocks ($2.0\text{--}2.6 \text{ Mg m}^{-3}$).

Gravity corrections

Gravity corrections are made to eliminate the influence of all factors associated with the place of measurement. When the gravimetric surveys are conducted in a mine shaft, the gravity correction is most important. Gravity correction means taking into account the effect of gravity exerted by the shaft lining, its shaft tube and accompanying workings.

The gravity influence of the shaft lining has a significance when the thickness or type of lining material changes. Much bigger influence is exerted by the shaft tube as it affects the shape of the recorded Bouguer anomaly, mainly interval density calculations.

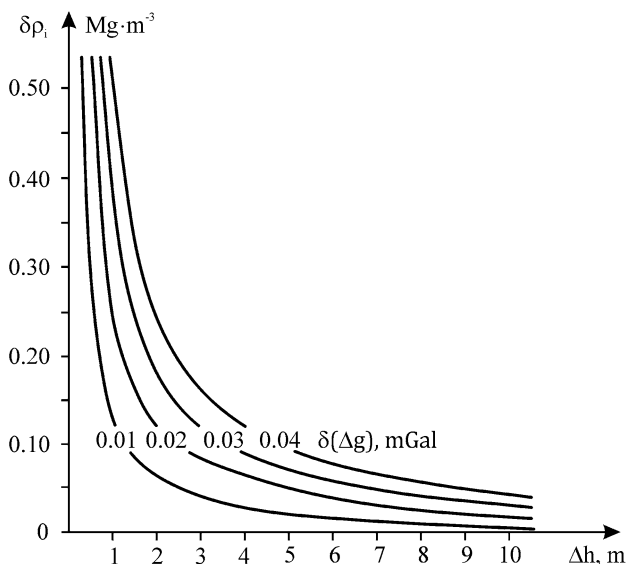


Fig. 3 Relations of error in calculated interval density $\delta\rho_i$ to error of gravimeter measurement $\delta(\Delta g)$ and vertical distance Δh of test stands in the mine shaft

The gravity activity of the shaft with its lining was accounted for by approximating these objects with a material line of constant density. Thus, calculated mining correction for a shaft does not allow for correct determining rock density beyond the shaft lining. This is connected with the varying lithology and so varying density of layers. For average values, we will obtain a shaft filled with rock material having density and location similar to that around the shaft.

To illustrate this, calculations of interval density were performed in one of the shafts in the Upper Silesian Coal Basin (USCB).

This shaft opens up a coal level 510 which is about 6 m thick and its bulk density equals to 1.35 Mg m^{-3} . Two measuring points were located within the level; therefore, the calculated interval density should correspond to the bulk density of hard coal. The results are presented in Fig. 4. The curves Δg^1 , Δg^2 , and Δg^3 are distributions of Bouguer anomalies calculated without and with mining corrections made for the shaft, curves Δg^2 and Δg^3 , respectively. The significant difference in the course of last two distributions results from the way in which the correction for the shaft was calculated. In the first case distribution, Δg^2 includes the correction calculated on the assumption that the shaft was approximated with a material line. The coal level 510 is deposited in the depth interval 262–268 m and the mining correction for this area equals to 0. Calculated densities of distribution Δg^1 and Δg^2 are identical and equal to 1.89 Mg m^{-3} , which does not correspond to the density of hard coal. Therefore, it is purposeful to make a vertical cylindrical model, parts of which would represent the placement of particular layers. In this situation, the Bouguer anomaly distribution starts to resemble the actual picture. After applying the above procedure, the calculated density equaled to 1.36 Mg m^{-3} (densigram ρ_i^3).

The second gravity correction does not necessarily have to be taken into account. It is a topographic correction Δg_t . The way of calculating it for points located under the surface is commonly known from the literature (Hammer 1939; Beyer 1979; Hearst et al. 1980; Fajkiewicz 1980). Exemplary calculations of this correction for selected terrain models are presented in Fig. 5.

The analysis of the distributions Δg_t reveals that for positive height difference in reference to the stroma shaft, the topographic correction is plus, and for negative, height difference is minus.

The shape and range of the topographic correction of gravity show that it influences only the calculated average density value (Madej 2002).

The sign of the change of average density, calculated without topographic correction, compared to the actual value is opposite to the sign of the topographic correction (Madej 1992).

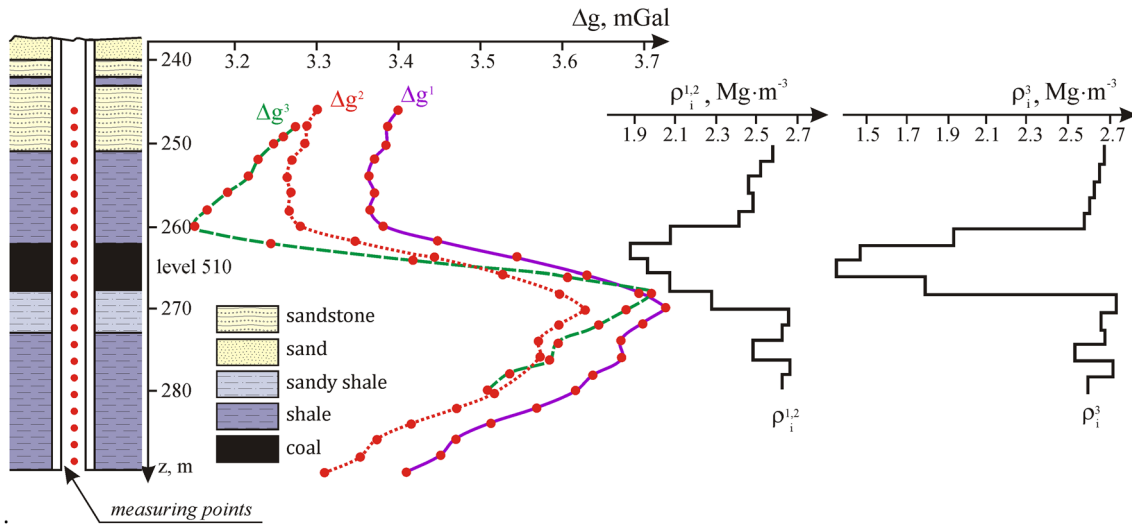
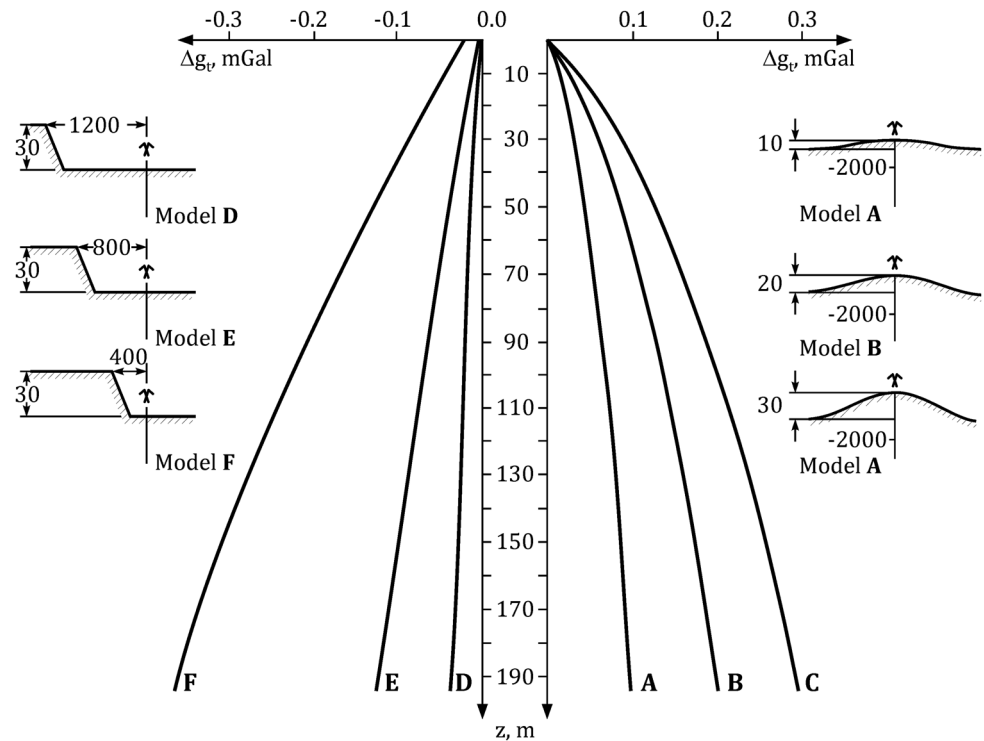


Fig. 4 Example of calculating interval density: Δg^1 , Δg^2 , and Δg^3 distribution of gravitational Bouguer anomaly calculated as follows: without gravity correction, with gravity correction by shaft assuming

its constant density and with variable density; ρ_i^1 , ρ_i^2 , and ρ_i^3 interval densities calculated based on the distributions Δg^1 , Δg^2 , and Δg^3

Fig. 5 Vertical distributions of topographic gravity for a selected terrain



Another correction to be necessarily taken into account in gravity measurements is the correction of gravity of drifts and workings leading to the shaft.

However, their gravity impact is limited to the initial section, as in the dependence shown in Fig. 6.

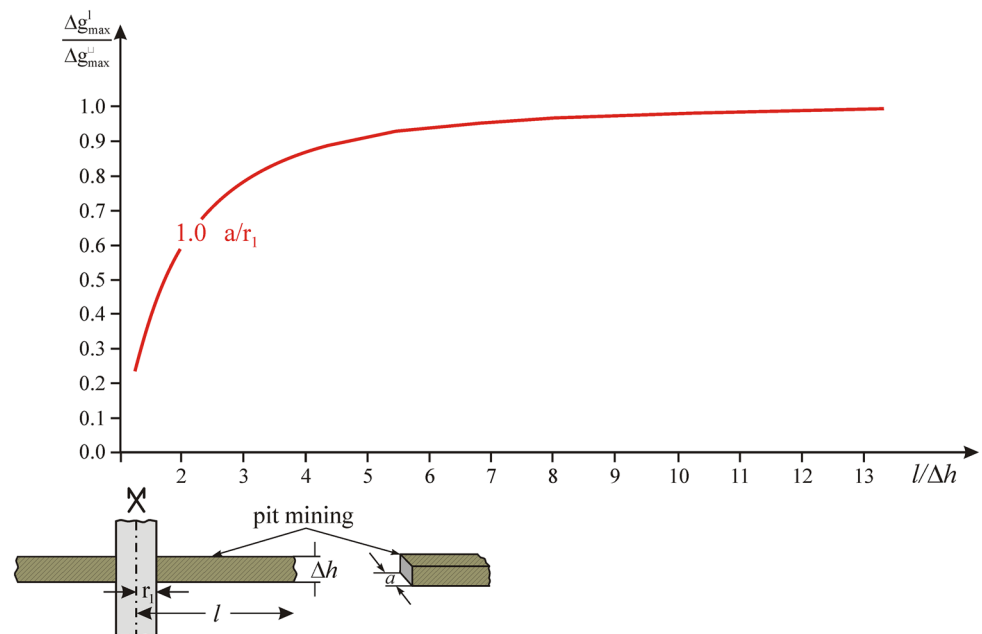
The dependence shows a relative gravity impact in the shaft axis depending on its relative length and related to its horizontal size. The presented plot reveals that the gravity

impact of the working acts on an area covering five times its horizontal size.

Methodics of interval density calculation

The previously discussed method of calculating density of rock layers around the shaft referred to a situation when the course of lithostratigraphic profile in the place where the

Fig. 6 Relative changes of gravity correction caused by sidewall in a function of its relative length and diameter



shaft was drilled is known. This profile could be used for constructing a depth model of rock layers around the shaft. This could guarantee that the calculated interval density values were congruent with the bulk density values. However, in a lack of any information about the lithostratigraphy of layers opened out through the shaft, the density is calculated in quite a different way, by iterations.

The cycle is initiated by calculating average and interval densities without accounting for the correction of shaft gravity. The correction is defined in the next step on the basis of previously calculated average and interval density values. Then, the density is determined for the second time, accounting for the mining correction, for the calculation of which densities established in the previous step were assumed. At the next stage, the calculation process is repeated several times to establish the density of rocks beyond the shaft lining.

The author's experience shows that such a complex calculation process requires 6–7 cycles to bring about density values close to the real ones.

An exemplary calculation cycle on a model of layers is presented in Fig. 7. It was assumed that a horizontal layer of rocks 2.6 Mg m^{-3} of density lies at a depth of 100–124 m. Above and below are layers of density 1.9 and 2.1 Mg m^{-3} , respectively.

The generated gravity measurements in a shaft allowed for determining the Bouguer anomaly Δg_B^l in Fig. 7a and the corresponding distribution of interval density changes ρ_{int}^l in Fig. 7b.

Densities ρ_{int}^l were calculated without mining correction for the shaft. The comparison of changes of density

distribution with the model ones shows that the biggest differences between them were observed at the shaft and sump pit from 0.09 to 0.4 Mg m^{-3} , respectively, and at the borders of the high-density layer from -0.1 to $\pm 0.15 \text{ Mg m}^{-3}$, respectively.

In the next step, the mining gravity correction for the shaft was determined, assuming that its density is constant and equals to the previously defined average value for the whole complex. This caused that only ρ_{int}^u values calculated in the area of the shaft outset and bottom stroma shaft and sump pit were congruent with the real values. At the border of the high-density layer, the distribution of density changes with depth was incorrect. Only the use of the iterative method of calculating influence of the shaft approached the calculated density values to the actual ones (Fig. 7c).

The distributions of mining correction for the shaft are presented in Fig. 7d. It was calculated on the assumption that the density of the shaft tube is constant distribution $\Delta g_g^{sz}(\bar{\rho}_1)$. The value of the correction increased in the area of stroma shaft and sump pit. Assuming the density of shaft sections in line with values calculated after ten iteration steps, the distribution of mining correction for the shaft took the form of a curve $\Delta g_g^{sz}(\rho_{\text{int}}^{10})$.

By assuming end values of the correction, we can certainly obtain correct density values of the layers.

The results of calculation of interval density for these layers are presented in Fig. 8. The density could be determined after only seven calculation cycles to obtain results congruent with the real values. Most importantly, this method does not require knowledge about the rocks which surround the shaft.

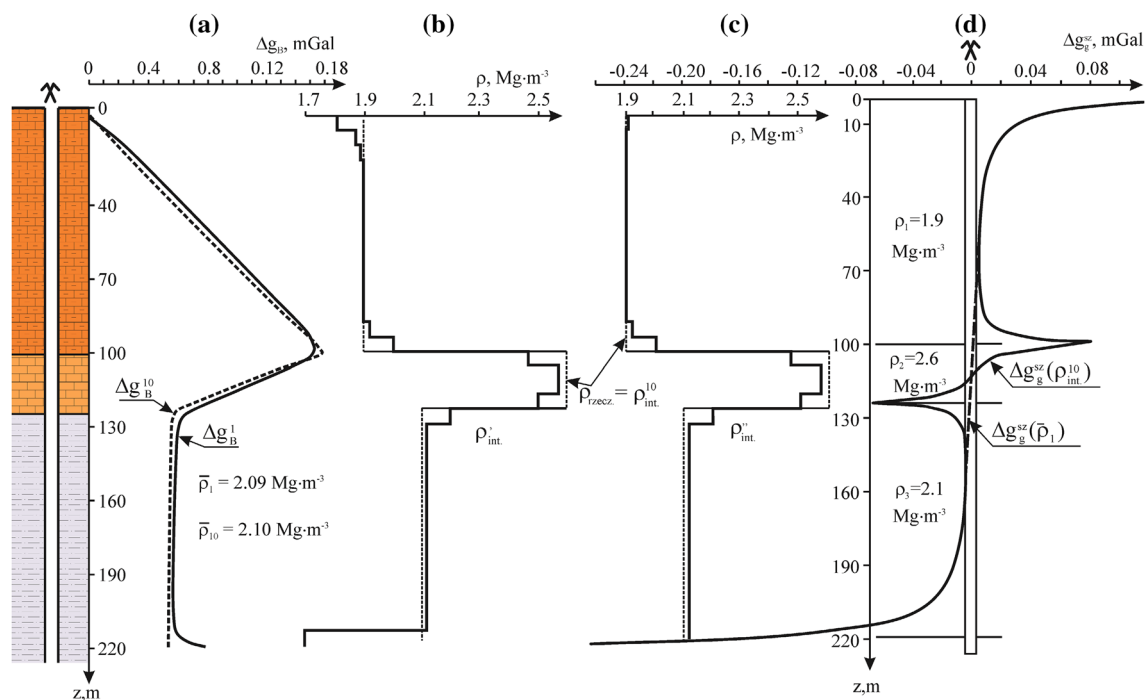


Fig. 7 Results of rock density calculations—different ways of accounting for mine shaft corrections (explain of symbols in text)

Distributions of Bouguer anomalies from simple structural forms

In gravimetric measurements performed in a shaft, it is most important to evaluate density changes in the immediate neighborhood of the shaft, right beyond its lining. Such assessment can significantly help determine conditions of safe operation of equipment and shaft utilities.

Having assumed the simplest rock mass model, when the layer is localized horizontally at a certain depth, the vertical distribution of Bouguer anomaly represents the gravity of the layer. This distribution is presented in Fig. 9. Its analysis reveals that the anomaly distributions were drawn from an unlimited plane-parallel layer and from the limited horizontal one. Accordingly, the shape of the Bouguer anomaly can be used for differentiating between unlimited layers and limited horizontally. A qualitative relation can be observed between the results of measurements and the geological build of the rock mass.

The gravimetric method used for vertical profiling is based on a regularity discovered by McCulloh (1965; Fig. 10).

This regularity indicates that about 95% of gravity effect from a horizontal, unlimited rock layer limited by measuring points from the top and from the bottom are generated by this part of the layer which adheres the borehole (or shaft lining) in an area five times as big as the thickness of the layer.

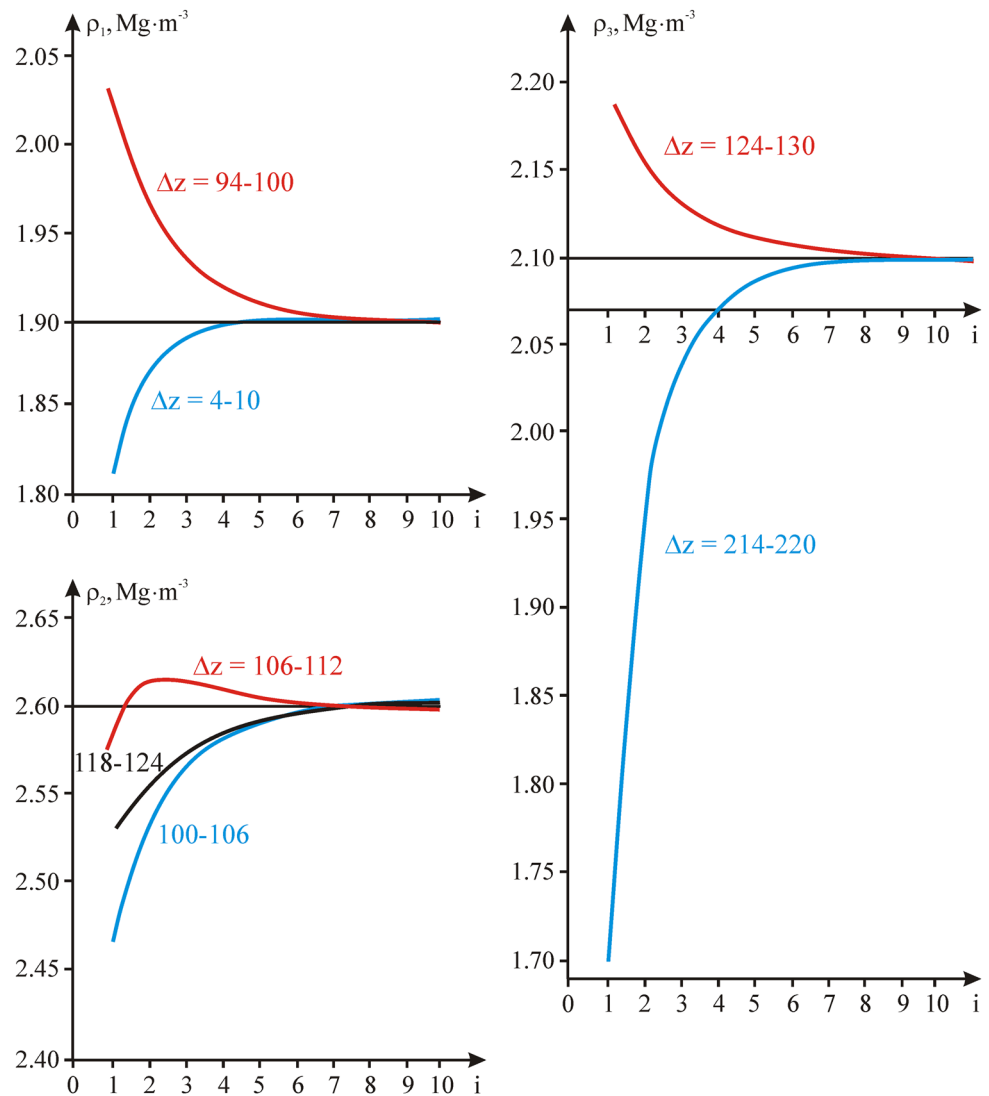
This dependence is illustrated by curve 8 in Fig. 10 (EDCON 1977). When the measurements are made in a mine shaft, this relation takes the form of a function of shaft radius and its proportion to the thickness of the analyzed layer (Madej 1988).

This dependence refers only to a situation when we analyze the distribution of measured gravity changes in a shaft without accounting for the mining gravity correction.

In this case, the vertical distribution of gravity for layers of limited horizontal range is presented in a plot in Fig. 11. This distribution reaches extreme values at points localized above and under the layer boundary by dz value. In vertical gravimetric measurements, the sign of vertical gravity changes at the interface of layers differing in bulk density. In other words, the location of point in which the anomalies distribution reaches extreme values is determined by the boundaries of layers. Therefore, to determine these boundaries, a suitable gravity correction for the presence of shaft barrel should be introduced to the measurement results. After doing so, the plot illustrating gravity changes takes the form, as shown in Fig. 11. The extreme values on anomaly curve determine boundaries of a layer which has different densities from the environment.

The vertical distribution of gravity, denoted as Δg_p in Fig. 12a, is the basic value and a source of information about the structure of the rock mass opened by the mine shaft. On this basis, the Bouguer anomaly can be calculated. For this purpose, the average change of gravity with

Fig. 8 Interval densities determined in successive calculation cycles for selected depth intervals



depth Δg_N is determined. This is a hypothetical change of gravity in a situation when the rock medium has a constant density. The Bouguer anomaly, i.e., $\Delta g_P - \Delta g_N$, constitutes a superposition of gravity impact of layers differing in density and heterogeneities in them, as presented in Fig. 12b. The distribution of this anomaly is a basic source material on the basis of which one may infer as to the geological build of the rock medium. This process is based on the documented relations of measured distribution with physical parameters of the analyzed structures and geological forms.

One of the characteristic vertical distributions of Bouguer anomaly is the contact of two layers of different bulk densities. Two variants of such an interface are shown in Fig. 13. Extreme value of distribution is well visible at the layers' boundary. The sign of the observed gravity anomaly is congruent with the sign of density contrast of the lower layer as referred to the environment.

The physical parameters of heterogeneous zones beyond the shaft lining can be assessed through gravimetric measurements performed in a shaft. The dependence between the amplitude of anomaly generated by the heterogeneous zone and its parameters in a function of the mean squared error of gravity is presented in Fig. 14.

Curves 1–5 represent relative density of heterogeneous zone drawn every 0.5 Mg m^{-3} within the range from -0.5 to -2.5 Mg m^{-3} .

And so, e.g., a rock void of density -2.5 Mg m^{-3} extending to a 1 m distance from the shaft lining (2 m radius) in a layer 1.3 m thick generates a gravity change equal to 0.04 mGal. In a shaft of a 3 m radius, the same amplitude corresponds to a larger void: 1.4 m horizontal range of and 1.75 m thick.

Vertical gravimetric surveys could be performed as time changes of gravity anomalies. They are applied in both boreholes and mine shafts (Fajkiewicz et al. 1986, 1988). The changing values of anomalies are caused by changes of

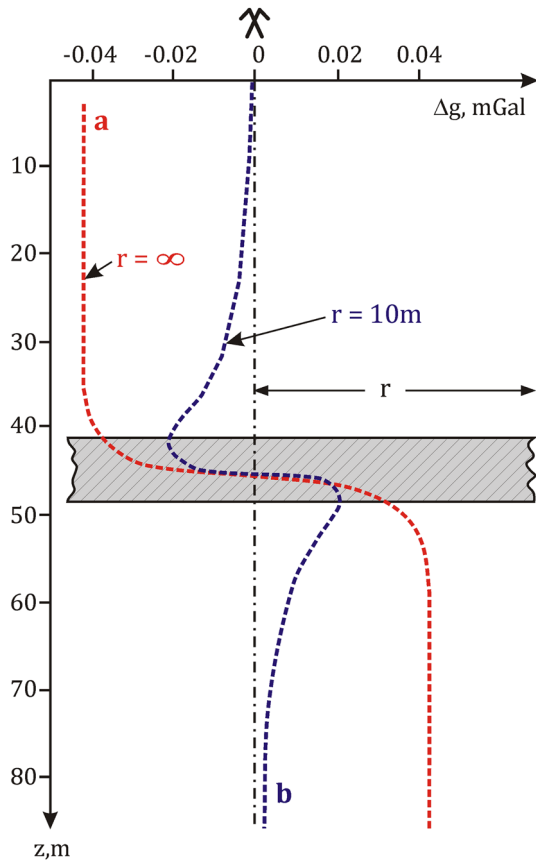


Fig. 9 Distributions of Bouguer anomaly in a shaft caused by a horizontal layer: **a** unlimited, **b** horizontally

physical parameters of the medium around the shaft, mainly density.

Time distributions of vertical gravity changes with the changing density in a plane-parallel layer are presented in Fig. 15.

Fig. 10 Relative vertical change of gravity caused by a heterogeneous zone outside of the shaft lining (Fajklewicz et al. 1986)

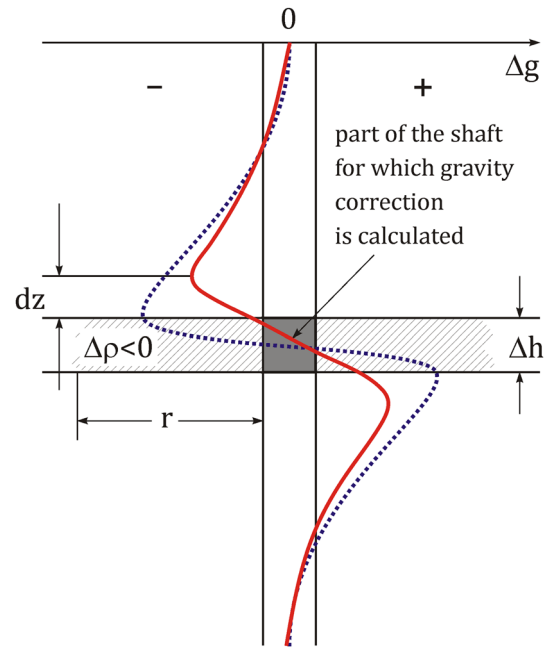
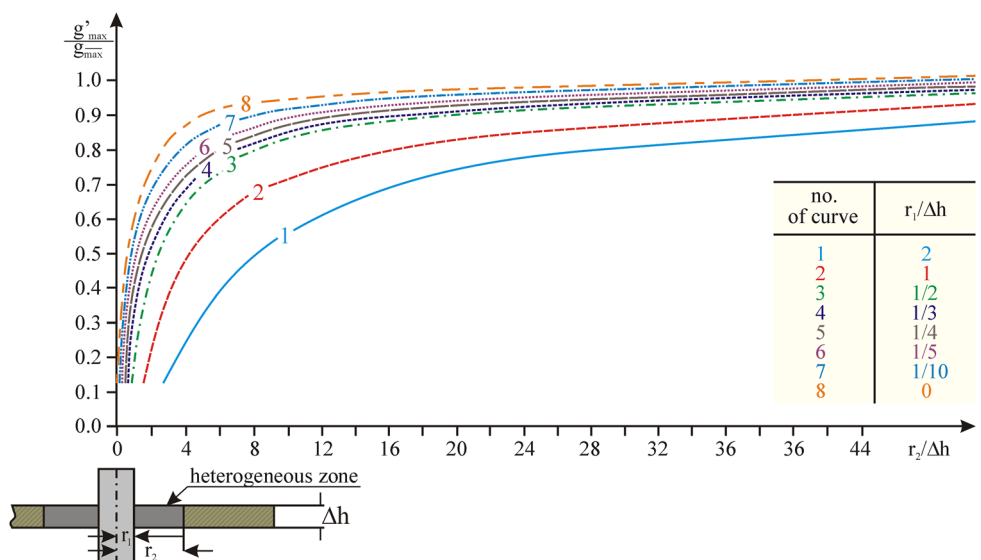


Fig. 11 Vertical distribution of gravity for a horizontal layer of limited size

The analysis of these distributions reveals that regardless the original contrast of layer's density in relation to its surrounding, the vertical gradient of gravity in the layer has the opposite sign to the sign of corresponding density changes. An analogous situation can be observed, while tracing density changes in a horizontally limited layer. The results are presented in Fig. 16, where a characteristic shape of distributions of gravity anomaly and its changes caused by the geometry of the horizontally limited layer is well visible, it look Fig. 9.

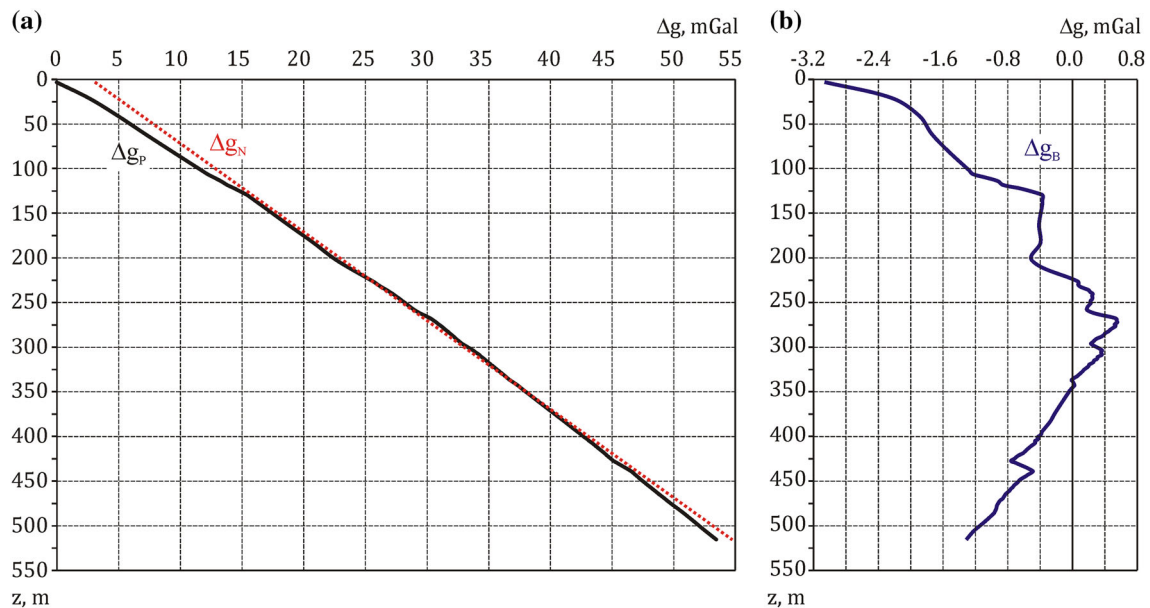


Fig. 12 Vertical distribution of gravity **a** and its Bouguer anomaly **b**, Δg_P measured value of gravity Δg , Δg_N average value of Δg , and Δg_B value of Bouguer anomaly

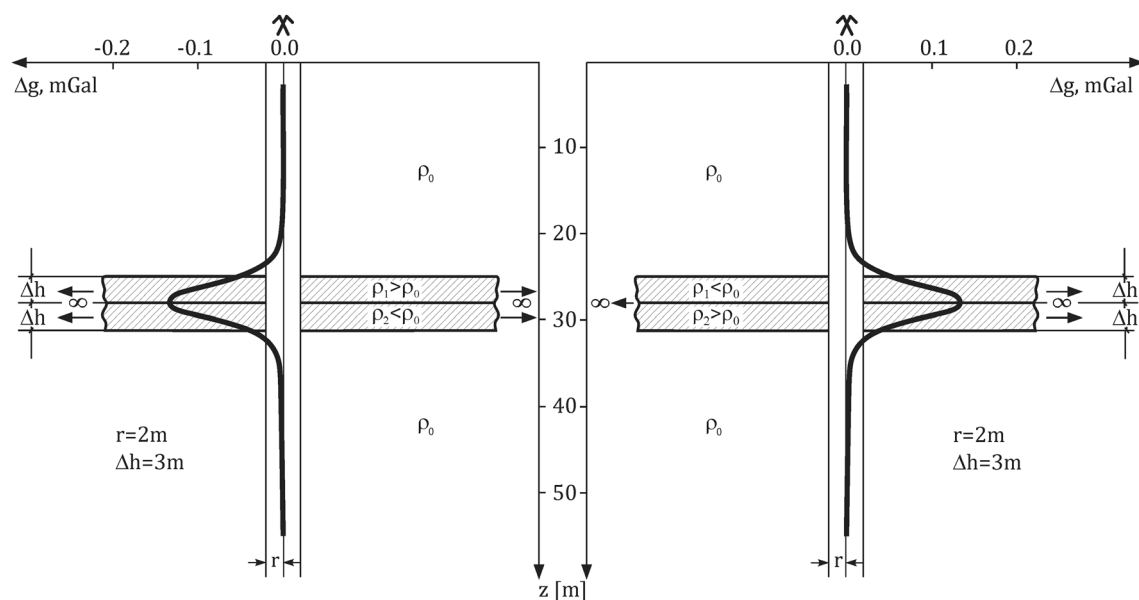


Fig. 13 Vertical distributions of gravity for a system of two plane-parallel layers

Selected practical examples

Authors presented results of nine (out of ten or so) gravity analyses of shafts. They are presented in Figs. 17, 18, and 19. There are distributions of Bouguer anomaly and the respective densigrams: average density $\bar{\rho}$ and interval density ρ_i . Bearing in mind the way in which the latter was calculated, it would be more appropriate to call it complex density. Here, the shape of distribution of the registered Bouguer anomaly can be divided into sections

differing in vertical gradient of gravity. The previous analyses reveal that each change of the gradient causes a change of density. As it can be seen on the figures, the anomaly distribution was approximated with straight lines. Each change of direction corresponds to a boundary of the complexes.

The results of analyses of three shafts with a similar geological structure are presented in Fig. 17. Carboniferous rocks are deposited under a small Quaternary overburden. The distributions of Bouguer anomaly and the

Fig. 14 Distribution of boundary amplitudes of gravity anomalies real to measurement error in a function of parameters of heterogeneous zone around the shaft of radius 2 m (Fajkiewicz et al. 1986)

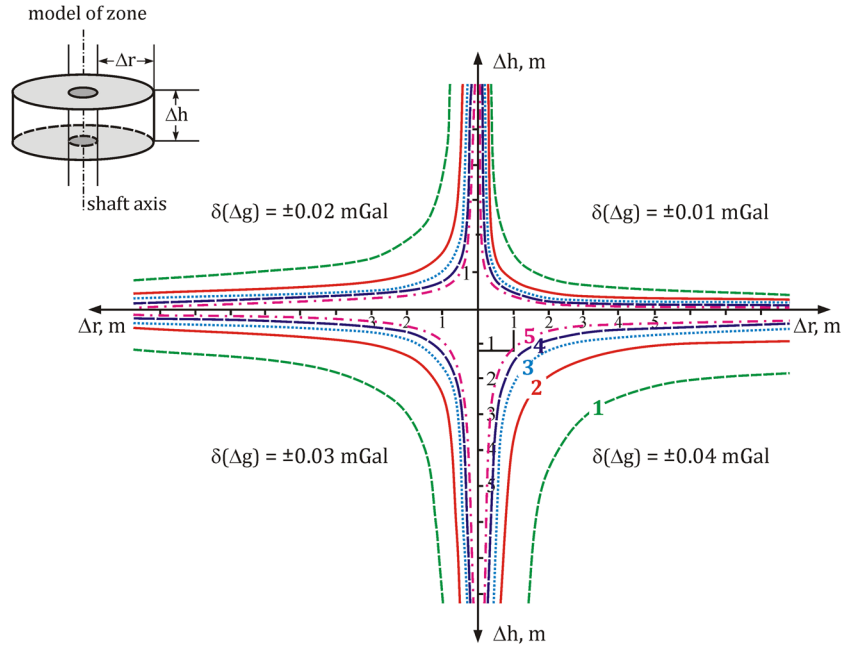


Fig. 15 Relation of gravity changes with density changes in a plane-parallel layer

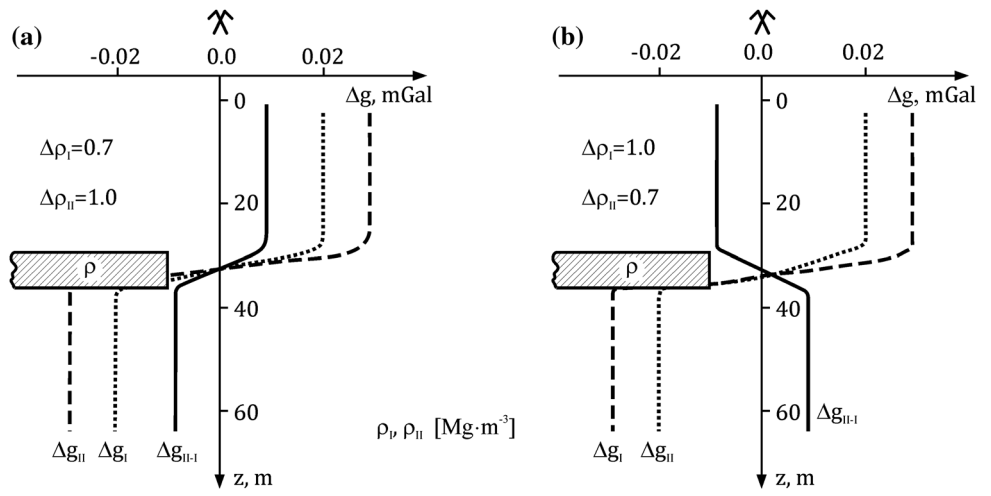
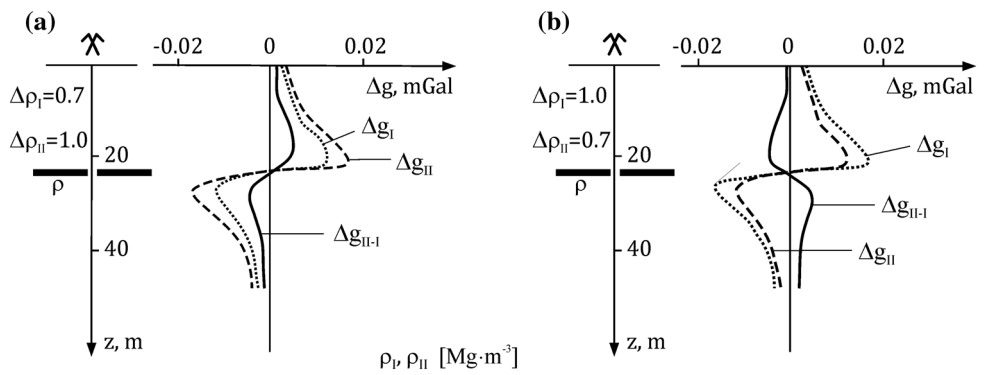


Fig. 16 Dependence of gravity changes and density changes in a horizontally limited layer



corresponding densigrams in neighboring Wirek and Nowy Wirek shafts differ very little. A distinct density boundary can be observed between the Quaternary and Carboniferous

strata. The successive density boundaries between rock complexes are also encountered in the Carboniferous at a depth of 200 and 530 m.

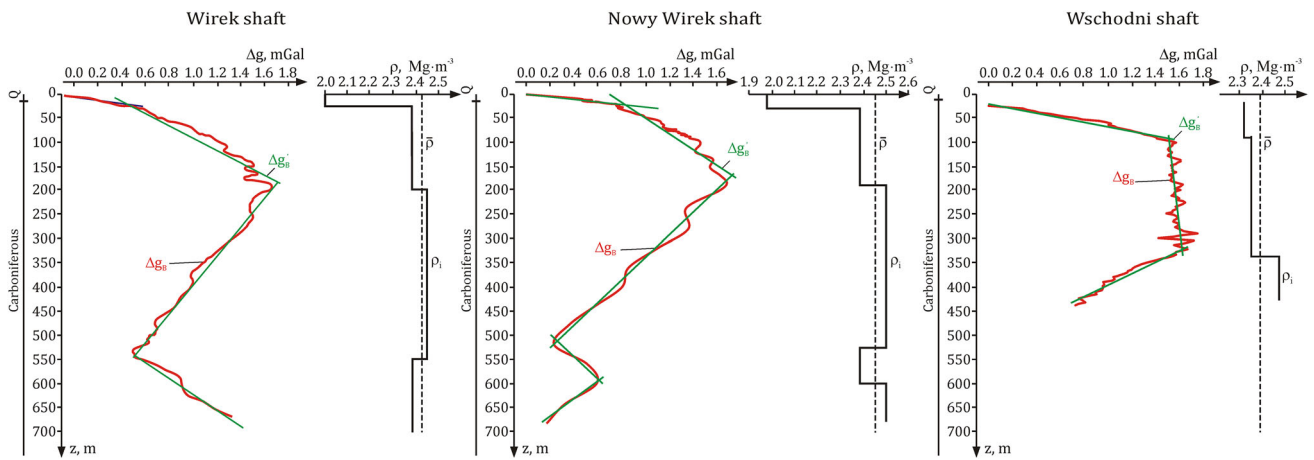


Fig. 17 Vertical distributions of Bouguer gravity anomaly Δg_B , their generalized courses $\Delta g'_B$, and the corresponding densigrams of complex density ρ_i in selected shafts

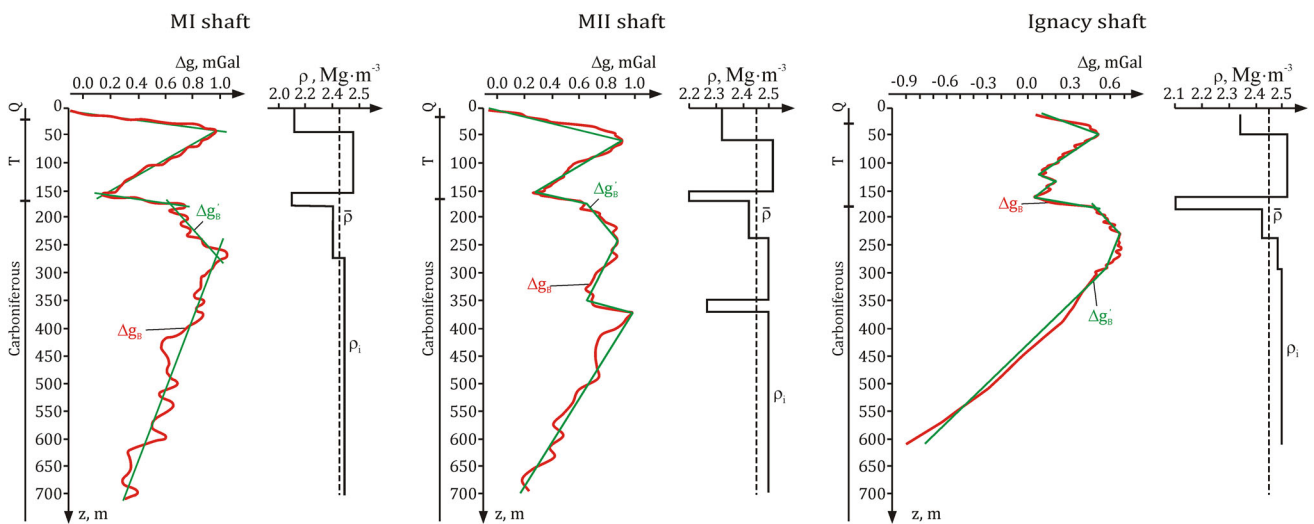


Fig. 18 Vertical distributions of Bouguer gravity anomaly Δg_B , their generalized courses $\Delta g'_B$, and the corresponding densigrams of complex density ρ_i in selected shafts

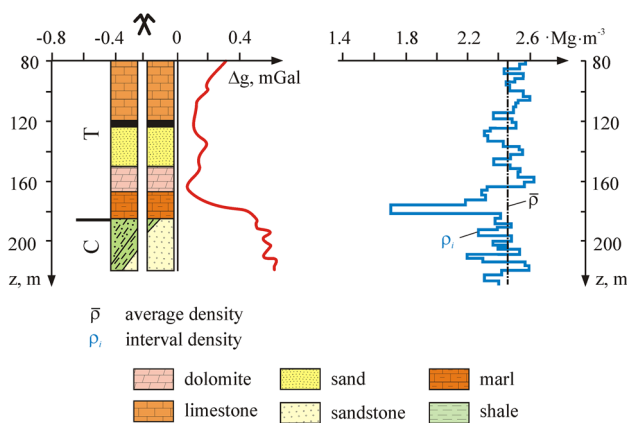


Fig. 19 Ignacy shaft. Vertical distribution of Bouguer gravity anomaly Δg and the corresponding densigram of interval density ρ_i

In Wschodni shaft, also in the Carboniferous complex, two density boundaries were found at 100 and 330 m of depth. Numerous coal seams are present between them hence the diversified picture of gravity changes in this interval. Attention should be paid to a zone between 300 and 305 m, where the vertical gravity was anomalous. It corresponds to a coal bed of much lower density than the rocks in the roof and the bottom.

Much bigger lithostratigraphic and density diversification can be observed in the successive examples, as presented in Fig. 18. They represent distributions of Bouguer anomaly and densigrams corresponding to the geological build, i.e., Quaternary sediments, Triassic, and Carboniferous rocks. In the first two closely neighboring shafts (MI and MII), the first density boundary from the outset was observed in the Triassic at a depth of about 50 m.

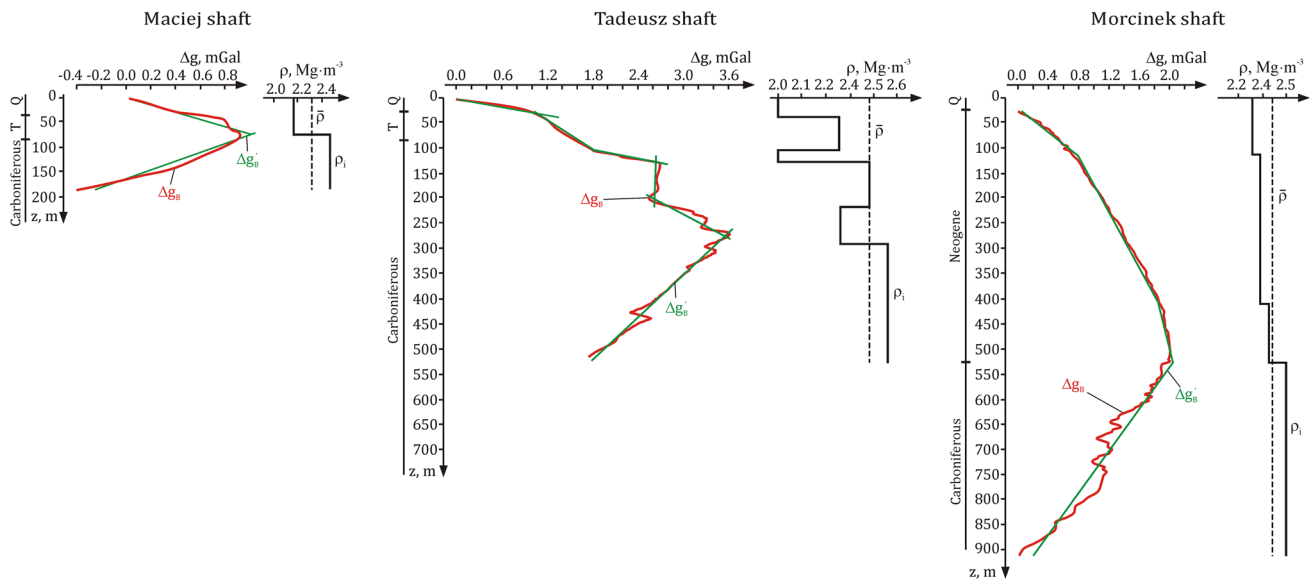


Fig. 20 Vertical distributions of Bouguer gravity anomaly Δg_B , their generalized courses $\Delta g'_B$, and the corresponding densigrams of complex density ρ_i in selected shafts

Above are rocks of density ranging from 0.2 to 0.4 Mg m^{-3} ; these were smaller values than the underlying Triassic rocks. This loosening of the Triassic strata has an effect on the direction of geotechnical conditions at this depth, which may have significance for the safe extraction of these shafts.

It seems that equally important is the density boundary between Triassic and Carboniferous (both shafts at about 150 m of depth). Below, there is a layer of too low density ca. 0.5 Mg m^{-3} as compared to the density of rocks lying under and above this layer. The loosening was observed in the Carboniferous, and the loose material was probably strongly soaked with water.

Another low-density layer was also discovered in a Carboniferous interval in MII shaft at 350–375 m.

The distribution of Bouguer anomaly in Ignacy shaft (Fig. 18) provides many interesting pieces of information, e.g., that the low-density rock boundary reaches to a depth of 50 m, i.e., deeper than the boundary between Quaternary and Triassic marls. Hence, the conclusion that the density of the latter layer is lower than values given in the table. However, the most important result of analyses refers to the depth interval 80–200 m. This fragment of anomaly distribution is presented in Fig. 19. In this interval, the most important part of analysis of gravity changes is conducted for 160 and 180 m of vertical profile. The thickness of this zone has low complex density equal to 1.7 Mg m^{-3} . Originally, in view of measurements conducted prior to sinking the shaft, the lower density zone was deposited in an interval 175–180 m; this was quicksand. The gravimetric surveys revealed that the quicksand zone increased by 15 m upward.

All of the examples presented in Fig. 20 deserve equal attention. And so, in Maciej shaft, the low-density rocks of the Carboniferous overburden are not only of Quaternary but also of Triassic origin. This generates considerable hazard for the stability of the shaft, especially that an intensified water flow was observed at the shaft lining (Fajkiewicz et al. 1986) resulting in the washing out of rock material.

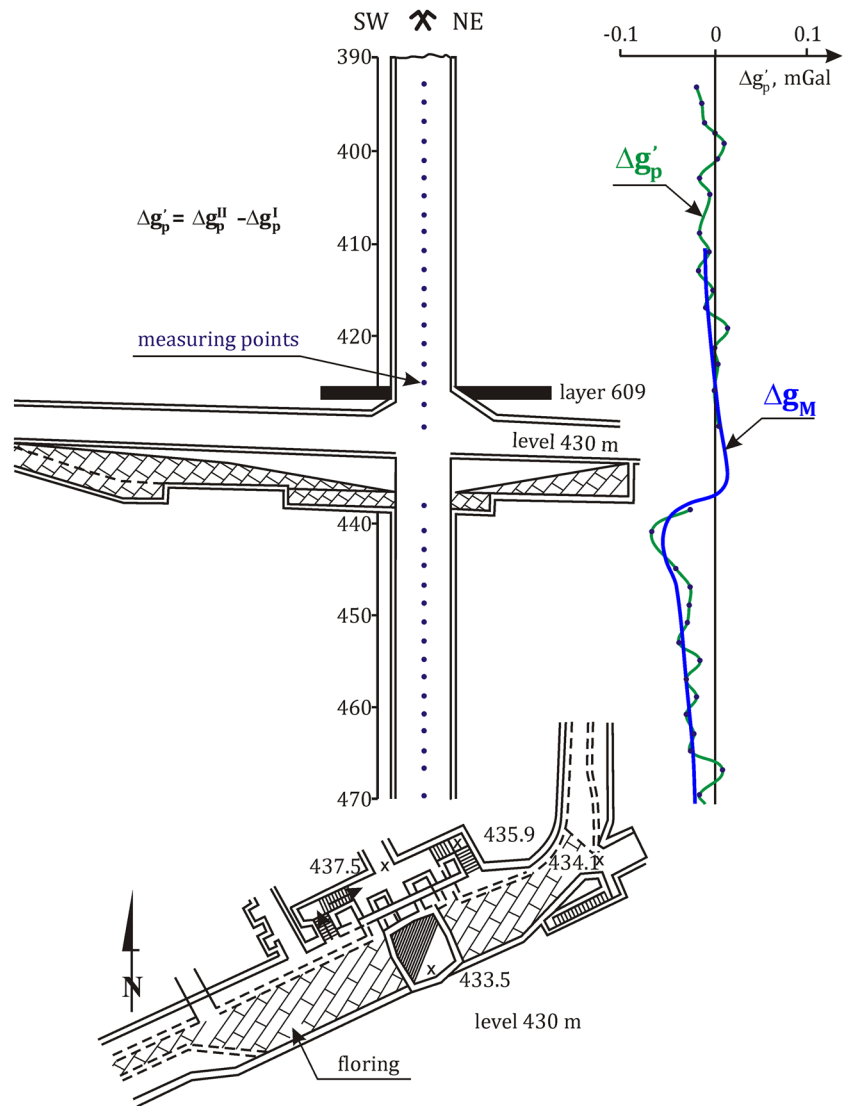
In the roof part of Tadeusz shaft, there was observed a layer of considerably lower density (by ca. 0.5 Mg m^{-3}) as compared to the Triassic rocks above it and the Carboniferous bed. This shaft was commissioned and the gravimetric surveys performed during the closing operations turned out to be useful.

The liquidation of a shaft starts with backfilling of workings in the immediate neighborhood of the shaft. The quality of the backfilling was analyzed with the use of gravimetric methods employing measurement of the vertical gravity before and after backfilling.

The results are presented in Fig. 21. The observed time difference of gravity $\Delta g'_p$ corresponds to distribution Δg_M . It is equal to the gravitational impact of mass, the geometry of which is shown in the model of filling. The liquidation of the pit has not been obviously done well.

The last presented object is Morcinek shaft. The results of gravimetric measurements performed to a depth of over 900 m reveal a slightly varied shape of distribution of Bouguer anomaly (Fig. 20). The extreme of the distribution defines the Neogene/Carboniferous boundaries. The plot and the densigram show that the density of rocks systematically increased to this boundary $2.3\text{--}2.5 \text{ Mg m}^{-3}$. Anomalies related to the presence of many coal seams

Fig. 21 Results of gravimetric modeling in the area of level 430 in Tadeusz shaft, Δg_p^I , Δg_p^{II} measuring series, Δg_M model schedule of gravity



strongly manifest themselves in the Carboniferous complex. This can be observed in the depth interval 660–750 m deep.

Special attention should be paid to the analysis of distribution of gravity in depth interval 210–310 m. This distribution is presented in Fig. 22 as a residual anomaly.

During complex density calculations (curve 2 in Fig. 22), a density difference of 0.04 Mg m^{-3} was found on the interface of layers at the depth of the girders, i.e., ca. 260 m. Extreme values of interval density determined for the successive measuring points (curve 1 in Fig. 22) are 2.35 Mg m^{-3} in the layer limited by girders 55 and 57 and 2.44 Mg m^{-3} in a layer between girders 61 and 63. Attention should be paid to the fact that the average density of the complex within which these two layers occur equals to 2.40 Mg m^{-3} .

To solve the problem, a high weight was attributed to determining complex densities as being much more accurate than the interval density. Complex densities were

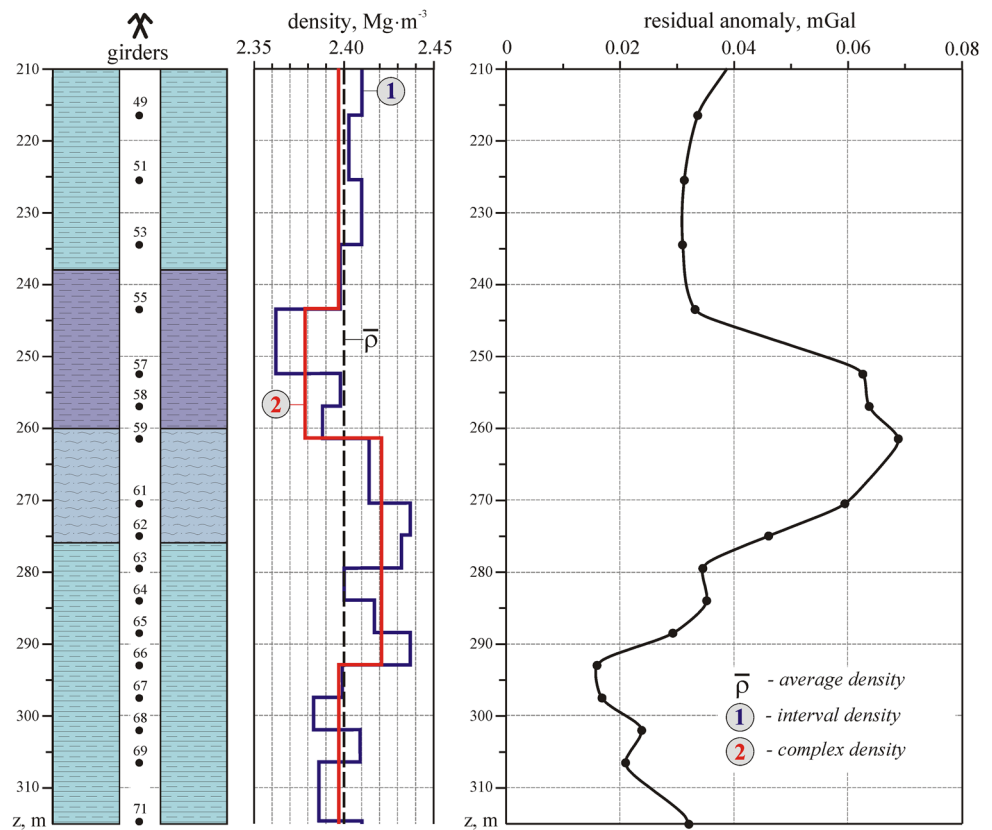
determined with accuracy to $\pm 0.007 \text{ Mg m}^{-3}$, whereas interval densities were burdened with an error of $\pm 0.013 \text{ Mg m}^{-3}$, i.e., twice as high.

The two layers contacted at a depth at which a damage in the shaft lining was observed. The increase of density in the entire range between girders 59–66 over the lithological boundary between the on lying silts and the underlying siltstones could be explained by higher side pressure of the complex. This also explains the small vertical deformation in this depth interval, discussed by Podgórski et al. (1993).

Concluding remarks

The presented rudiments of use of the vertical profiling method in mine shafts guarantee results, on the basis of which geotechnical conditions around the shaft can be assessed.

Fig. 22 Results of gravimetric measurement in Morcinek shaft



The method for calculating interval and complex densities is considered to be particularly useful. In this method, it is the mining correction for the shaft barrel which decides about the correct determining of density of rocks beyond the shaft lining. When the lithostratigraphic profile is known, the shaft barrel is built of parts which correspond to the location of layers, for which the mining correction has been calculated. Otherwise, the iteration method has to be involved for calculating density values.

The vertical distributions of Bouguer anomalies for simple structural forms are indicative of a relation between these distributions and the geological build.

The time analyses of vertical gravity changes provide significant pieces of information about the dynamics of effects taking place beyond the shaft lining.

The presented examples of use of the vertical gravimetric method confirm its high efficiency for evaluating the state of rock mass beyond the shaft lining.

Open Access This article is distributed under the terms of the Creative Commons Attribution 4.0 International License (<http://creativecommons.org/licenses/by/4.0/>), which permits unrestricted use, distribution, and reproduction in any medium, provided you give appropriate credit to the original author(s) and the source, provide a link to the Creative Commons license, and indicate if changes were made.

References

- Beyer LA (1979) Terrain corrections for borehole and gravity measurements. *Geophysics* 44:1584–1587
- EDCON (1977) Borehole gravity density logging. EDCON, Denver
- Fajkiewicz Z (1956), O podziemnych pomiarach grawimetrycznych w zastosowaniu do górnictwa węglowego. Wyniki prac na kopalni Miechowice. *Archiwum Górnicztwa*, t.1, z.4, 324–355
- Fajkiewicz Z (1980) Mikrograwimetria górnicza. Wyd Śląsk Katowice 264
- Fajkiewicz Z, Jakiel K, Madej J (1986) Wykrywanie metodą grawimetryczną pustek powstających za obudową szybu i zagrożeń z nimi związanych, *Zeszyty Naukowe Politechniki Śląskiej*, z. 149:221–231
- Fajkiewicz Z, Zespołem Z (1984) Profilowanie grawimetryczne w szybie “Maciej” w KWK “W. Pstrowski”, *Archiwum KWK “W. Pstrowski”*, Zabrze
- Fajkiewicz Z, Jakiel K, Madej J, Radomiński J (1988) Wyniki pionowego profilowania grawimetrycznego wykonanego w szybach Górnośląskich Kopalń Węgla Kamiennego “W. Pstrowski” i “Miechowice”, *Publications of the Institute of Geophysics Polish Academy of Science M-10* (213), pp 17–33
- Hammer S (1939) Terrain corrections for gravimeter stations. *Geophysics* 4:184–194
- Hearst JR, Schmoker JW, Carlson RC (1980) Effects of terrain on borehole gravity data, 1980. *Geophysics* 45:234–243
- Łój M (2012) Gravity vertical profiling in the shaft mining “Sośnica-Makoszowy”, surface Geoscience 2012 European meeting of environmental and engineering geophysics: remote sensing workshop: 3–5 September 2012, Paris, France, European Association of Geoscientists and Engineers, e-ISBN: 978-90-73834-34-7

- Łukawczenko PJ (1948) K woprosu ob izmierenijach siły tiazesti w burowych skważinach, Prikladnaja geofizyka, 4
- Madej J (1988) Wybrane problemy metodyki pomiarów grawimetrycznych w szybach górniczych. Zeszyty Naukowe AGH, nr 1218. Geofizyka Stosowana z 1:269–278
- Madej J (1992) Pionowe profilowanie grawimetryczne w badaniach strukturalnych górotworu. Zeszyty Naukowe AGH nr 1480, Geofizyka Stosowana, z. 11, Kraków 1992, 114s
- Madej J (2002) Pionowe profilowanie grawimetryczne w szybach górniczych, Mat. Konf.: XXV ZSMG pt: Geotechnika i budownictwo specjalne, Zakopane 18-22.03.2002, KGBiG AGH, 411–425
- McCulloch H (1965) A confirmation by gravity measurements of an underground density profile on core densities. Geophysics 30:1108–1132
- Podgórski K (1993) Analiza zachowania się szybów głównych KWK Morcinek na tle zjawisk zachodzących w dużych obszarach górotworu o nierównomiernym stopniu naruszenia eksploatacją górniczą. ŚliTG Zesp. Rzeczoznawców, Katowice
- Snyder DD (1976) The Bouguer gravity anomaly—application to interpreting borehole gravity surveys, transactions: paper AA1-AA20, 17th Annual Logging Symposium. SPWLA

Subdiffusion of volcanic earthquakes

Sumiyoshi Abe^{1,2,3} · Norikazu Suzuki⁴

Received: 2 March 2017 / Accepted: 13 March 2017 / Published online: 28 March 2017
© Institute of Geophysics, Polish Academy of Sciences & Polish Academy of Sciences 2017

Abstract A comparative study is performed on volcanic seismicities at Icelandic volcano, Eyjafjallajökull, and Mt. Etna in Sicily from the viewpoint of complex systems science, and the discovery of remarkable similarities between them is reported. In these seismicities as point processes, the jump probability distributions of earthquakes (i.e., distributions of the distance between the hypocenters of two successive events) are found to obey the exponential law, whereas the waiting-time distributions (i.e., distributions of inter-occurrence time of two successive events) follow the power law. A careful analysis is made about the finite size effects on the waiting-time distributions, and the previously reported results for Mt. Etna (Abe and Suzuki 2015) are reinterpreted accordingly. It is shown that the growth of the seismic region in time is subdiffusive at both volcanoes. The aging phenomenon is commonly observed in the “event-time-averaged” mean-squared displacements of the hypocenters. A comment is also made on (non-)Markovianity of the processes.

Keywords Subdiffusion · Volcanic seismicity · Finite-size effects · Power-law waiting-time distributions · Exponential jump probability distributions · (Non-)Markovianity

Introduction

Deeper understanding of volcanic seismicity is not only of academic interest but also of obvious importance for mitigation of disaster by eruption, since volcanic earthquakes always occur prior to eruption, although eruption does not necessarily take place after their occurrence.

Traditional geophysical approaches suggest that actually this phenomenon is challenging also for science of complex systems. They involve complexity of the high-level regarding accumulation of stress at faults inside a volcano due to quite a few factors including propagating/inflating/magma-filled dikes, groundwater transport through porous media and nontrivial geometry of the shape of magma migration (Roman and Cashman 2006; Turcotte 1997; Zobin 2012). Thus, volcanic seismicity results from interplay of diverse complex dynamics on complex architecture at various scales.

It should also be noted that the problem of earthquake-volcano coupling is equally challenging even for non-volcanic earthquakes (Hill et al. 2002).

In a situation where fundamental dynamics governing a system under consideration is largely unknown, the first step toward extracting information about it is to phenomenologically characterize the properties of correlation contained. For this purpose, we have recently studied the feature of diffusion of volcanic earthquakes at Mt. Etna (Abe and Suzuki 2015). There, we have discovered that the volcanic seismicity as a point process exhibits

The original version of this article was revised: modifications have been made to the Figure 1. Full information regarding corrections made can be found in the erratum for this article.

✉ Sumiyoshi Abe
suabe@sf6.so-net.ne.jp

- ¹ Physics Division, Faculty of Information Science and Engineering, Huaqiao University, Xiamen, China
- ² Department of Physical Engineering, Mie University, Mie, Japan
- ³ Institute of Physics, Kazan Federal University, Kazan, Russia
- ⁴ College of Science and Technology, Nihon University, Funabashi, Chiba, Japan

subdiffusion. To understand this behavior, we have analyzed the spatio-temporal properties of the process and have found that the jump probability distribution (i.e., distribution of the distance between the hypocenters of two successive events) obeys the exponential law, whereas the waiting-time distribution (i.e., distribution of inter-occurrence time, or calm time, of two successive events) follows the power law. These results suggest that the spatial aspect of the process is normal in spite of the presence of the complex architecture, and the anomaly originates from the nontrivial nature of the temporal aspect, although there are no physical reasons for separability of these two, in general.

Now, after the work Abe and Suzuki (2015), we have noticed that the finite size effects may play a significant role in the discussion about diffusion of volcanic earthquakes and, in particular, the value of the exponent in the power-law waiting-time distribution can be sensitive to the effects. To clarify this point, it is desirable to develop a comparative study of seismicities at Mt. Etna and other volcanoes.

The purpose of the present work was to execute such a comparative study on the volcanic seismicities at the volcano, Eyjafjallajökull, in Iceland and Mt. Etna in Sicily. We carefully examine the finite size effects and generalize our previous results (Abe and Suzuki 2015). As will be seen, they share the remarkable common natures in their seismicities as point processes. Both of them are subdiffusive with the values of the anomalous diffusion exponent close to each other. The jump probability distributions are of the exponential type, whereas the waiting-time distributions obey the power law, the exponent of which turns out to be sensitive to the data size. In addition, for both volcanoes, the aging phenomenon is observed for the “event-time-averaged” mean-squared displacements. We also make a comment on existence of the long-term memory effect in the context of violation of the scaling relation to be satisfied by a class of singular Markovian processes.

This paper is organized as follows: in “[Subdiffusion in volcanic seismicities](#)”, the subdiffusive nature of volcanic seismicity as a point process is demonstrated. In “[Spatial properties](#)”, the jump probability distributions of the volcanic earthquakes are analyzed. The aging phenomenon is also discussed there. In “[Temporal properties](#)”, the waiting-time distributions are studied. It is shown how the power-law exponent is sensitive to the data size, in general. In “[A comment on \(non-\)Markovianity](#)”, a brief discussion is made about a possible violation of the singular Markovian scaling relation. In “[Concluding remarks](#)”, the results obtained are summarized.

The datasets employed in the present work are available at (A) <http://hraun.vedur.is/ja/viku> for Eyjafjallajökull and (B) <http://www.ct.ingv.it/uifs/analisti/catalogolist.php> for Mt. Etna.

Subdiffusion in volcanic seismicities

First of all, we present in Fig. 1 the patterns of spread of volcanic earthquakes at Eyjafjallajökull and Mt. Etna. There, one recognizes the signs of diffusion. However, the comparison between panels (A) and (B) shows that the pattern at Eyjafjallajökull is visually more heterogeneous than the one at Mt. Etna. This might be due to the fact that, in contrast to Mt. Etna, Eyjafjallajökull is not isolated, being with neighboring volcanoes. Accordingly, one would naively imagine that significant differences may exist in the spatio-temporal natures of their seismicities. Quite remarkably, however, they turn out to share similar properties.

We note that Fig. 1 plots the epicenters, but in what follows we will deal with the hypocenters.

As in the work of Abe and Suzuki (2015), we characterize these diffusive patterns in the following way. Consider a sphere with radius l at time t that encloses all earthquakes that occurred during the time interval $[0, t]$, where the initial time, 0, is adjusted to the occurrence time of the first event in a point process defined by a sequence extracted from the data under consideration. The collection of such spheres should be concentric with the center fixed at the hypocenter of the first event in the sequence. In other words, l at t is the largest value among the distances of all events from the first event. This idea is analogous to the concept of *mean maximal excursions* (Tejedor et al. 2010). Then, we describe the diffusion property as follows:

$$l \sim t^\alpha, \quad (1)$$

where α is a positive constant termed the diffusion exponent. Here, we are using the notation slightly different from that in our previous paper (Abe and Suzuki 2015). Familiar normal diffusion has $\alpha = 1/2$, whereas $\alpha \neq 1/2$ in anomalous diffusion (Bouchaud and Georges 1990; Metzler et al. 2014): subdiffusion (superdiffusion) if $\alpha < 1/2$ ($\alpha > 1/2$).

In Fig. 2, we present the plots of the law in Eq. (1) for the volcanic seismicities at (A) Eyjafjallajökull and (B) Mt. Etna. The datasets employed here are as follows:

- (A-1) During 19:34:21.840 on 2 March 2010 and 08:15:57.078 on 23 July 2010, 63.503°N to 63.750°N latitude and −19.749°E to −19.024°E longitude. The total number of events contained is 4000.
- (A-2) During 19:34:21.840 on 2 March 2010 and 04:28:6.578 on 16 March 2014, 63.415°N to 63.750°N latitude and −19.888°E to −18.754°E longitude. The total number of events contained is 12,000.

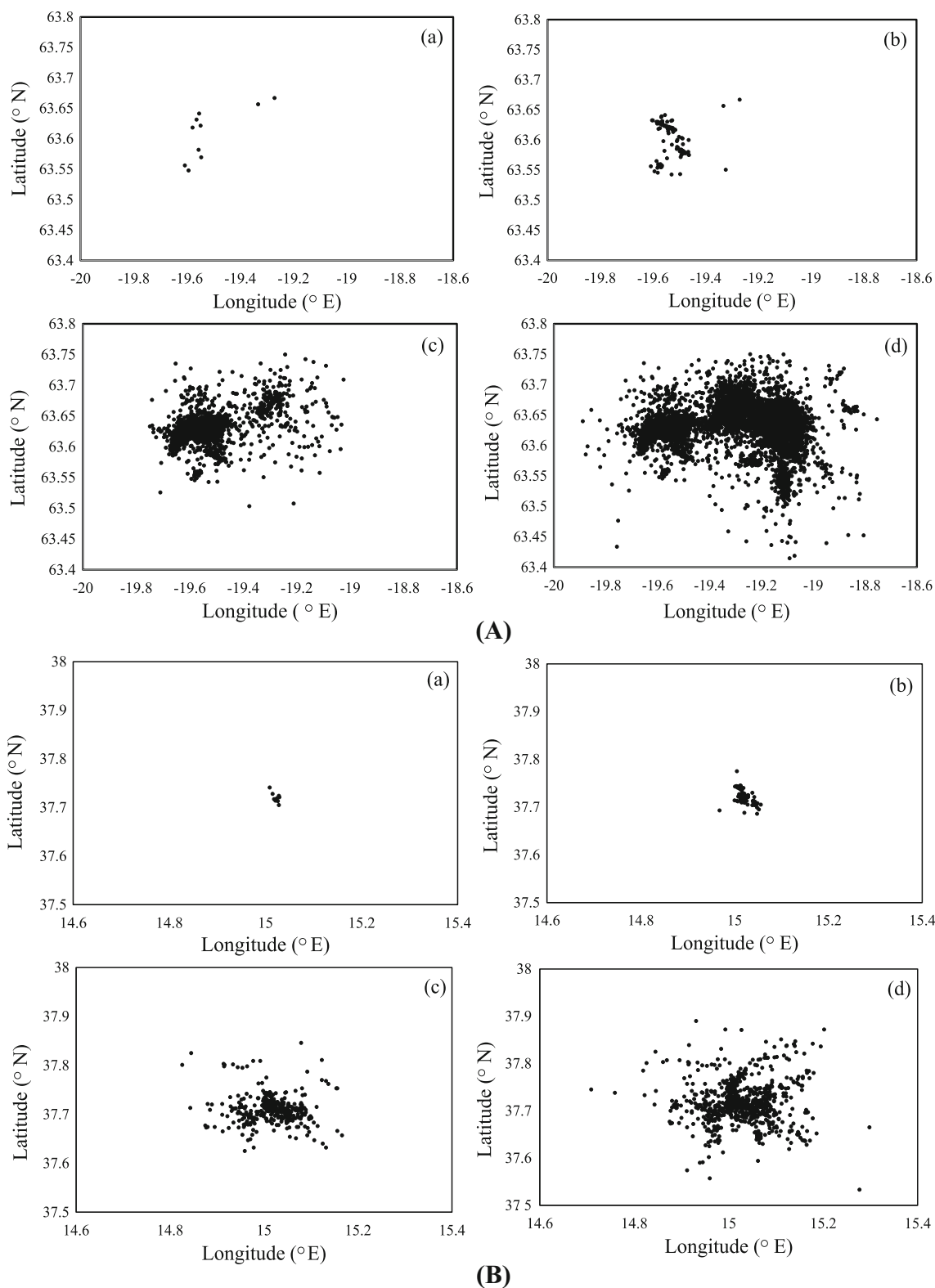


Fig. 1 Plots of epicenters of the volcanic earthquakes. **A** Eyjafjallajökull with the initial event at 19:34:21.84 on 2 March 2010 [the first (a) 10, (b) 100, (c) 4000, (d) 12,000 events] and **B** Mt. Etna with the initial event at 22:34:14 on 12 July 2001 [the first (a) 10, (b) 100, (c) 500, (d) 1000 events]

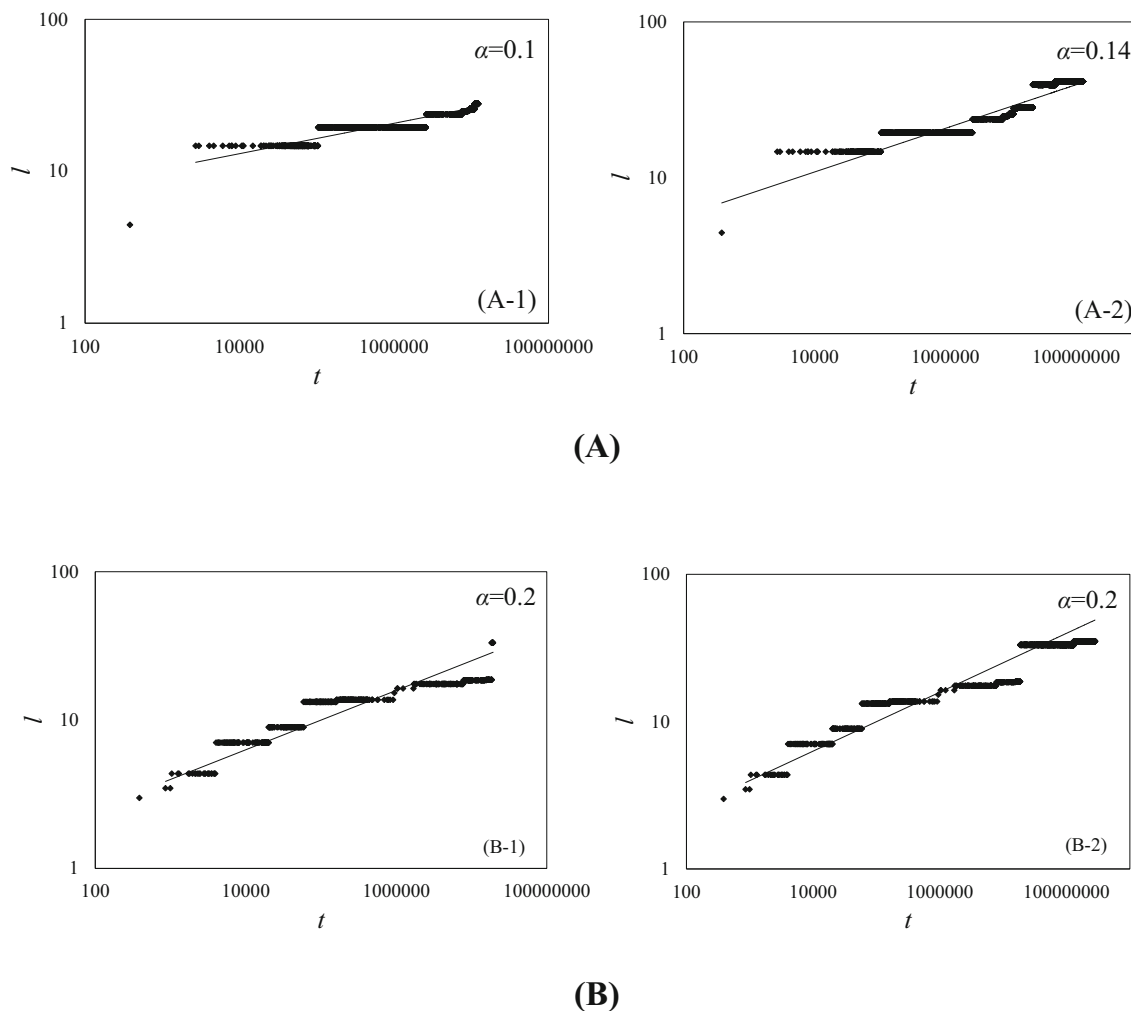


Fig. 2 The log–log plots of the radius l [km] with respect to (conventional) time t [s]. The *straight lines* describe the law in Eq. (1)

- (B-1) During 22:34:14 on 12 July 2001 and 01:25:36 on 20 February 2002, 37.533°N to 37.890°N latitude and 14.826°E to 15.277°E longitude. The total number of events contained is 600.
- (B-2) During 22:34:14 on 12 July 2001 and 16:26:35 on 7 June 2010, 37.509°N to 37.898°N latitude and 14.706°E to 15.298°E longitude. The total number of events contained is 5000.

As can be seen there, the values of the diffusion exponent are much smaller than $1/2$. Therefore, we conclude that the volcanic seismicities exhibit subdiffusion. We note that the growth of l is discontinuous and the step-like behavior appears. l remains constant for a certain duration of time and then abruptly increases. Because of the finiteness of the volcanoes in size, the horizontal length of the step becomes unboundedly large in a later stage and then l stops increasing in time. Such a stage is irrelevant to diffusion. This point can clearly be seen for Mt. Etna since it is isolated. However, the situation is much more involved

in the case of Eyjafjallajökull, which has the neighbors. These issues lead to importance of the finite size effects in the diffusion processes, as will be seen below.

Closing this section, we emphasize that the data intervals mentioned above will always be fixed in the subsequent analysis.

Spatial properties

Here, first we discuss the jump probability distribution, $P_J(\rho)$, where ρ is the three-dimensional distance between two successive earthquakes. In the work of Abe and Suzuki (2003), we have studied this quantity for non-volcanic seismicity and have found that it obeys a statistically exotic law characterized by the distribution decaying faster than the exponential-class ones. However, in the case of volcanic seismicity, it turns out not to be exotic at all.

In Fig. 3, we present the plots of the jump probability distributions for the datasets mentioned in “[Subdiffusion in](#)

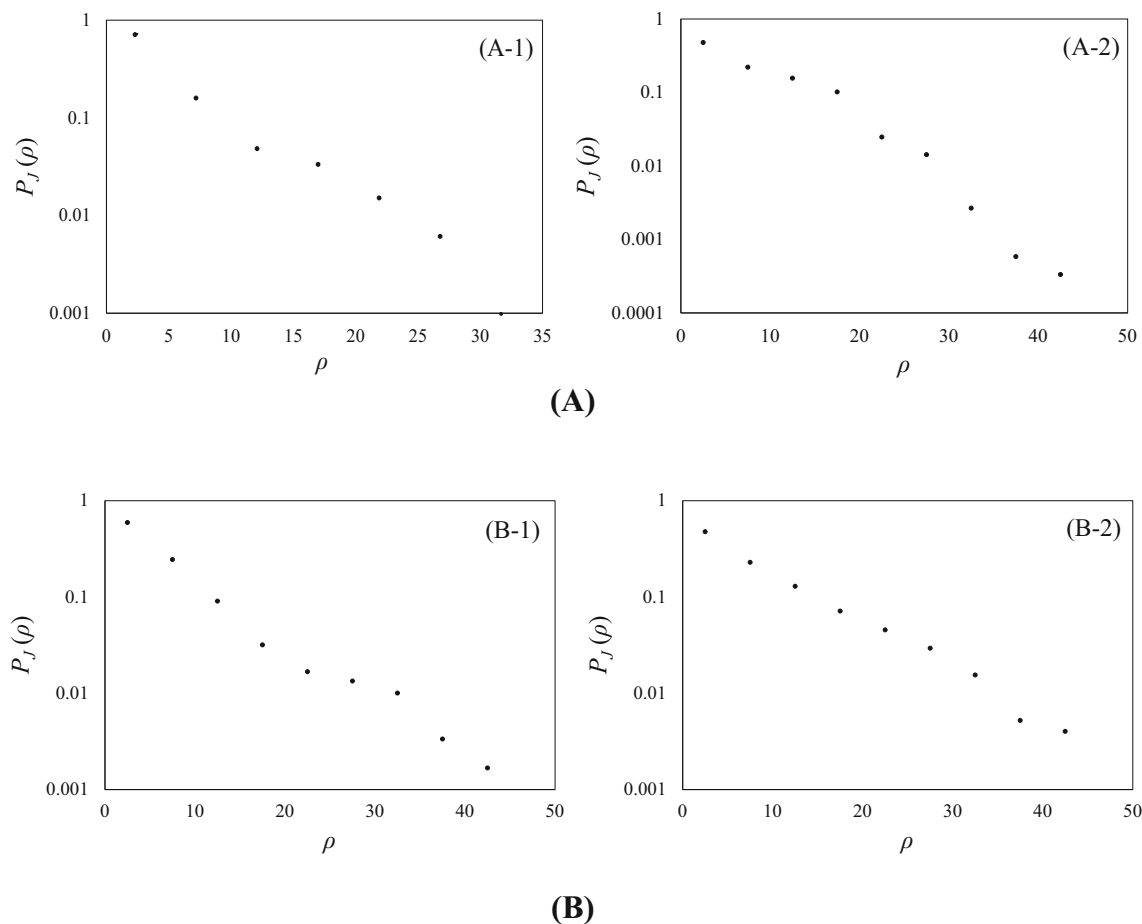


Fig. 3 The semi-log plots of the normalized jump probability distributions $P_J(\rho)$ [1/km] with respect to ρ [km]. The values of ρ_0 in Eq. (2) are (A-1) 5.0 km, (A-2) 5.0 km, (B-1) 7.5 km, (B-2) 8.5 km. The histograms are made with the bin size 5.0 km

volcanic seismicities”. The result shows that it well obeys the exponential law

$$P_J(\rho) \sim \exp(-\rho/\rho_0) \tag{2}$$

at both volcanoes. Here, ρ_0 is a positive constant having the dimension of length and its values are given in the caption. This quantity may give information about the spatial scale of each volcano. However, we note that its value depends on the data size. In fact, ρ_0 in (B-1) is different from that given in our previous work (Abe and Suzuki 2015).

The law in Eq. (2) means that the spatial property of the process is not anomalous and no long jumps are important, in contrast, e.g., to Lévy flights (Shlesinger et al. 1995). Since long jumps enhance diffusion, their absence is consistent with subdiffusion concluded in the preceding section. However, the final conclusion should not be made until the temporal property of the process is examined.

Second, we discuss nonstationarity of the process. For this purpose, we take the series $\{\mathbf{r}_k\}_{k=0,1,2,\dots}$, with \mathbf{r}_k

being the hypocenter of the k -th event. The index k plays a role of the internal time referred to as *event time*. Then, we consider the event-time-averaged mean-squared displacement defined by (Abe and Suzuki 2015)

$$\overline{\delta^2(n; a, N)} = \frac{1}{N-n} \sum_{m=a}^{a+N-n-1} (\mathbf{r}_{m+n} - \mathbf{r}_m)^2, \tag{3}$$

where a , n and N are referred to as the *aging event time*, *lag event time* and *measurement event time*, respectively, provided that $N - n$ should be much larger than unity. [The upper limit of the summation on the right-hand side of Eq. (6) in the paper of Abe and Suzuki (2015) should read as the one in Eq. (3) above, but this change is negligibly small for the result given there]. $\overline{\delta^2}$ can be regarded as a discrete event-time version of the time-averaged mean-squared displacement studied in the recent works (Metzler et al. 2014; Schulz et al. 2014).

In Fig. 4, we present the plots of the quantity in Eq. (3) for some values of the aging event time. The data intervals

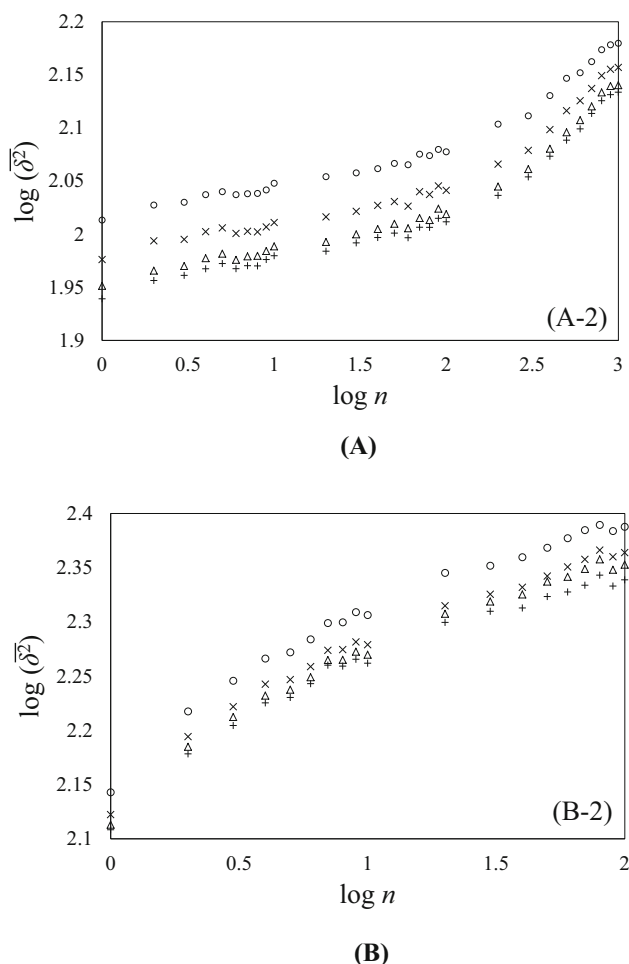


Fig. 4 The log–log plots of the event-time-averaged mean-square displacement. The values of the aging a and the measurement event time N are **A** $+$ ($a = 0$), Δ ($a = 200$), \times ($a = 500$), \circ ($a = 1000$), $N = 11000$, and **B** $+$ ($a = 0$), Δ ($a = 50$), \times ($a = 100$), \circ ($a = 300$), $N = 4700$. All quantities are dimensionless

considered here are (A-2) and (B-2) mentioned in the preceding section. The aging phenomenon is clearly observed at both Eyjafjallajökull and Mt. Etna: there is a monotonic increase of $\overline{\delta^2}$ with respect to the aging event time. This fact, originally found for Mt. Etna (Abe and Suzuki 2015), implies that the sequence of the hypocenters belongs to a specific class of *nonstationary* point processes.

Temporal properties

Since the jump probability distribution is not anomalous, the subdiffusive nature discussed in “[Subdiffusion in volcanic seismicities](#)” is supposed to be concerned with long waiting time τ between two successive events that suppresses diffusion. In this section, we show that this is indeed the case.

In Fig. 5, we present the plots of the waiting-time distributions. Once again, the data intervals employed here are the same as the ones in “[Subdiffusion in volcanic seismicities](#)”. As expected from the above consideration, the distributions, in fact, decay as the power law

$$P_W(\tau) \sim \tau^{-1-\mu}. \quad (4)$$

Here, the notation different from that in the paper of Abe and Suzuki (2015) is used for the exponent. In this respect, it may be worth mentioning that the power-law waiting-time distribution is observed also for non-volcanic earthquakes (Abe and Suzuki 2005).

It is of importance to note that the value of the exponent is different for different size of data interval. In Fig. 6, we show how μ depends on the data size. There, we see a remarkable similarity between Eyjafjallajökull and Mt. Etna, apart from the fact that the volcanic seismicity at Eyjafjallajökull is much more active than that at Mt. Etna in the data intervals considered. We wish to point out that both of the values of μ at Eyjafjallajökull and Mt. Etna seem to converge to a common value $\mu \cong -0.14$ as the size of the interval increases, suggesting the existence of *universality* in a certain sense.

We wish to emphasize that, in the above, “size” is the length of the conventional time interval of the data and is not of the event time. According to our analysis, as long as the number of events is employed, the data collapse as in Fig. 6 cannot be established. As mentioned above, the volcanic seismicity at Eyjafjallajökull is much more active than that at Mt. Etna. This implies that the event time as the internal time reveals the difference between these two seismicities. Further study is needed for deeper understanding of this issue regarding the concept of time in complex systems.

A comment on (non-)Markovianity

Another temporal property of interest is the decay rate of the number of events. Let $N(t)$ be the number of events that occurred in the time interval $[t_0, t]$, where t_0 is a fixed time. We are particularly interested in data intervals, in which the rate decays as the power law: $dN(t)/dt \sim A/t^p$, where p and A are positive constants. This may remind one of the Omori–Utsu law (Omori 1894; Utsu 1961) for the temporal pattern of aftershocks following a main shock. We note, however, that in the present case the initial event in the data interval under consideration does not necessarily correspond to the one with a large value of magnitude. Now, it is convenient to employ the integrated form of the law:

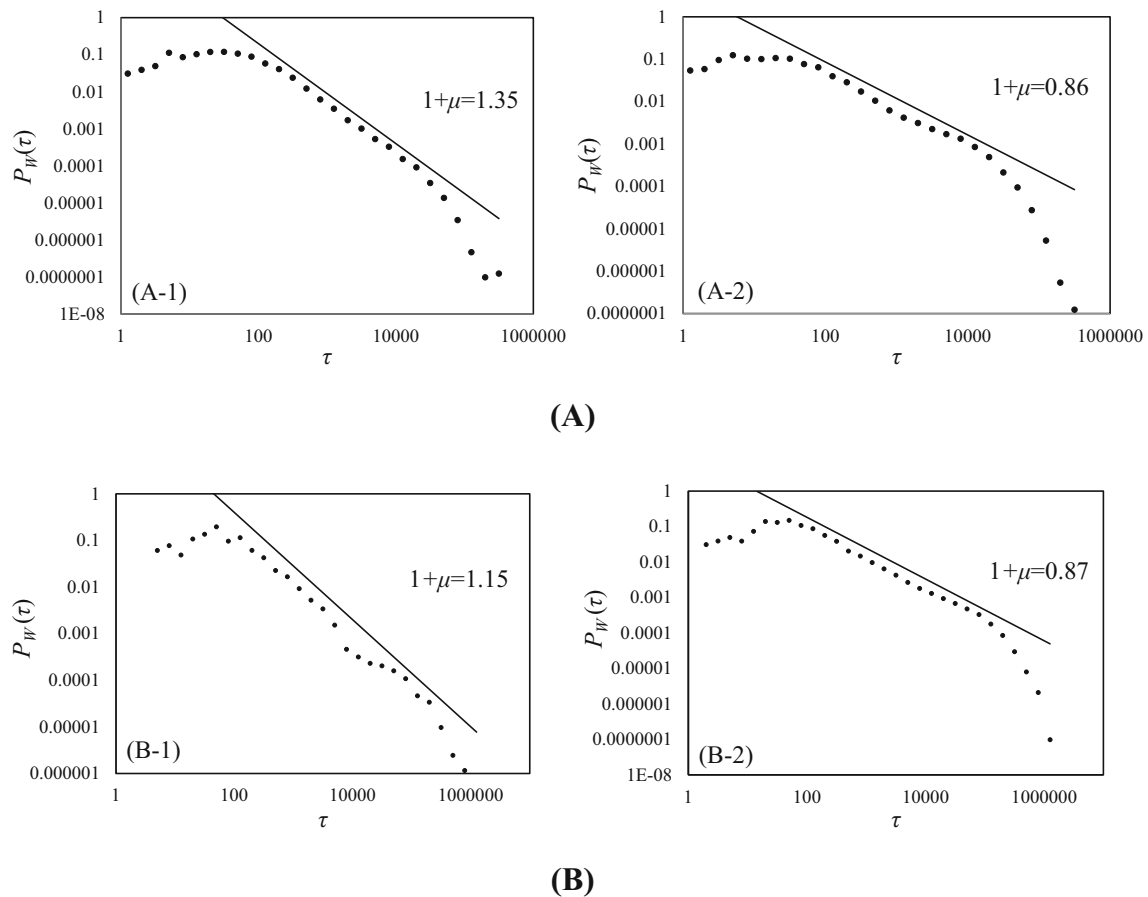


Fig. 5 The log–log plots of the normalized waiting-time distribution $P_W(\tau)$ (1/s) with respect to the waiting time τ (s). The bin size for making the histograms is fixed in such a way that each decade contains five points

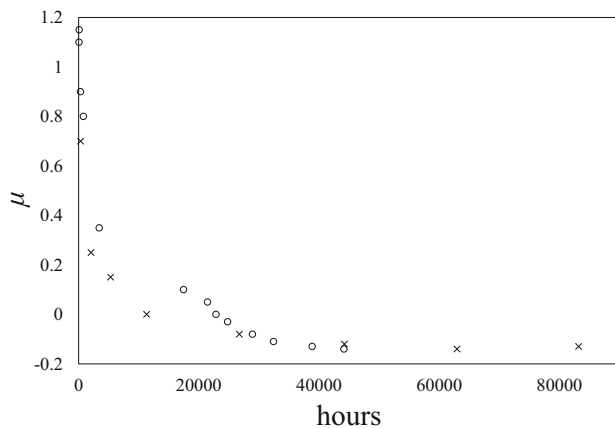


Fig. 6 Dependence of the exponent μ of the waiting-time distributions on the size of data intervals measured in the unit of 1 h from the initial events given in “Subdiffusion in volcanic seismicities”. \circ (Eyjafjallajökull) and \times (Mt. Etna). Possible error bars are not indicated, since a primary concern here is to show the gross behavior of μ with respect to the size of the data intervals

$$N(t) - N(t_0) \sim \begin{cases} A (t^{1-p} - t_0^{1-p}) / (1-p) & (p \neq 1) \\ A \ln(t/t_0) & (p = 1) \end{cases} \quad (5)$$

In Fig. 7, we show how the frequency of occurrence of events in the dataset (B-1) in “Subdiffusion in volcanic seismicities” varies in time. There, a noticeable trend can be recognized in the subinterval indicated by the left–right arrow. (On the other hand, no such trends could be found for Eyjafjallajökull. Accordingly, here we only analyze the data taken from Mt. Etna.) In Fig. 8, we present the plots of both Eq. (5) and the waiting-time distribution for the subinterval in Fig. 7. (Recall that the value of the exponent of the power-law waiting-time distribution depends on the data size). It is mathematically known (Barndorff-Nielsen et al. 2000) that, for a class of singular Markovian processes with both p and μ being in the range $(0, 1)$, there holds the following scaling relation:

$$p + \mu = 1. \quad (6)$$

In other words, violation of this relation implies that the system has a long-term memory. Now, from Fig. 8, we approximately estimate $p + \mu \cong 1.23$. Thus, the process in the data interval under consideration seems to be non-

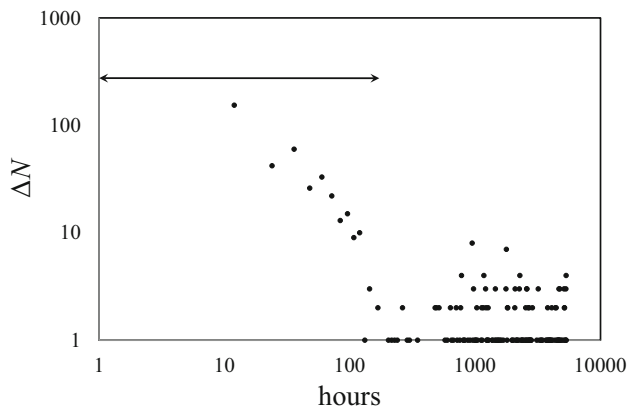


Fig. 7 The log–log plot of the number of events occurred per 12 h, ΔN , at Mt. Etna with respect to the duration of time measured in the unit of 1 h from the initial events given in “Subdiffusion in volcanic seismicities”. The subinterval indicated by the left–right *arrow* is between 22:34:14 on 12 July 2001 and 12:17:05 on 19 July 2001. The total number of events contained is 390

Markovian. This point is analogous to that in non-volcanic seismicity. We have previously studied a similar issue for earthquake aftershocks (Abe and Suzuki 2009, 2012). There, we have reported significant violation ($\sim 50\%$) of Eq. (6), leading to the fact that any model assuming Markovianity of aftershock sequence should be reconsidered. However, the violation of the scaling relation here is not so significant.

As additional information, we also point out that Eq. (6) has also been discussed in other contexts, including laser cooling of atoms (Bardou et al. 2002) and acoustic emissions from plunged granular materials to examine the (non-)Markovianity (Tsuji and Katsuragi 2015).

As mentioned above, we could not apply the scaling method to the volcanic seismicity of the data intervals considered here for Eyjafjallajökull, and, therefore, other approaches are needed for examining (non-)Markovianity for its seismicity. The best we can say at present is that volcanic seismicity seems to possess elements of non-Markovianity in general, and this point is consistent with the complex natures of the phenomenon that we have observed in the present work.

Concluding remarks

We have performed a comparative study of diffusion of volcanic earthquakes at Eyjafjallajökull and Mt. Etna. We have found that at both of them the phenomenon is subdiffusive, characterized by the values of the anomalous diffusion exponent close to each other. Then, we have analyzed the spatio-temporal properties of the volcanic seismicities as point processes. We have shown that the

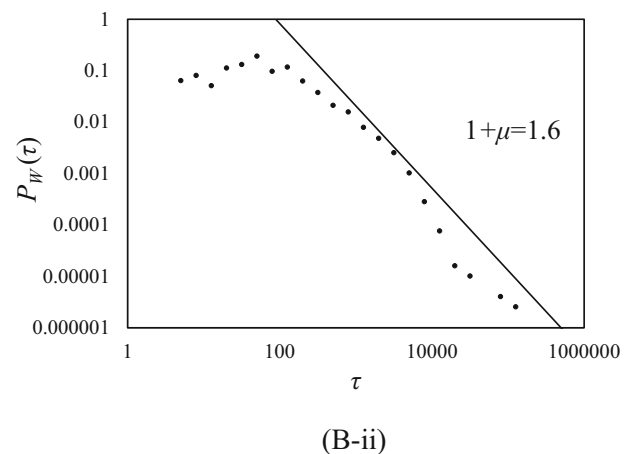
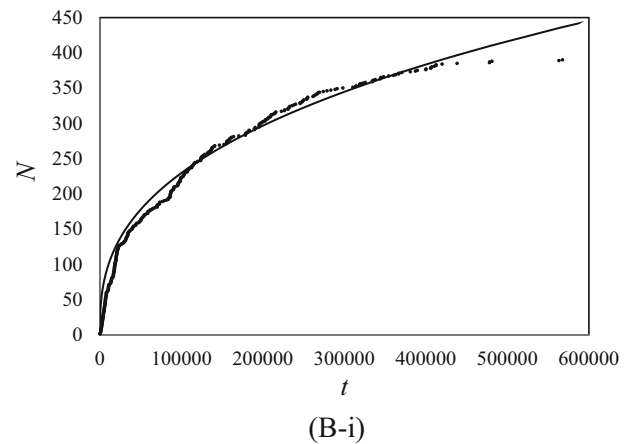


Fig. 8 The log–log plots of **B-i** the cumulative number of events, N , in Eq. 5 with $t_0 \equiv 0$ being adjusted to the occurrence time of the first event contained in the datasets in “Subdiffusion in volcanic seismicities” and **B-ii** the corresponding waiting-time distribution, $P_W(\tau)$ (1/s) with respect to the waiting time τ (s) in the selected subinterval in Fig. 7. The *solid curve* in **B-i** describes the law in Eq. (5) with $A \cong 1.20 s^{p-1}$ and $p \cong 0.63$. The bin size for making the histogram in **B-ii** is fixed in such a way that each decade contains five points

jump probability distributions for these volcanoes obey the exponential law, whereas the waiting-time distributions do the power law. We have examined how the exponent of the power-law waiting-time distribution is sensitive to the data size. These show that the seismicities at these volcanoes share the remarkable common features, indicating universalities of the findings presented here. Furthermore, we have also analyzed the occurrence rate of volcanic earthquakes in time to examine if the volcanic seismicity is (non-)Markovian.

Previously, we have discussed (Abe and Suzuki 2015) that all of four celebrated theoretical approaches to anomalous diffusion, i.e., fractional kinetics of continuous-time random walks, fractional Brownian motion, fractal

random walks and nonlinear kinetics, do not seem to offer a deciding explanation of subdiffusion of volcanic earthquakes. The present work, however, shows that the value of the exponent of the power-law waiting-time distribution is sensitive to the data size, in general, implying that further studies are needed. We would also like to stress that any new theoretical development in anomalous diffusion, e.g., a recent work (Boon and Lutsko 2017), may contribute to understanding the physics of volcanic seismicity.

Acknowledgements The works of SA and NS have been supported in part by the Grant-in-Aid for Scientific Research from the Japan Society for the Promotion of Science under the contracts (No. 26400391 and No. 16K05484). SA has also been supported in part by the High-End Foreign Expert Program of China and by the Program of Competitive Growth of Kazan Federal University by the Ministry of Education and Science of the Russian Federation.

References

- Abe S, Suzuki N (2003) Law for the distance between successive earthquakes. *J Geophys Res* 108(B2):2113. doi:[10.1029/2002JB002220](https://doi.org/10.1029/2002JB002220)
- Abe S, Suzuki N (2005) Scale-free statistics of time interval between successive earthquakes. *Physica A* 350(2–4):588–596. doi:[10.1016/j.physa.2004.10.040](https://doi.org/10.1016/j.physa.2004.10.040)
- Abe S, Suzuki N (2009) Violation of the scaling relation and non-Markovian nature of earthquake aftershocks. *Physica A* 388(9):1917–1920. doi:[10.1016/j.physa.2009.01.031](https://doi.org/10.1016/j.physa.2009.01.031)
- Abe S, Suzuki N (2012) Aftershocks in modern perspectives: complex earthquake network, aging, and non-Markovianity. *Acta Geophys* 60(3):547–561. doi:[10.2478/s11600-012-0026-8](https://doi.org/10.2478/s11600-012-0026-8)
- Abe S, Suzuki N (2015) Anomalous diffusion of volcanic earthquakes. *EPL* 110(5):59001. doi:[10.1209/0295-5075/110/59001](https://doi.org/10.1209/0295-5075/110/59001)
- Bardou F, Bouchaud JP, Aspect A, Cohen-Tannoudji C (2002) Lévy statistics and laser cooling: how rare events bring atoms to rest. Cambridge University Press, Cambridge
- Barndorff-Nielsen OE, Benth FE, Jensen JL (2000) Markov jump processes with a singularity. *Adv Appl Probab* 32(3):779–799. doi:[10.1017/S0001867800010259](https://doi.org/10.1017/S0001867800010259)
- Boon JP, Lutsko JF (2017) Temporal diffusion: from microscopic dynamics to generalised Fokker–Planck and fractional equations. *J Stat Phys* 166(6):1441–1454. doi:[10.1007/s10955-017-1716-z](https://doi.org/10.1007/s10955-017-1716-z)
- Bouchaud JP, Georges A (1990) Anomalous diffusion in disordered media: statistical mechanisms, models and physical applications. *Phys Rep* 195(4–5):127–293. doi:[10.1016/0370-1573\(90\)90099-N](https://doi.org/10.1016/0370-1573(90)90099-N)
- Hill DP, Pollitz F, Newhall C (2002) Earthquake–volcano interactions. *Phys Today* 55(11):41–47. doi:[10.1063/1.1535006](https://doi.org/10.1063/1.1535006)
- Metzler R, Jeon JH, Cherstvy AG, Barkai E (2014) Anomalous diffusion models and their properties: non-stationarity, non-ergodicity, and ageing at the centenary of single particle tracking. *Phys Chem Chem Phys* 16(44):24128–24164. doi:[10.1039/c4cp03465a](https://doi.org/10.1039/c4cp03465a)
- Omori F (1894) On the after-shocks of earthquakes. *J Coll Sci Imp Univ Tokyo* 7(2):111–200
- Roman DC, Cashman KV (2006) The origin of volcano-tectonic earthquake swarms. *Geology* 34(6):457–460. doi:[10.1130/G22269.1](https://doi.org/10.1130/G22269.1)
- Schulz JHP, Barkai E, Metzler R (2014) Aging renewal theory and application to random walks. *Phys Rev X* 4(1):011028. doi:[10.1103/PhysRevX.4.011028](https://doi.org/10.1103/PhysRevX.4.011028)
- Shlesinger MF, Zaslavsky GM, Frisch U (eds) (1995) Lévy flights and related topics in physics. Springer, Heidelberg
- Tejedor V, Bénichou O, Voituriez R, Jungmann R, Simmel F, Selhuber-Unkel C, Oddershede LB, Metzler R (2010) Quantitative analysis of single particle trajectories: mean maximal excursion method. *Biophys J* 98(7):1364–1372. doi:[10.1016/j.bpj.2009.12.4282](https://doi.org/10.1016/j.bpj.2009.12.4282)
- Tsuji D, Katsuragi H (2015) Temporal analysis of acoustic emission from a plunged granular bed. *Phys Rev E* 92(4):042201. doi:[10.1103/PhysRevE.92.042201](https://doi.org/10.1103/PhysRevE.92.042201)
- Turcotte DL (1997) *Fractals and chaos in geology and geophysics*, 2nd edn. Cambridge University, Cambridge
- Utsu T (1961) A statistical study on the occurrence of aftershocks. *Geophys Mag* 30(4):521–605
- Zobin VM (2012) *Introduction to volcanic seismology*, 2nd edn. Elsevier, London

Erratum to: Subdiffusion of volcanic earthquakes

Sumiyoshi Abe^{1,2,3} · Norikazu Suzuki⁴

Published online: 26 April 2017

© Institute of Geophysics, Polish Academy of Sciences & Polish Academy of Sciences 2017

Erratum to: Acta Geophys.
DOI 10.1007/s11600-017-0029-6

The original version of this article unfortunately contained errors. The presentation of Fig. 1 was incorrect. The corrected Fig. 1 is given below. The original article has been corrected.

The online version of the original article can be found under
doi:[10.1007/s11600-017-0029-6](https://doi.org/10.1007/s11600-017-0029-6).

✉ Sumiyoshi Abe
suabe@sf6.so-net.ne.jp

- ¹ Physics Division, Faculty of Information Science and Engineering, Huaqiao University, Xiamen, China
- ² Department of Physical Engineering, Mie University, Mie, Japan
- ³ Institute of Physics, Kazan Federal University, Kazan, Russia
- ⁴ College of Science and Technology, Nihon University, Funabashi, Chiba, Japan

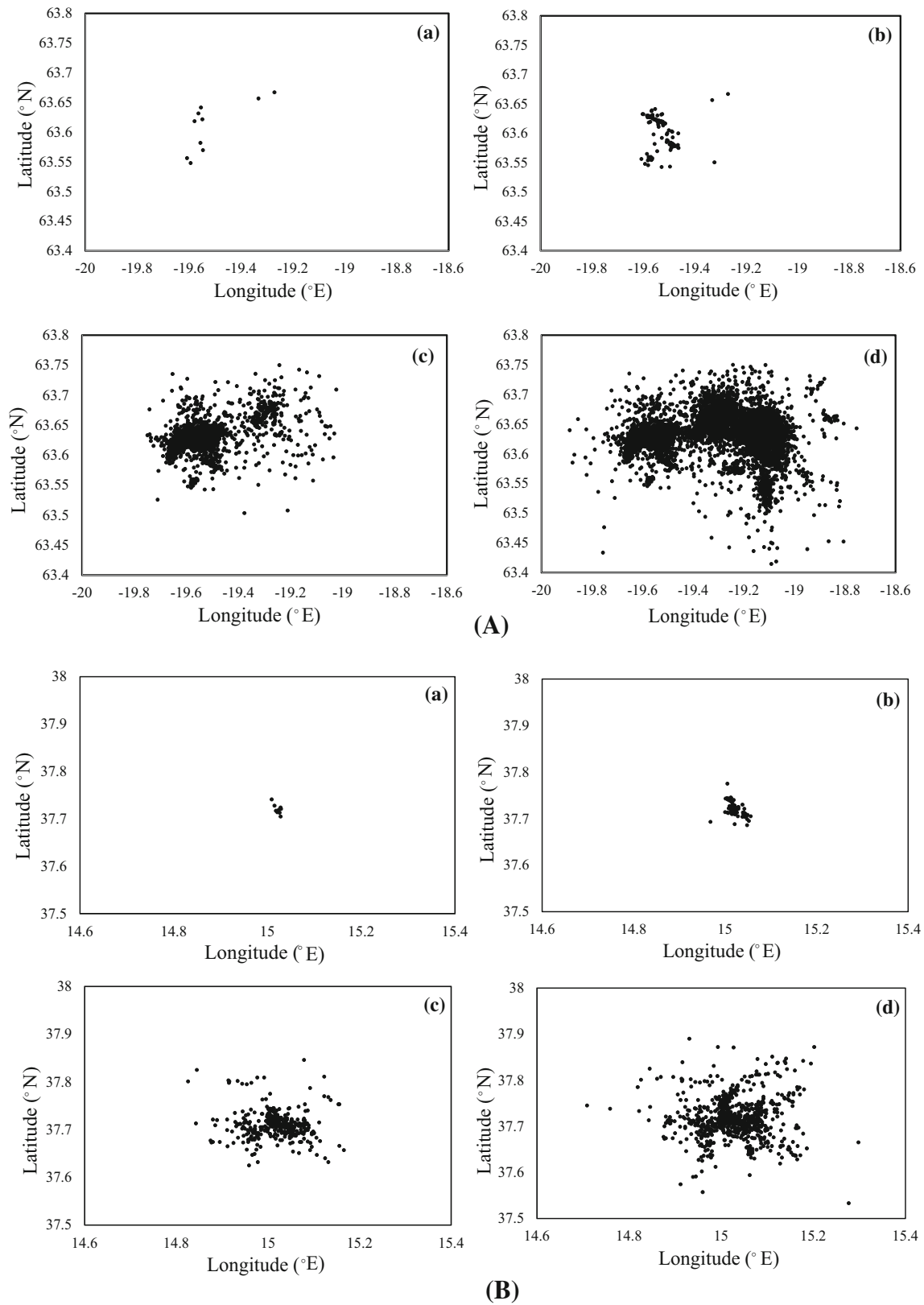


Fig. 1 Plots of epicenters of the volcanic earthquakes. **A** Eyjafjallajökull with the initial event at 19:34:21.84 on 2 March 2010 [the first (a) 10, (b) 100, (c) 4000, (d) 12,000 events] and **B** Mt. Etna with

the initial event at 22:34:14 on 12 July 2001 [the first (a) 10, (b) 100, (c) 500, (d) 1000 events]

Time-dependent seismic hazard in Bobrek coal mine, Poland, assuming different magnitude distribution estimations

Konstantinos Leptokaropoulos¹ · Monika Staszek¹ · Szymon Cielesta¹ · Paweł Urban¹ · Dorota Olszewska¹ · Grzegorz Lizurek¹

Received: 28 December 2016 / Accepted: 29 December 2016 / Published online: 25 January 2017
© The Author(s) 2017. This article is published with open access at Springerlink.com

Abstract The purpose of this study is to evaluate seismic hazard parameters in connection with the evolution of mining operations and seismic activity. The time-dependent hazard parameters to be estimated are activity rate, Gutenberg–Richter *b*-value, mean return period and exceedance probability of a prescribed magnitude for selected time windows related with the advance of the mining front. Four magnitude distribution estimation methods are applied and the results obtained from each one are compared with each other. Those approaches are maximum likelihood using the unbounded and upper bounded Gutenberg–Richter law and the non-parametric unbounded and non-parametric upper-bounded kernel estimation of magnitude distribution. The method is applied for seismicity occurred in the longwall mining of panel 3 in coal seam 503 in Bobrek colliery in Upper Silesia Coal Basin, Poland, during 2009–2010. Applications are performed in the recently established Web-Platform for Anthropogenic Seismicity Research, available at <https://tcs.ah-epos.eu/>.

Keywords Induced seismicity · Magnitude distribution · Bobrek mine · Time-dependent hazard assessment

Introduction

Earthquake catalogs constitute a robust and beneficial tool for a variety of seismic analyses. Since seismicity is directly associated with physical quantities and mechanical properties of the crust such as strain accumulation, pore–fluid interactions and frictional response of the rupture zones, earthquakes provide a major source of information that cannot be usually obtained by direct measurements. Spatial and temporal seismicity rate anomalies are essentially reported as the most frequent intermediate-term precursory phenomenon in timescales varying from a few days to several years. The use of the well-established Gutenberg–Richter (G–R) law has been routinely incorporated into many seismic hazard assessment studies (e.g., Cornell 1968; Convertito et al. 2012). Alternatively, non-parametric approaches can be performed for hazard assessment evaluation under certain conditions (e.g., Kijko et al. 2001; Lasocki and Orlecka-Sikora 2008).

Seismic events may be controlled by either natural or anthropogenic factors. During the last decades, the rising demands for energy and minerals have sharpened the problem of hazards induced by exploration and exploitation of georesources (Davis et al. 2013). Among the diverse technologies capable of inducing earthquakes, one of the most well studied origins of anthropogenic hazard is underground mining. The undesirable rockmass response to mining operations was firstly observed back in the eighteenth century and during the last years it is being constantly reviewed and documented (e.g., Gibowicz and Lasocki 2001; Li et al. 2007; Gibowicz 2009, and references therein). A variety of factors control the rockmass fracturing and nucleation process in mines such as tectonic stresses accumulation, removal of material from the mine, explosions and the interaction among seismic events and

✉ Konstantinos Leptokaropoulos
kleptoka@igf.edu.pl

¹ Institute of Geophysics, Polish Academy of Sciences, Warsaw, Poland

rockbursts. The instability of mining activities, especially when they are extended, may result in the residual subsidence and localized or generalized collapsing, potentially with significant societal and economic impacts. There are numerous documented cases where mining-induced seismicity has caused personnel injuries, production losses, extensive damage to infrastructure, collapse of drifts and stopes, and occasionally, fatalities. For all these reasons, seismic hazard assessment in mines is a task of paramount importance.

The purpose of this study is to evaluate seismic hazard parameters in connection with the evolution of mining operations and therefore to detect a causative relationship between seismic events and mining operations. The time-dependent hazard parameters to be estimated are the activity rate, the Gutenberg–Richter b -value, the mean return period and the exceedance probability of a prescribed magnitude for selected time windows related with the advance of the mining front. Four magnitude distribution estimation methods are applied and the results obtained from each one are compared with each other. Those approaches are maximum likelihood using the unbounded Gutenberg–Richter relation-based model (GRU), maximum likelihood using the upper-bounded Gutenberg–Richter relation-based model (GRT), unbounded non-parametric kernel estimation (NPU) and upper-bounded non-parametric kernel estimation (NPT). In addition, three different ways to construct subsequent datasets are applied: Time windows of constant duration, time windows with constant event number and time windows corresponding to constant front advance position. The spatial constraints are set in terms of the distance perpendicular and normal to the mining front at each time point (beginning and ending of time windows). The method is applied and results are discussed for the longwall mining of panel 3 in coal seam 503 in Bobrek colliery in Upper Silesia Coal Basin (USCB) in Poland, during 2009–2010. As shown in Fig. 1, this is a large area where coal mining has been carried out since the

eighteenth century and continues till nowadays in more than thirty mines in which coal is exploited by applying the longwall method.

Data

Bobrek Mine is a hard coal mine located in Bytom city in the area of USCB, Poland (Fig. 1). USCB constitutes one of the most seismically active mining areas worldwide, with almost 56,000 mining tremors of energy $E > 10^5$ J recorded between 1974 and 2005 (Stec 2007). The analysis of our study was based on selected set of data connected with exploitation in panel No. 3 in coal seam 503. This dataset is retrieved due to the specially organized virtual Laboratory for Monitoring Mining Induced Seismicity (LMMIS) where seismic data and technological data, such as mining front advance, were gathered. The seismic data had been prepared based on integration of two seismological networks operating at different scales (registration of events in the near and far seismic field). Additionally, information about the geology and the tectonics of the area was available. This set of data is integrated as an episode, which comprehensively describes a geophysical process induced or triggered by human technological activity, posing hazard for populations, infrastructure and the environment. All the data from this episode are available on TCS-AH platform as BOBREK MINE: local seismicity linked to longwall mining (<https://tcs.ah-epos.eu/#episodes:BOBREK>).

During underground mining works of longwall panel 3/503, a total of 2996 seismic events were recorded and analyzed, with a seismic energy greater than 10^2 J (local magnitude $M_L > 0.1$), occurred from April 12th, 2009 until July 8th, 2010. The strongest observed events with local magnitudes equal to 2.9, 3.7, 3.0 and 2.8 (seismic energy greater than 10^7 J) took place on May 20th 2009, December 16th 2009, February 5th 2010 and March 3rd 2010,

Fig. 1 The location of the Bobrek mine in Upper Silesia Coal Basin, Poland. Figure comes from TCS-AH platform <https://tcs.ah-epos.eu/>

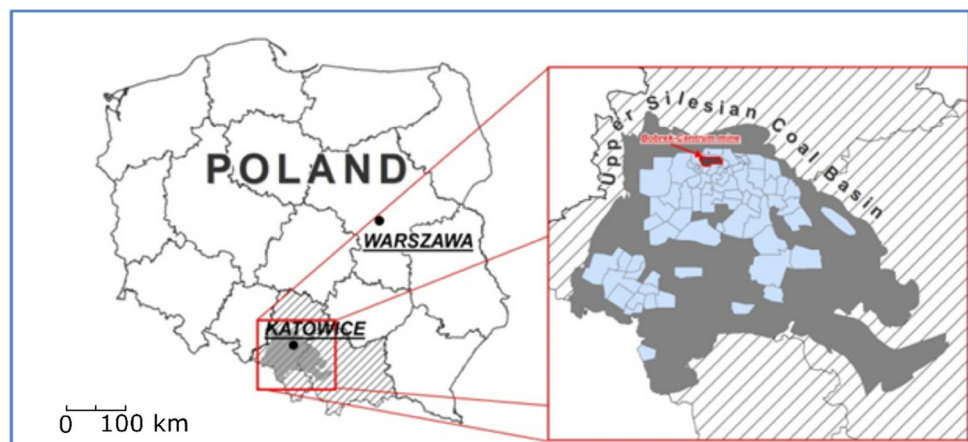


Table 1 Events with $M_L \geq 2.8$ which occurred in analyzed period of time

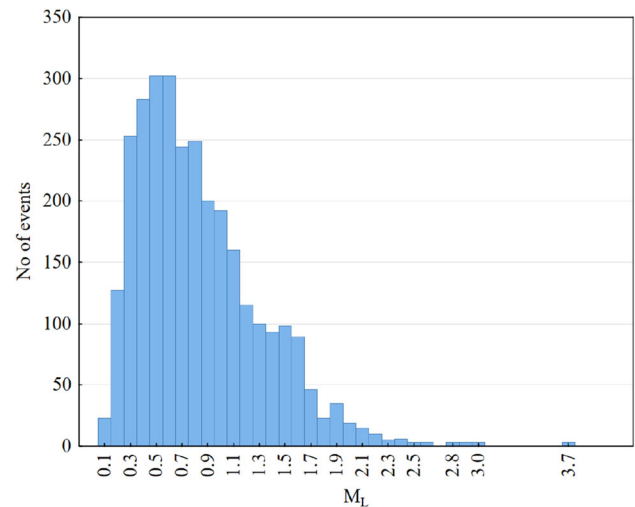
ID	Occurrence time	M_L
1	20-May-2009, 14:28:48	2.9
2	16-Dec-2009, 02:06:37	3.7
3	05-Feb-2010, 10:59:18	3.0
4	11-Mar-2010, 00:07:21	2.8

respectively (Table 1). Figure 2 shows the local magnitude histogram. The information about positions of the longwall excavation front advance in Bobrek mine is given as polygon coordinates in different time moments. The distance between subsequent positions of the mining front is approximately 50 m and time interval is one month. The foci of the seismic events caused by underground mining operations in panel No. 3, the locations of underground seismic stations and the position of the mining front advance during excavation of that longwall are demonstrated in Fig. 3 (figure is a snapshot of 3D visualization available via TCS-AH platform). The average seismic activity of the panel 3/503 was 6.6 events per day (Fig. 4). However, this rate is far from being considered as stable since there are significant seismic activity changes in time. In Fig. 4 it is shown that seismicity rates start growing from the beginning of November 2009. Then, the largest event occurred ($M_L = 3.7$). The highest seismic activity equal to 18.4 events per day was observed from middle of January up to the middle of April 2010 and during that period two other strongest events occurred.

Methodology

Four different magnitude distribution estimation methods are applied presented in the following sub-sections. Hazard parameters are calculated and plotted for each one of the time windows for which sufficient data are available in order to perform the necessary calculation. A different minimum number of events in each window is considered for the calculations to be performed, according to the method selected: for unbounded Gutenberg–Richter method it is 7; for upper-bounded Gutenberg–Richter method it is 15; and for non-parametric kernel-based methods it is 50 events.

Note that for the Unbounded models (GRU and NPU) an infinite upper magnitude limit, M_{\max} , is considered whereas in the Truncated (upper-bounded) approaches (GRT and NPT) M_{\max} is evaluated using the Kijko–Sellevoll generic formula (Kijko and Sellevoll 1989; Kijko 2004; Lasocki and Urban 2011). If convergence is not reached the Robson and Whitlock (1964) simplified formula is used:

**Fig. 2** Histogram of local magnitude of seismic events

$M_{\max} = 2M_{\max\text{obs}} - M_{\max2\text{obs}}$, where $M_{\max\text{obs}}$ and $M_{\max2\text{obs}}$ stand for the largest and second largest magnitudes in a given catalog, respectively.

The hazard parameters evaluated in this study are the mean return period for a specified magnitude and the exceedance probability of a specified magnitude to be exceeded within a certain time period. The mean return period of magnitude M is the average elapsed time between the consecutive earthquakes of magnitude M . Given the mean activity rate for events with $M \geq M_{\min}$, λ , in a specified time period and the corresponding cumulative magnitude distribution function, $F(M)$, the mean return period is estimated as:

$$T = \frac{1}{\lambda(1 - F(M))} \quad (1)$$

The exceedance probability of a specified magnitude, M , during a predefined time period, Δt , is given as

$$P = 1 - e^{-\lambda\Delta t(1-F(M))}. \quad (2)$$

The cumulative magnitude distribution function, $F(M)$, is calculated with respect to the selected method:

Unbounded GR law (GRU)

Assume that the unlimited Gutenberg–Richter relation leads to the exponential model of distribution for events with magnitude above the catalog completeness level M_{\min} . Under this assumption, an infinitely large maximum magnitude is possible. The shape parameter of this distribution and consequently the G–R b -value is estimated by maximum likelihood method (Aki 1965; Utsu 1999) with the Probability Density Function (PDF) of magnitudes given as:

$$f(M) = \beta e^{-\beta(M - M_{\min} + \frac{M}{2})} \quad (3)$$

Fig. 3 Distribution of seismic events during excavation of longwall panel no. 3 in Bobrek Mine. *Black triangles* represent the nearest seismic stations, and *black lines* show the subsequent positions of the longwall excavation front advance

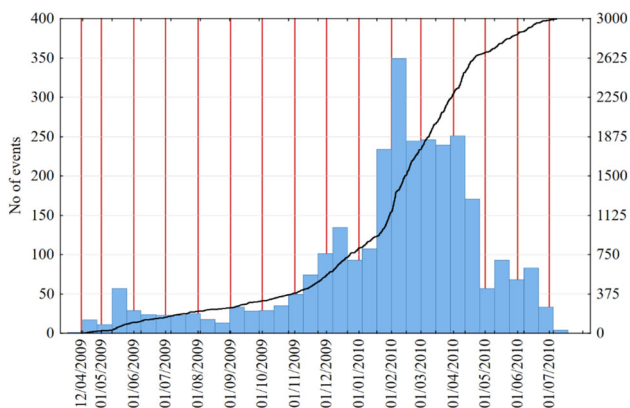
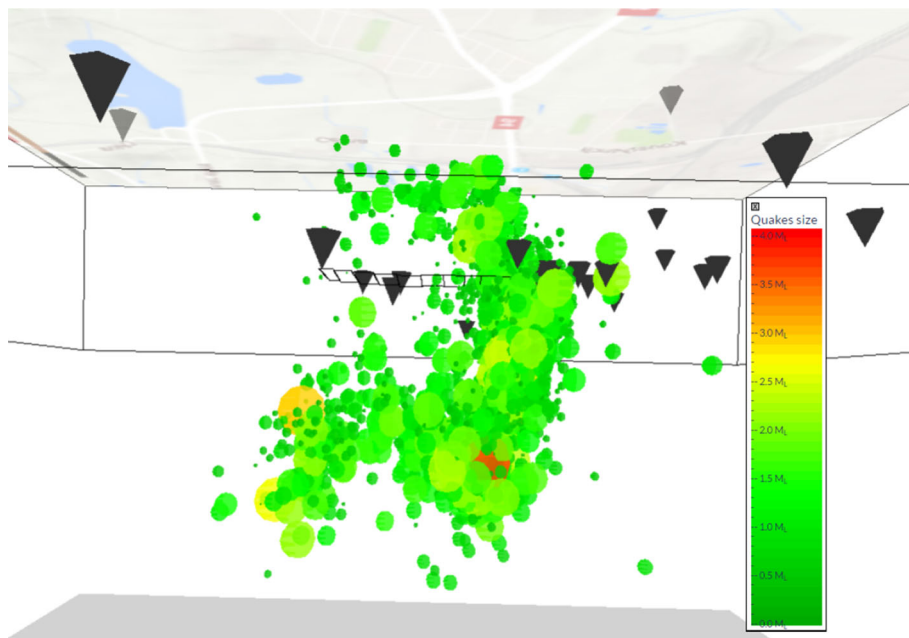


Fig. 4 Seismic activity plot. *Blue bars* show the number of events per 2 weeks. *Black line* is cumulative number of events. *Red lines* represent the date of mining front localization

with parameter $\beta = \ln 10 \cdot b$, where b stands for the well-known G–R b -value, which is estimated by the well-known Aki (1965) maximum likelihood estimator as:

$$b = \frac{1}{\ln(10)[\langle M \rangle - (M_{\min} - \Delta M/2)]}, \tag{4}$$

where $\langle M \rangle$ is the sample mean of the considered events. The introduction of term $\Delta M/2$ accounts for a correction for the finite binning width of the catalog, ΔM (Utsu 1966; Bender 1983), which is equal to the minimum non-zero difference among data. The corresponding Cumulative Distribution Function (CDF) of (3) is:

$$F(M) = \begin{cases} 1 - e^{-\beta(M - M_{\min} + \Delta M/2)} & \text{for } M \geq M_{\min}, \\ 0 & \text{otherwise} \end{cases} \tag{5}$$

Truncated GR law (GRT)

The assumption on the upper-bounded Gutenberg–Richter relation leads to the upper truncated exponential model of distribution for events with magnitude above the catalog completeness level M_{\min} . The PDF of magnitudes is given as (Page 1968; Kijko and Sellevoll 1989, also for b -value evaluation):

$$F(M) = \begin{cases} \frac{\beta e^{-\beta(M - M_{\min} + \Delta M/2)}}{1 - e^{-\beta(M_{\max} - M_{\min} + \Delta M/2)}} & \text{for } M_{\min} \leq M \leq M_{\max}, \\ 0 & \text{otherwise} \end{cases} \tag{6}$$

With β and $\Delta M/2$ as explained in Eqs. (3) and (4). The corresponding CDF of (6) is:

$$F(M) = 1 \begin{cases} 0 & \text{for } M < M_{\min} \\ \frac{1 - e^{-\beta(M - M_{\min} + \Delta M/2)}}{1 - e^{-\beta(M_{\max} - M_{\min} + \Delta M/2)}} & \text{for } M_{\min} \leq M \leq M_{\max} \\ 1 & \text{for } M > M_{\max} \end{cases} \tag{7}$$

Non-parametric approaches (NPU and NPT)

The kernel estimator approach proposed by Kijko et al. (2001) is a non-parametric (model free or data driven) alternative for estimating the magnitude distribution functions. This non-parametric approach is based on the kernel density estimator that totals the symmetric probability densities (kernels), individually associated with data points as (Parzen 1962; Silverman 1986):

$$\hat{f}_M(M|\{M_i\}, h) = \frac{1}{nh} \sum_{i=1}^n K\left(\frac{M - M_i}{h}\right) \quad (8)$$

where h is a non negative smoothing parameter (bandwidth), M_i are the magnitudes and $K(x)$ is a kernel function. The Kernel estimations chosen here for probability density (9) and cumulative distribution (10) have the forms of those adopted by Lasocki and Orlecka-Sikora (2008):

$$\hat{f}_M(M) = \frac{\sum_{i=1}^n \frac{1}{a_i h} e^{-\frac{1}{2} \left(\frac{M - M_i}{a_i h}\right)^2}}{(\sqrt{2\pi}) \sum_{i=1}^n \left[\Phi\left(\frac{M_{\max} - M_i}{a_i h}\right) - \Phi\left(\frac{M_{\min} - M_i}{a_i h}\right) \right]} \quad (9)$$

$$\hat{F}_M(M) = \frac{\sum_{i=1}^n \left[\Phi\left(\frac{M - M_i}{a_i h}\right) - \Phi\left(\frac{M_{\min} - M_i}{a_i h}\right) \right]}{\sum_{i=1}^n \left[\Phi\left(\frac{M_{\max} - M_i}{a_i h}\right) - \Phi\left(\frac{M_{\min} - M_i}{a_i h}\right) \right]}, \quad (10)$$

where n is the sample size, $\Phi(x)$ is the standard Gaussian cumulative distribution, a_i ($i = 1, 2, \dots, n$) are the local bandwidth factors and m_i , are the magnitudes with $M_{\min} \leq M \leq M_{\max}$. Note that M_{\min} is equal to the completeness threshold of a given catalog. It is assumed that the magnitude distribution is unlimited from the right hand side (i.e., infinite maximum magnitude). The shape of the kernel estimates depends primarily on the value of h . From the point of view of the use of estimators (9), (10) in the hazard analysis, a global, integrant agreement between the actual density and its estimates is of the utmost importance. Therefore, we select the smoothing factor applying the least squares cross-validation technique that requires minimizing the integral of the squared difference between the actual density, $f(\xi)$, and the estimate (e.g. Bowman et al. 1984):

$$\hat{f}(\xi) = \int_{-\infty}^{\infty} [\hat{f}(\xi) - f(\xi)]^2 d\xi \quad (11)$$

It has been shown (Kijko et al. 2001) that in the case of the Gaussian kernel this criterion is fulfilled if h is the root of the equation:

$$\sum_{i,j} \left\{ \left[\frac{(M_i - M_j)^2}{2h^2} - 1 \right] \exp\left[-\frac{(M_i - M_j)^2}{4h^2} \right] - 2 \left[\frac{(M_i - M_j)^2}{h^2} - 1 \right] \exp\left[-\frac{(M_i - M_j)^2}{2h^2} \right] \right\} = 2n \quad (12)$$

The local bandwidth factors, $\{\alpha_i\}$ can modify the width of the kernels at certain data points. Due to the fact, that the most important for the hazard analysis range of magnitudes, is that of the larger values, where the data are very sparse, the present version of the estimators uses the bandwidth factors that widen the kernels associated with

data points from this range (Lasocki and Orlecka-Sikora 2008):

$$a_1 = \frac{1}{\left[\frac{\hat{f}(M_i|\{M_i\}, h)}{g} \right]^{1/2}}, \quad (13)$$

where \hat{f} , is the constant kernel estimator in the unbounded magnitude range, and

$$g = \left[\prod_{i=1}^n \hat{f}(M_i|\{M_i\}, h) \right]^{1/n} \quad (14)$$

is the geometric mean of all constant kernel estimates (Silverman 1986).

Parameter values defined

Mining tremors occurrence is strongly associated with the excavation operations and therefore, seismicity properties and hazard parameters are estimated as a function of time and front advance. For this purpose, only the fraction of events which satisfies predefined properties is considered for such calculations. These events are selected after applying the following constrains: The completeness magnitude of the catalog was identified by considering the stations distances from the focal areas and the signal to noise ratio (Mutke et al. 2016). In such way M_{\min} was set equal to 0.6. The margin along front strike (equal for both directions of the front strike) and distance along the front advance (equal for both in front of and behind the front) was set equal to 50 and 100 m, respectively, following Kozłowska (2013). Calculations were performed for overlapping time windows generated in three different modes: According the “time mode”, events included in subsequent 30-day time windows were considered, overlapping per 1 day. In this approach time windows of the same span are used for hazard parameter evolution estimation. In the “events mode”, the time windows are selected in such a way that they include equal number of events (also overlapping per one day) and therefore the parameter estimation errors are comparable in all the datasets. Finally, in the “front mode”, a subsequent time window starts at the time point when the front advance is moved from the position it was in the beginning of the previous time window, to a distance indicated by a predefined value. In this case, the time windows correspond to approximately equal material mass removal from the mine (those windows are also overlapping per 1 day). The parameters set for our analysis in those three modes were 30 days in the “time mode”, 80 events in the “event mode” and 50 meters in the “front mode”. Finally, the event magnitude for the mean return period and the exceedance probability evaluation was set to 3.0, equal to the second largest magnitude in the dataset.

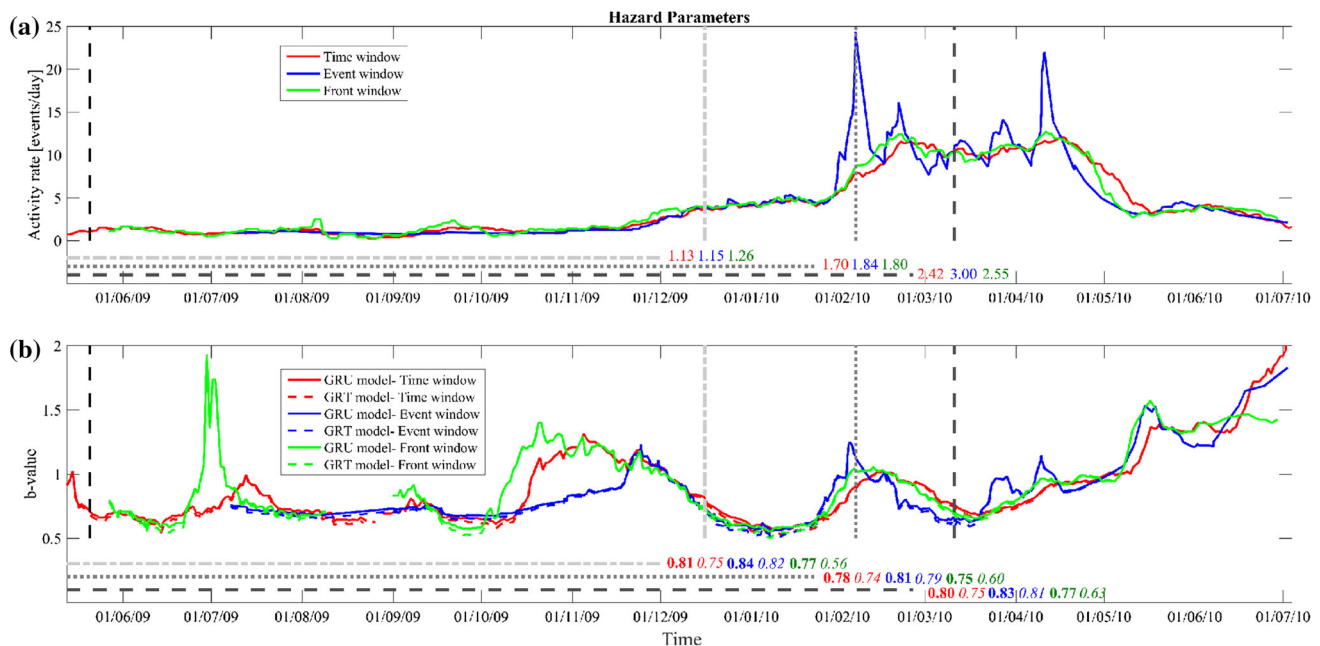


Fig. 5 Changes of seismic activity rate **(a)** and b -value **(b)** in time calculated using: time windows of 30 days, event windows of 80 events, front windows of 50 m (see text for details). Strong events are

plotted with gray dashed vertical lines. Gray horizontal lines indicate time periods chosen to calculate mean values of parameters (indicated by the numbers in colored fonts)

Results

We analyzed changes of seismic activity rate, b -value, return period of $M_L = 3.0$ and exceedance probability of $M_L = 3.0$ (within 30 days) as a function of time before the occurrence of strong events with $M_L \geq 2.8$ (Figs. 5, 6, 7). Four events with such magnitudes occurred in analyzed period of time (Table 1). In further analyses, we considered only events with IDs 2–4, because of the too short time period between the initiation of registrations and occurrence of the event with ID 1.

It can be observed that in the case of events (2) and (3) activity rate increases, although in different manner, before the occurrence of considered events (Fig. 5a). The opposite statement can be done for event (4), where for both time and front windows activity rate decreases before the event. However, slight increase shortly before the event is observable in the case of event window mode which due to the constant amount of events in each window is more sensitive in detecting sudden changes in occurrence rates. Additionally, it is worth mentioning that only the curve resulting from event windows shows a evident peak in activity rate before event (3). In the case of other windows the increase is slight.

Changes in b -values before the occurrence of strong events are also not completely consistent with each other. Before events (2) and (4) decrease of b -value can be observed. However, before the occurrence of event (3), b -value increases in the case of all window types. Again,

changes in the case of curve obtained using event window mode are the largest (Fig. 5b).

To describe quantitatively how distribution of hazard parameters changes before high magnitude events, we compared the last value of given parameter calculated before the occurrence of the event with the mean value of the same parameter calculated in time window from the beginning of observations to 14 days before considered event (Fig. 5). The time period of 14 days was chosen on the basis of observations of parameter changes before the big events (Fig. 5). The results reveal that seismic activity rate ratio is >1 for all events and window types, with a maximum value of 13.23 for event window for event (3) (Fig. 8a). b -value ratios of events (2) and (4) have generally values <1 , what is a result of b -value decrease before big events mentioned earlier, however, for the event (3) the ratio of b -values are highly above 1 (Fig. 8b).

The values of exceedance probability of $M_L = 3.0$ (within 30 days) and return period of $M_L = 3.0$ just before the occurrence of events (2), (3) and (4) are plotted in Fig. 9. It can be observed that exceedance probability values obtained using Gutenberg–Richter methods are much higher than those estimated with non-parametric kernel methods (Fig. 9). Only event windows used in kernel methods give significantly high probabilities in case of events (3) and (4). Additionally, the increase of exceedance probability calculated with kernel methods occurs just before high magnitude events (Fig. 6), which makes it difficult to use for prediction purposes. On the contrary,

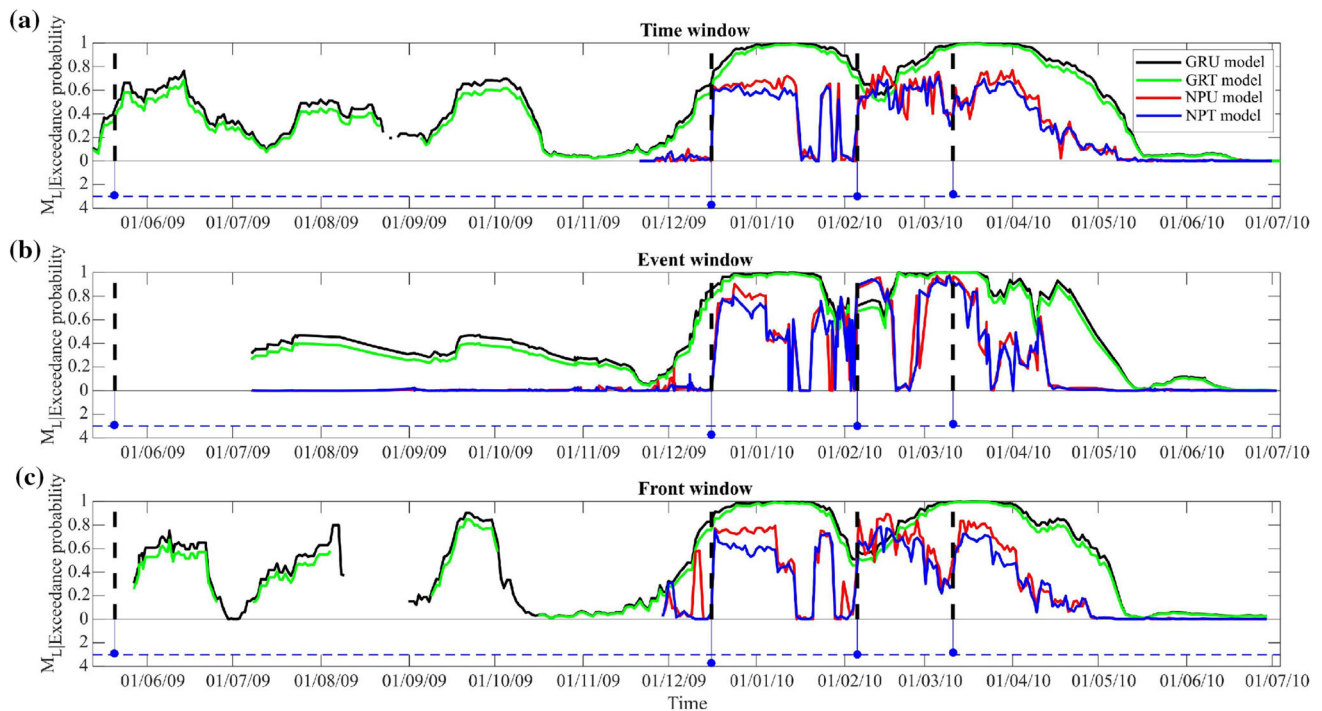


Fig. 6 Exceedance probability of $M_L = 3$ calculated using: time windows of 30 days (a), event windows of 80 events (b), front windows of 50 m (c)

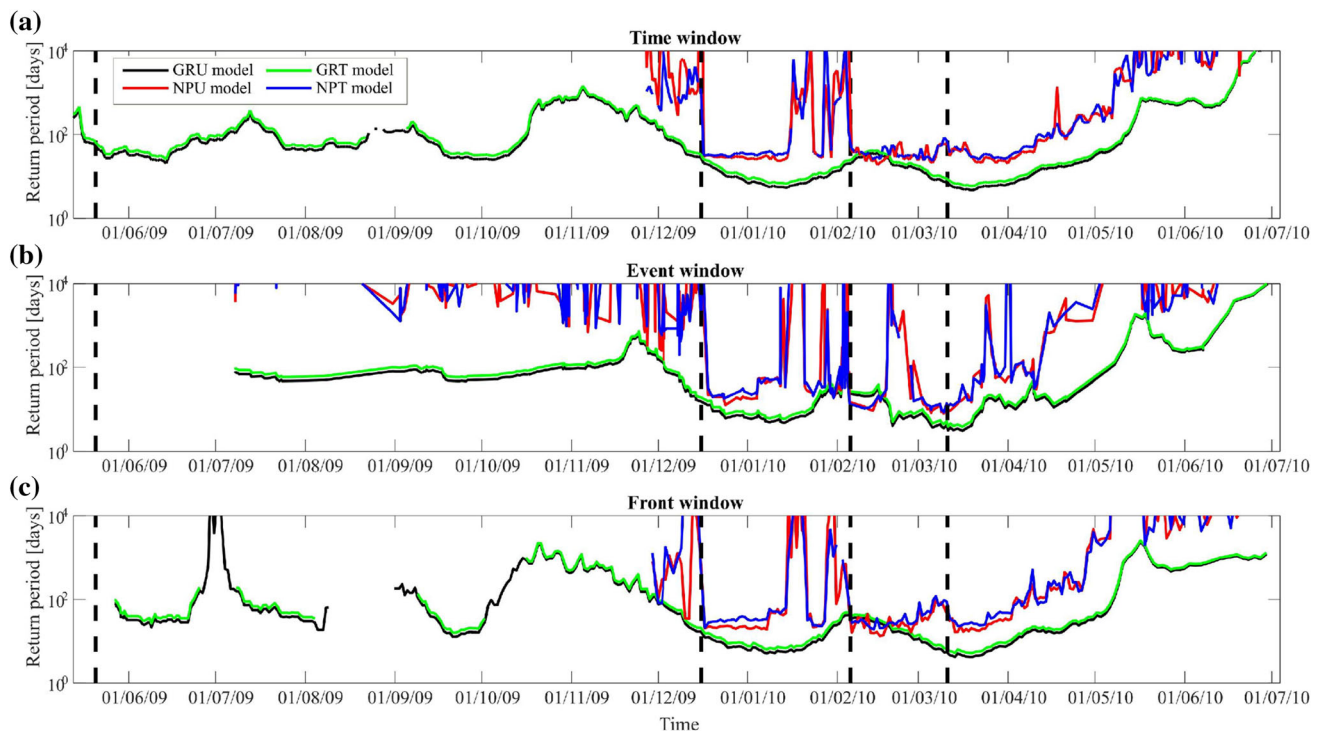


Fig. 7 Return period of $M_L = 3$ calculated using: time windows of 30 days (a), event windows of 80 events (b), front windows of 50 m (c)

changes of exceedance probability obtained using Gutenberg–Richter approaches are much more gradual, and thereby it is easier to follow the observed trend.

Return periods of $M_L = 3.0$ calculated with non-parametric kernel methods are comparable to those calculated with Gutenberg–Richter methods only in case of event (3)

(Fig. 10). In all other cases, the values of kernel estimations of return periods are much higher. It is worth mentioning that in the case of event (3), kernel-based return periods for event

windows are even lower than Gutenberg–Richter ones. In case of event (4), the lowest kernel return periods are also calculated on the basis of event windows (Fig. 10). These and previous observations can lead us to a conclusion that non-parametric kernel-based methods give compatible hazard results only if event window is used for calculations (i.e., meaning constant number of events in variable size window).

Previous analysis (Fig. 8, 9, 10) of parameters' changes before events (2), (3) and (4) leads us to the following conclusions concerning expectance of events on the basis of time-dependent hazard calculations. First, on the basis of temporal changes of activity rate, *b*-value, exceedance probability and return period, event (4) can be considered as the most expected one (activity rate increase, *b*-value decrease, high exceedance probability according to all methods, relatively short return period). Second, estimations of exceedance probability and return period with kernel-based methods do not give any possibility to predict the event (2) despite the fact that activity rate and *b*-value changes can suggest the occurrence of an impending strong event.

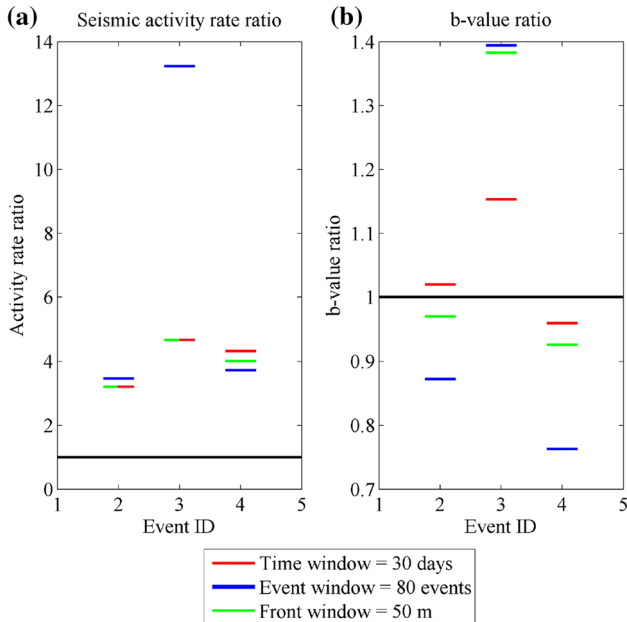


Fig. 8 Ratios of the last values of activity rate (a) and *b*-value (b) before events (2), (3) and (4) to the mean values of these parameters calculated in time periods marked in Fig. 5. Black solid lines indicate ratio value equal 1

Discussion and conclusions

The use of fundamental observational and empirical parameters such as activity rate and G–R *b*-value may prove to be helpful in evaluation of seismic hazard for

Fig. 9 Exceedance probability values before events (2), (3) and (4) calculated with unbounded Gutenberg–Richter (a), upper-bounded Gutenberg–Richter (b), unbounded kernel (c) and upper-bounded kernel (d) methods. Black solid lines indicate exceedance probability equal 0.5

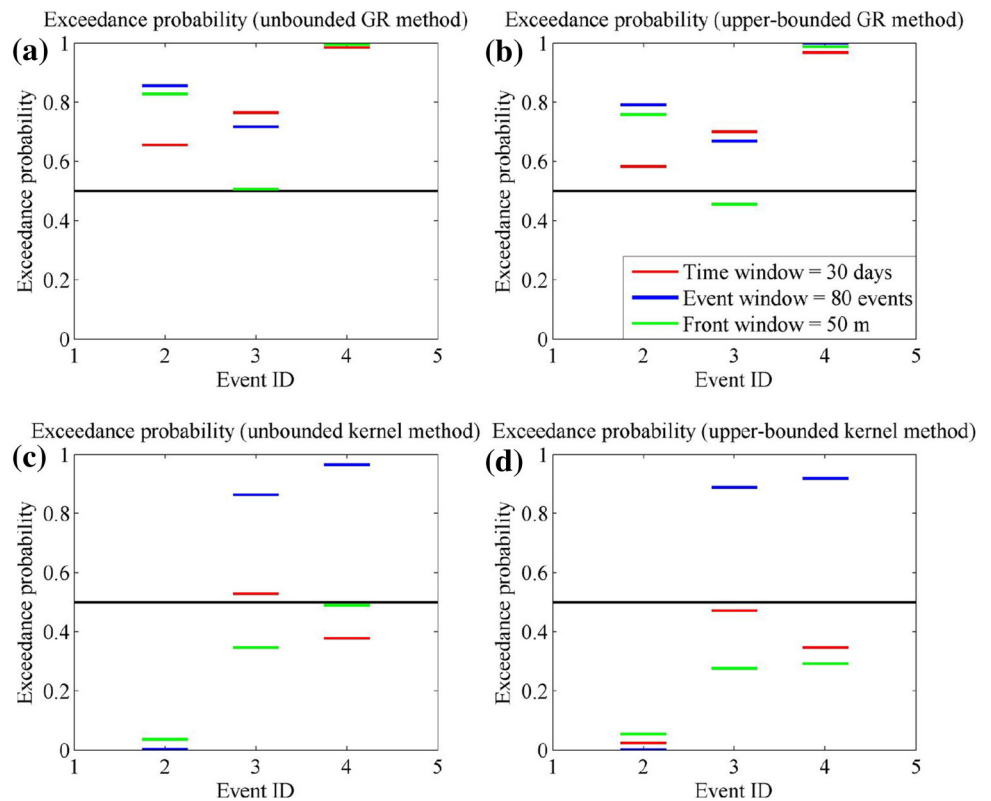
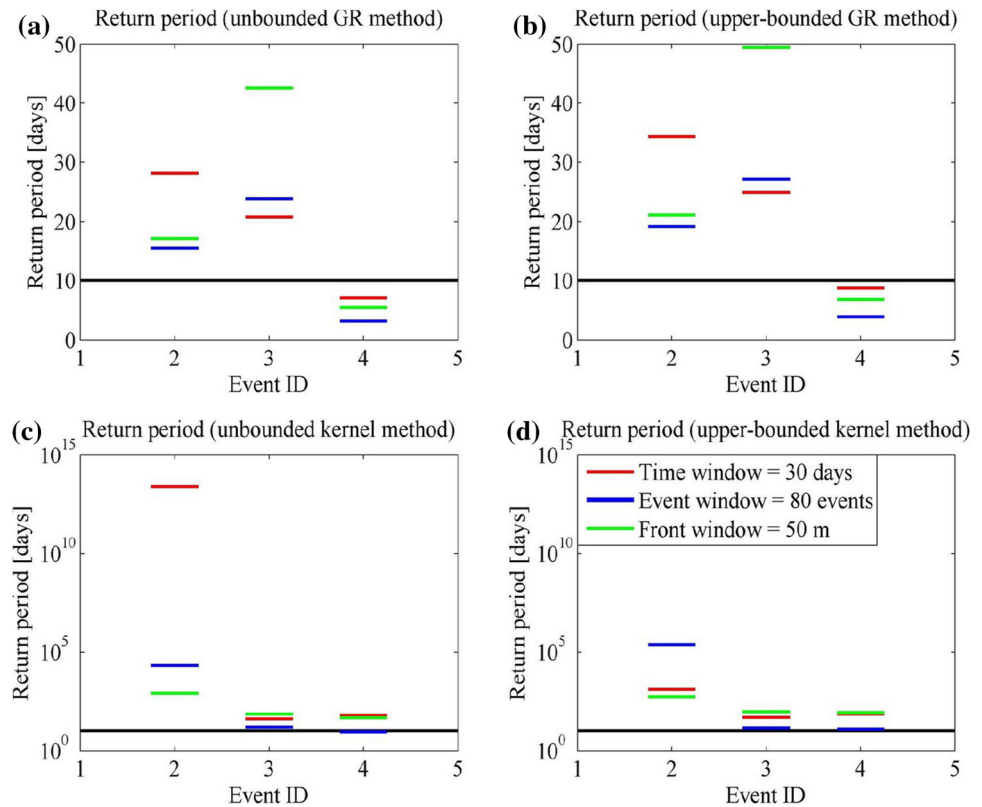


Fig. 10 Return period values before events (2), (3) and (4) calculated with unbounded Gutenberg–Richter (a), upper-bounded Gutenberg–Richter (b), unbounded kernel (c) and upper-bounded kernel (d) methods. *Black solid lines* indicate return period equal 10



specific study areas such as longwall mining. The G–R b -value has a clear physical interpretation, defining the relative proportion of the number of large events to small events. Anomalies in seismicity rates and b -value can be considered as an indicator of the stress state in rock mass (e.g., low b -values may indicate growing of stress, Scholz 1968). These anomalies are capable to lead to strong tremors and thus provide high seismic risk. Information of such kind can, therefore, be a premise for the decision to use specific measures to prevent bumps and adjust mining operations. Probability of the strong events occurring is higher when b -value is decreasing and simultaneously activity rate is increasing. In the present study, this case is clearly observed for events 2 and 4 for all window types (with the exception of b -value for event 2, which slightly increases when time window is considered). However, the activity rate is increased in all cases studied (Fig. 8a).

The need of introducing a non-parametric estimation for magnitude distribution arose from observed deviations of specific catalogs from G–R law in both natural and induced seismicity. Especially, induced seismicity exhibits diverse seismogenic processes in comparison with natural seismicity and it strongly depends on the human technological and production activities (Kijko et al. 1987; Trifu et al. 1993; Fritschen 2010; Maghsoudi et al. 2014). Two causes had been considered responsible for inconsistency of G–R law with the observed events distribution. The coupling

between tectonic stresses and mining activities in Bobrek mine has been studied by Marcak and Mutke (2013). Specifically for event 2, Kozłowska et al. (2016) showed that it was a tectonic event triggered by the ongoing exploitation and that the subsequent seismicity was a result of combined tectonic, coseismic and mining-induced stresses.

First, this inconsistency was attributed to the presence of broadly defined types of mining events (e.g., Gibowicz and Kijko 1994): events directly related to the mining operations and events resulting from the release of residual tectonic stresses accumulated in the rock mass. These two types of events are characterized by extensively different properties and features. Second, the non-linearity was attributed to the local geology and tectonics, i.e., heterogeneity and discontinuity of the rock structures with different thickness, strength, different in various parameters. For example, Naoi et al. (2014) showed that the distribution of magnitudes is consistent with the G–R relationship only when events closely linked to blasting are not taken into account.

As a result, magnitude distribution complexity may arise, characterized by number of modes or bumps in magnitude density. Evidences for the existence of multimodal earthquake size distribution were presented in many papers (e.g., Gibowicz and Kijko 1994; Gibowicz and Lasocki 2001; Lasocki and Orlecka-Sikora 2008).

Magnitude distribution may statistically significantly differ from the exponential distribution but the differences may be small (Urban et al. 2016). G–R model seems often inadequate to describe the earthquake size distribution.

To evaluate which estimation method would be more appropriate in our dataset, we performed statistical tests to examine the compatibility of earthquake size distribution with exponential distribution. First, we used Kolmogorov–Smirnov (K–S) goodness-of-fit one-sample test to check whether earthquake size distribution statistically differs from the exponential distribution. Details of this procedure and the corresponding findings in several cases of induced seismicity are described in the paper of Urban et al. (2016). Second, we examined the earthquake size distribution for its complexity using smoothed bootstrap test for multimodality. Multimodality test allows us to examine the presence of irregularities in the distribution of given magnitude values by demonstrating the presence of more than one mode or more than one bump in the probability density function (Lasocki and Papadimitriou 2006; Lasocki and Orlecka-Sikora 2008). These features indicate the presence and mixing of different processes generating the events.

To perform the multimodality and K–S tests, first the randomization of any observed magnitude has been done within the rounding error. Randomization of magnitude was carried out by transformation (Lasocki 2001; Lasocki and Papadimitriou 2006)

$$\hat{M} = F^{-1} \{u[F(M + 0.5\delta M) - F(M - 0.5\delta M)] + F(M - 0.5\delta M)\}, \quad (15)$$

where \hat{M} and M are randomized and observed magnitude values, respectively, Δ is accuracy of magnitude estimation, u is the value from uniform distribution $[0, 1]$, $F(\cdot)$ is magnitude CDF, and $F^{-1}(\cdot)$ is its inverse function.

In the K–S test case, we test the null hypothesis H_0 : the distribution of magnitude is exponential. To verify H_0 , we estimate p values and compare them with the adopted significance level $\alpha = 0.05$. A small p value suggests that the null hypothesis may be false. In the test for multimodality case, we test two null hypotheses: H_0^1 : density function of earthquake size distribution has no more than 1 mode; H_0^2 : density function of earthquake size distribution has no more than 1 bump. Due to the fact that the magnitude randomization gives slightly different p -values and significances of the considered null hypotheses, we assumed as a final value its mean value (from 1000 magnitude randomized catalogs) considering their standard deviation as well.

The results from K to S test strongly suggest that earthquake size distribution is not exponential with mean

p equal to 4.6×10^{-7} and standard deviation equal 3.9×10^{-7} . Because we estimate G–R b -value from the sample it requires calculation of additional statistics (D_m) (Urban et al. 2016). The value of the (D_m) is 2.82 which confirms previous results with the significance at least equal to 0.01.

The mean significance of considered null hypotheses from test for multimodality is 0.11 for H_0^1 with standard deviation equal 0.02 and 0.04 for H_0^2 with standard deviation equal 0.02. The results indicated that with 89–96% probability magnitude distribution is more complex than linear model.

Based on the results of K–S test and smoothed bootstrap test for multimodality, the non-parametric method for estimate of hazard parameters would be more appropriate. On the other hand, non-parametric technique starts to be effective for sample sizes starting from 200 events (Kijko et al. 2001). However, the hazard analysis performed in the present study considers time windows which contain diverse and mainly smaller number of events. Taking into account the size of the dataset we may conclude that segmentally, the G–R model is a good approximation for this type of analysis, providing also more comprehensive and stable results.

As a summary, we conclude to the following points:

- The obtained results strongly depend on the data number contained in the analyzed windows. According to that, event window approach may be preferable because it leads to identical or at least comparable uncertainties of the estimated parameters (equal size data samples are tested—see “Appendix A”).
- Unbounded and upper-bounded GR approaches lead to similar results (see also “Appendix A”). In the same way, unbounded and upper-bounded non-parametric methods also lead to similar results. On the other hand, there are distinct differences between parametric and non-parametric estimation techniques.
- Kernel-based methods exhibit sharp fluctuations of estimated parameter values, which are essentially, not practical in terms of prediction implications for datasets of such size. However, they seem to provide consistent results when event windows are considered.
- On the basis of all methods’ results, the last event (4) can be considered as the most expected one. It should be noted that there are several other windows for which exceedance probability is practically 1, when the G–R approaches are considered.
- The analysis of the catalog as a whole strongly indicates that earthquake size distribution does not obey G–R relation. However, smaller datasets in the analyzed windows show that G–R relation is an adequate approximation providing more stable results.

Acknowledgements The authors would like to thank Stanisław Lasocki for his valuable comments regarding methodological issues. The comments and suggestions of two anonymous reviewers were much appreciated. This work was supported within statutory activities No3841/E-41/S/2016 of Ministry of Science and Higher Education of Poland. This work was accomplished in the framework of IS-EPOS: Digital Research Space of Induced Seismicity for EPOS Purposes project, funded by the National Centre for Research and Development in the Operational Program Innovative Economy in the years 2013–2015 and EPOS Implementation Phase project funded from the Horizon 2020—Research and Innovation Framework Programme, call H2020—INFRADEV-1-2015-1 in the years 2015–2019. All calculations and some of the figures were made into the IS-EPOS web-platform for anthropogenic seismicity research available at <https://tcs.ah-epos.eu/>.

Open Access This article is distributed under the terms of the Creative Commons Attribution 4.0 International License (<http://creativecommons.org/licenses/by/4.0/>), which permits unrestricted use, distribution, and reproduction in any medium, provided you give appropriate credit to the original author(s) and the source, provide a link to the Creative Commons license, and indicate if changes were made.

Appendix A

b-Values uncertainties

The *b*-values together with their uncertainties are demonstrated in this appendix (Fig. 11). Unbounded and upper

bounded G–R model provide identical results in the vast majority of cases. The upper and lower bounds in the figure correspond to one standard deviation of the Aki's maximum likelihood estimation, given by:

$$\sigma_b = \frac{b}{\sqrt{N}} \quad (\text{A1})$$

where, N , is the sample size. It is shown that these boundaries are almost constant in the event window case (middle frame) but they exhibit significant fluctuations in the other two cases (time window and front window).

Apparently, it is impossible to provide a straightforward comparison regarding the efficiency of each window selection method, since there is no direct correspondence among those windows (each method produces unique windows with different time range and data included). However, we may draw some conclusions concerning the average behavior of these methods. As illustrated in Figs. 12 and 13, in both variations of Gutenberg–Richter law, the event window method leads to the smallest errors in comparison with the time and front windows. Almost two-thirds of the error values when event window is considered are below 0.1 and the maximum error values do not exceed 0.2. Time and front windows on the other hand reproduce larger error values (both average and maximum error values).

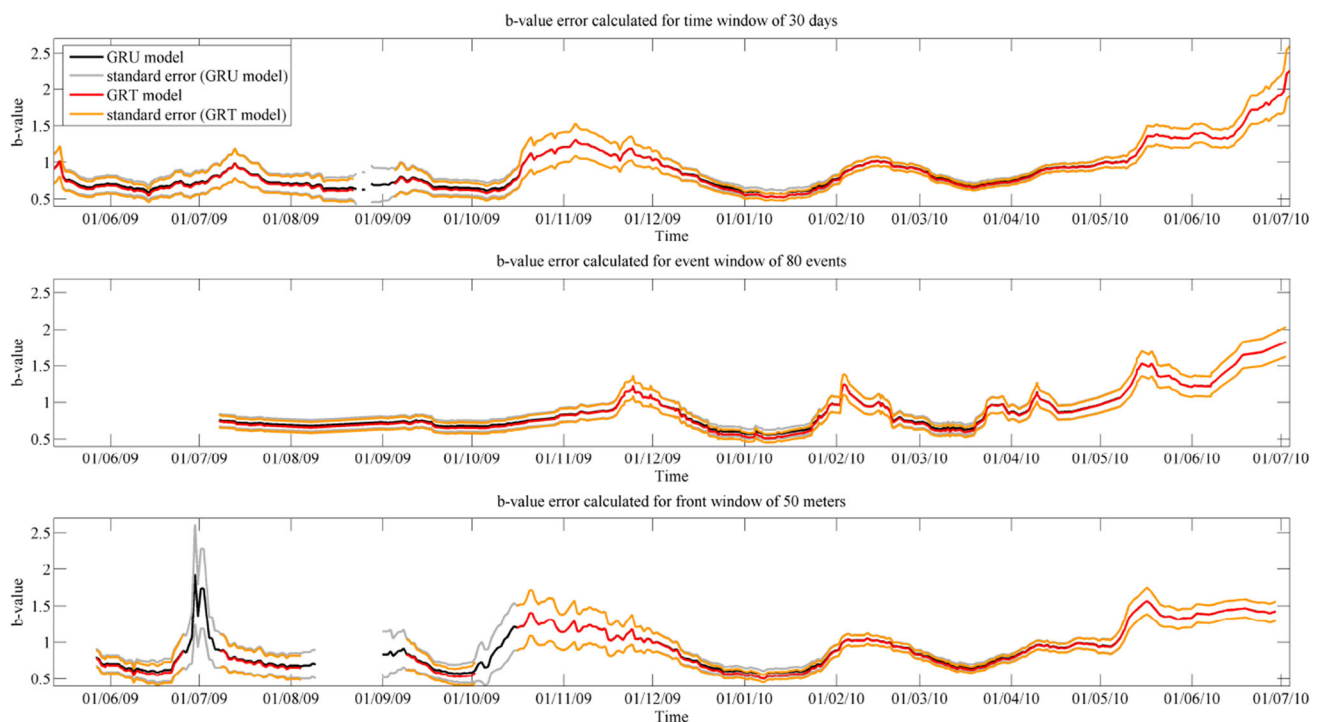


Fig. 11 *b*-values estimated by the unbounded Gutenberg–Richter (black curve) and upper-bounded Gutenberg–Richter (red curve), together with their respective standard errors (gray and yellow curves,

respectively) for all datasets corresponding to time windows (upper frame), event windows (middle frame) and front windows (lower frame)

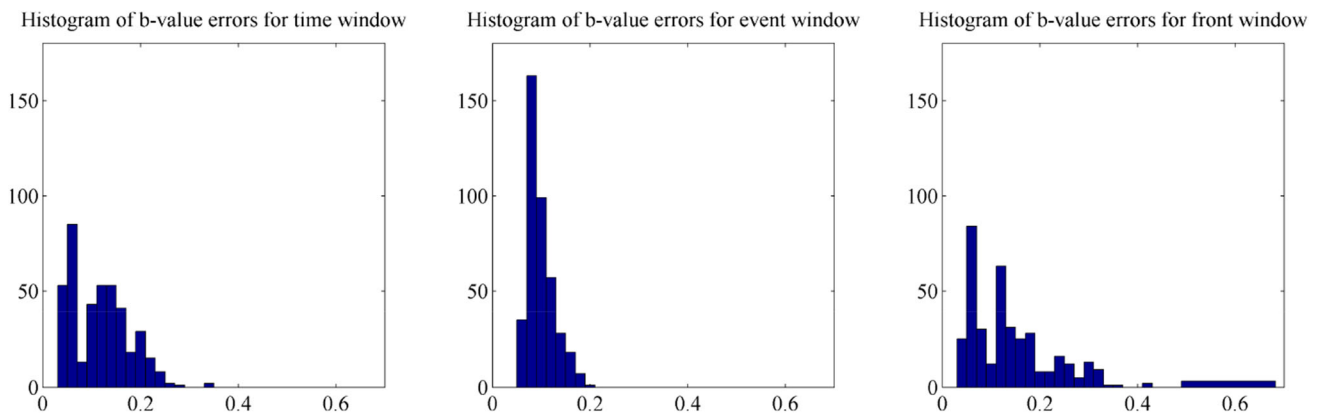


Fig. 12 Histograms with b -value standard errors for the 3 methods of window selection, assuming the unbounded Gutenberg–Richter approach

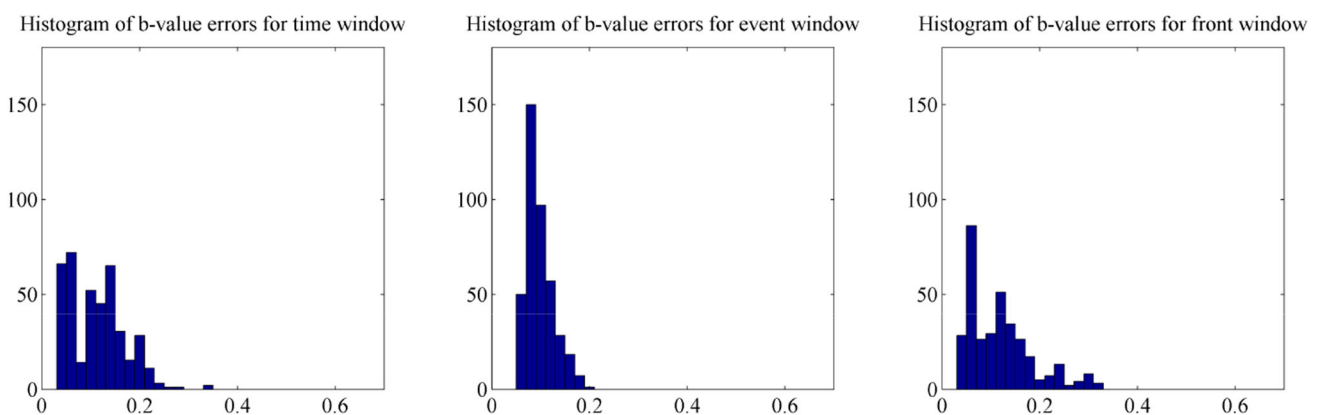


Fig. 13 Histograms with b -value standard errors for the 3 methods of window selection, assuming the upper-bounded Gutenberg–Richter approach

Following these results we may conclude that although the number of the events determines the individual estimation accuracy for each data set, the constant event window is in general more accurate in calculation of b -values and consequently of hazard parameters. This is also valid for the non-parametric (purely data driven) approaches which are even more sensitive to the sample size. In addition, constant event approach not only ensures a lower average error, but also a comparable error in all windows created, since all datasets exhibit exactly the same sample size.

Appendix B

TCS-AH web platform (<https://tcs.ah-epos.eu/>)

The IS-EPOS IT-platform is an open virtual access point for researchers studying anthropogenic seismicity and related hazards into European Plate Observing System—Anthropogenic Hazards Thematic Core Services (EPOS

AH-TCS). IS-EPOS platform constitutes a digital research space for providing a permanent and reliable access to advanced Research Infrastructures (RI) to the Induced Seismicity (IS) Community. This objective is implemented as a prototype which offers access to various datasets related to selected anthropogenic seismicity cases, specialized software for elementary and advanced data analysis and document repository. The relevant seismic and non-seismic data are gathered in the so-called episodes of induced seismicity. The IS-EPOS platform integrates presently seven episodes of anthropogenic seismicity respectively linked to underground hard rock and coal mining in Poland, shale gas extraction in UK, hydroelectric energy production (Poland and Vietnam) and geothermal energy production experiment in Germany. The researcher accessing the platform can make use of low level software services for data browsing, selecting and visualizing and a number of high level services for advanced data processing out of which the probabilistic seismic analysis service group is particular rich. The IS-EPOS platform is a working prototype of AH-TCS belonging to pan-European

multidisciplinary research platform created within EPOS long term plan for integration of national and transnational research infrastructures for solid earth science in Europe. Platform is available for registered users for free (<https://tcs.ah-epos.eu>). For purpose of this work two services were used: Time-Dependent Seismic Hazard (in mining front surroundings) and Time-Dependent Seismic Hazard (in mining a selected area). The episodes data, access to services and document repository and come of the source codes are available for registered users.

References

- Aki K (1965) Maximum likelihood estimate of b in the formula $\log N = a - bM$ and its confidence limits. *Bull Earthq Res Inst Tokyo Univ* 43:237–239
- Bender B (1983) Maximum likelihood estimation of b -values for magnitude grouped data. *Bull Seismol Soc Am* 73:831–851
- Bowman AW, Hall P, Titterton DM (1984) Cross-validation in non-parametric estimation of probabilities and probability densities. *Biometrika* 71:341–351
- Convertito V, Maercklin N, Sharma N, Zollo A (2012) From induced seismicity to time-dependent seismic hazard. *Bull Seismol Soc Am* 102:2563–2573
- Cornell AC (1968) Engineering seismic risk analysis. *Bull Seismol Soc Am* 58:1583–1606
- Davis R, Foulger G, Bindley A, Styles P (2013) Induced seismicity and hydraulic fracturing for the recovery of hydrocarbons. *Mar Petrol Geol* 45:171–185
- Fritschen R (2010) Mining-induced seismicity in the Saarland, Germany. *Pure Appl Geophys* 167:77–89
- Gibowicz S (2009) Seismicity induced by mining: recent research. *Adv Geophys* 51:1–53
- Gibowicz SJ, Kijko A (1994) An introduction to mining seismology. Academic Press, San Diego
- Gibowicz SJ, Lasocki S (2001) Seismicity induced by mining: ten years later. *Adv Geophys* 44:39–181
- Kijko A (2004) Estimation of the maximum earthquake magnitude, m_{max} . *Pure Appl Geophys* 161:1655–1681. doi:10.1007/s00024-004-2531-4
- Kijko A, Sellevoll MA (1989) Estimation of earthquake hazard parameters from incomplete data files. Part I. Utilization of extreme and complete catalogs with different threshold magnitudes. *Bull Seismol Soc Am* 79:645–654
- Kijko A, Drzezla B, Stankiewicz T (1987) Bimodal character of the distribution of extreme seismic events in Polish mines. *Acta Geophys Pol* 35:157–166
- Kijko A, Lasocki S, Graham G (2001) Nonparametric seismic hazard analysis in mines. *Pure Appl Geophys* 158:1655–1676
- Kozłowska M (2013) Analysis of spatial distribution of mining tremors occurring in rudna copper mine (Poland). *Acta Geophys* 61:1156–1169
- Kozłowska M, Orlecka-Sikora B, Rudziński Ł, Cielesta S, Mutke G (2016) Atypical evolution of seismicity patterns resulting from the coupled natural, human-induced and coseismic stresses in a longwall coal mining environment. *Int J Rock Mech Min Sci* 68:5–15
- Lasocki S (2001) Quantitative evidences of complexity of magnitude distribution in mining-induced seismicity: Implications for hazard evaluation. In: van Aswegen G, Durrheim RJ, Ortlepp WD (eds), Proceedings of the fifth international symposium on rockbursts and seismicity in mines (RaSiM 5) ‘Dynamic rock mass response to mining’. South African Institute of Mining and Metallurgy, Johannesburg, 543–550
- Lasocki S, Orlecka-Sikora B (2008) Seismic hazard assessment under complex source size distribution of mining-induced seismicity. *Tectonophysics* 456:28–37
- Lasocki S, Papadimitriou EE (2006) Magnitude distribution complexity revealed from seismicity in Greece. *J Geophys Res.* doi:10.1029/2005JB003794
- Lasocki S, Urban P (2011) Bias, variance and computational properties of Kijko’s estimators of the upper limit of magnitude distribution, M_{max} . *Acta Geophys* 59:659–673
- Li T, Cai MF, Cai M (2007) A review of mining-induced seismicity in China. *Int J Rock Mech Min* 44:1149–1171
- Maghsoudi S, Hainzl S, Cesca S, Dahm T, Kaiser D (2014) Identification and characterization of growing large-scale enechelon fractures in a salt mine. *Geophys J Int* 196:1092–1105. doi:10.1093/gji/ggt443
- Marcak H, Mutke G (2013) Seismic activation of tectonic stresses by mining. *J Seismol* 17:1139–1148
- Mutke G, Pierzyna A, Barański A (2016) b -Value as a criterion for the evaluation of rockburst hazard in coal mines. In: Mitri HS, Shnorhokian S, Kumral MK, Sasmito A, Sainoki A (eds), Proceedings of 3rd international symposium on mine safety, science and engineering, August 13–19 2016, Montreal, Canada, 1–5
- Naoi M, Nakatani M, Horiuchi S, Yabe Y, Philipp J, Kgarume T, Morema G, Khambule S, Masakale T, Ribeiro L, Miyakawa K, Watanabe A, Otsuki K, Moriya H, Murakami O, Kawakata H, Yoshimitsu N, Ward A, Durrheim R, Ogasawara H (2014) Frequency-magnitude distribution of $-3.7 \leq M_W \leq 1$ mining-induced earthquakes around a mining front and b value invariance with post-blast time. *Pure Appl Geophys* 171:2665–2684. doi:10.1007/s00024-013-0721-7
- Page R (1968) Aftershocks and microaftershocks. *Bull Seismol Soc Am* 58:1131–1168
- Parzen E (1962) On estimation of a probability density function and mode. *Ann Math Stat* 33:1065–1076
- Robson DS, Whitlock JH (1964) Estimation of a truncation point. *Biometrika* 51(1–2):33–39. doi:10.1093/biomet/51.1-2.33
- Scholz C (1968) The frequency-magnitude relation of microfracturing in rock and its relation to earthquakes. *Bull Seism Soc Am* 58:399–415
- Silverman BW (1986) Density estimation for statistic and data analysis. Chapman and Hall, London, p 175
- Stec K (2007) Characteristics of seismic activity of the Upper Silesian Coal Basin in Poland. *Geophys J Int* 168(2):757–768
- Trifu CI, Urbancic TI, Young RP (1993) Non-similar frequency-magnitude distribution for $m < 1$ seismicity. *Geophys Res Lett* 20:427–430
- Urban P, Lasocki S, Blascheck P, do Nascimento AF, Giang NV, Kwiatek G (2016) Violations of Gutenberg–Richter in anthropogenic seismicity. *Pure Appl Geophys* 173:1517–1537
- Utsu T (1966) A statistical significance test of the difference in b -value between two earthquake groups. *J Phys Earth* 14:37–40
- Utsu T (1999) Representation and analysis of the earthquake size distribution: a historical review and some new approaches. *Pure Appl Geophys* 155:509–535

Non-stationarity and internal correlations of the occurrence process of mining-induced seismic events

Dorota Olszewska¹  · Stanislaw Lasocki¹ · Konstantinos Leptokarpoulos¹

Received: 2 January 2017 / Accepted: 1 March 2017 / Published online: 17 March 2017

© Institute of Geophysics, Polish Academy of Sciences & Polish Academy of Sciences 2017. This article is an open access publication

Abstract A point process, e.g., the seismic process, is potentially predictable when it is non-stationary, internally correlated or both. In this paper, an analysis of the occurrence process of mining-induced seismic events from Rudna copper mine in Poland is presented. Stationarity and internal correlation are investigated in complete seismic time series and segmentally in subseries demonstrating relatively stable seismicity rates. It is shown that the complete seismic series are non-stationary; however, most of their shorter subseries become stationary. In the stationary subseries, the distribution of interevent time is closer to the exponential distribution, which is characteristic for the Poisson process. However, in most of these subseries, the differences between the interevent time and Poisson distributions are still significant, revealing correlations among seismic events.

Keywords Stationary seismic process · Mining-induced seismicity · Internal correlations

Introduction

Among the various types of natural hazards, earthquakes constitute a phenomenon responsible for numerous casualties and huge socio-economic impact every year. The study of earthquakes has routinely been performed in two separate ways (e.g., Vere-Jones 2010): Physical modelling is based on the underlying physics of the seismogenic processes and accompanying effects, and stochastic

modelling. This latter family of models includes a vast number of statistical algorithms and methodologies applied in both natural (e.g., Gardner and Knopoff 1974; Kiremidijan and Anagnos 1984) and induced (Baecher and Keeney 1982; Lasocki 1992a, b; 1993) seismicity. Stochastic models are increasingly applied since the last decades because of the development and installation of extensive and efficient networks resulting to high-quality seismic data in many sites worldwide.

If a seismic process is to be predictable, then it must be either non-stationary or internally correlated or both, i.e., it cannot be fully random. Gardner and Knopoff (1974) analysed the earthquake catalog of South California after removing aftershocks. They found that whereas the original catalog was non-Poissonian, after aftershock removal through declustering, it became Poissonian. This means that the seismic process of main-shocks occurrence was a stationary Poisson process, whereas the aftershock generation was highly dependent on time as well as the aftershock occurrences were correlated (interrelated). This phenomenon is still investigated in global catalogs (e.g., Lombardi and Marzocchi 2007) or for local seismicity (e.g., Gkarlaouni et al. 2015).

The need for improving the accuracy of seismic hazard assessment increases the interest in earthquake occurrence models, which assume some kind of time-dependence. Undoubtedly, an increase of seismological data quality, both in terms of completeness level and focal parameter accuracy, helps investigating this feature. In the specific case of mining-induced seismicity, the time-variation of mining operations leads to the time variability of the occurrence process of seismic events. Thus, its dependence on time is expected and was already studied elsewhere (e.g., Lasocki 1992a; Kijko 1997). The variability in time of seismicity is also considered in many studies carried out

✉ Dorota Olszewska
dolszewska@igf.edu.pl

¹ Institute of Geophysics, Warsaw, Poland

for mining areas (e.g., Lasocki and Orlecka-Sikora 2008). Lasocki (1992a) showed that mining seismic events do not constitute a Poisson process. However, the seismicity rates change slowly in time and the seismic process can be considered as stationary for short time periods (~ 50 days).

In the present paper, we study in detail the time series of seismic events from a mine for investigating properties of the event occurrence process. The study mining area is the Legnica-Głogów Copper District (LGCD) in southern Poland, where approximately 3.5 thousand events above local magnitude 1.0 (completeness of catalog is 1.2) are annually recorded. Occasional strong events, which may result in rockbursts, are a combined effect of the mining operations, natural and human-induced stresses, and interaction among the seismic events. Therefore, the seismic process due to time-varying mining activity is non-stationary and irregular, so the dependent fraction of seismicity is hard to be identified and removed by generic declustering algorithms. For this reason, the seismic series from specified time-space clusters of seismicity (in certain zones defined by Orlecka-Sikora and Lasocki 2002) were chosen and their stationary parts were selected for internal correlation study. The results are complemented with an uncertainty analysis.

Methods and data used

Methods

Interevent times of a stationary Poisson occurrence process follow the exponential distribution. The corresponding cumulative distribution function is:

$$F(\tau) = 1 - \exp(-\lambda\tau), \quad (1)$$

where λ is the constant mean event rate of the process.

We study here the coefficient of randomness in one-dimensional space, ν (Matsumura 1984):

$$\nu = \frac{E[X]^2}{E[X^2]}, \quad (2)$$

where $E[X]$ is the first raw moment and $E[X^2]$ is the second raw moment of the interevent time distribution. For fully random occurrence process (a Poisson process), the ratio, ν equals:

$$\nu = \frac{\int_{-\infty}^{+\infty} \tau \exp(-\lambda\tau) d\tau}{\int_{-\infty}^{+\infty} \tau^2 \exp(-\lambda\tau) d\tau} = \frac{\left(\frac{1}{\lambda}\right)^2}{\left(\frac{2}{\lambda^2}\right)} = \frac{1}{2}. \quad (3)$$

The process is regular when ν is greater than 0.5 and clustered when ν is smaller than 0.5. In these cases, the interaction between events is present. In general, a repelling interaction leads to a regular pattern and attractive interaction leads to clustered pattern.

Confidence intervals of ν are assessed from estimates of this parameter from 1000 bootstrap replicas of the original data samples of interevent times. The limits of confidence intervals are evaluated as 5 and 95% percentiles. Thus, the analysis is performed on 95% confidence level.

The null hypothesis that the interevent time distribution is exponential is studied by means of the Anderson–Darling test (Stephens 1974). Its rejection indicates that the occurrence process is not a Poisson one.

The next estimated parameter is the Hurst exponent, H (Hurst 1951), based on the classical rescaled range (R/S) analysis (for a detailed description of the method, see Lomnitz 1994 and the references therein). When a process does not possess long memory (has independent increments), H equals 0.5. The process has long memory and is persistent, when H is greater than 0.5, and is anti-persistent when H is smaller than 0.5. This parameter has been used to analyse long memory of natural (e.g., Correig et al. 1997; Xu and Burton 2006; Gkarlaoui et al. 2017) and induced seismic processes (e.g., Węglarczyk and Lasocki 2009). Here, we investigate the long memory property in the interevent time series. The statistical significance of the estimate H is obtained, using the method from Węglarczyk and Lasocki (2009).

Table 1 Parameters of the analysed series of mining events

Event series	Time period of the series	Magnitude median and range	No. of events	Activity rate (event per month)
Z_20.1	04 Apr. 1985–05 Sep. 2004	1.6 [1.2–4.1]	1245	5.4
Z_23.1	12 Apr. 1980–23 Sep. 2004	1.7 [1.2–4.1]	1592	5.4
Z_26	20 Nov. 1984–16 Sep. 2004	1.6 [1.2–3.8]	2678	11.3
Z_27	19 Apr. 1986–22 Sep. 2004	1.6 [1.2–3.7]	2207	10.0
Z_28	28 Mar. 1988–19 Sep. 2004	1.6 [1.2–3.7]	620	3.1
Z_30.1	27 Apr. 1990–18 May 2002	1.7 [1.2–3.6]	817	5.7
Z_31	01 Jan. 1980–20 Oct. 1990	1.5 [1.2–3.5]	2664	20.6
Z_35	26 Nov. 1991–11 Sep. 2004	1.7 [1.2–3.7]	711	4.6

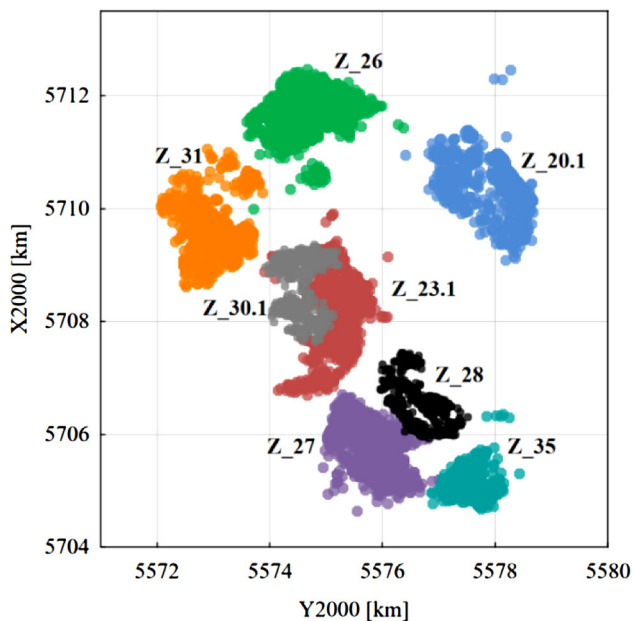


Fig. 1 Spatial distribution of the analysed clusters of mining events (both axes are in local coordinate system)

Data

The seismic catalog from 1984 up to 2004 of Rudna mine from Legnica Glogow Copper District (LGCD) of Poland was analysed. LGCD is a region in south-west of Poland where copper-ore is exploited from ore bearing layers at the depths between 900–1100 m. The underground mining in Rudna mine in the studied period induced 15.8 thousand of registered events from magnitude 0.9 up to 4.2, so there were about 800 events per year.

Seismicity induced by mining forms distinct space-time clusters or space-time zones (Orlecka-Sikora and Lasocki 2002). In this paper, the analysis was done for 8 such clusters, which had different activity rates, maximum magnitudes, locations, and occurrence time periods (see Table 1; Figs. 1 and 2).

Non-stationarity of the seismic event occurrence process

Anderson–Darling (A–D) test was performed to test the null hypothesis that the distribution of interevent time was exponential. This distribution was significantly different than the exponential distribution in all analysed event series; in all cases, the p values of the null hypothesis of A–D test are smaller than 5×10^{-4} . This indicates that the background seismic processes were not Poissonian.

Next, the coefficients of randomness, ν , were calculated and the Hurst exponents, H , were estimated for the analysed event series (Table 2). The coefficients of randomness are

smaller than 0.5 for all series at the significance level 0.95. The Hurst exponents for all cases are significantly greater than 0.5. However, these features as well as the misfit of the exponential distribution are most likely due to non-stationarity of the processes, which is clearly visible in Fig. 2.

To have a better insight into the process properties, we calculated the coefficients of randomness for the subseries formed by gradually removing smaller events from the initial event series. Figure 3 shows the changes of ν and the corresponding 90% confidence intervals as functions of the cut-off magnitude levels for the studied series. The minimum number of samples, for which ν were calculated, was set equal to 10 events. The coefficient of randomness tended to the value 0.5 when smaller events were removed. These results suggest that the process of generating stronger events is a stationary Poisson process or at least it is close to the Poisson process. Similar results and the same conclusion were presented by Lasocki (1992a). Such a ‘self-randomization’ of the series takes place for different cut-off magnitudes between 2.05 and 3.2. In two cases of Z_31 and Z_35 series, when the greatest cutoffs were applied, the coefficient of randomness became significantly greater than 0.5, suggesting a regular behavior of the subseries.

The next part of the study was to check the extent of non-randomness in the studied data sets. For this purpose, the coefficient of randomness was calculated in sliding data windows which were being moved over the initial data series. The lengths of the windows were 300, 200, 100, and 50 events, consecutively, and the windows were advanced of 10 events in the first three cases of the window lengths and of 5 events for 50-event windows. Figure 4 shows ν and 90% confidence intervals calculated in the aforementioned sliding windows for series Z_27 and Z_28, as examples. The interevent times for shorter subseries tended to follow the exponential distribution; the shorter subseries were, the more of them exhibited the Poisson process property. However, even for the shortest considered subseries of 50 events, some traces of clustered or regular behavior remained. This indicates that some parts of the analysed series were so strongly non-stationary that they still exposed this feature even in the shortest fragments of the initial series. One can see in Fig. 4 that the 50 element subseries exhibited a regular behavior when the activity rate was growing and a clustered behavior when the activity rate was considerably irregular.

Internal correlation of the tremors occurrence process

The stationarity of the event series is an essential prerequisite for the studies of internal correlations, which occur when data show internal dependency like stress transfer,

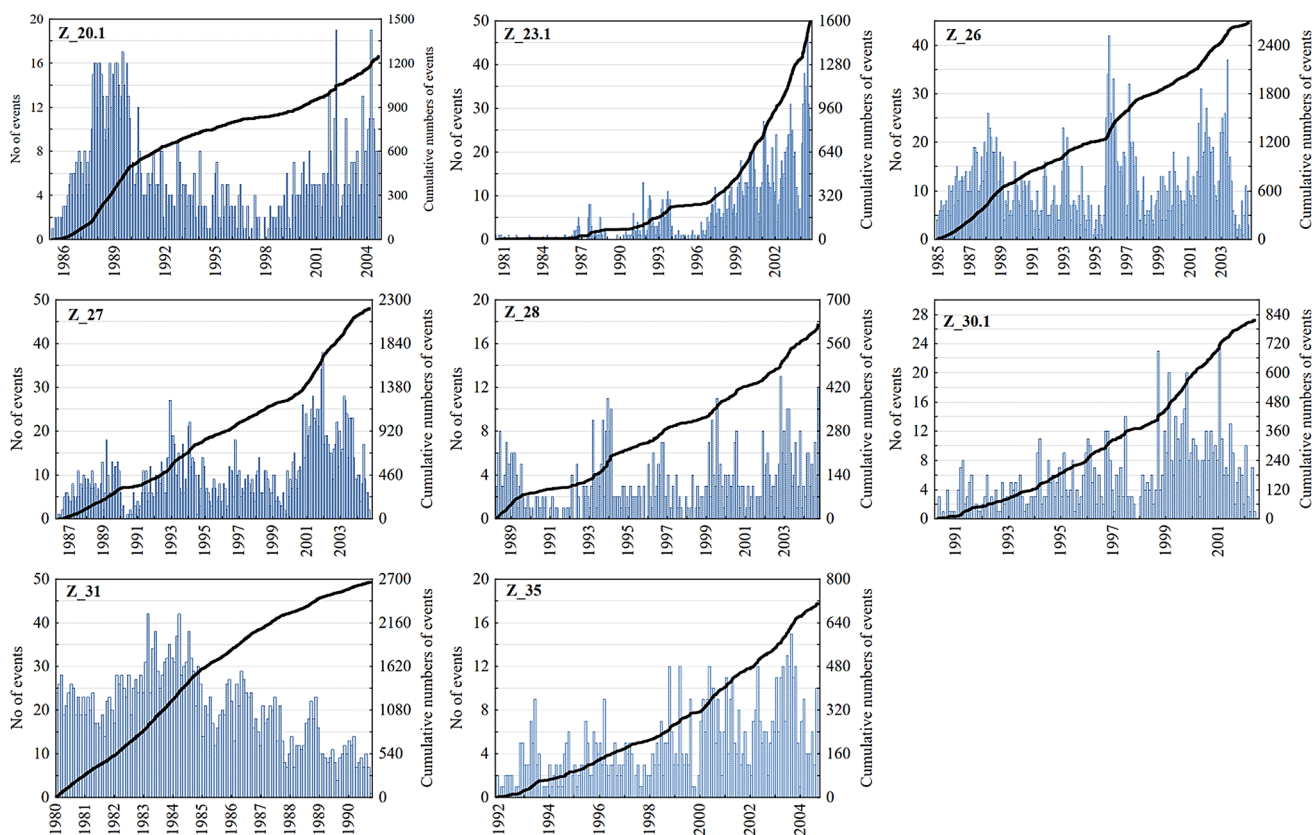


Fig. 2 Monthly activity rates (*bars*) and cumulative numbers of events (*solid black*) for the analysed event series

Table 2 Results of the analysis of the complete event series and the subseries created by removing smaller events

Event series	The coefficient of randomness ν and 90% confidence intervals	Estimates of Hurst coefficient (H)	The lowest left-hand side limit of magnitude range, in which the seismic process became a stationary Poisson process
Z_20.1	0.31 [0.27; 0.36]	0.81	2.75
Z_23.1	0.05 [0.04; 0.08]	0.77	3.05
Z_26	0.35 [0.31; 0.38]	0.77	2.95
Z_27	0.31 [0.27; 0.37]	0.73	3.20
Z_28	0.36 [0.33; 0.40]	0.83	2.55
Z_30.1	0.32 [0.28; 0.36]	0.72	2.05
Z_31	0.42 [0.37; 0.47]	0.62	2.65
Z_35	0.38 [0.35; 0.41]	0.68	2.30

The values of coefficient of randomness and Hurst exponent, which significantly deviate from 0.5, are in bold

seasonality, etc. Therefore, to get insight into internal correlations of the studied seismic processes, we had to extract stationary subseries from the clearly non-stationary initial series. First, to do this, we made use of the results of above presented analysis of Matsumura coefficient of randomness in sliding windows. We extracted those fragments, for which the coefficients of randomness in

consecutive windows did not deviate from the value 0.5 (under 90% confidence probability). The examples of such an extraction from series Z_27 and Z_28 are presented in Fig. 4 as light pink fields. The basic parameters of the extracted subseries are given in Table 3.

The value 0.5 of the coefficient of randomness indicates fully random, that is also stationary behavior; therefore, the

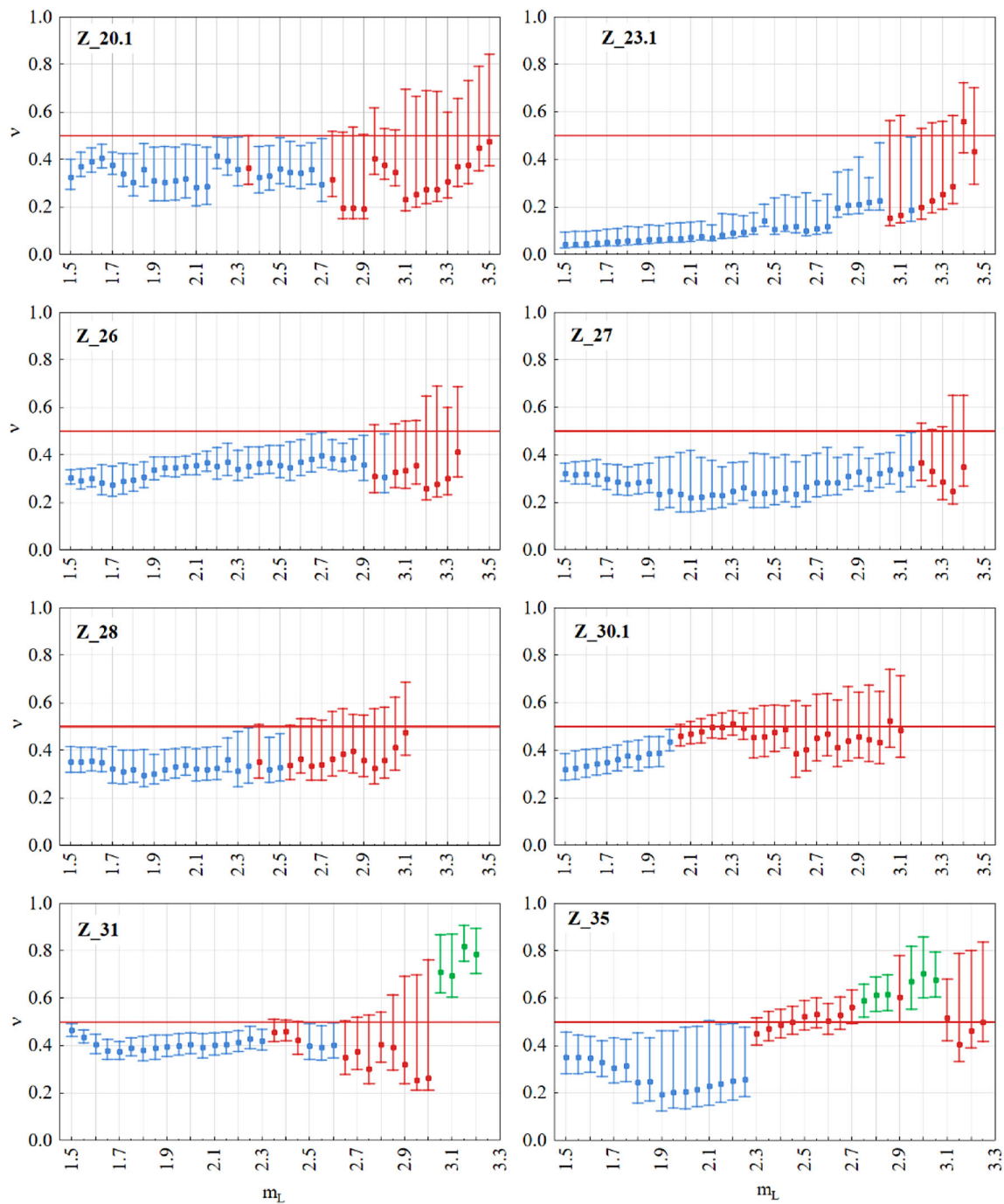


Fig. 3 Coefficient of randomness as a function of magnitude cut-off levels determining subseries of the initial event series. The vertical bars represent 90% confidence intervals of the coefficient and are in

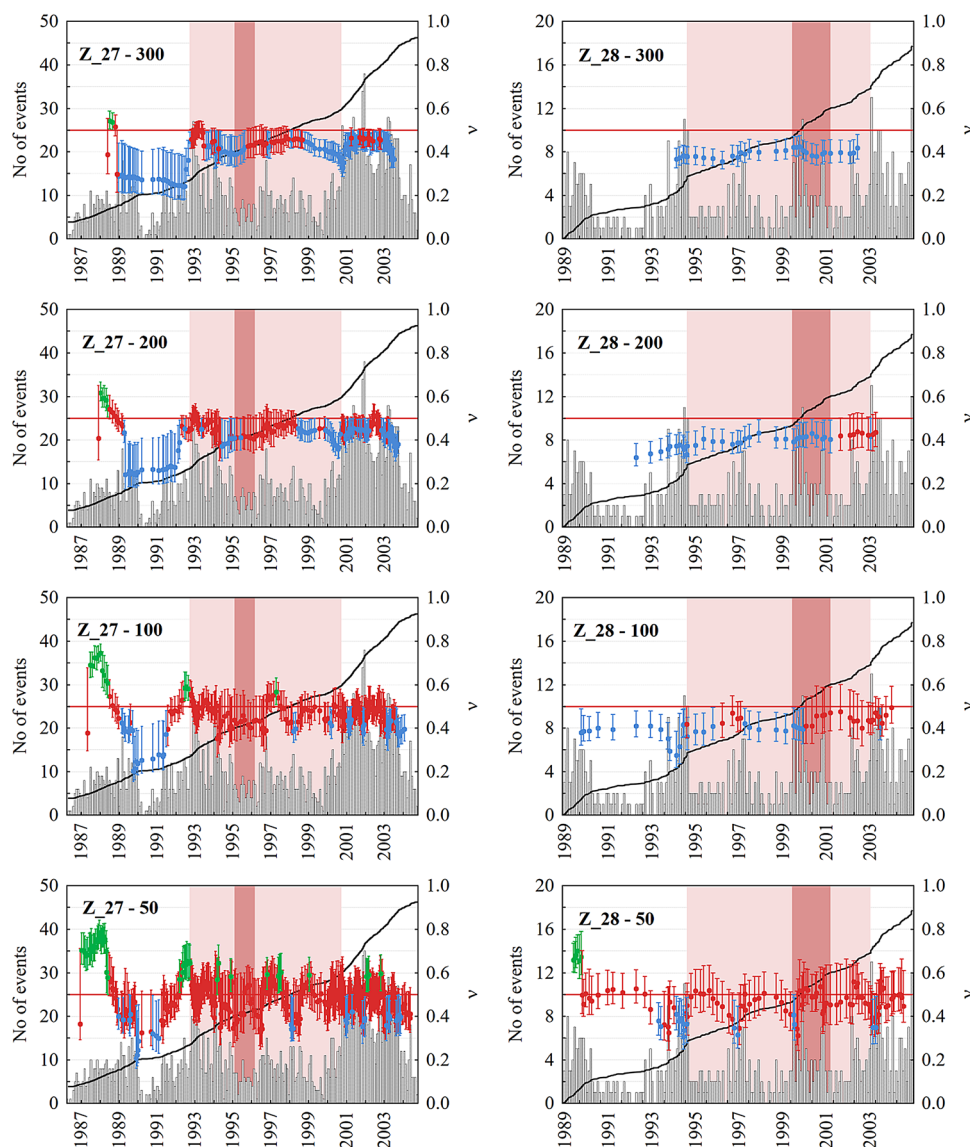
selected subseries were expected to be stationary. To confirm this conclusion, we tested the stationarity of the selected subseries by means of the Priestley–Subba Rao (PSR) test (Priestley and Subba Rao 1969). Contrary to the expectations, the test showed that the subseries were still non-stationary. The test p value for the null hypothesis of stationarity was in all cases less than 0.015. These results

blue for a clustered process, in red for a random process, and in green for a regular process

evidence that the Matsumura coefficient of randomness is not sufficient to indicate by itself randomness of an event series in a one-dimensional case.

In this connection, we continued the selection of stationary subseries. Now, as a possible candidate for the stationary subseries, we were taking that fragment of the initial series, for which the coefficient of randomness was

Fig. 4 Monthly activity rate of the event series Z_{27} and Z_{28} with coefficient of randomness for sliding windows comprising 300, 200, 100, and 50-event subseries, respectively. The vertical bars represent 90% confidence intervals of the coefficient, and are in blue for a clustered process, in red for a random process, and in green for a regular process. Pink fields indicate the considered candidates for stationary subseries; magenta fields indicate the finally selected stationary subseries. See: text for further explanations



close to 0.5 but also maintained relatively stable values. The candidate could not have also gaps in the seismic activity, which we ascertained through a visual inspection of the histogram of seismic activity for the candidate. Finally, we checked the stationarity of the newly selected subseries by means of the PSR test. All the newly selected subseries turned to be stationary. However, the sizes of the subseries were considerably reduced, which is illustrated by magenta fields in Fig. 4. Basic parameters of these newly selected stationary subseries are given in Table 4.

The A–D test was applied to the stationary subseries to check the exponentiality of the interevent time distribution. The test results are shown in Table 5. In six out of eight studied cases, the null hypothesis on exponentiality was turned down at the significance level 0.05. In the remaining two cases of the subseries $ssZ_{20.1}$ and ssZ_{28} , the A–D

test did not indicate significant deviations of interevent time distribution from the exponential distribution at the prescribed significance level.

As shown in Table 5, in all eight cases, the 90% confidence intervals of v included 0.5—the value characteristic for a fully random Poisson process. It, therefore, could not be excluded that the event occurrence process was Poissonian. At the same time, the A–D test rejected the hypothesis on exponentiality of the interevent time, i.e., turned down the hypothesis that the occurrence process was Poissonian in six out of eight cases. To interpret these seemingly ambiguous results, we recall the inherent property of hypotheses testing. A null hypothesis can be either rejected at a prescribed significance level—the alternative hypothesis is true, or the null hypothesis cannot be rejected, which does not mean that the null hypothesis is true. In

Table 3 Parameters of the subseries, which were thought to be stationary based on the results of coefficient of randomness analysis in sliding windows

Subseries name	Time period of the subseries	Magnitude median and range	No. of events	Activity rate (events per month)
sZ_20.1	31 Oct. 1989–22 Nov. 1992	1.6 [1.2–2.8]	193	5.3
sZ_23.1	03 Mar. 1998–09 Sep. 2003	1.7 [1.2–4.1]	910	14.0
sZ_26	09 Oct. 1988–28 Aug. 1995	1.7 [1.2–3.6]	658	8.0
sZ_27	17 Sep. 1992–28 Sep. 2000	1.7 [1.2–3.7]	854	8.9
sZ_28	03 Feb. 1994–07 Oct. 2002	1.6 [1.2–3.6]	287	2.8
sZ_30.1	03 Aug. 1991–04 Sep. 1998	1.8 [1.2–3.3]	364	4.3
sZ_31	09 Jan. 1985–20 Oct. 1990	1.7 [1.2–3.5]	1074	15.5
sZ_35	26 Nov. 1991–24 Sep. 1998	1.8 [1.2–3.7]	254	3.1

Table 4 Parameters of the finally selected stationary subseries, which were used in the internal correlation study

Sub series name	Time period of the subseries	Magnitude median and range	No. of events	Activity rate (events per month)
ssZ_20.1	25 Sep. 1991–16 May. 1994	1.6 [1.2–3.5]	121	3.8
ssZ_23.1	01 Oct. 1990–14 Aug. 2000	1.7 [1.2–3.7]	265	13.9
ssZ_26	04 Apr. 1989–13 Feb. 1991	1.7 [1.2–3.4]	197	8.8
ssZ_27	08 Feb. 1995–09 Mar. 1996	1.7 [1.2–3.6]	79	6.1
ssZ_28	20 Jan. 1999–18 Nov. 2000	1.5 [1.2–3.2]	97	4.4
ssZ_30.1	16 Jun. 1994–14 Jun. 1995	1.6 [1.2–3.2]	64	5.4
ssZ_31	10 Jan. 1985–25 May 1986	1.5 [1.2–3.1]	348	21.2
ssZ_35	27 Aug. 1995–26 Apr. 1997	1.9 [1.2–3.1]	76	3.8

Table 5 Results of the analyses of the stationary parts of event series

Event series	PSR test results <i>p</i> value for H ₀ : stationarity	A–D test results <i>p</i> value for H ₀ : exponentiality	The coefficient of randomness ν and its 90% confidence intervals	Hurst coefficient, <i>H</i> and the 5% critical value for H ₀ : the process does not have long memory
ssZ_20.1	0.23	0.1408	0.46 [0.40; 0.54]	0.70; 0.72
ssZ_23.1	0.12	0.0005	0.49 [0.45; 0.52]	0.57; 0.67
ssZ_26	0.62	0.0005	0.47 [0.42; 0.52]	0.60; 0.69
ssZ_27	0.26	0.0089	0.45 [0.36; 0.58]	0.63; 0.77
ssZ_28	0.19	0.9836	0.50 [0.44; 0.58]	0.51; 0.75
ssZ_30.1	0.53	0.0005	0.50 [0.44; 0.58]	0.55; 0.83
ssZ_31	0.21	0.0039	0.52 [0.49; 0.55]	0.55; 0.66
ssZ_35	0.12	0.0336	0.48 [0.43; 0.57]	0.45; 0.38

The values, which lead to rejection of the respective null hypothesis, are in bold

case when it cannot be rejected, it is either true or a combination of the sample representativeness and the verification method is not powerful enough to reject this

hypothesis. Only the rejection of the null hypothesis is truly conclusive, the opposite leaves the inference in an ‘unknown’ state. In this connection, we accept the results of

the A–D test. Based on its results, we conclude that the earthquake occurrence process in mines even in its stationary parts can be and more often is non-Poissonian (not fully random).

In the last part of the analysis, we estimated Hurst exponent and the 95% critical values for the null hypothesis that the interevent time series did not have long memory. The values of Hurst exponent, shown in Table 5, in neither case differed significantly from the respective values indicating lack of the long memory property. However, this might be due to shortness of the stationary subseries.

Conclusions

Our analysis evidences that interevent times in the studied series of seismic events induced by mining do not follow an exponential distribution. The background seismic process is not a stationary Poisson process.

The time dependency of the seismic process is visible in series, which contain smaller, numerous events. Series comprising only stronger events exhibit stationarity. This indicates the importance of keeping the completeness levels of seismic systems as low as possible, because information on variability of a seismic process in time is the necessary condition for prediction.

The studied seismic process turns out to be non-stationary, but its time variability is slow. Shorter subseries of the initial series cease to exhibit this non-stationarity, and most of the 50 elements subseries look like drawn from stationary processes. The slow variability in time of the seismic process makes it possible to estimate time-dependent process parameters by means of moving data windows technique.

In stationary segments of the initial seismic series, the interevent time distributions are closer to the exponential distribution, but most of them are still not exponential. The occurrence process is not a Poisson process, which suggests indirectly that the process is internally correlated. These internal correlations do not seem to have a long range—they are not confirmed by the R/S analysis. However, the results of R/S analysis are uncertain, because the stationary segments were short.

In overall, in seismic hazard assessments in the first approximation, such stationary segments (windows) can be regarded as outcomes of Poisson processes. However, more detailed insights into the seismic hazard in mines require further studies of the nature of correlations among seismic events to account for these correlations in hazard analyses.

Acknowledgements This work was supported within statutory activities No 3841/E-41/S/2017 of the Ministry of Science and Higher Education of Poland.

Open Access This article is distributed under the terms of the Creative Commons Attribution 4.0 International License (<http://creativecommons.org/licenses/by/4.0/>), which permits unrestricted use, distribution, and reproduction in any medium, provided you give appropriate credit to the original author(s) and the source, provide a link to the Creative Commons license, and indicate if changes were made.

References

- Baecher GB, Keeney RL (1982) Statistical examination of reservoir-induced seismicity. *Bull Seismol Soc Am* 72:553–569
- Correig AM, Urquizu M, Vila J, Marti J (1997) Analysis of temporal occurrence of seismicity at Deception Island (Antarctica): a nonlinear approach. *Pure Appl Geophys* 149:553–574. doi:10.1007/s000240050041
- Gardner JK, Knopoff L (1974) Is the sequence of earthquakes in southern California, with aftershocks removed, Poissonian? *Bull Seismol Soc Am* 64:1363–1367
- Gkaraouni C, Lasocki S, Papadimitriou E, Tsaklidis G (2017) Hurst analysis of seismicity in Corinth rift and Mygdonia graben (Greece). *Chaos Solitons Fractals* 96:30–42. doi:10.1016/j.chaos.2017.01.001
- Hurst H (1951) Long term storage capacity of reservoirs. *Trans Am Soc Civ Eng* 116:770–799
- Kijko A (1997) Keynote lecture: seismic hazard assessment in mines. In: Gibowicz SJ, Lasocki S (eds) *Rockburst and seismicity in mines*. Rotterdam, Balkema, pp 247–256
- Kiremidijan AS, Anagnos T (1984) Stochastic slip predictable model for earthquake occurrences. *Bull Seismol Soc Am* 74:739–755
- Lasocki S (1992a) Non-poissonian structure of mining induced seismicity. *Acta Mont* 84:51–58
- Lasocki S (1992b) Weibull distribution for time intervals between mining tremors. *Publs Inst Geophys Pol Acad Sci* 16(245):241–260
- Lasocki S (1993) Weibull distribution as a model for sequence of seismic events induced by mining. *Acta Geophys Pol* 41:101–112
- Gkaraouni C, Lasocki S, Papadimitriou E (2015) Investigation of earthquake magnitude and interevent time distribution in Corinth Gulf and Mygdonia basin with the use of stochastic tools. In: *Proceedings of the 28th panhellenic statistics conference*. Greek Statistical Institute, pp 385–399
- Lasocki S, Orlecka-Sikora B (2008) Seismic hazard assessment under complex source size distribution of mining-induced seismicity. *Tectonophysics* 456:28–37. doi:10.1016/j.tecto.2006.08.013
- Lombardi AM, Marzocchi W (2007) Evidence of clustering and nonstationarity in the time distribution of large worldwide earthquakes. *J Geophys Res* 112:B02303. doi:10.1029/2006JB004568
- Lomnitz C (1994) *Fundamentals of earthquake prediction*. Wiley, New York
- Matsumura S (1984) A one-parameter expression of seismicity patterns in space and time. *Bull Seismol Soc Am* 74:2559–2576
- Orlecka-Sikora B, Lasocki S (2002) Clustered structure of seismicity from the Legnica–Glogow copper district. *Publ Inst Geophys Pol Acad Sci* 24(340):105–119 (in Polish with English abstract)
- Priestley MB, Subba Rao T (1969) A test for non-stationarity of time-series. *J R Stat Soc Ser B (Methodol)* 31(1):140–149
- Stephens MA (1974) EDF statistics for goodness of fit and some comparisons. *J Am Stat Assoc* 69:730–737
- Vere-Jones D (2010) *Foundations of statistical seismology*. *Pure Appl Geophys* 167:645–653

- Węglarczyk S, Lasocki S (2009) Studies of short and long memory in mining-induced seismic processes. *Acta Geophys* 57:696–715. doi:[10.2478/s11600-009-0021-x](https://doi.org/10.2478/s11600-009-0021-x)
- Xu Y, Burton PW (2006) Time varying seismicity in Greece: Hurst's analysis and Monte Carlo simulation applied to a new earthquake catalogue for Greece. *Tectonophysics* 423:125–136. doi:[10.1016/j.tecto.2006.03.006](https://doi.org/10.1016/j.tecto.2006.03.006)

Application of a linked stress release model in Corinth Gulf and Central Ionian Islands (Greece)

Ourania Mangira¹  · Georgios Vasiliadis² · Eleftheria Papadimitriou¹

Received: 28 December 2016 / Accepted: 13 March 2017 / Published online: 25 March 2017
© Institute of Geophysics, Polish Academy of Sciences & Polish Academy of Sciences 2017

Abstract Spatio-temporal stress changes and interactions between adjacent fault segments consist of the most important component in seismic hazard assessment, as they can alter the occurrence probability of strong earthquake onto these segments. The investigation of the interactions between adjacent areas by means of the linked stress release model is attempted for moderate earthquakes ($M \geq 5.2$) in the Corinth Gulf and the Central Ionian Islands (Greece). The study areas were divided in two subareas, based on seismotectonic criteria. The seismicity of each subarea is investigated by means of a stochastic point process and its behavior is determined by the conditional intensity function, which usually gets an exponential form. A conditional intensity function of Weibull form is used for identifying the most appropriate among the models (simple, independent and linked stress release model) for the interpretation of the earthquake generation process. The appropriateness of the models was decided after evaluation via the Akaike information criterion. Despite the fact that the curves of the conditional intensity functions exhibit similar behavior, the use of the exponential-type conditional intensity function seems to fit better the data.

Keywords Stress transfer · Interactions · Conditional intensity function · Corinth Gulf · Ionian Islands

Introduction

The stress release model (SRM) was developed by Vere-Jones (1978) as a stochastic expansion of the elastic rebound theory (Reid 1910). This deterministic model assumes that the elastic stress is accumulated due to the long-term tectonic loading, and is released when it surpasses a certain level, i.e., the strength of the medium during the earthquake occurrence. The energy release should allow a certain time period to elapse until the re-accumulation of the energy and the genesis of a subsequent earthquake. Isham and Westcott (1979) first examined such a procedure, called a self-correcting point process, which automatically corrects a deviation from the mean number of points.

In a self-correcting process, the points display a repressive behavior, i.e., the occurrence of an event delays the occurrence of a subsequent event. It has been noticed very often though that shortly after a strong earthquake, a second one follows, with a long-term weak clustering characterizing all main shocks (Kagan and Jackson 1991). Gabrielov and Newman (1994) also support that a period of activation rather than a period of quiescence is observed after a main event and sometimes other earthquakes of comparable magnitude follow. This behavior could be explained with stress transfer between adjacent areas, and the idea is incorporated in the linked stress release model (LSRM) introduced by Liu et al. (1999). The interactions between different parts of an area are investigated in order to assess the impact an earthquake has on the seismicity of each part, and can provoke either damping or excitation of the earthquake activity in an adjacent subarea.

✉ Ourania Mangira
omangira@geo.auth.gr

Georgios Vasiliadis
gvasil@math.auth.gr

Eleftheria Papadimitriou
ritsa@geo.auth.gr

¹ Geophysics Department, School of Geology, Aristotle University of Thessaloniki, 54124 Thessaloniki, Greece

² Department of Informatics Engineering, TEI of West Macedonia, 52100 Kastoria, Greece

The stress release models (SRM) were widely applied during last decades for seismic hazard evaluation. The applications involve historical earthquakes from different regions worldwide, like China, Japan, Taiwan and New Zealand (e.g., Zheng and Vere-Jones 1994; Lu et al. 1999; Lu and Vere-Jones 2000; Bebbington and Harte 2003; Lu 2005; Imoto and Hurukawa 2006). In many of these studies, the main purpose was to identify statistically distinct regions by means of the AIC. Bebbington and Harte (2001) gave emphasis to the statistical behavior of the linked stress release model (LSRM) and suggested methods for checking the significance of the predicted interactions including residual process analysis and Monte Carlo simulation. Besides historical catalogs, synthetic earthquake catalogs were used for applying SRM (Liu et al. 1999; Lu and Vere-Jones 2001). The LSRM was also used to formulate a stochastic model for aftershocks (Borovkov and Bebbington 2003). More recently, information gains and entropy scores were proposed for scoring probability forecasts and trying to quantify the predictability of the stress release model (Bebbington 2005; Harte and Vere-Jones 2005). Comparisons were also made using Molchan's v - τ diagram. A different approach is presented by Rotondi and Varini (2006, 2007) and Varini and Rotondi (2015) who analyzed stress release models from the Bayesian viewpoint, whereas Jiang et al. (2011) developed a new multidimensional SRM involving a coseismic stress transfer model.

Aiming to investigate the strong earthquake occurrence in two areas that frequently accommodate disastrous ($M \geq 6.0$) earthquakes, the Corinth Gulf and the Central Ionian Islands, the SRMs are applied. The earthquake interaction is examined between two subareas in which both study areas were subdivided. In the case of the Corinth Gulf, the area was subdivided into its western and eastern parts and in the case of the Central Ionian Islands, the two subareas consist of the Kefalonia (south part) and Lefkada (northern part) subareas. The application is performed by means of the conditional intensity function, and in particular of exponential type, like in the classical case, and of Weibull type. We will try to interpret and compare the results obtained from the two function types for determining which model is the most appropriate to explain the earthquake generation process.

Formulation of the models

Simple stress release model (SSRM)

In the simple stress release model (SSRM), the probability of an earthquake occurrence is determined by a quantity representing the stress level in an area (Vere-Jones and

Deng 1988). The evolution of stress $X(t)$ as a function of time, could be written as

$$X(t) = X(0) + \rho t - S(t), \quad (1)$$

where $X(0)$ is the initial stress value, ρ is the loading rate and $S(t)$ is the accumulated stress release from earthquakes within the area over the period $(0, t)$, i.e.,

$$S(t) = \sum_{t_i < t} S_i, \quad (2)$$

where t_i , S_i are the origin time and the stress release, respectively, associated with the i th earthquake.

The amount of stress released during an earthquake can be approximated by empirical relations. Bufe and Varnes (1993) suggest that a measure of the total energy released is the cumulative Benioff strain, i.e., $S(t) = \sum_{i=1}^{N(t)} E_i^{1/2}$, where E_i is the seismic energy of the i th earthquake and $N(t)$ stands for the number of earthquakes till time t . The seismic energy released is given by the relation $E = 10^{3/2M} + \text{const}$ (Kanamori and Anderson 1975). Then

$$S = 10^{0.75(M - M_{\text{th}})}, \quad (3)$$

where M is the earthquake magnitude and M_{th} the smallest magnitude appeared in the dataset.

The stochastic behavior of the model is characterized by the conditional intensity function $\lambda^*(t)$ (Daley and Vere-Jones 2003), which is assumed to have the exponential form

$$\begin{aligned} \lambda^*(t) &= \Psi(X(t) = \exp\{\mu + v[X(0) + \rho t - S(t)]\}) \\ &= \exp\{a + v[\rho t - S(t)]\} \\ &= \exp\{a + b[t - cS(t)]\}, \end{aligned} \quad (4)$$

where a, b, c are the parameters to be fitted. The estimation is performed numerically by maximizing the log-likelihood function

$$\log L = \sum_{i=1}^{N(T)} \log \lambda^*(t) - \int_0^T \lambda^*(u) du, \quad (5)$$

where $(0, T)$ is the observational interval and $N(T)$ is the total number of events in $(0, T)$.

A Weibull-type conditional intensity function (c.i.f.) might be additionally applied, because it is among the most commonly used ones in survival analysis and quite flexible since it is related to a number of other probability distributions. The following form for the conditional intensity function is assumed (Votsi et al. 2011)

$$\lambda^*(t) = \lambda \gamma X(t)^{\gamma-1} = \lambda \gamma (X(0) + \rho t - S(t))^{\gamma-1} \quad (6)$$

The parameters to be estimated are $\lambda, \gamma, X(0), \rho$.

Linked stress release model (LSRM)

The incorporation of the interactions between different subareas, which is not taken into account in the formulation of the SSRM, leads to the linked stress release model (LSRM). The stress evolution in the i subarea is now written

$$\lambda_i^*(t) = \exp \left\{ a_i + b_i \left[t - \sum_j c_{ij} S(t, j) \right] \right\}, \quad (7)$$

where $S(t, j)$ stands for the accumulated stress release in the j subarea over the period $(0, t)$ and θ_{ij} measures the fixed ratio of stress release, which is transferred from the j to the i subarea. It is plausible to set $\theta_{ii} = 1$, since it is assumed that at least a significant amount of the accumulated energy is released. Positive and negative values of θ_{ij} indicate damping and excitation, respectively.

In the original formulation of the LSRM it is assumed for each subarea a c.i.f. of the form

$$\lambda_i^*(t) = \Psi(X_i(t)) = \exp \left\{ a_i + v_i \left[\rho_i t - \sum_j \theta_{ij} S(t, j) \right] \right\}, \quad (8)$$

where $\alpha_i (= \mu_i + v_i X_i(0))$, v_i , ρ_i and θ_{ij} are the parameters to be fitted. Liu et al. (1998) achieve a more convenient parameterization by setting $b_i = v_i \rho_i$ and $c_{ij} = \theta_{ij} / \rho_i$.

$$\lambda_i^*(t) = \exp \left\{ a_i + b_i \left[t - \sum_j c_{ij} S(t, j) \right] \right\}, \quad (9)$$

where a_i , b_i , c_{ij} are the parameters to be fitted for each subarea i .

For the parameters to be estimated some restrictions exist that should be taken into account. The parameters $b_i = v_i \rho_i$ and $c_{ii} = 1/\rho_i$ should be positive, since the loading rate ρ_i and the sensitivity to stress change, v_i , take (only) positive values. On the contrary, c_{12} and c_{21} could take either positive or negative values, since they indicate the style of interactions between adjacent subareas, i.e., if they are inhibitory or excitatory.

Supposing that a Weibull-type conditional intensity function fits better the data, for each subarea i we assume that

$$\begin{aligned} \lambda_i^*(t) &= \lambda_i \gamma_i X_i(t)^{\gamma_i - 1} \\ &= \lambda_i \gamma_i \left(X_i(0) + \rho_i t - \sum_j \theta_{ij} S(t, j) \right)^{\gamma_i - 1} \end{aligned} \quad (10)$$

The parameters to be estimated are λ_i , γ_i , $X_i(0)$, ρ_i and θ_{ij} , where $\lambda_i > 0$ and $\gamma_i > 0$. The shape parameter γ determines the behavior of the conditional intensity function. A value of γ lower than 1 implies that the failure rate

decreases over time, whereas if $\gamma > 1$ there is an increasing hazard over time. The failure rate is constant over time when the shape parameter takes the value $\gamma = 1$, and in that case the Weibull distribution turns out to an exponential one. We impose the restriction of $\gamma \geq 1$ since earthquakes are more likely to occur as time advances.

It should be noticed that, for the number of parameters to be constrained, a large data sample is required. Since we assume that the occurrence of earthquakes reduces the probability of immediately subsequent events, we are only interested in the strong events which are of primary practical concern.

Study areas and data

Both study areas were extensively investigated since they have accommodated several destructive earthquakes that occurred both in historical and instrumental era. The Corinth rift (Fig. 1) consists of one of the most rapidly extending areas worldwide (Armijo et al. 1996). The high level of seismicity is testified by the historical as well as the instrumental records, with the maximum magnitude observed or ever reported hardly > 6.8 (Papazachos and Papazachou 2003), a fact that probably reflects the lack of continuity of fault segments (Jackson and White 1989). One observation worth to be mentioned here is the sequence of three earthquakes with $M \geq 6.3$ that occurred in 1981 in ten days in the eastern part of the Corinth Gulf (Console et al. 2013). The SSRM was applied in the western part of the Corinth Gulf by Rotondi and Varini (2006) with a smaller dataset of 20 earthquakes including events with $M \geq 5.0$ since 1945 and after performing Bayesian analysis.

The central Ionian Islands area (Fig. 2), which includes Lefkada and Kefalonia Islands, consists of one of the most

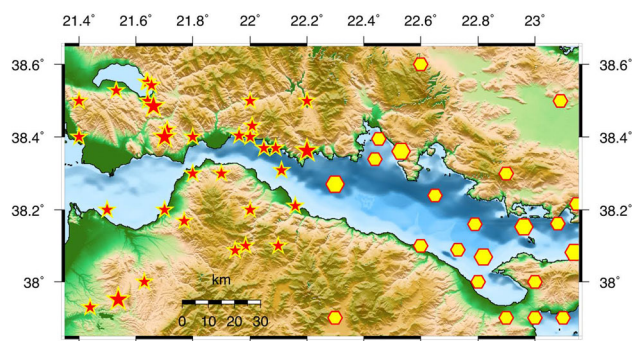


Fig. 1 Seismicity map for the Corinth Gulf showing earthquakes with magnitude $M \geq 5.2$ that occurred in the area since 1911. The events occurred in the western part are represented with red stars, whereas the ones occurred in the eastern part are represented with yellow hexagons. Their size is proportional to the earthquake's magnitude

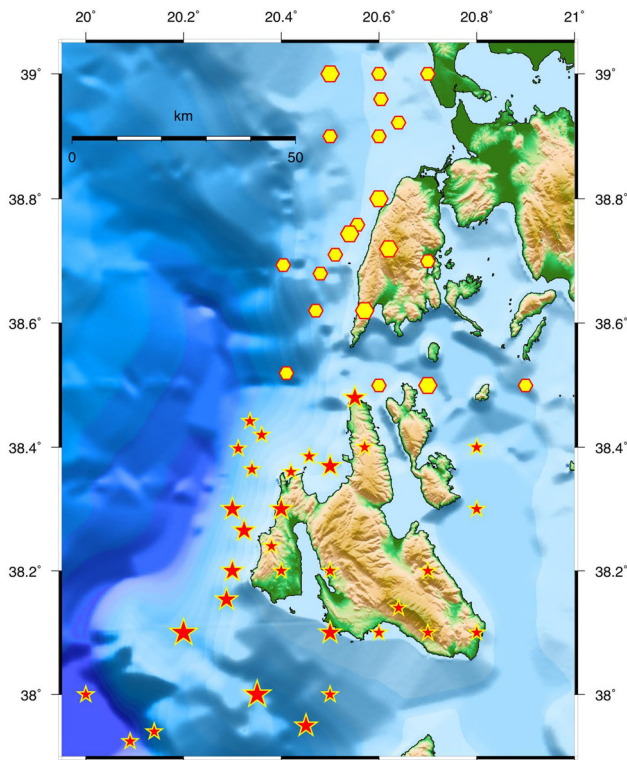


Fig. 2 Seismicity map for the Central Ionian Islands showing earthquakes with magnitude $M \geq 5.2$ that occurred in the area since 1911. The events occurred in the subarea of Kefalonia are represented with red stars, whereas the ones occurred in the subarea of Lefkada are represented with yellow hexagons. Their size is proportional to the earthquake magnitude

seismically active areas in the broader Aegean region, a fact that is clearly showed by the high seismic moment rate ($>10^{25}$ dyn cm year $^{-1}$) (Papazachos et al. 1997). The Kefalonia Transform Fault Zone (KTFZ) was recognized as responsible for the high seismicity levels of in the region, connecting the continental collision to the north with the oceanic subduction to the south (Scordilis et al. 1985). Seismicity is mainly observed in the sea area along the west shoreline and offshore of the two islands.

Lefkada Island has suffered many times from earthquakes occurring in the nearby Kefalonia Island, a fact that suggests possible coupling between the Lefkada and Kefalonia faults (Papadimitriou 2002). Therefore, it is particularly interesting to examine the interactions between earthquakes occurring in each subarea via stress release models. Votsi et al. (2011) were the first to apply stress release models to this area. Two different complete datasets were used in their study, one comprising earthquakes with $M \geq 6.0$ in the period 1862–2008 for the application of the SSRM and one comprising earthquakes with magnitudes $M \geq 5.2$ that occurred from 1911 to 2008, for the application of the LSRM. In the second case, the magnitude threshold is lower since more data are needed when

applying the LSRM due to the larger number of parameters. The division of the subareas of Kefalonia and Lefkada is slightly different than the one chosen in this study, as well as the dataset used (period selected, magnitude cut-off). In this paper, a so-called Weibull model was also proposed, suggesting a conditional intensity function of Weibull form in the case of the SSRM, i.e., taking the entire study area as one, which was served as a basic idea in our study.

For both study areas, the magnitude threshold was set as low as $M_{th} = 5.2$ from January 1st, 1911 to December 31st, 2015 to obtain the largest and longest possible complete earthquake catalog. The data used are taken from the catalog compiled in the Geophysics Department of Aristotle University of Thessaloniki (Aristotle University of Thessaloniki Seismological Network 1981). In the case of the Corinth Gulf, the catalog comprises 61 events, 36 of which occurred in the western and 25 in the eastern part. In the case of the Central Ionian Islands, 74 events in total were used, with the most seismically active subarea of Kefalonia comprising 41 events, and the Lefkada subarea including 33.

Application of the models

As mentioned above, the estimation of the parameters is performed by maximizing the log-likelihood function. The optimization algorithm is usually executed many times starting from different initial values of the parameters randomly drawn from the parameter space. The estimated parameters are those corresponding to the maximum among the derived maximum log-likelihood values. To achieve successful convergence as well as minimize randomness, the initial points were not randomly selected, but after scanning numerically the parameter space and taking into account the restrictions of the models. A Newton-type algorithm (specifically the BFGS method) was then performed, where the initial parameters are those found by the above search.

Particular caution should be given to the application of the Weibull-type LSRM, since the form of the conditional intensity function may create problems when estimating the model parameters. Negative values for the stress function $X_i(t)$ lead to negative values for the conditional intensity function, which is unacceptable. The optimization algorithm was created for exclusion of the problematic points. Constraints are set so that the quantity which is interpreted as stress in each subarea, $X_i(t)$, takes only positive values. The final points therefore do not create any problem in the optimization process.

The evaluation of the models could be performed by means of the Akaike information criterion (AIC) which is used as a measure of distinction between the two

competing models (Akaike 1974). The AIC represents a method of penalizing additional parameters in a model to avoid over-fitting.

Application of the SRMs to the Corinth Gulf

LSRM: exponential-type conditional intensity function

The LSRM is applied for investigating coupling between two subareas in the Corinth Gulf, i.e., the western and eastern part, where the conditional intensity function is of exponential type (9). The parameters are derived through the MLE method. Additional constraints are put such that the parameters b_1, b_2, c_{11} and c_{22} take only positive values. In order to estimate constrained parameters with the MLE method, each positive parameter is re-parametrized as an exponential function of a parameter lying on the real line. The estimated parameters are presented in Table 1, along with the corresponding standard errors and the 90% confidence intervals. The maximum value of the log-likelihood function is -132.508 .

Both transfer parameters c_{ij} are positive, which indicates inhibitory behavior, suggesting that earthquake occurrence in one subarea reduces the activity in the second one. Figure 3 shows the conditional intensity function for the western (Fig. 3a) and eastern (Fig. 3b) part, respectively. In the same figures, the earthquake magnitudes versus time are plotted for the same dataset in order to see the relation between the events and the c.i.f.. Particularly we may observe that in the eastern part (Fig. 3b) the stress drops appear to be larger when an event occurs in the western part rather than in the eastern subarea itself, which is evidenced by the large value of the parameter c_{21} showing correlation between the two subareas. The loading rate of the eastern part—and not the triggering from the western part—seems to designate the earthquake occurrence.

LSRM: Weibull-type conditional intensity function

The LSRM with Weibull-type conditional intensity function given in (10) is applied in an effort to find a better fitting to the data of the Corinth Gulf. Using a BFGS optimization algorithm, the maximum value of the log-likelihood function is found to be -133.9383 under appropriate constraints, meaning that the parameters $\lambda_i, \gamma_i, \rho_i$ are positive alike the stress function $X_i(t)$. The estimate of gamma does not turn out to be >1 , $\gamma_i > 1$, by simply setting the restriction $\gamma_i > 0$. The restriction of $\gamma_i > 1$ is necessary therefore for the failure rate of the Weibull-type LSRM being increased.

Table 2 shows the estimated parameters, the standard errors and the 90% confidence intervals for the LSRM applied in the same dataset. The results are in accordance with the ones using an exponential-type conditional intensity function. The parameters θ_{12} and θ_{21} are positive, indicating damping of each subarea due to earthquakes occurring in the adjacent subarea. We notice though that the confidence interval for both transfer parameters, θ_{12} and θ_{21} , contain positive as well as negative values indicating that the influence of the one part to the other is not robust in the sense that the parameter could also take the value 0 since it is included in the confidence interval. This is partly in accordance with the case using the exponential-type conditional intensity function, where both transfer parameters were found positive and the parameter θ_{21} was strictly positive. The conditional intensity functions for both subareas are shown in Fig. 4.

The evaluation of the models is performed by means of the Akaike information criterion (AIC), as mentioned before. The value of the log-likelihood function is greater when using an exponential-type c.i.f., and the value of the AIC is smaller since in this case the model parameters are 8, less than in the Weibull-type c.i.f. case by two. We can

Table 1 LSRM's estimated parameters, standard errors and confidence intervals when using an exponential-type conditional intensity function

Parameter	Estimate		Standard error		90% Confidence interval	
	Corinth Gulf	Central Ionian Islands	Corinth Gulf	Central Ionian Islands	Corinth Gulf	Central Ionian Islands
a_1	-1.993	0.250	0.449	0.420	(-2.731, -1.255)	(-0.441, 0.942)
a_2	-1.601	0.470	0.607	0.387	(-2.599, -0.602)	(-0.166, 1.107)
b_1	0.040	0.027	0.036	0.754	(0.022, 0.072)	(0.008, 0.093)
b_2	0.046	0.040	0.522	0.469	(0.019, 0.108)	(0.018, 0.087)
c_{11}	0.681	0.117	0.861	2.517	(0.165, 2.802)	(0.002, 7.341)
c_{12}	0.360	1.406	0.352	0.857	(-0.219, 0.940)	(-0.003, 2.816)
c_{21}	1.698	0.241	0.929	0.223	(0.169, 3.227)	(-0.127, 0.608)
c_{22}	0.171	1.147	2.532	0.491	(0.003, 11.025)	(0.511, 2.573)

Fig. 3 The exponential-type conditional intensity function versus time for each subarea of the Corinth Gulf, fitted to the catalog of earthquakes with $M \geq 5.2$ that occurred since 1911. **a** Western part. **b** Eastern part

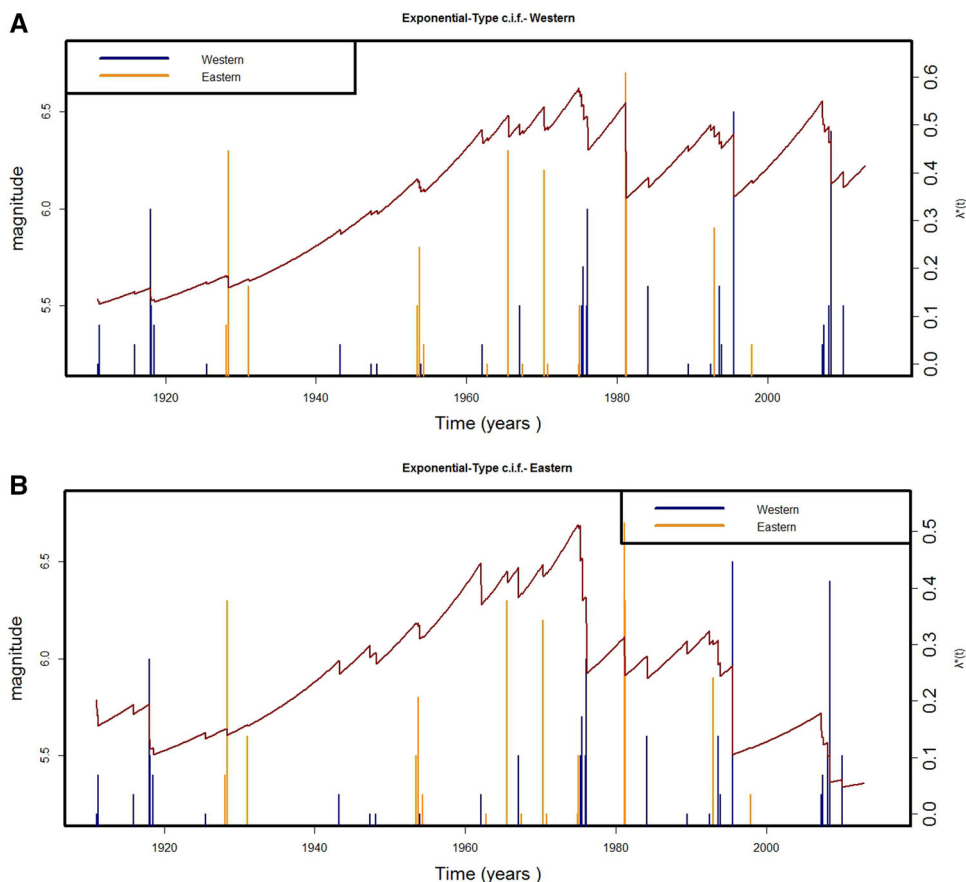


Table 2 LSRM’ estimated parameters, standard errors and confidence intervals when using a Weibull-type conditional intensity function

Parameter	Estimate		Standard error		90% Confidence interval	
	Corinth Gulf	Central Ionian Islands	Corinth Gulf	Central Ionian Islands	Corinth Gulf	Central Ionian Islands
λ_1	0.125	0.012	0.647	4.590	(0.043, 0.362)	$(6.2 \times 10^{-6}, 22.505)$
λ_2	0.003	0.0003	2.391	7.403	$(6.6 \times 10^{-5}, 0.173)$	$(1.68 \times 10^{-9}, 59.265)$
γ_1	1.234	1.717	0.369	1.304	(1.128, 1.429)	(1.084, 7.128)
γ_2	1.950	2.354	0.470	1.005	(1.439, 3.057)	(1.259, 8.069)
$X_1(0)$	37.826	112.107	4.270	12.185	(30.801, 44.850)	(176.554, 180.507)
$X_2(0)$	68.572	178.531	8.052	1.202	(55.327, 81.817)	(62.58, 94.60)
ρ_1	2.056	2.045	0.332	0.590	(1.191, 3.551)	(0.748, 5.398)
ρ_2	1.434	1.430	0.351	0.815	(0.805, 2.555)	(0.374, 5.467)
θ_{12}	1.500	0.769	1.934	1.265	(-1.681, 4.681)	(-1.311, 2.850)
θ_{21}	1.800	0.957	1.527	0.841	(-0.713, 4.312)	(-0.426, 2.341)

thus argue that we can avoid over-fitting since the use of the two extra parameters is not necessary finally.

Independent SRM: exponential-type conditional intensity function

As mentioned in the previous section, by checking the interval estimation of the transfer parameters c_{ij} , we may see that only the parameter c_{21} is positive, meaning that one-way

interaction is established. We cannot argue about the way earthquakes occurring in the eastern part influence the western part. Since 0 is included in the interval estimation of c_{12} , we applied the SRM separately in the western part of the Corinth Gulf, i.e., under the assumption that earthquakes occurring in the eastern part don’t affect the ones of the western part. The parameters shown in Table 3 are estimated through the MLE method and the conditional intensity function versus time is plotted in Fig. 5.

Fig. 4 The Weibull-type conditional intensity function versus time for each subarea of the Corinth Gulf, fitted to the catalog of earthquakes with $M \geq 5.2$ that occurred since 1911. **a** Western part. **b** Eastern part

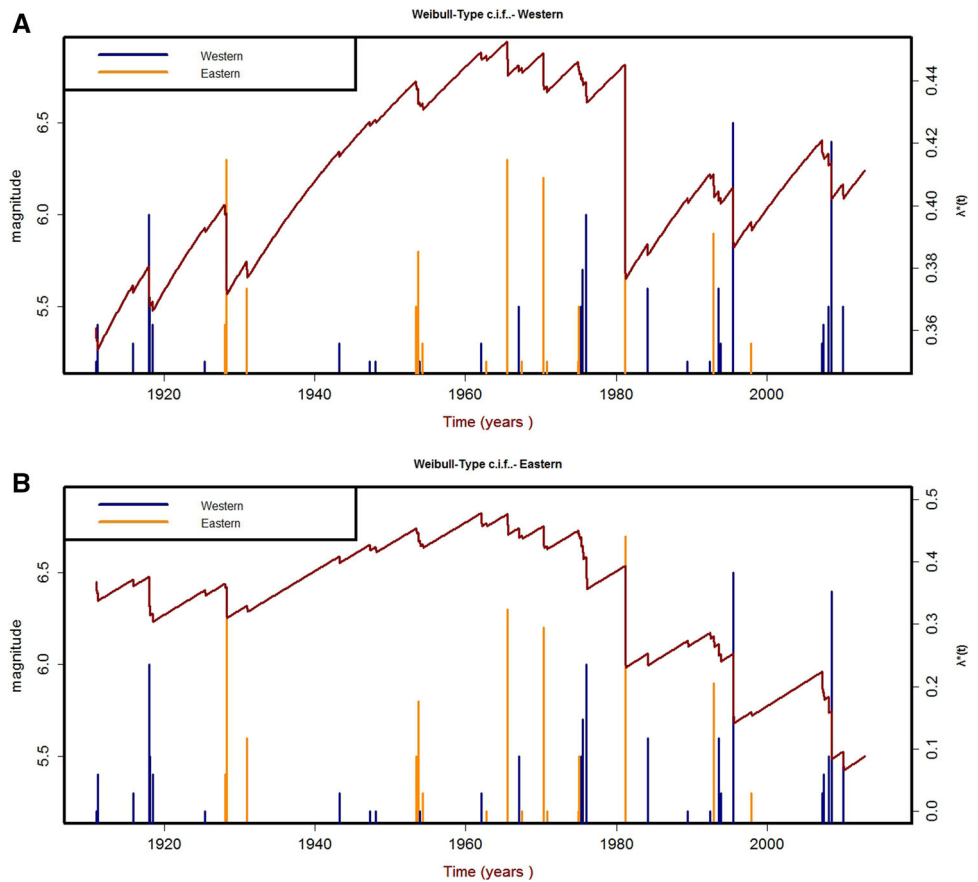


Table 3 Estimated parameters, standard errors and confidence intervals for the ISRM (western part of the Corinth Gulf) and the SSRM when using an exponential-type conditional intensity function

Parameter	Estimate		Standard error		90% Confidence interval	
	ISRM (western part)	SSRM	ISRM (western part)	SSRM	ISRM (western part)	SSRM
a	-1.708	-0.865	0.420	0.326	(-2.399, -1.018)	(-1.403, -0.328)
b	0.026	0.014	0.016	1082	(0.0001, 0.052)	(0.002, 0.086)
c	1.089	0.468	0.492	0.573	(0.280, 1.898)	(0.182, 1.201)

Fig. 5 The exponential-type conditional intensity function versus time when applying the ISRM to the western part of the Corinth Gulf

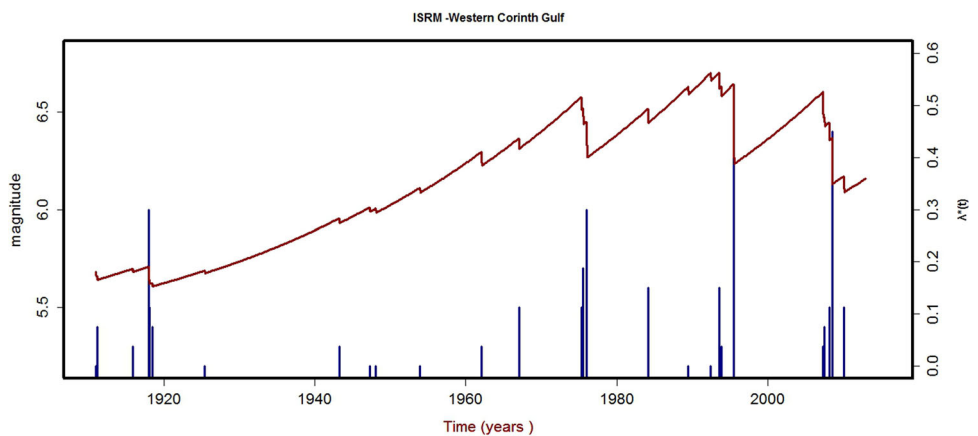
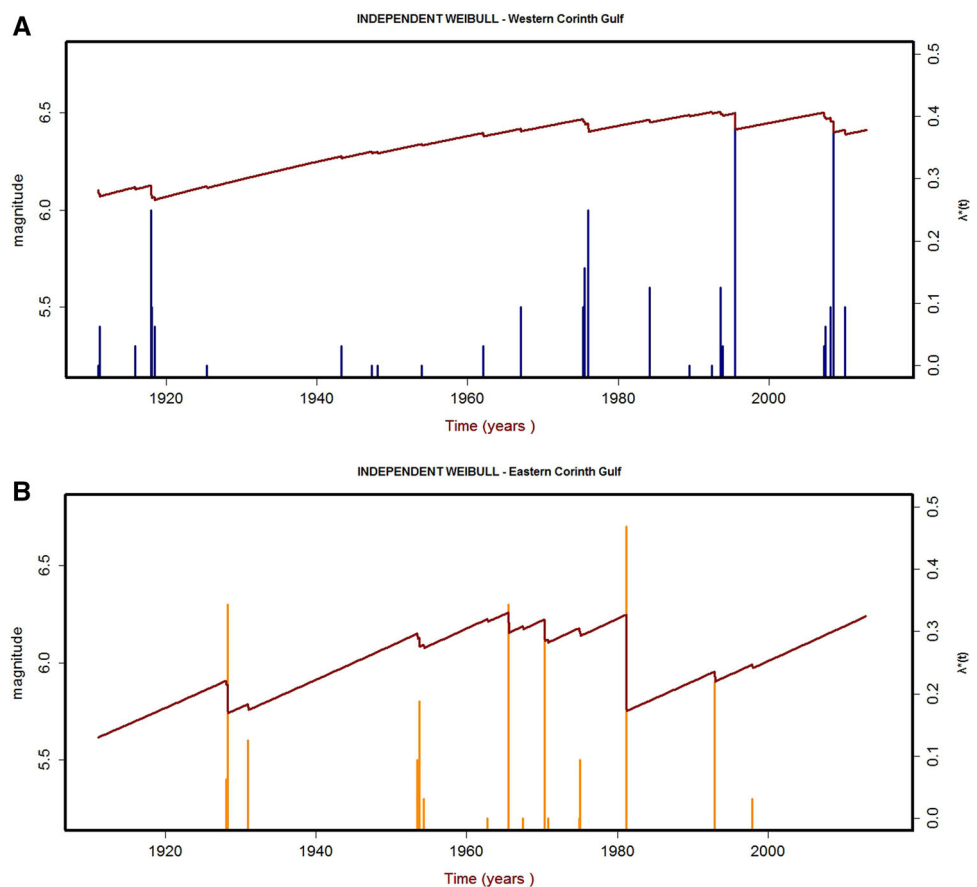


Table 4 Estimated parameters, standard errors and confidence intervals for the ISRM and SSRM in the Corinth Gulf when using a Weibull-type conditional intensity function

Parameter	Estimate			Standard error			90% Confidence interval		
	ISRM (western part)	ISRM (eastern part)	SSRM	ISRM (western part)	ISRM (eastern part)	SSRM	ISRM (western part)	ISRM (eastern part)	SSRM
λ	0.023	0.002	0.009	4.813	7.761	3.812	$(8.3 \times 10^{-6}, 63.254)$	$(4.7 \times 10^{-9}, 577.4)$	$(1.7 \times 10^{-5}, 4.618)$
γ	1.530	2.071	1.776	0.654	0.890	0.415	(0.522, 4.489)	(0.479, 8.958)	(0.898, 3.512)
$X(0)$	50.296	29.698	75.041	5.027	7.293	10.214	(42.027, 58.565)	(17.770, 41.696)	(58.239, 91.843)
ρ	1.050	1.127	1.863	0.980	0.634	0.398	(0.210, 5.263)	(0.397, 3.199)	(0.968, 3.588)

Fig. 6 The Weibull-type conditional intensity function versus time when applying the ISRM to the **a** western part, **b** eastern part of the Corinth Gulf

Independent SRM: Weibull-type conditional intensity function

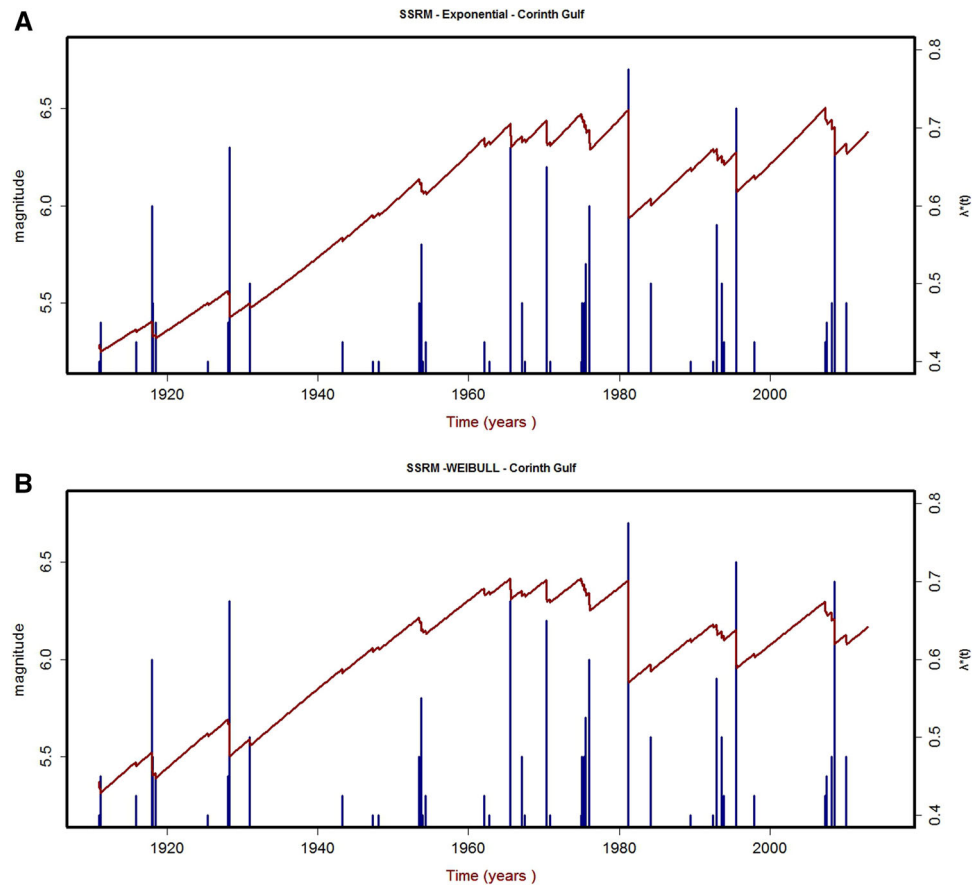
The interval estimation of both c_{12} and c_{21} transfer parameters in the case of the Weibull-type c.i.f., contain the value 0. It is, therefore, plausible to apply the independent stress release model (ISRM), i.e., apply the SSRM in each subarea separately. The estimated parameters for both parts of the Corinth Gulf are shown in Table 4, along

with the corresponding standard errors and the 90% confidence intervals, and the conditional intensity functions are shown in Fig. 6a, b, respectively.

SSRM: exponential-type conditional intensity function

A more profound and complete investigation of the best model fitting the dataset requires the application of the SSRM. In the SSRM, no spatial interactions of earthquake

Fig. 7 The conditional intensity function versus time when applying the SSRM to the Corinth Gulf using **a** an exponential-type c.i.f., **b** a Weibull-type c.i.f



occurrence through stress transfer are considered between different parts and for this reason the study area is considered as one entity. Thus, a c.i.f. of exponential-type (4) is used, resulting in the parameters presented in Table 3 and the corresponding plot in Fig. 7a.

SSRM: Weibull-type conditional intensity function

The alternative form (5) suggesting a Weibull-type c.i.f. is also used. The four estimated parameters (Table 4) are derived through the MLE method and particularly by means of the BFGS optimization algorithm with constraints not only for the parameters to be positive but also for affirming that $X(t)$ takes only positive values. The conditional intensity function versus time is plotted in Fig. 7b, where the two plots of the simple stress release models are similar. Under this assumption the two models are equivalent. Based on the information criteria, the exponential-type c.i.f. should be preferred (approximately difference of 2 in AIC). Based exclusively on the AIC, we could select the SSRM versus the LSRM, but since we are interested in the interactions between the subareas and at least one confidence interval takes only positive values we can still claim that the LSRM could interpret the seismicity of the area.

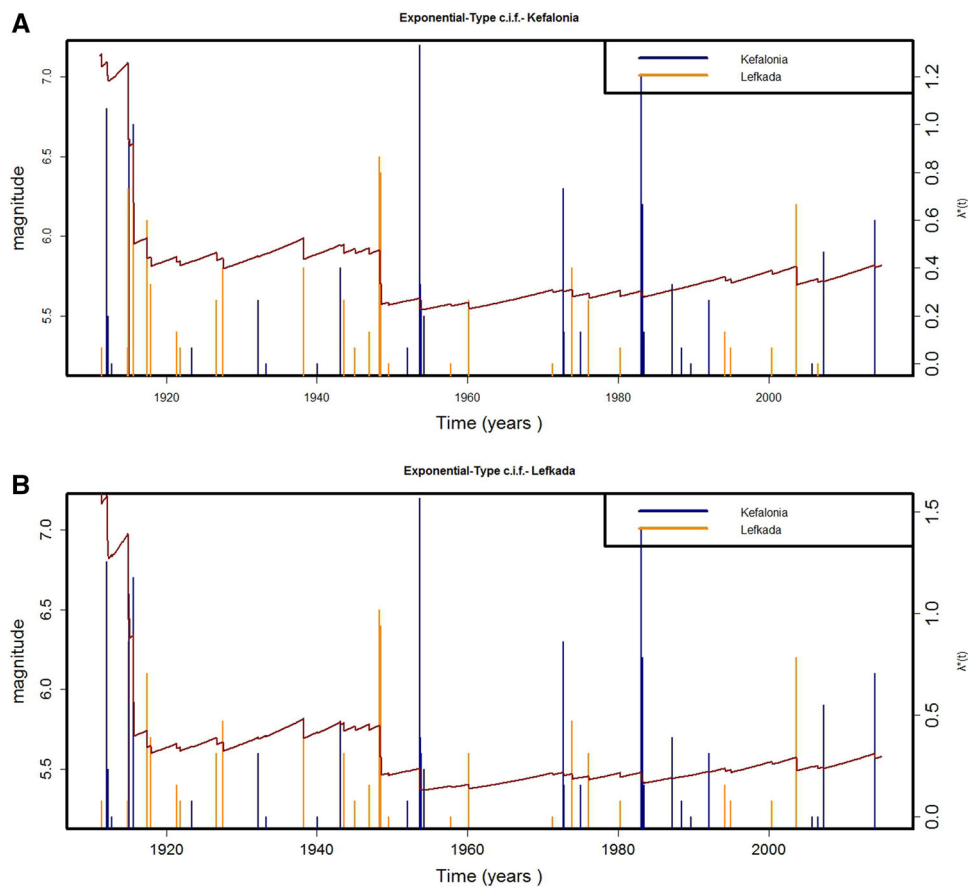
Application of the LSRM to the area of Central Ionian Islands

LSRM: exponential-type conditional intensity function

As in the case of the Corinth Gulf, the maximum likelihood estimation method is used in the application of the LSRM to the Central Ionian Islands area in order to estimate the model parameters. Constraints are put such that the confidence intervals for the parameters b_i and c_{ii} contain only positive values. The model parameters as well as the standard errors and the 90% confidence intervals are shown in Table 1. The log-likelihood function attains the maximum value of -143.166 .

In Fig. 8 the conditional intensity functions versus time are plotted for both subareas of Kefalonia and Lefkada, along with the temporal distribution of the earthquake magnitudes. We observe that the curves display high values at the beginning of the study period followed by a sudden decrease. This is due to the positive values of a_1 and a_2 , since the conditional intensity functions at time $t = 0$ take the value $\lambda^*(0) = \exp\{a\}$. Besides, due to the lack of preceding information the first period results cannot be unambiguously considered as reliable and might not be taken into account. Based on the estimated parameters we

Fig. 8 The exponential-type conditional intensity function versus time for each subarea of the Central Ionian Islands, fitted to the catalog of earthquakes with $M \geq 5.2$ that occurred since 1911. **a** Kefalonia. **b** Lefkada



can interpret the behavior of the conditional intensity functions for the two subareas. Both transfer parameters are positive, implying inhibitory behavior. The parameter c_{21} was found to be positive; the 90% confidence interval though contains also negative values meaning that the interactions are not robust in the sense that the parameter could also take the value 0 since it is included in the confidence interval.

We can also see that the application of the LSRM reveals that the loading rate $\rho_1 = 1/c_{11}$ of the subarea of Kefalonia is higher than the one of Lefkada, which is in accordance with the tectonic loading in the two subareas quantified by seismological and geodetic observations. In any case, there is close resemblance between the two curves indicating the strong relationship between earthquakes occurring in the two subareas.

LSRM: Weibull-type conditional intensity function

The LSRM is applied to the central Ionian Islands under the assumption of the Weibull-type conditional intensity function. The Newton-type optimization algorithm led to the parameters values presented in Table 2. The maximum value of the log-likelihood function is computed and found equal to -145.4507 . Both transfer parameters θ_{12} and θ_{21}

are estimated and found to be positive. The 90% confidence intervals though are not strictly positive, indicating that the style of interactions between the two subareas based on the LSRM cannot be unambiguously certified. The two curves of the conditional intensity functions (Fig. 9) display similar behavior. The loading rate, ρ_1 , is higher in Kefalonia, which agrees with the more frequent and larger magnitude here than in Lefkada.

The two competing models are assessed via the AIC. The estimated maximum log-likelihood is slightly greater in the classical LSRM than in the Weibull-type LSRM and additionally, the fact that AIC penalizes the extra parameters, the “classical” model of the exponential form is proved to be better. Therefore, although the proposed model of the Weibull form seems to interpret the behavior and the interactions between the two subareas in a similar way with the exponential form, the two extra parameters do not add enough information and, therefore, the new form against the classical one is selected.

ISRM: exponential-type conditional intensity function

The interval estimation presented in Table 4 shows that stress transfer—and particularly damping—is established from the subarea of Lefkada to the subarea of Kefalonia,

Fig. 9 The Weibull-type conditional intensity function versus time for each subarea of the Central Ionian Islands, fitted to the catalog of earthquakes with $M \geq 5.2$ that occurred since 1911

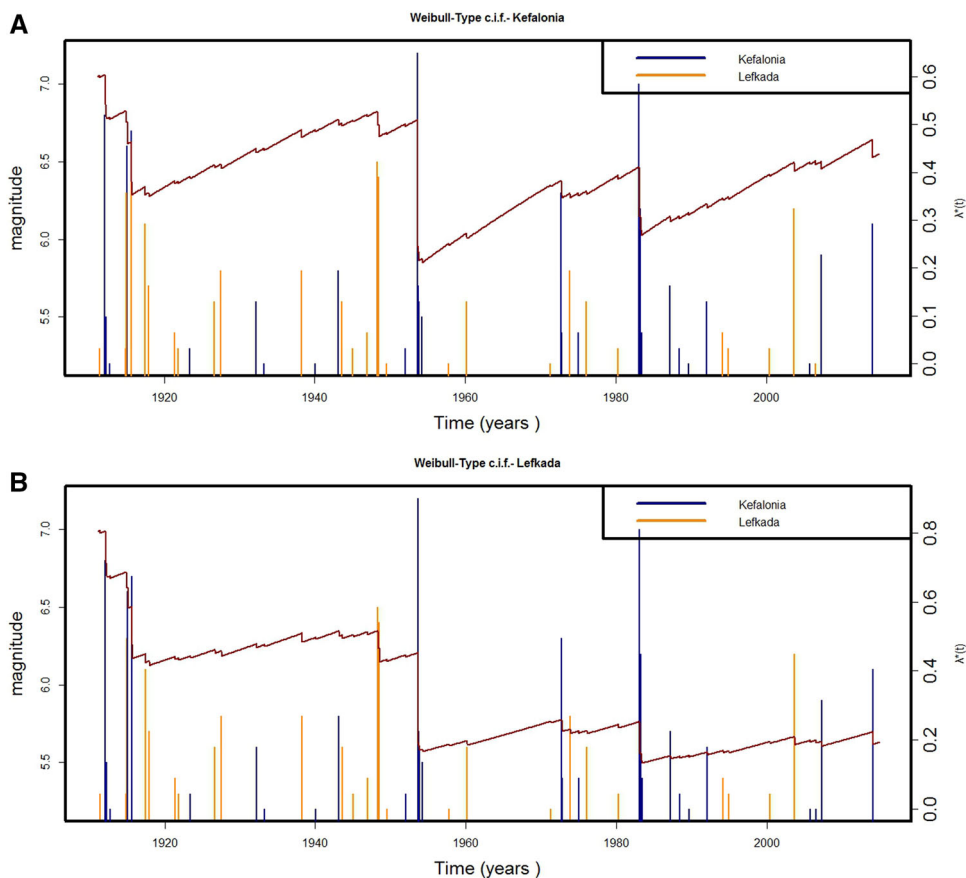


Table 5 Estimated parameters, standard errors and confidence intervals for the ISRM (Lefkada) and the SSRM when using an exponential-type conditional intensity function

Parameter	Estimate		Standard error		90% Confidence interval	
	ISRM (Lef.)	SSRM	ISRM (Lef.)	SSRM	ISRM (Lef.)	SSRM
a	0.172	0.654	0.415	0.317	(-0.511, 0.855)	(0.133, 1.174)
b	0.013	0.018	1.343	0.918	(0.001, 0.115)	(0.004, 0.082)
c	2.721	0.654	0.836	0.402	(0.688, 10.762)	(0.337, 1.267)

Fig. 10 The exponential-type conditional intensity function versus time when applying the ISRM to the subarea of Lefkada

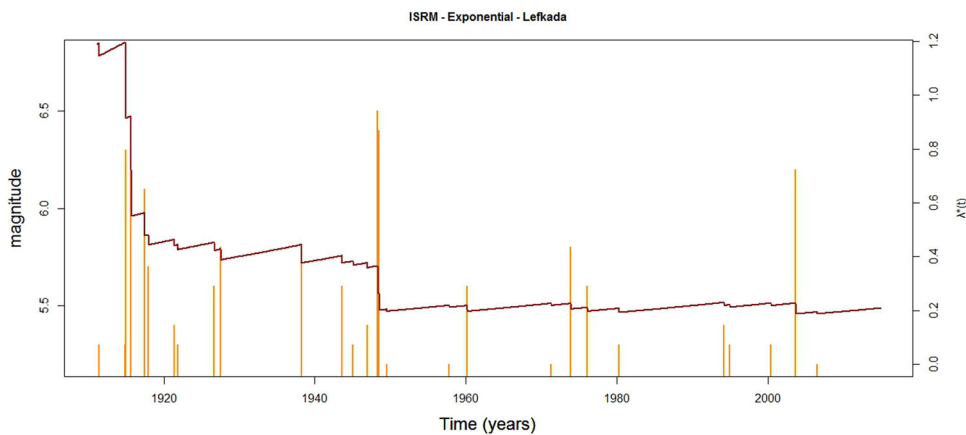


Fig. 11 The Weibull-type conditional intensity function versus time when applying the ISRM to the subarea of **a** Kefalonia, **b** Lefkada

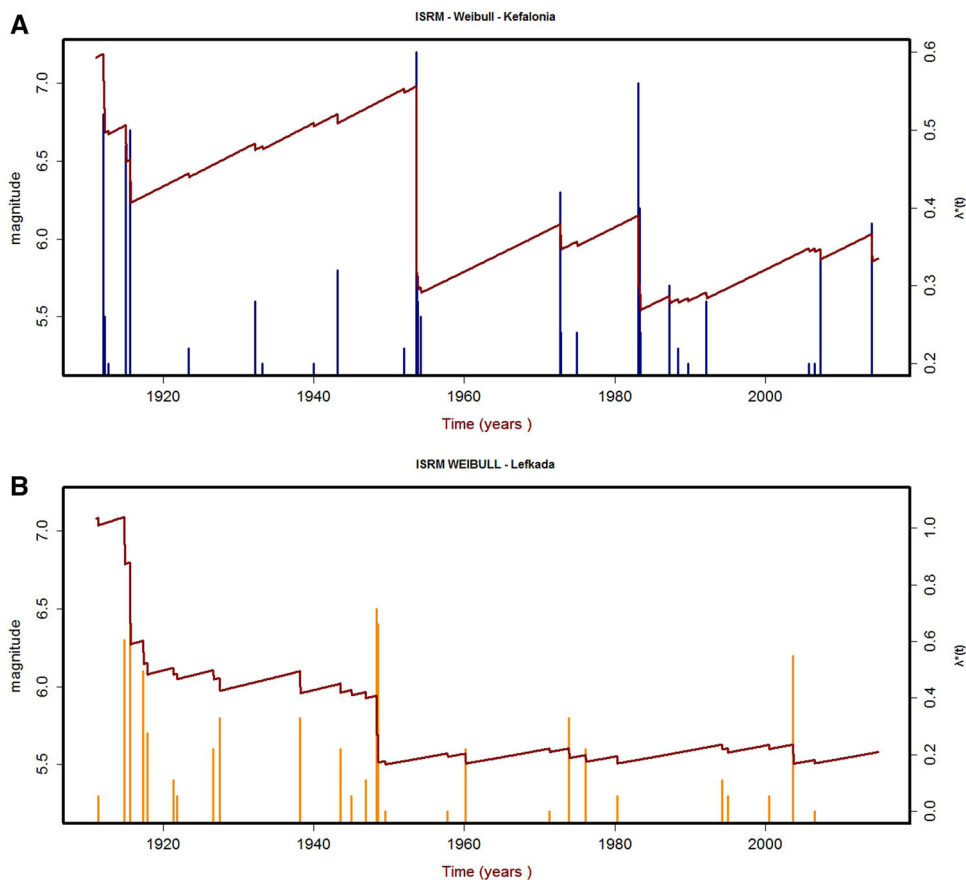


Table 6 Estimated parameters, standard errors and confidence intervals for the ISRM and SSRM in central Ionian Islands when using a Weibull-type conditional intensity function

Parameter	Estimate			Standard error			90% Confidence interval		
	ISRM (Kef.)	ISRM (Lef.)	SSRM	ISRM (Kef.)	ISRM (Lef.)	SSRM	ISRM (Kef.)	ISRM (Lef.)	SSRM
λ	0.0009	0.0005	0.005	7.340	6.367	3.307	$(5.3 \times 10^{-9}, 162.23)$	$(1.4 \times 10^{-8}, 16.941)$	$(2.2 \times 10^{-5}, 1.190)$
γ	2.131	2.564	1.985	0.646	0.521	0.317	(0.737, 6.164)	(1.088, 6.040)	(1.178, 3.345)
$X(0)$	155.051	74.063	152.116	6.563	25.856	9.506	(144.255, 165.848)	(31.530, 116.595)	(136.48, 167.75)
ρ	1.178	0.399	1.759	0.474	0.521	0.190	(0.541, 2.568)	(0.169, 0.940)	(1.287, 2.404)

while the reverse interaction cannot be fully justified. Therefore, the seismicity of the Lefkada subarea can be modeled by means of the ISRM. The estimated parameters are presented in Table 5 and the corresponding c.i.f. is shown in Fig. 10.

ISRM: Weibull-type conditional intensity function

Since both confidence intervals for the parameters θ_{ij} contain the value 0, the interactions between the two subareas are not robust when using a Weibull-type c.i.f. Thus, the ISRM is applied—under appropriate restrictions—using a c.i.f. of the

form of Eq. (6) to fit separately data from the two subareas. The two curves are plotted in Fig. 11.

SSRM: exponential and Weibull-type conditional intensity function

The SSRM was applied for the entire central Ionian Islands area using the two types of the c.i.f. (Tables 5, 6, respectively). The AIC prefers the exponential c.i.f. for better fitting of the data, since the criterion favors the models with fewer parameters. The plots for the two different cases reveal similar behavior (Fig. 12).

Fig. 12 The conditional intensity function versus time when applying the SSRM to the Central Ionian Islands using **a** an exponential-type c.i.f., **b** a Weibull-type c.i.f

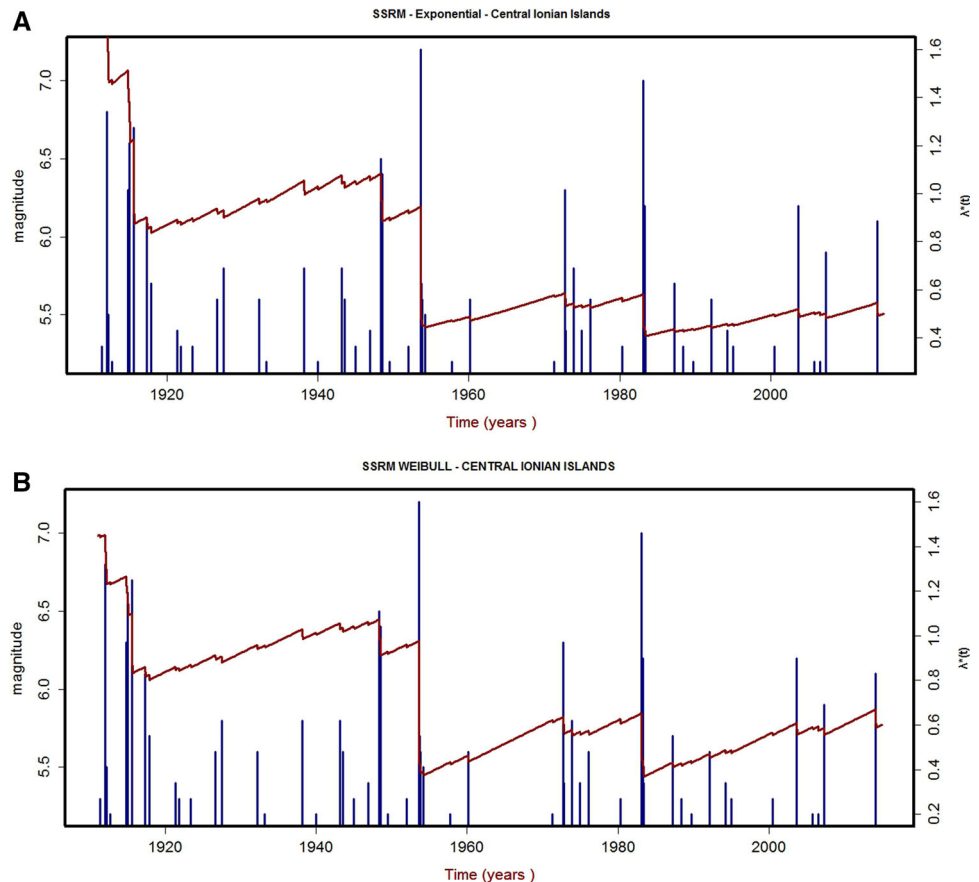
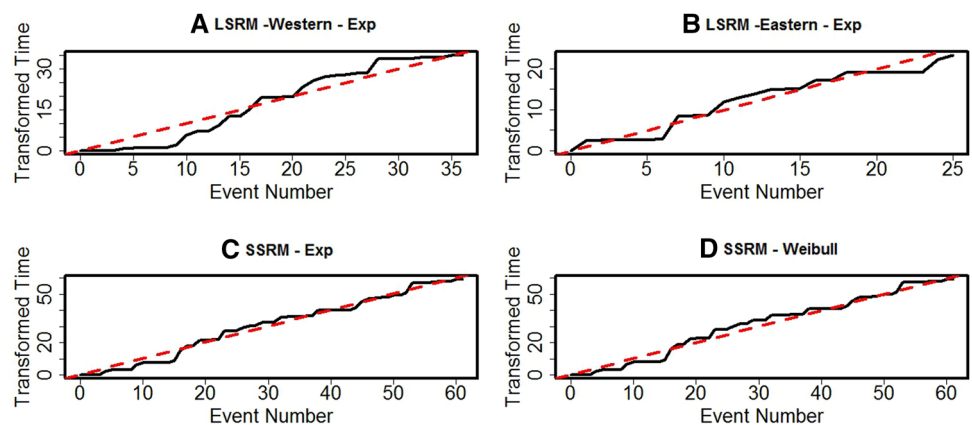


Fig. 13 Residual analysis of **a** the LSRM for the western part of the Corinth Gulf using an exponential c.i.f., **b** the LSRM for the eastern part of the Corinth Gulf using an exponential c.i.f. **c** the SSRM using an exponential c.i.f. **d** the SSRM using a Weibull-type c.i.f



Model fitting

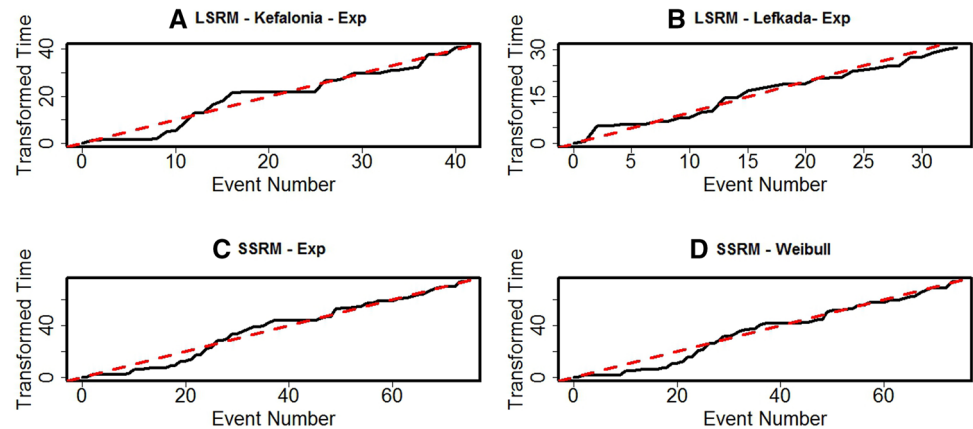
For the model evaluation a residual analysis is performed (Ogata 1981). The goodness-of-fit of a point process model is tested using time transformation. The transformed process will be unit-rate Poisson, if the true model is adequately explained, whereas systematic deviation of the data from the fitted model would mean that an important feature is not yet included in the model. Residual analysis is performed to the models applied for both study areas. Figures 13 and 14 show some of the results for the sake of brevity. In general, the

real number of events is in agreement with the number of events that emerges from the models. We should also notice that the results favor the use of the exponential c.i.f..

Discussion and conclusions

In summary, despite its simplicity, the LSRM achieves to combine simple and basic ideas into a stochastic framework and could be taken into account as a first step towards the understanding of coupling and the interactions between

Fig. 14 Residual analysis of **a** the LSRM for the subarea of Kefalonia using an exponential c.i.f. **b** the LSRM for the subarea of Lefkada using an exponential c.i.f. **c** the SSRM using an exponential c.i.f. **d** the SSRM using a Weibull-type c.i.f.



areas. It is applied to fit earthquake data from the Corinth Gulf and the central Ionian Islands areas, which are among the most seismically active ones in Europe. The behavior of the point process is determined by the conditional intensity function (c.i.f.). A Weibull-type c.i.f. is proposed, as a more flexible alternative than the one having an exponential-type. Although the curves are quite similar, the Akaike information criterion, which is used in order to evaluate competing models, in both cases clearly favors the use of the “classical” exponential form. The regionalization is an important aspect that arises when applying LSRM. In our case, the two study areas are divided based on seismotectonic criteria, comprise enough data for the numerical optimization to be performed.

The interaction between different parts of an area is of major importance. An earthquake could accelerate or delay a second one, even at a quite distant area within a period of some years. Although the results do not reveal clearly the kind of interactions and the coupling between subareas, evidence is provided that the interactions imply damping from each subarea to another in both cases, the Corinth Gulf and central Ionian Islands. The motivation of finding out the style of interactions led to the application of the SSRM in the cases where the relation between earthquakes occurring in each subarea could not be proved.

The SSRM was applied in the western part of the Corinth Gulf by Rotondi and Varini (2006), and their results although based on different data samples and regionalization, are similar with ours regarding the shape and the trend of the conditional intensity functions. Our results regarding the central Ionian Islands are also comparable with those of Votsi et al. (2011) since both transfer parameters are found positive in both studies.

Particular attention was paid to computational issues. One of the main drawbacks of the maximum likelihood estimation (MLE) method, which is adopted for parameter estimation, is the sensitivity on the initial values used. The parameter space was scanned numerically using a dense

grid after taking also into account the model restrictions. These values were then used for examining the convergence and investigating the maximum of the log-likelihood function. Besides point estimation, interval estimation was also performed for the results to be more robust. The aim of stochastic modeling is the combination of both geophysical meaning and algorithm convergence.

Acknowledgements The authors would like to express their sincere appreciation to Prof. Tsaklidis for his valuable comments and critically reading of the manuscript. The maps were produced using the GMT software (Wessel and Smith 1998) Geophysics Department contribution 000.

References

- Akaike H (1974) A new look at the statistical model identification. *IEEE Trans Autom Control* 19(6):716–723
- Aristotle University of Thessaloniki Seismological Network (1981) Permanent regional seismological network operated by the aristotle university of thessaloniki. International Federation of Digital Seismograph Networks. Other/ Seismic Network. doi:10.7914/SN/HT
- Armijo R, Meyer B, King GCP, Rigo A, Papanastassiou D (1996) Quaternary evolution of the Corinth Rift and its implications for the late Cenozoic evolution of the Aegean. *Geophys J Int* 126:11–53
- Bebbington M (2005) Information gains for stress release models. *Pure Appl Geophys* 162:2229–2319
- Bebbington M, Harte D (2001) On the statistics of the linked stress release process. *J Appl Probab* 38:176–187
- Bebbington M, Harte D (2003) The linked stress release model for spatio-temporal seismicity: formulations, procedures and applications. *Geophys J Int* 154:925–946
- Borovkov K, Bebbington M (2003) A simple two-node stress transfer model reproducing Omori’s law. *Pure Appl Geophys* 160:1429–1445
- Bufe C, Varnes D (1993) Predictive modeling of the seismic cycle of the greater San Francisco bay region. *J Geophys Res* 98:9871–9883
- Console R, Falcone G, Karakostas V, Murru M, Papadimitriou E, Rhoades D (2013) Renewal models and coseismic stress transfer in the Corinth Gulf Greece, fault system. *J Geophys Res* 118:3655–3673

- Daley D, Vere-Jones D (2003) An introduction to the theory of point processes, vol 1, 2nd edn. Springer, New York, pp 211–287
- Gabrielov A, Newman WI (1994) Seismicity modelling and earthquake prediction: a review. In: Newman WI, Gabrielov A, Turcotte DL (eds) Nonlinear dynamics and predictability of geophysical phenomena. Am Geophys Union, Washington, DC, pp 7–13
- Harte DS, Vere-Jones D (2005) The entropy score and its uses in earthquake forecasting. *Pure Appl Geophys* 162:1229–1253
- Imoto M, Huruikawa N (2006) Assessing potential seismic activity in Vrancea, Romania, using a stress-release model. *Earth Planets Space* 58:1511–1514
- Isham V, Westcott M (1979) A self-correcting point process. *Stoch Process Appl* 8:335–347
- Jackson JA, White NJ (1989) Normal faulting in the upper continental crust: observations from regions of active extension. *J Struct Geol* 11:15–36
- Jiang M, Zhu S, Chen Y, Ai Y (2011) A new multidimensional stress release statistical model based on coseismic stress transfer. *Geophys J Int* 187:1479–1494
- Kagan Y, Jackson D (1991) Long-term earthquake clustering. *Geophys J Int* 104:117–133
- Kanamori H, Anderson DL (1975) Theoretical basis of some empirical relations in seismology. *Bull Seismol Soc Am* 65(5):1073–1095
- Liu J, Vere-Jones D, Ma L, Shi Y, Zhuang JC (1998) The principal of coupled stress release model and its application. *Acta Seismologica Sinica* 11:273–281
- Liu C, Chen Y, Shi Y, Vere-Jones D (1999) Coupled stress release model for time-dependent seismicity. *Pure Appl Geophys* 155:649–667
- Lu C (2005) The degree of predictability of earthquakes in several regions of China: statistical analysis of historical data. *J Asian Earth Sci* 25:379–385
- Lu C, Vere-Jones D (2000) Application of linked stress release model to historical earthquake data: comparison between two kinds of tectonic seismicity. *Pure Appl Geophys* 157:2351–2364
- Lu C, Vere-Jones D (2001) Statistical analysis of synthetic earthquake catalogs generated by models with various levels of fault zone disorder. *J Geophys Res* 106(B6):11115–11125
- Lu C, Harte D, Bebbington M (1999) A linked stress release model for historical Japanese earthquakes: coupling among major seismic regions. *Earth Planets Space* 51:907–916
- Ogata Y (1981) On Lewis's simulation method for point processes. *IEEE Trans Inf Theory* 27:23–31
- Papadimitriou EE (2002) Mode of strong earthquake recurrence in the Central Ionian Islands (Greece): possible triggering due to Coulomb stress changes generated by the occurrence of previous strong shocks. *Bull Seismol Soc Am* 92(8):3293–3308
- Papazachos BC, Papazachou CC (2003) The earthquakes of Greece. Ziti Publications, Thessaloniki
- Papazachos BC, Karakaisis GF, Papadimitriou EE, Papaioannou ChA (1997) Time dependent seismicity in the Alpine-Himalayan belt. *Tectonophysics* 271:295–324
- Reid H (1910) The mechanics of the earthquake, The California earthquake of april 18, 1906. Report of the state investigation commission, vol 2. Carnegie Institution of Washington, Washington, DC, pp 16–28
- Rotondi R, Varini E (2006) Bayesian analysis of marked stress release models for time-dependent hazard assessment in the western Gulf of Corinth. *Tectonophysics* 423:107–113
- Rotondi R, Varini E (2007) Bayesian inference of stress release models applied to some seismogenic zones. *Geophys J Int* 169:301–314
- Scordilis EM, Karakaisis GF, Karakostas BG, Panagiotopoulos DG, Comninakis PE, Papazachos BC (1985) Evidence for transform faulting in the Ionian Sea: The Cephalonia island earthquake sequence of 1983. *Pure Appl Geophys* 123:388–397
- Varini E, Rotondi R (2015) Probability distribution of the waiting time in the stress release model: the Gompertz distribution. *Environ Ecol Stat* 22:493–511
- Vere-Jones D (1978) Earthquake prediction—a statistician's view. *J Phys Earth* 26(2):129–146
- Vere-Jones D, Deng YL (1988) A point process analysis of historical earthquakes from North China. *Earthq Res China* 2:165–181
- Votsi I, Tsaklidis G, Papadimitriou E (2011) Seismic hazard assessment in Central Ionian Islands Area based on stress release models. *Acta Geophys* 59:701–727
- Wessel P, Smith WHF (1998) New, improved version of the generic mapping tools released. *Trans Am Geophys Union* 79:579
- Zheng X, Vere-Jones D (1994) Further applications of the stochastic stress release model to historical earthquake data. *Tectonophysics* 229:101–121

Study of the seismic activity in central Ionian Islands via semi-Markov modelling

Christina Elisavet Pertsinidou^{1,3} · George Tsaklidis¹ · Eleftheria Papadimitriou²

Received: 28 December 2016 / Accepted: 17 April 2017 / Published online: 25 April 2017
© Institute of Geophysics, Polish Academy of Sciences & Polish Academy of Sciences 2017

Abstract The seismicity of the central Ionian Islands ($M \geq 5.2$, 1911–2014) is studied via a semi-Markov chain which is investigated in terms of the destination probabilities (occurrence probabilities). The interevent times are considered to follow geometric (in which case the semi-Markov model reduces to a Markov model) or Pareto distributions. The study of the destination probabilities is useful for forecasting purposes because they can provide the more probable earthquake magnitude and occurrence time. Using the first half of the data sample for the estimation procedure and the other half for forecasting purposes it is found that the time windows obtained by the destination probabilities include 72.9% of the observed earthquake occurrence times (for all magnitudes) and 71.4% for the larger ($M \geq 6.0$) ones.

Keywords Semi-Markov model · Destination probabilities · Entrance probabilities · Seismic hazard assessment

Introduction

The semi-Markov model describes the temporal evolution of a system, where its current state depends only on the previous one and the involved interevent times of the process can follow any desired distribution (Barbu and Limnios 2008). When it is applied to an earthquake catalogue (where the system states represent magnitude classes and the interevent time corresponds to the elapsed time between two successive earthquakes), then the model can provide useful probabilities for the earthquake occurrences. It is also applied in many fields such as, meteorology, medicine and DNA analysis. For example, applications in DNA analysis can be found in Barbu and Limnios (2008).

A semi-Markov chain was firstly applied on the seismic zones of the circum-Pacific belt for investigating the large ($M \geq 7.8$) earthquakes recurrence (Patwardhan et al. 1980). Historical seismicity data were used and the estimated interevent times and magnitudes were close to the observed seismicity. Cluff et al. (1980) studied the Wasatch fault zone (Utah) and calculated the occurrence probability of at least one earthquake with $M \geq 6.5$ in each one of the Kaysville and Hubble Creek segments. They found that if the elapsed time after an earthquake occurrence with $M \geq 6.5$ was 2200 years, then the probability for another large event to occur in the Kaysville segment in a 50-year period is 0.8.

Anagnos and Kiremidjian (1984) applied a semi-Markov model to the Parkfield segment of the San Andreas Fault. They considered the case of Weibull distributed interevent times and found that the occurrence probabilities within 20 years increased with time. To the contrary these probabilities were found to be constant for the Poisson model. Lutz and Kiremidjian (1995) developed a generalized semi-Markov process for the northern San Andreas

✉ Christina Elisavet Pertsinidou
p.eli.christina@gmail.com

George Tsaklidis
tsaklidi@math.auth.gr

Eleftheria Papadimitriou
ritsa@geo.auth.gr

¹ Department of Mathematics, Aristotle University of Thessaloniki, Thessaloniki, Greece

² Department of Geophysics, Aristotle University of Thessaloniki, Thessaloniki, Greece

³ Université de Technologie de Compiègne, Sorbonne Universités, LMAC Laboratoire de Mathématiques Appliquées de Compiègne, Compiègne, France

Fault which was divided into three segments, i.e., the North Coast, the San Francisco Peninsula and the South Santa Cruz Mountains segments. These segments were further separated into cells (20 km each) and the states of the model corresponded to the amount of slip accumulated on each of these cells. By performing simulations, it was found that an earthquake with $M_w \geq 6.5$ was anticipated to occur every 64.5 years and an earthquake with $M_w \geq 7.9$ every 345 years.

Al-Hajjar and Blanpain (1997) selected random after-shock sequences from the seismic database “Commissariat à l’Energie Atomique” from different regions around the world and formed 223 datasets (1984–1989) each one containing one mainshock and the respective aftershock sequence. They adopted semi-Markov modelling selecting four magnitude categories $5.5 \leq M_1 < 6.5$, $4.5 \leq M_2 < 5.5$, $3.5 \leq M_3 < 4.5$ and $M_4 < 3.5$. They studied the aftershock activity duration, which was found to be equal to 130 days for mainshocks of category M_1 and 58 days for mainshocks of the second class.

Altinok and Kolcak (1999) applied a semi-Markov model in the north Anatolian fault zone ($M \geq 5.5$, 1902–1992). They evaluated magnitude to magnitude interval transition probabilities and found out that a moderate event ($5.5 \leq M < 6.0$) will be probably followed by another moderate one, with a decreasing probability, whereas a larger one ($6.0 \leq M$) will be followed by a moderate event with an increasing probability.

Sadeghian et al. (2008) developed semi-Markov models to study the seismicity of Iran for forecasting the time, location and magnitude of an earthquake occurrence. They divided the study area into zones and classified the 3179 events of the dataset (1973–2007) into five classes, i.e., $3.1 \leq m_b \leq 3.6$, $3.6 < m_b \leq 4.8$, $4.8 < m_b \leq 5.4$, $5.4 < m_b \leq 6.3$, $6.3 < m_b \leq 7.1$. With respect to the estimated probabilities 42% of the last 179 earthquakes were forecasted in all dimensions, 16% of these earthquakes were forecasted only as for their location, 16% only as for their magnitude and 26% of the earthquakes were not forecasted at all. Masala (2012) applied homogeneous and non-homogeneous discrete time semi-Markov models using a dataset (1900–2002) from the Italian National Institute of Geophysics and Volcanology. The data were classified into three states with $M_w < 4.7$, $4.7 \leq M_w < 5.0$ and $M_w \geq 5.0$. The interevent time distribution was considered to follow the generalized Weibull distribution. The estimated transition probabilities were found to decrease with time in case of $i = j$ (for two successive earthquake categories) and increase with time when $i \neq j$ for all the models. The probability that the ensuing earthquake will be of category j within a time interval Δx given that the previous earthquake was of state i and occurred at time t_0 , was found to increase with respect to Δx and t_0 .

Votsi et al. (2012) applied a continuous-time semi-Markov model to a complete catalog from the North Aegean Sea ($M \geq 5.5$, 1953–2007). The data were classified into three states (categories) $5.5 \leq M \leq 5.6$, $5.7 \leq M \leq 6.0$ and $6.1 \leq M \leq 7.2$. It was found that the probability of an earthquake occurrence increases with time while the estimated hitting times for different subregions (with similar fault characteristics) present similar values.

The seismicity of the same area was studied (1845–2008, $M \geq 6.5$) via a discrete-time semi-Markov model (Pertsinidou 2013) assuming that the interevent times follow either geometric or discrete Weibull distributions. The data were classified into two or three categories. Different state classification and distribution consideration is important since the model that better describes the area’s seismicity is unknown and thus further investigation is required. The model parameters were estimated and the kernel probabilities were evaluated for all cases. The geometric probabilities of the 3D model were found to decay faster with time with respect to the discrete Weibull probabilities, as expected. An interesting result derived for all the different case studies, is that a smaller earthquake occurrence ($6.5 \leq M < 7.0$) is anticipated to be followed by a large event ($M \geq 7.0$) mostly within the next 5 years.

The present research aims to extend the study in Pertsinidou (2016) of the central Ionian Islands seismicity (1911–2014, $M \geq 5.2$) by considering semi-Markov models with geometric or Pareto distributed interevent times. More precisely, in “Study area and data used” the study area and the data are presented. In “Definition of the semi-Markov context” the semi-Markov context is provided and explained thoroughly. In “Destination probabilities for the model with geometric interevent times” and “Destination probabilities for the model with Pareto distributed interevent times” the interevent times are considered to follow geometric and Pareto distributions in order to demonstrate how these characteristic distributions can be used for the evaluation of the model’s destination probabilities. The estimation procedure of the model’s parameters is achieved using the whole dataset. In “Optimal model” the optimal model is selected by means of the Akaike and Bayesian information criteria. In “Forecasting with the model with geometric interevent times” and “Forecasting using the model with Pareto distributed interevent times” we use the first half of the data for reestimating the model parameters and the other half for forecasting purposes. In “Optimal model” the optimal model of “Forecasting with the model with geometric interevent times” and “Forecasting using the model with Pareto distributed interevent times” is selected. In “Conclusions” conclusions are discussed.

Study area and data used

The study area includes the Kefalonia and Lefkada Islands (Fig. 1) where strong ($M \geq 6.0$) earthquakes frequently occur (Papadimitriou 2002). The area is dominated by the Kefalonia Transform Fault Zone (KTFZ) of dextral strike-slip character (Scordilis et al. 1985), joining a continental collision to the north, between the Apulian microplate and Greek mainland, and subduction of the Eastern Mediterranean oceanic plate under the Aegean microplate to the south. The boundaries of this zone are well confined according to its seismotectonic and structural characteristics (Kokinou et al. 2006) and the complexity of the seismicity behaviour is highlighted (Karakostas and Papadimitriou 2010).

The dataset is comprised by earthquakes with magnitude $M \geq 5.2$ that occurred from 1911 to 2014 (<http://geophysics.geo.auth.gr/ss/>), and is used in order to set up a semi-Markov model, with time unit of one month. The catalogue is complete for this time period and magnitude. When two (or more) earthquakes occur in the same time unit only the larger one is considered. The data (80 events) are classified into two categories, i.e., state 1: $5.2 \leq M < 6.0$ and state 2: $M \geq 6.0$. For the data classification we take into consideration that an adequate number of earthquakes must be included in each category for the estimation procedure to be statistically robust. Moreover, events with $M \geq 6.0$ can cause severe damage in the study area and moderate seismicity ($5.2 \leq M < 6.0$) can also be

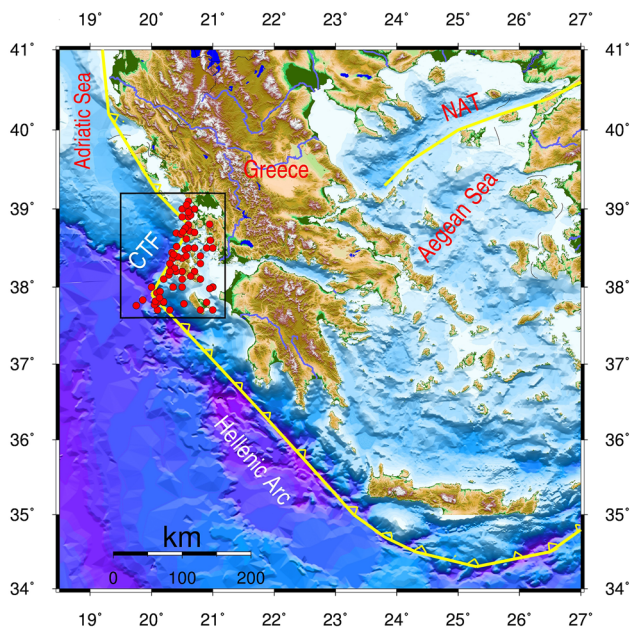


Fig. 1 The main seismotectonic characteristics of the Aegean region. NAT North Aegean Trough, CTF Cephalonia Transform Fault. The study area is indicated by a rectangle and the epicenters of the earthquakes of the dataset are plotted as red circles

disastrous for inhabited areas. Figure 2 depicts the earthquake magnitudes that occurred in the study area from 1911 to 2014. Table 1 presents the mean value as well as the variance of these magnitudes firstly for the entire dataset and then for the aforementioned two categories.

Definition of the semi-Markov context

Following Barbu and Limnios (2008), we define J_n as the system’s state (earthquake category) at the n th jump time S_n (time of the n th earthquake occurrence). We denote by $X_n := S_n - S_{n-1}$ ($n \in \mathbb{N}^*$), with $X_0 := 0$, the interevent time J_{n-1} , between the $(n - 1)$ th and the n th earthquake. We also denote by $P = (p_{ij})_{i,j \in E}$ the transition matrix of the model, i.e.,

$$p_{ij}(k) := \mathbb{P}(X_{n+1} = k | J_n = i, J_{n+1} = j), \quad k \in \mathbb{N}, \quad (1)$$

which represents the probability that an earthquake of category i will be followed by an earthquake of category j , and by $f_{ij}(\cdot)$ the common probability function of the interevent times X_{n+1} , $n \in \mathbb{N}$, conditioned on J_n and J_{n+1} :

$$f_{ij}(k) := \mathbb{P}(X_{n+1} = k | J_n = i, J_{n+1} = j), \quad k \in \mathbb{N}. \quad (2)$$

The semi-Markov chain is denoted by $Z = (Z_k)_{k \in \mathbb{N}}$. The maximum likelihood estimation of the (i, j) -element of the P matrix is $\hat{p}_{ij}(M) = N_{ij}(M)/N_i(M)$, where $N_i(M)$ represents the number of earthquakes of category i up to time M and $N_{ij}(M)$ stands for the number of two successive earthquakes of states i, j up to time M . The survival function of the interevent time distribution is defined as (Howard 1971)

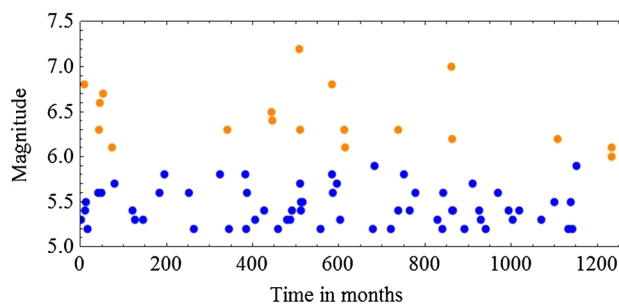


Fig. 2 Graph of the earthquake magnitudes that occurred in the study area (from 1911 to 2014) vs time in months

Table 1 Mean and variance of the earthquake magnitudes

	Mean magnitude	Magnitude variance
Entire dataset	5.68	0.23
State 1 ($5.2 \leq M < 6.0$)	5.44	0.042
State 2 ($M \geq 6.0$)	6.43	0.11

$$\bar{f}_{ij} = \sum_{m=f+1}^{\infty} f_{ij}(m), \quad k = 0, 1, 2, \dots \tag{3}$$

Now, let $e_{ij}(z|u)$ denote the entrance probability, i.e., the probability for the chain which entered state i at time 0 to enter state j at time u with z transitions by that time (Howard 1971). In other words, $e_{ij}(z|u)$ represents the probability for an earthquake of category j to occur at time u given that an earthquake of category i occurred at time 0, and the number of earthquakes in the time period $(0, u]$ is z . The entrance probability $e_{ij}(z|u)$ is given by the recursion (4)

$$e_{ij}(z|u) = \delta_{ij}\delta(u)\delta(z) + \sum_{r=1}^N \sum_{m=1}^u p_{ir}f_{ir}(m)e_{rj}(z-1|u-m) \tag{4}$$

where

$$\delta_{ij} = \begin{cases} 1 & \text{if } i = j \\ 0 & \text{if } i \neq j \end{cases} \quad \text{and} \tag{5}$$

$$\delta(z) = \begin{cases} 1 & \text{if } z = 0 \\ 0 & \text{elsewhere} \end{cases} \quad \text{and} \quad e_{ij}(0|u) = \delta_{ij}\delta(u)$$

Here we are interested in the destination (occurrence) probability $\gamma_{ijq}(z|u)$, defined as the probability for a chain which was in state i at a starting time 0, to enter state j at time u with z transitions by that time and will make its next transition to state q . This quantity corresponds to the probability that given that an earthquake of state i occurred at the starting time 0, an earthquake of state j will occur at time u , whereas in the period $(0, u]$ the number of earthquakes will be z , and the event of state j will be followed by an event of state q . For this application, u represents time units in months. The following recursion demonstrates that the destination probability $\gamma_{ijq}(\cdot|\cdot)$ is the convolution of the entrance probability $e_{ij}(\cdot|\cdot)$ and the survival function of the interevent time distribution $\bar{f}_{jq}(u-m)$ multiplied by the transition probability p_{jq} (Howard 1971), that is

$$\gamma_{ijq}(z|u) = \sum_{m=1}^u e_{ij}(z|m)p_{jq}\bar{f}_{jq}(u-m), \tag{6}$$

where $i, j, q, z, u = 1, 2, \dots, \mathbb{N}$. For a better understating, Fig. 3 illustrates the afore-described semi-Markov model.

Destination probabilities for the model with geometric interevent times

Firstly, we consider geometric distributed interevent times with probability mass function (Alhajj 2014)

$$f_{ij}(k) = (1 - a_{ij})^{k-1}a_{ij}, \quad k \in \{1, 2, 3, \dots\}$$

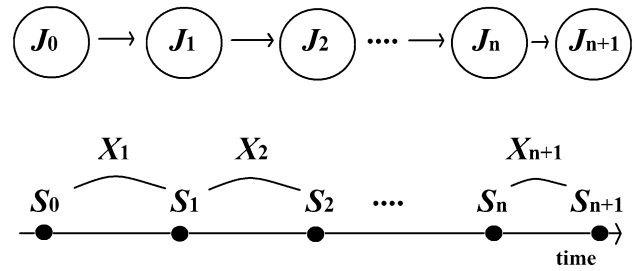


Fig. 3 Semi-Markov model. J_n earthquake category, S_n time of the n th earthquake occurrence, X_{n+1} interevent time

where $0 < a_{ij} < 1$ is the success probability. Notice that in this case the semi-Markov model reduces to a Markov model. The evaluated transition probability matrix P is given by

$$P = \begin{pmatrix} 0.7705 & 0.2295 \\ 0.6842 & 0.3158 \end{pmatrix},$$

indicating that there is a higher probability for an earthquake of category 1 to be followed by one of the same state ($p_{11} = 0.7705$), whereas an event of category 2 will be followed by one of state 1 with probability $p_{21} = 0.6842$.

The maximum likelihood estimator for the parameter of the geometric distribution is $\hat{a}_{ij} = 1/\bar{X}_n$, where \bar{X}_n represents the mean value of the interevent times. The estimated interevent time distributions are:

$$f_{11}(k) = (1 - 0.0561)^{k-1}0.0561, \quad f_{12}(k) = (1 - 0.0617)^{k-1}0.0617,$$

$$f_{21}(k) = (1 - 0.1057)^{k-1}0.1057, \quad f_{22}(k) = (1 - 0.1724)^{k-1}0.1724.$$

The matrix which provides the survival functions of the geometrically distributed interevent times is

$$\bar{F}(k) = \begin{pmatrix} (1 - 0.0561)^k & (1 - 0.0617)^k \\ (1 - 0.1057)^k & (1 - 0.1724)^k \end{pmatrix}$$

where the (i, j) -element is given by the Eq. (7):

$$\bar{f}_{ij}(k) = \sum_{m=k+1}^{\infty} (1 - a_{ij})^{(m-1)}a_{ij} = (1 - a_{ij})^k. \tag{7}$$

Next, by applying the Mann–Whitney (Mann and Whitney 1947) and the Anderson–Darling (Anderson and Darling 1952) tests (see Belosta 2015) it is found that for all the cases the p values are larger than $\alpha = 0.05$. Hence, the geometric distribution assumption for describing the interevent times cannot be rejected. We would like to mention that these tests are usually implemented in the case of continuous distributions, such as the Pareto of the next section.

As an example it will be shortly presented that the destination probabilities can be used to model the magnitude category of three earthquakes as well as the occurrence time of the second. Analytical discussion and forecasting results are demonstrated in “Forecasting with the model with geometric interevent times” and “Forecasting using the model with Pareto distributed interevent

times”. Let us consider that we start to observe the process on 24-05-1911 when an earthquake of state (category) 1 occurs ($M = 5.3$). We know that the next state-2 event occurred on 24-01-1912 ($M = 6.8$) and the elapsed time between these earthquakes is $u = 8$ months. We want to evaluate the probability that the third event will be of state $q = 1$ or $q = 2$. The evaluated destination (occurrence) probabilities are $\gamma_{121}(1|8) = 0.0422$ and $\gamma_{122}(1|8) = 0.0154$, respectively. Therefore, it is 2.74 times more probable the third event to be of state 1, and observing our data we realize that this is true. The fact that the calculated probabilities are rather small is because there exist too many different combinations of the parameters i, j, q, z, u (explained in “Definition of the semi-Markov context”) and each case exhibits a certain probability, however, even if they are small they are comparable.

Aiming now at investigating the more probable occurrence time of a state-2 event (earthquake), given that the previous one was of state 1 (on 07-1961) and the next event will be of state 2 we calculate the probabilities $\gamma_{122}(1|u)$ for $0 < u < 50$ months. Figure 4 illustrates that the more probable occurrence time is almost 9 months because it corresponds to the maximum value in the graph and this is in agreement with the data. The forecasting ability of the model with geometric distributed interevent times is further studied in “Forecasting with the model with geometric interevent times”.

Destination probabilities for the model with Pareto distributed interevent times

Pareto is a characteristic continuous heavy tailed distribution, that allows the interevent times to take larger values compared to other common distributions. It is also used by

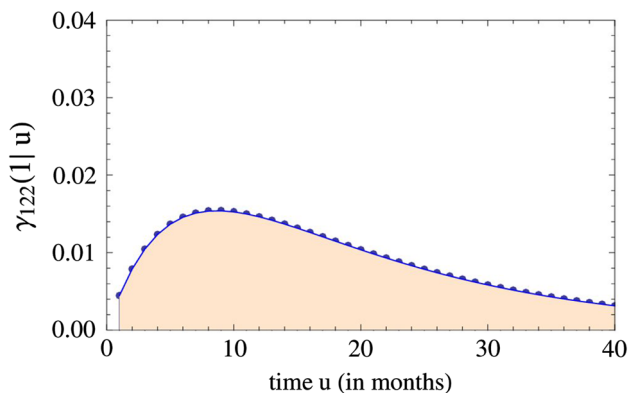


Fig. 4 The destination (occurrence) probabilities $\gamma_{122}(1|u)$ illustrate that the first earthquake of state 2 (10-04-1962) is more probable to occur almost 9 months after the 07-1961

Kagan (2002) to describe the seismic moment-frequency relation. Despite the fact that we consider discrete-time semi-Markov modelling, we will use the Pareto distribution as an approximation because the interevent times of our dataset were found to take also very large values. Relation (8) presents the probability density function (pdf) of the Pareto distribution (Malik 1970)

$$f(k) = \frac{ab^a}{k^{a+1}}, \quad k \geq b, b > 0, a > 0. \tag{8}$$

The maximum likelihood estimators of the parameters a and b are (Malik 1970)

$$\hat{b} = \min_i(k_i), \quad (i = 1, 2, \dots, n) \quad \text{and} \tag{9}$$

$$\hat{a} = \frac{n}{\sum_i (\ln(k_i) - \ln \hat{b})}.$$

Thus, the estimated probability density functions are found to be,

$$f_{11}(k) = \frac{0.418}{k^{0.418+1}}, \quad f_{12}(k) = \frac{0.465}{k^{0.465+1}},$$

$$f_{21}(k) = \frac{0.823}{k^{0.823+1}}, \quad f_{22}(k) = \frac{0.904}{k^{0.904+1}}.$$

The survival function of the interevent time distribution is

$$\bar{f}(k) = \sum_{m=k+1}^{\infty} f(m) = \alpha b^a \zeta(1 + a, 1 + k) \tag{10}$$

where ζ denotes the Hurwitz Zeta function given by relation (11), (Miller and Adamchik 1998)

$$\zeta(s, r) = \sum_{n=0}^{\infty} \frac{1}{(n+r)^s}. \tag{11}$$

By applying the Mann–Whitney test it was found that for all the cases the p values are larger than $\alpha = 0.05$, which means that the Pareto distribution can be accepted as an approximation. As in “Destination probabilities for the model with geometric interevent times”, we consider that we start to observe the process on 24-05-1911 when an event of state 1 occurs ($M = 5.3$). Given that the next state-2 earthquake occurred on 24-01-1912 ($M = 6.8$) the elapsed time is $u = 8$ months while $z = 1$ (z is analytically explained in “Study area and data used”), we will calculate the probability of the third earthquake occurrence. The respective probabilities are $\gamma_{121}(1|8) = 0.039$ and $\gamma_{122}(1|8) = 0.0161$, which means that it is 2.41 times more probable the third event to be of state 1 rather than state 2.

The destination probabilities derived while using the Pareto distribution are larger compared to the probabilities derived through the geometric distributions, however, the graphs for the Pareto do not present a maximum in their curves and in this sense they do not provide useful results concerning the earthquake occurrence time.

Optimal model

In this section we select the optimal model by means of the Akaike (AIC) (Akaike 1974) and Bayesian (BIC) (Schwarz 1978) information criteria. The AIC value is $AIC = 2k - 2\ln(L)$ where k is the number of free parameters of the model and L denotes the likelihood value. The semi-Markov model with the smaller AIC and BIC values is considered to be the optimal. The likelihood function of a semi-Markov model is (Barbu and Limnios 2008)

$$L(M) = \prod_{k=1}^{N(M)} P_{J_{k-1}J_k} f_{J_{k-1}J_k}(X_k) \tag{12}$$

The BIC value is provided by the formula $BIC = k\ln(m) - 2\ln(L)$, where m represents the number of observations. From Table 2 it is concluded that the optimal model is the one with the geometric interevent times.

Forecasting with the model with geometric interevent times

In this section we aim to test the forecasting performance of the model with geometric interevent times. For that reason, we will now use for the estimation process only the first 42 earthquakes of our catalog that occurred in the time interval 1911–1959 and we will use the remaining 38 events for forecasting purposes. The reestimated transition probability matrix is:

$$P = \begin{pmatrix} 0.754 & 0.246 \\ 0.82 & 0.18 \end{pmatrix}$$

The geometric probability mass functions of the interevent times are:

$$f_{11}(k) = (1 - 0.052)^{k-1} \cdot 0.052, \quad f_{12}(k) = (1 - 0.087)^{k-1} \cdot 0.087, \\ f_{21}(k) = (1 - 0.258)^{k-1} \cdot 0.258, \quad f_{22}(k) = (1 - 0.12)^{k-1} \cdot 0.12.$$

The matrix with the survival functions of the interevent times is:

$$\bar{F}(k) = \begin{pmatrix} (1 - 0.052)^k & (1 - 0.087)^k \\ (1 - 0.258)^k & (1 - 0.12)^k \end{pmatrix}.$$

We assume that we start to observe the process on 23-02-1960 when a state-1 earthquake occurred. Given that the

next state-1 earthquake occurred on 05-11-1960, and that the elapsed time is $u = 9$ months (and $z = 1$), we will calculate the probability that the third event will be of state 1 or 2. The corresponding destination probabilities are $\gamma_{111}(1|9) = 0.173$ and $\gamma_{112}(1|9) = 0.048$ which means that it is 3.6 times more probable the third earthquake to be of state 1 instead of 2. Observing our data, we get that the next event occurred on 19-07-1961 and it was of state 1. It is illustrated in Fig. 5 that the most probable earthquake succession at every time unit given that $z = 1$ (z is explained in “Study area and data used”) is of the form $i = 1, j = 1, q = 1$, i.e., three events of state 1. Indeed, from the data that we left out of the catalog this is the pattern for 20 out of 28 (71.42%) cases.

Let us consider now that the process is observed on 17-09-1972 when a state-2 earthquake occurred. Given that the next state-1 event occurred on 10-1972, the elapsed time is $u = 1$ month (and $z = 1$), we will evaluate the probability that the third event will be either of state 1 or 2. The corresponding destination probabilities are $\gamma_{211}(1|1) = 0.159$ and $\gamma_{212}(1|1) = 0.052$, i.e., it is 3.057 times more probable for the third earthquake to be of state 1 instead of 2. Figure 6 shows that when an event of category $i = 2$ occurs, then it is more probable to be followed by two ensuing events both of state 1 at every time unit. In fact, from 1959 onwards the pattern $i = 2, j = 1, q = 1$ occurred in four out of six cases.

Based on the dataset up to 1959 we evaluate the more probable time windows for an earthquake occurrence. It can be observed in Table 3 that the maximum destination (occurrence) probability for each graph is provided along with the corresponding time u (in months). Some probability values (even the maximum) are small and this happens because there exist too many different combinations of the parameters i, j, q, k, u , defined in “Definition of the semi-Markov context”. Observing the earthquakes that we left out of the catalog we realize that they belong in the aforementioned time windows for 72.9% of all cases and 71.4% for the larger ($j = 2$) events. As an example the time windows for the destination probabilities $\gamma_{211}(1|u)$ and $\gamma_{111}(1|u)$ of Table 3 are illustrated in Figs. 7 and 8, respectively.

Concerning the results demonstrated in Table 3, the destination probability provides the probability of three successive earthquakes as well as the anticipated time of the second. This probability as well as an earthquake

Table 2 AIC and BIC values for the different semi-Markov models

	Model with geometric interevent times	Model with Pareto interevent times
Log-likelihood $\log(L(M))$	−332.008	−341.332
AIC	676.016	702.664
BIC	690.308	726.484

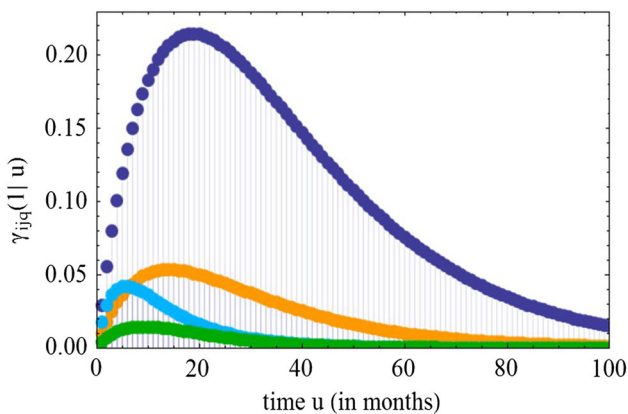


Fig. 5 Destination (occurrence) probabilities. Dark blue $\gamma_{111}(1|u)$, orange $\gamma_{112}(1|u)$, light blue $\gamma_{121}(1|u)$, green $\gamma_{122}(1|u)$

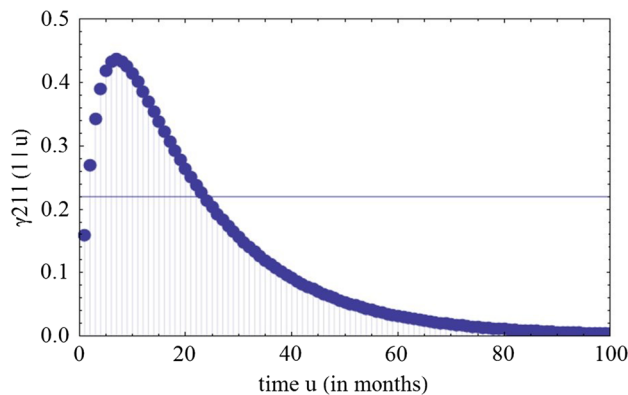


Fig. 7 The destination (occurrence) probability graph demonstrates that there is a higher probability ($p > 0.22$) of an earthquake of state 2 to be followed by an event of state 1 in the next 15–25 months

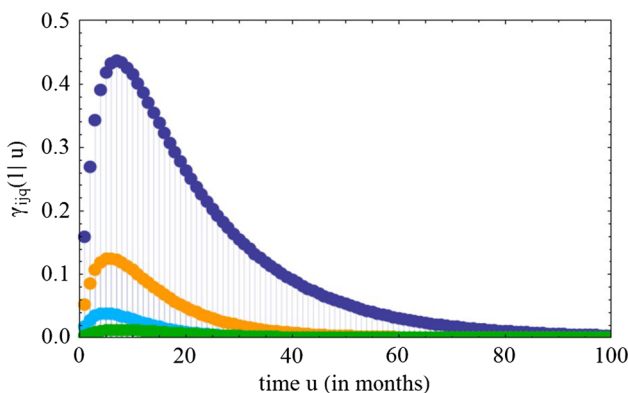


Fig. 6 Destination (occurrence) probabilities. Dark blue $\gamma_{211}(1|u)$, orange $\gamma_{221}(1|u)$, light blue $\gamma_{221}(1|u)$, green $\gamma_{222}(1|u)$

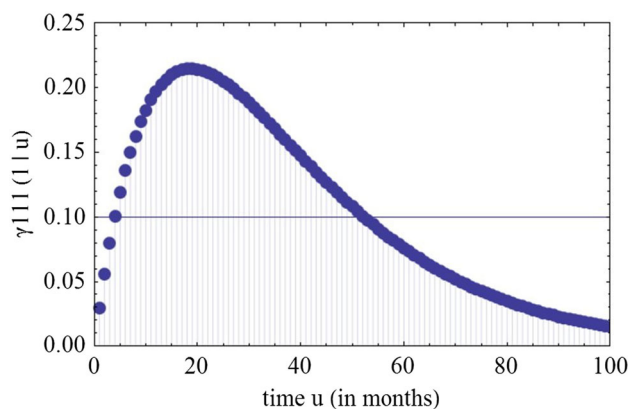


Fig. 8 The destination (occurrence) probability graph demonstrates that there is a higher probability ($p > 0.1$) of an earthquake of state 1 to be followed by an event of state 1 in the next 4–30 months

Table 3 Estimation of the time u (in months) that an earthquake of state j will follow an earthquake of state i

$\gamma_{ijq}(1 u)$	i	j	q	u (time in months)	p	Max $p(u)$
$\gamma_{121}(1 u)$	1	2	1	5–20	>0.02	0.044 (5)
$\gamma_{211}(1 u)$	2	1	1	15–25	>0.22	0.45 (8)
$\gamma_{111}(1 u)$	1	1	1	4–30	>0.1	0.22 (18)
$\gamma_{112}(1 u)$	1	1	2	8–31	>0.035	0.052 (15)
$\gamma_{122}(1 u)$	1	2	2	8–15	>0.012	0.014 (10)
$\gamma_{221}(1 u)$	2	2	1	2–17	>0.03	0.04 (5)
$\gamma_{212}(1 u)$	2	1	2	1–10	>0.055	0.123 (5)
$\gamma_{222}(1 u)$	2	2	2	5–10	>0.007	0.012 (8)

The last column demonstrates indicatively the maximum probability in each graph and the corresponding month (u)

occurrence time is not obvious a priori. Furthermore, it is important to investigate the magnitude category of an ensuing event because a state 1 or 2 event will not cause the same disasters or human loss.

Forecasting using the model with Pareto distributed interevent times

The forecasting performance of the Pareto distributed interevent times will now be tested. As in the previous section, the first half part of the dataset will be used for reestimating the model parameters and the other half for forecasting purposes. The reestimated parameters of the Pareto distributions according to relation (9) are:

$$\hat{a}_{11} = 0.427, \quad \hat{a}_{12} = 0.511, \quad \hat{a}_{21} = 1.033, \quad \hat{a}_{22} = 1.27$$

$$\hat{b}_{11} = 1, \quad \hat{b}_{12} = 1, \quad \hat{b}_{21} = 1, \quad \hat{b}_{22} = 2.$$

The interevent time distributions become:

$$f_{11}(k) = \frac{0.427}{k^{0.427+1}}, \quad f_{12}(k) = \frac{0.511}{k^{0.511+1}},$$

$$f_{21}(k) = \frac{1.033}{k^{1.033+1}}, \quad f_{22}(k) = \frac{1.27 \times 2^{1.27}}{k^{1.27+1}}.$$

The survival functions of the interevent times with respect to relations (10) and (11) are:

$$\bar{F}(k) = \begin{pmatrix} 0.427\zeta(1.427, 1+k) & 0.511\zeta(1.511, 1+k) \\ 1.033\zeta(2.033, 1+k) & 1.27 \times 2^{1.27}\zeta(2.27, 1+k) \end{pmatrix}.$$

Let us now consider that we start to observe the process on 04-11-1973 when an event of category 1 occurred. The ensuing earthquake of class 1 occurred on 14-12-1974 and the elapsed time is $u = 13$ months (while $z = 1$). The probabilities that the third successive event will be of state 1 or 2 are $\gamma_{111}(1|13) = 0.206$ and $\gamma_{112}(1|13) = 0.056$, respectively. Thus, it is 3.67 times more probable for the third event to be of state 1. Indeed, according to the data the next earthquake occurrence on 18-01-1976 was of category 1. Figure 9 demonstrates that at every time unit u the most probable earthquake succession is of the form $i = 1, j = 1, q = 1$ as it was for the model with the geometrically distributed interevent times too. However, the shape of the graphs does not present a maximum and for that reason the most probable time window for an earthquake occurrence can not be estimated as before.

Assuming that we start observing the process on 23-03-1983 when an earthquake of category 2 occurs, knowing that the ensuing event on 14-05-1983 was of state 1, while the elapsed time is $u = 2$ months and $z = 1$, we will evaluate the probability the third event to be of state 1 or 2. It is $\gamma_{211}(1|2) = 0.728$ and $\gamma_{212}(1|2) = 0.234$. This means that it is 3.11 times more probable the next earthquake to be of state 1. Indeed the next event on 31-08-1985 was a state-1 event. Figure 10 shows that an event of category $i = 2$, will be probably followed by two successive events both of state 1 at every time unit. This was also the case for the model with geometrically distributed interevent times as explained in the previous section. Comparing Figs. 5, 6 with 9 and 10 we conclude that the destination probabilities for the model with Pareto distributed interevent times are the largest in all cases.

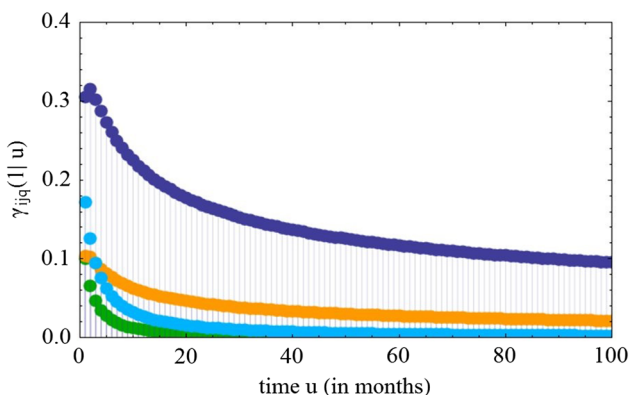


Fig. 9 Destination (occurrence) probabilities. *Dark blue* $\gamma_{111}(1|u)$, *orange* $\gamma_{112}(1|u)$, *light blue* $\gamma_{121}(1|u)$, *green* $\gamma_{122}(1|u)$

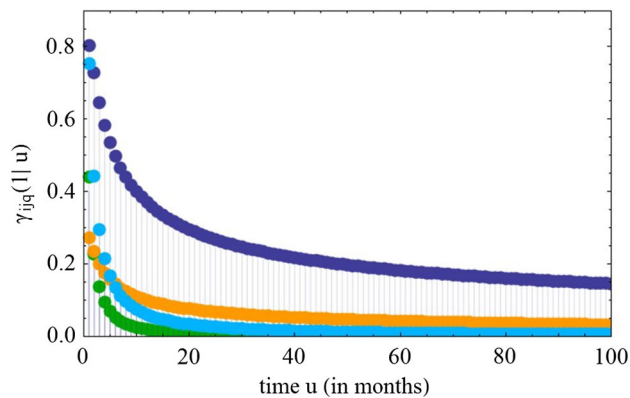


Fig. 10 Destination (occurrence) probabilities. *Dark blue* $\gamma_{211}(1|u)$, *orange* $\gamma_{212}(1|u)$, *light blue* $\gamma_{221}(1|u)$, *green* $\gamma_{222}(1|u)$

Table 4 AIC and BIC values for the different semi-Markov models

	Model with geometric interevent times	Model with Pareto interevent times
Log-likelihood Log ($L(M)$)	-164.424	-167.573
AIC	340.849	355.145
BIC	351.13	372.281

Optimal model

The models of “Forecasting with the model with geometric interevent times” and “Forecasting using the model with Pareto distributed interevent times” will be compared by means of the Akaike and Bayesian information criteria (see also “Optimal model”). As it can be observed in Table 4 the optimal model is the one with geometric interevent times because it provides the smaller criteria values. We would like to recall that the Pareto distribution has more parameters than the geometric and that both criteria penalize the number of model parameters. The difference in the values of Tables 2 and 4 can be explained by the fact that fewer observations are used for the estimation procedure of “Forecasting with the model with geometric interevent times” and “Forecasting using the model with Pareto distributed interevent times” and this affects the log-likelihood value.

Conclusions

The seismicity of the central Ionian Islands area (1911–2014, $M \geq 5.2$) is investigated via semi-Markov modelling. Firstly we consider the interevent times (times elapsed between two successive earthquakes) to be geometrically distributed because it was found that they lead to adequate forecasting of earthquake occurrences in the

North Aegean Sea (Pertsinidou 2013), and secondly, we consider Pareto distributions, as an approximation, because the interevent times of our dataset take also very large values. The quantities of interest are the destination (occurrence) probabilities evaluated by a recursive formula. These probabilities (which concern the 3-tuples of consecutive earthquake occurrences in the data list), the elapsed time between the first and the second, and the number of events that occurred in between, are used for the seismic hazard assessment. The results demonstrate that either for the geometric or the Pareto distribution, the probabilities adequately describe an earthquake magnitude class, obtaining larger values. Moreover, the destination probability graphs for the geometric distributions present a maximum in their curves, providing time windows for the more probable earthquake occurrence time. The optimal model according to the Akaike and Bayesian information criteria is the one with geometric interevent times. The forecasting performance of the models is tested, using the first half of the dataset for reestimating the model parameters and the other half for forecasting purposes and it was found that 72.9% of all earthquakes and 71.4% of the larger ($j = 2$) events belong to the more probable time windows, provided by the model with geometric interevent times.

References

- Akaike H (1974) A new look at the statistical model identification. *IEEE Trans Autom Control* 19(6):716–723. doi:10.1109/TAC.1974.1100705
- Alhajj R, Rokne J (2014) *Encyclopedia of social network analysis and mining, probability distributions*. Springer, New York, pp 1374–1375. doi:10.1007/978-1-4614-6170-8_100157
- Al-Hajjar J, Blanpain O (1997) Semi-Markovian approach for modelling seismic aftershocks. *Eng Struct* 19(12):969–976. doi:10.1016/S0141-0296(97)00006-0
- Altinok Y, Kolcak D (1999) An application of the semi-Markov model for earthquake occurrences in North Anatolia, Turkey. *J Balkan Geophys Soc* 2(4):90–99
- Anagnos T, Kiremidjian AS (1984) Stochastic time-predictable model for earthquake occurrences. *Bull Seism Soc Am* 74(6):2593–2611
- Anderson TW, Darling DA (1952) Asymptotic theory of certain “goodness of fit” criteria based on stochastic processes. *Ann Math Stat* 23(2):193–212
- Barbu VS, Limnios N (2008) *Semi-Markov chains and hidden semi-Markov models toward applications. Their use in reliability and DNA analysis*. Springer, New York, p 209
- Belosta CG (2015) Anderson-Darling GoF test. R statistical package. doi:https://cran.r-project.org/web/packages/ADGofTest/index.html
- Cluff LS, Patwardhan AS, Coppersmith KJ (1980) Estimating the probability of occurrences of surface faulting earthquakes on the Wasatch fault zone, Utah. *Bull Seism Soc Am* 70(5):1463–1478
- Howard R (1971) *Dynamic probabilistic systems: semi-Markov and decision processes*, vol 2. Wiley, New York
- Kagan Y (2002) Seismic moment distribution revisited: I. Statistical results. *Geophys J Int* 148(3):520–541. doi:10.1046/j.1365-246x.2002.01594.x
- Karakostas V, Papadimitriou E (2010) Fault complexity associated with the 14 August 2003 M_w 6.2 Lefkada, Greece, aftershock sequence. *Acta Geophys* 58(5):838–854. doi:10.2478/s11600-010-0009-6
- Kokinou E, Papadimitriou E, Karakostas V, Kamberis E, Vallianatos F (2006) The Kefalonia Transform Zone (offshore Western Greece) with special emphasis to its prolongation towards the Ionian Abyssal Plain. *Marine Geophys Res* 27(4):241–252. doi:10.1007/s11001-006-9005-2
- Lutz KA, Kiremidjian AS (1995) A stochastic model for spatially and temporally dependent earthquakes. *Bull Seism Soc Am* 85(4):1177–1189
- Malik HJ (1970) Estimation of the parameters of the Pareto distribution. *Metrika* 15(1):126–132. doi:10.1007/BF02613565
- Mann HB, Whitney DR (1947) On a test of whether one of two random variables is stochastically larger than the other. *Ann Math Stat* 18(1):50–60
- Masala G (2012) Earthquakes occurrences estimation through a parametric semi-Markov approach. *J Appl Stat* 39(1):81–96. doi:10.1080/02664763.2011.578617
- Miller J, Adamchik VS (1998) Derivatives of the Hurwitz Zeta function for rational arguments. *J Comput Appl Math* 100(2):201–206. doi:10.1016/S0377-0427(98)00193-9
- Papadimitriou E (2002) Mode of strong earthquake recurrence in the Central Ionian Islands (Greece): possible triggering due to Coulomb stress changes generated by the occurrence of previous strong shocks. *Bull Seismol Soc Am* 92(8):3293–3308. doi:10.1785/0120000290
- Patwardhan AS, Kulkarni RB, Tocher D (1980) A semi-Markov model for characterizing recurrence of great earthquakes. *Bull Seismol Soc Am* 70(1):323–347
- Pertsinidou CE, Tsaklidis G, Papadimitriou E (2013) Seismic hazard assessment in the northern Aegean Sea (Greece) through discrete semi-Markov modeling. In: *Proceedings 13th int. Congr. Geol. Soc. Greece*, 5–8 September 2013, vol 3. Chania, Greece, pp 1417–1428
- Pertsinidou CE, Tsaklidis G, Papadimitriou E (2016) Modeling the seismicity of central Ionian Islands with semi-Markov models. In: *Proc. 14th int. Congr. Geol. Soc. Greece*, 25–27 May 2016, vol 3, Thessaloniki, Greece, pp 1399–1411. doi:http://www.geosociety.gr/index.php/en/publications-en/2000/255-1-14th-25-5-2016-en
- Sadeghian R, Jalali-Naini GR, Sadjadi J, Fard NH (2008) Applying semi-Markov models for forecasting the triple dimensions of next earthquake occurrences: with case study in Iran Area. *Int J Ind Eng Prod Res* 19(4):57–67
- Schwarz G (1978) Estimating the dimension of a model. *Ann Stat* 6(2):461–464
- Scordilis EM, Karakaisis GF, Karacostas BG, Panagiotopoulos DG, Comninakis PE, Papazachos BC (1985) Evidence for transform faulting in the Ionian Sea: the cephalonia island earthquake sequence of 1983. *Pure Appl Geoph* 123(3):388–397. doi:10.1007/BF00880738
- Votsi I, Limnios N, Tsaklidis G, Papadimitriou E (2012) Estimation of the expected number of earthquake occurrences based on semi-Markov models. *Methodol Comput Appl Probab* 14(3):685–703. doi:10.1007/s11009-011-9257-4

Application of complex network theory to the recent foreshock sequences of Methoni (2008) and Kefalonia (2014) in Greece

D. Chorozoglou¹ · D. Kugiumtzis² · E. Papadimitriou¹

Received: 31 December 2016 / Accepted: 17 April 2017 / Published online: 28 April 2017
© Institute of Geophysics, Polish Academy of Sciences & Polish Academy of Sciences 2017

Abstract Seismic hazard evaluation before recent strong main shocks in the area of Greece is attempted using prior seismicity on the basis of earthquake network theory. The connections of earthquake networks are constructed from successive earthquakes and the nodes are represented by cells of normal grids that were considered superimposed on the study areas. The dynamic evolution of the network structure is examined at sliding windows for identifying periods of statistically significant change, i.e., the network structure differentiation from that of a random network, where the structure is characterized by selected network measures, including the index of small-worldness property. By studying the structure of complex earthquake network, a distinct dynamic evolution is revealed, 2 months before the main shock occurrence. Particularly, the network measures, such as clustering coefficient and small-worldness index, tend to increase before and exhibit an abrupt jump at the time of the main shock occurrence, and then slowly decrease and become stable with small variations as before.

Keywords Cells · Main shocks · Complex networks · Clustering coefficient · Random network

✉ D. Chorozoglou
chorozod@geo.auth.gr

D. Kugiumtzis
dkugiu@auth.gr

E. Papadimitriou
ritsa@geo.auth.gr

¹ Geophysics Department, Aristotle University of Thessaloniki, GR54124 Thessaloniki, Greece

² Department of Electrical and Computer Engineering, Aristotle University of Thessaloniki, Thessaloniki, Greece

Introduction

The study of statistical properties of seismicity (Utsu 2002) is of great interest, because it may give insight into the complex physical mechanisms that cause earthquakes. The most commonly used models are the Poisson model, assuming that the earthquake occurrences are independent in space and time (Cornell 1968; Lomnitz 1974; Bath 1978; Brillinger 1982; Lomnitz and Nava 1983). Markov chain models are also used for earthquake probability estimation, which contrary to the Poisson models, assume that all events are dependent on one another in space and time (Howard 1971; Tsapanos and Papadopoulou 1999; Nava et al. 2005; Herrera et al. 2006). Concerning the short-term forecast of main shocks at the level of few days or even few months, it was found that the number of foreshocks, i.e., earthquakes occurring before main shock, is time dependent. It was found that the rate of foreshock occurrence increases as the time of the mainshock approaches and is described by a power-law function (Papazachos 1975), the number of foreshocks diminishes as the magnitude difference between the main shock and the foreshocks increases (Kagan and Knopoff 1978), the seismicity increases approximately as the inverse of time before main shock (Jones and Molnar 1979), large events are followed by aftershock sequences obeying the Omori law and preceded by localized foreshocks, which are initiated after a time period of seismic quiescence (Hainzl et al. 1999), studying the annual rate of occurrence, it is found that in areas of positive pre-stress changes, a sharp increase of the number of earthquakes is observed several years before the occurrence of the main shock (Karakostas 2009), and the b value of the strong foreshock stage (last 10 days before the mainshock) was significantly lower than that in the aftershock sequence (Papadopoulos et al. 2010).

Considerable research work was accomplished on network theory and its applications in different disciplines ranging from communication and economics to biology and neuroscience (Wang and Chen 2003; Emmert-Streib and Dehmer 2010; Rubinov and Sporns 2010). In Seismology, it was introduced recently by Abe and Suzuki (2004a) to study seismicity as a spatio-temporal complex system. The complex network theory provides a new insight and perspective in analyzing seismicity patterns for seismic hazard assessment (Abe and Suzuki 2004a, b, 2007; Baiesi and Paczuski 2004, 2005; Barrat et al. 2008; Newman 2010; Daskalaki et al. 2014). Global physical properties of seismicity can be explored by examining the geometrical (topological) and dynamic characteristics (measures). The changes in the structure of the network can reveal a main shock occurrence a few days before its occurrence (Abe and Suzuki 2009).

The aim of this paper is the application of the tools of the complex network theory to identify potential spatio-temporal foreshock patterns for the short-term earthquake forecasting or hazard assessment (Abe and Suzuki 2004a, b, 2006, 2007). The construction of earthquake networks is attempted, where the nodes of networks are the cells of normal grids superimpose onto the study areas, which are the areas around the epicenters of two main shocks that occurred in 2008 and 2014 in Greece, and the connections, simple and weighted, between them are given by the time succession of two earthquakes in any cell. The main shocks of $M = 6.8$ and $M = 6.1$ occurred near Methoni and in Kefalonia Island, respectively, and information on their aftershock sequences were taken from relevant studies (Roumelioti et al. 2009; Karakostas et al. 2014). After constructing the earthquake networks, its measures are computed on non-overlapping sliding windows of 30 day duration, for a period of 300 days before to 150 days after both main shocks. Significant changes in the underlying earthquake network topology are assessed statistically by contrasting the structure of the original earthquake network to that from random networks.

Methodology

The term network implies the graph $G = (N, E)$ that is defined by the nodes and the connections between them, where N is the set of nodes and E the set of connections. The network connections can be directed or undirected, weighted, or simple (binary). For any two nodes, i and j , the distance $d(i, j)$ for simple connections, or $d(i, j)^W$ for weighted connections between them, is defined as the length of the shortest path from i to j if the nodes are connected and called neighbors, whereas $d(i, j) = \infty$ or $d(i, j)^W = \infty$ otherwise.

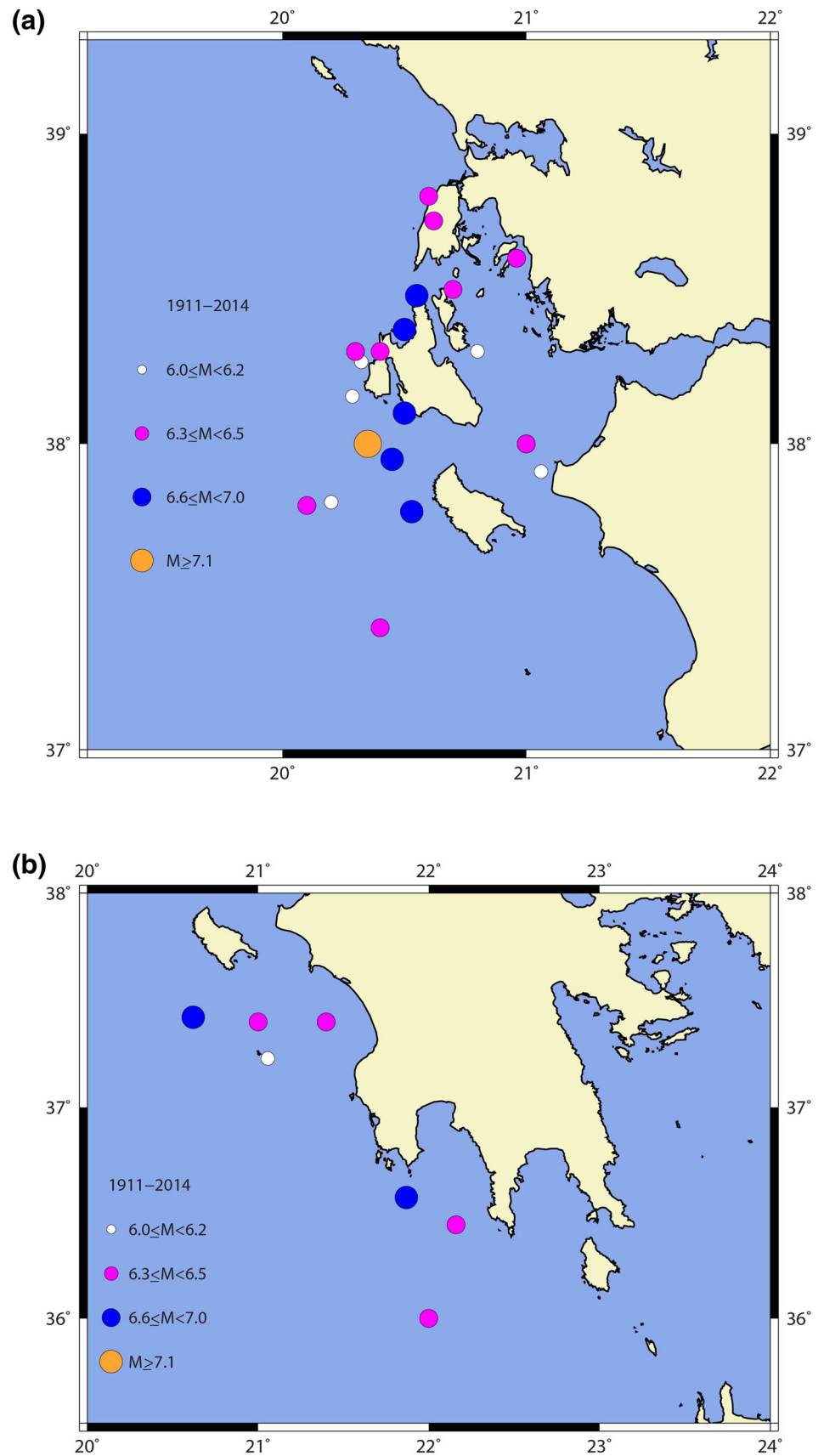
Construction of complex networks based on seismicity

The study areas, which are among the most seismically active in the entire Mediterranean region, have accommodated strong ($M > 6.0$) main shocks recently. The first area, which consists part of the western Hellenic arc, is characterized by continuous high activity as a result of the subduction of the oceanic crust of the eastern Mediterranean beneath the Aegean microplate (Fig. 1a). In 2008, an intense seismic sequence took place south of the city of Methoni, with three events of $M > 6.0$, the largest one being of $M = 6.8$ and is considered as a target main shock in this study (Roumelioti et al. 2009). The second study area is part of the Kefalonia Transform Fault Zone (KTFZ), which almost 100 km long, consisting of the Kefalonia and Lefkada Fault branches, and linking the continental collision with the oceanic subduction zones, in the Ionian Sea (Fig. 1b). The fault zone follows the submarine Kefalonia valley, west of the island chain from Lefkada to Kefalonia. In 2014, two main shocks of $M = 6.1$ and $M = 6.0$ occurred in about 1 week difference and were associated with adjacent fault segments located along the western part of Kefalonia Island (Karakostas et al. 2014). A normal grid is considered, centered at each main shock epicenter and consisting of 16 cells of equal area. In the case when at least one earthquake with magnitude exceeding a predefined threshold occurs inside each cell, then this is considered as one of the nodes of the earthquake network. Two successive strong earthquakes define a connection between the respective nodes if the nodes are different and a loop if they are identical. The connections and loops represent the correlations between two successive earthquakes. It has been shown that a future earthquake may be triggered by an immediately preceding strong earthquake which is more than 1000 km far away from the next earthquake (Steeple and Steeples 1996). Thus, a directed network with direction from a strong earthquake to the next one is constructed regardless of their spatial distance. The same behavior on the distances is also observed for earthquakes with small magnitudes.

Formation of adjacency and weighted matrix

The network of N nodes is fully defined by a square matrix of size $|N| \times |N|$ and the value at each position $(i, j) \in E$ of this matrix indicates the connection between nodes i and j . When the connections are binary, this matrix is called adjacency matrix $A = \{a_{ij}\}, i, j = 1, \dots, |N|$, where $|N|$ is the cardinality of N , and $a_{ij} = 1$ if there is a connection between nodes i and j , and $a_{ij} = 0$ otherwise. If the connections are directed connections, A is non-symmetric. For

Fig. 1 Study areas in **a** at Ionian Islands and in **b** at southwest Peloponnese, with the epicentral distribution of the strong ($M \geq 6.0$) main shocks in the period 1911–2014



binary connections, only the occurrence of successive strong earthquakes from cell i to cell j is of interest, meaning that multiple such successions within the study temporal window are not accounted for. The adjacency matrix A does not fully exploit the information on the strong historical earthquakes. Therefore, we consider also the weighted matrix $W = \{w_{ij}\}, i, j = 1, \dots, |N|$, constructed as follows at each time window. A square non-symmetric matrix $S = \{s_{ij}\}$ is created, where s_{ij} takes either an integer value indicating how many times the succession of earthquakes appears for each pair (i, j) of nodes, or a positive real value indicating the sum of the seismic moments M_0 released in all successions of strong earthquakes between nodes i and j , where M_0 refers to the second earthquake. The seismic moment is calculated from the empirical relation $\log M_0 = 1.5M + 16.01$, where M is the earthquake magnitude (Kanamori and Anderson 1975). For both cases, the components s_{ij} are normalized by their maximum to give the weights $w_{ij} = s_{ij}/\max\{s_{ij}\}$, of the weighted matrix W .

Summarizing, the weighted connections indicate the sum of the number of successive earthquakes or seismic moments M_0 released for each pair of nodes, whereas the simple connections indicate the succession of earthquakes regardless of the number of successions or seismic moment which is released between the nodes. In the analysis, we consider both types of networks given by the weight matrix W and the adjacency matrix A , respectively.

Complex network measures

The characteristics of the structure of the earthquake network of binary or weighted connections are quantified by appropriate network measures computed on A and W , respectively. Three of them are mathematically defined in Table 1 and discussed in the following along with a particular measure quantifying the small-world property (Rubinov and Sporns 2010).

The simplest and most known network measure is the degree centrality for simple connections and strength centrality for weighted connections. This measure indicates the

number of connections or the sum of weights of each node. Particularly, the in-strength, k_i^{in} , is the sum of weighted connections directed to the node i and the out-strength, k_i^{out} , is the sum of weighted connections that leave the node i . In-degree and out-degree are defined in the same way. Essentially, the measures quantify whether a node is active in the network. The average degree and strength centrality is the average of k_i^{in} over all nodes (being the same for k_i^{out}). For all the network measures presented below, the average measure is defined similarly.

The next widely used network measure is the clustering coefficient, which estimates the tendency of any node i to form groups (triads) of nodes in the network. A high value of the average clustering coefficient indicates higher likelihood existence of “clique” (clique is a group of fully connected nodes). The characteristic path length of a node i is the average of the shortest distances from node i and any other node. Nodes not being connected (the distance is infinite) are not considered in the calculations. The average characteristic path length characterizes the overall coherence of the network. The eccentricity of a node i is the maximum distance between node i and any other node in the network. Low value of average eccentricity means that the distances between most of the nodes are small. Finally, we consider the global efficiency, which is inversely proportional to the characteristic path length. The smaller the distances between the network nodes are, the higher the global efficiency, meaning easier information flow in the network.

The small-world network (Watts and Strogatz 1998) is characterized by the smallest possible steps between nodes. The authors defined this term for networks having similar characteristic path length, but higher clustering coefficient as compared to a corresponding random network. For a given network with average characteristic path length L and average clustering coefficient C and a random network with L_{rand} and C_{rand} , respectively, the property of the small-world is verified when $\lambda = \frac{L}{L_{\text{rand}}} \geq 1$ and $\gamma = \frac{C}{C_{\text{rand}}} \gg 1$, and quantified by a large value of the so-called small-worldness measure S , defined as $S = \frac{\gamma}{\lambda} = \frac{C/C_{\text{rand}}}{L/L_{\text{rand}}}$.

Table 1 Mathematical definitions of the measures for a node i of a network with binary and weighted directed connections

Binary	Weighted
Clustering coefficient $C_i = \frac{\sum_{j,m} a_{ij} a_{jm} a_{mi}}{k_i^{\text{out}}(k_i^{\text{out}} - 1)}$	$C_i^W = \frac{\sum_{j,m} w_{ij} w_{jm} w_{mi}}{(k_i^{\text{out}} + k_i^{\text{in}})(k_i^{\text{out}} + k_i^{\text{in}} - 1) - 2 \sum_j w_{ij} w_{ji}}$
Characteristic path length $L_i = \frac{1}{N-1} \sum_{j,j \neq i} d_{ij}$	$L_i^W = \frac{1}{N-1} \sum_{j,j \neq i} d_{ij}^W$
Eccentricity $e_i = \max_j \{d(i, j)\}$	$e_i^W = \max_j \{d^W(i, j)\}$

For the calculation of the network measures, the Matlab functions of the Brain Connectivity Toolbox were applied <https://sites.google.com/site/bctnet/measures>.

Complex network randomization

To assess the change of network measures across successive time windows, the measure value of the original network was compared with the one of a corresponding random network. This random network is constructed by randomizing the connections of the original network preserving certain features from the original network, such as the average (or total) degree or strength centrality (Newman 2010). A stricter condition is the preservation of the degree or strength centrality of each node (Molloy and Reed 1995; Newman et al. 2001; Maslov and Sneppen 2002; Del Genio et al. 2010).

The classical algorithm of Maslov and Sneppen (2002) for producing randomized networks with the same number of simple (binary) connections of each node is used here. In the case where one needs to maintain the out-degree of each node, the steps are as follows: for two randomly selected connections (i, j) and (k, l) of the original network, the end nodes j and l are interchanged giving rise to the connections (i, l) and (k, j) . If these connections are not already included in the network, then they are created and the first two connections are deleted; otherwise, the step is repeated. After several iterations, this process creates a randomized variant of the original network that preserves the number of out-connections at each node. In addition, the algorithm which maintains the total strength for producing randomized networks with weighted connections is used in our analysis. This algorithm applies less strict condition but is simpler than the one of Maslov and Sneppen (2002), because it maintains the out-strength (sum of weights) of original network based on randomly shuffling the weighted connections and not for every node.

Application and results

The application includes the network analysis, by studying the structure of earthquake network on non-overlapping sliding windows before two recent main shocks that occurred in Kefalonia island on the 26th of January 2014, with $M = 6.1$, and in the offshore area west of Methoni on the 14th of February 2008, with $M = 6.8$. The first aim is to investigate whether the structure of earthquake network, focusing on global characteristics, can reveal a strong main shock occurrence a few days before and second if there is a node

(focusing on local characteristics), or otherwise a cell, which plays an important role in the earthquake network.

Description of the analysis

For each study area, we created a square grid centered at the main shock epicenter with a side of 2.0° , which is divided into 16 cells with a side of 0.5° , where seismicity activity is examined (Fig. 2).

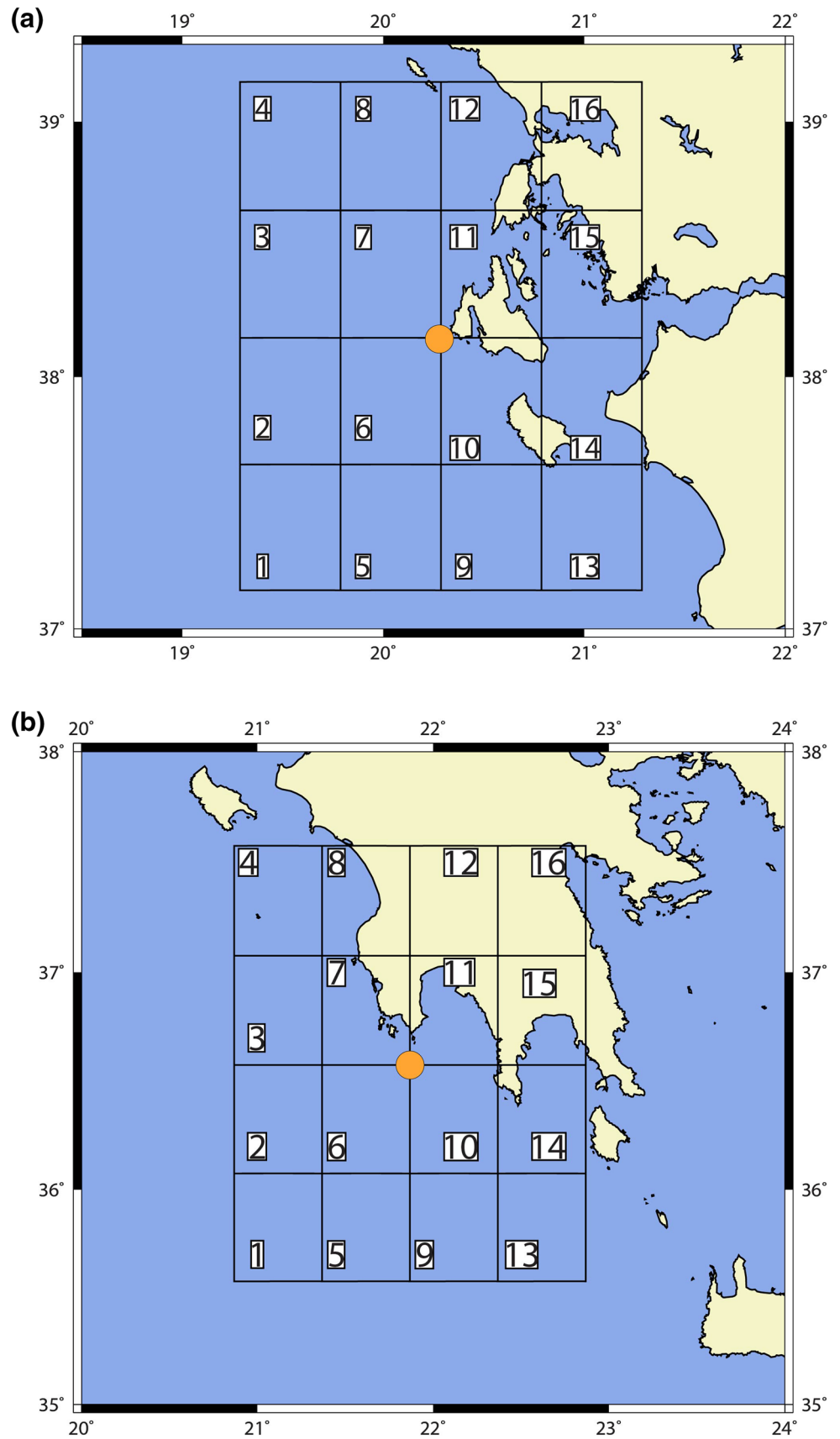
The 16 seismicity cells represent the nodes of the earthquake network and the connections are given by two successive earthquakes between the respective nodes. The simple connections are given by the adjacency matrix A , which is constructed by the succession of earthquakes without multiple connections. In addition, the weighted connections are given by the weighted matrix W which is defined by the sum of the number of successive earthquakes or by the sum of the seismic moment, M_0 , released for each pair of nodes (seismic cells). To study the evolution of the earthquake network structure before the main shock, we compute the global and local network measures (clustering coefficient, characteristic path length, eccentricity, global efficiency, and the small-world index) on non-overlapping sliding windows of 30 days, sliding across a time period that spans from 300 days before to 150 days after the main shock, which means ten and five sliding windows before and after the main shock, respectively. The use of the sliding window allows the tracing of the temporal changes in the network topology (structure).

To detect statistically significant changes in the network structure, we use randomized networks that either maintains the total strength (for weighted connections) or the node degree centrality (for binary connections). For each sliding window, $B = 100$ random networks are generated for each of the two approaches of randomization, and thereafter, four network measures are computed. Having generated B randomized networks with any approach, we test the null hypothesis H_0 that the original network is random using a proper network measure as test statistic. Each network measure, q , is computed on the original network giving the value q_0 , and B randomized networks giving the values q_1, \dots, q_B . The p value of the test is

$$p = \begin{cases} \frac{2r_0}{B+1}, & \text{if } r_0 \leq \frac{B+1}{2} \\ \frac{2(1-r_0)}{B+1}, & \text{if } r_0 > \frac{B+1}{2} \end{cases} \quad (1)$$

where r_0 is the rank of q_0 in the ordered list of q_0, q_1, \dots, q_B , and H_0 is rejected if $p < a$, for a significance level a here being 0.05. Thus, significant changes in the characteristics of the seismic network across time windows can be traced with respect to the profile of the p value for the corresponding network measure.

Fig. 2 Normal grid that is centered at the epicenters of the Kefalonia in **a** and Methoni in **b** of $M = 6.1$ and $M = 6.8$, respectively, and superimpose on an area with dimensions $2^\circ \times 2^\circ$. The grid is divided into 16 cells



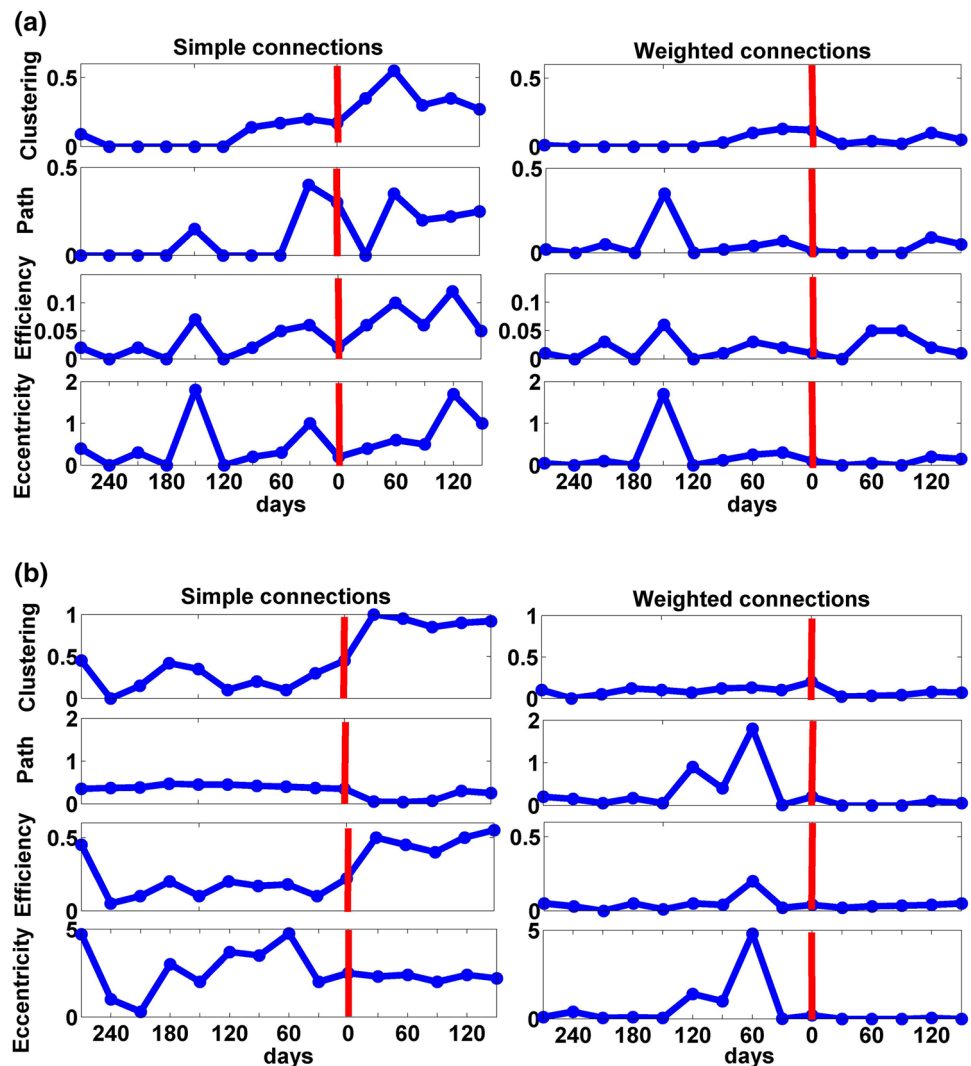
Complex network analysis before the main shocks occurrence

We focus on the case of the strong earthquake of $M = 6.1$ that occurred in the paliki Peninsula of Kefalonia island on 26 January 2014, with an epicenter located at 38.15 N, 20.28 E (Fig. 2a). The second main shock of $M = 6.8$ occurred in offshore the southwestern Peloponnese, to the town of Methoni, on 14 February 2008, with an epicenter located at 36.57 N, 21.86 E (Fig. 2b). The seismic catalog compiled in the Geophysics Department of the Aristotle University of Thessaloniki (<http://geophysics.geo.auth.gr/ss/>) consists our data source. In both cases, the seismic catalog includes crustal earthquakes (focal depth less than 40 km) and the completeness of data on the basis of the Gutenberg–Richter is $M_{thr} = 3.0$. The seismic catalog includes earthquakes that occurred 300 days (55 events) before to 150 days (727 events) after the main shock in the case of

Kefalonia, where as in Methoni includes 236 and 2125 events, before and after, respectively.

The time evolution of the network measures indicates the existence of three distinct structures (phases) before the main shocks. The first phase lasts up to 2 months (60 days) before the main shock as the network measures are stable with small variations. The second phase is around 2 months (60 days) before the main shock, where the network measures increase or decrease sharply, regarding the period where the foreshock sequence is developed. The third phase is after the main shock and is associated with the aftershock sequence (Fig. 3a, b). For example, the clustering coefficient is quite stable with small fluctuations until 2 months (60 days) before the main shock, rises abruptly during the last 2 months before shock (it has the highest value around 0.15 when the connections are weighted), and then decreases and stays at the same level as before the main shock. In terms of network structure interpretation, higher values of clustering coefficient imply

Fig. 3 Evolution of values of network measures in **a** for the main shock near Kefalonia and in **b** for the main shock near Methoni, where the vertical line denotes the time of main shock. The seismic measure for introducing the weighted connections is the number of earthquakes



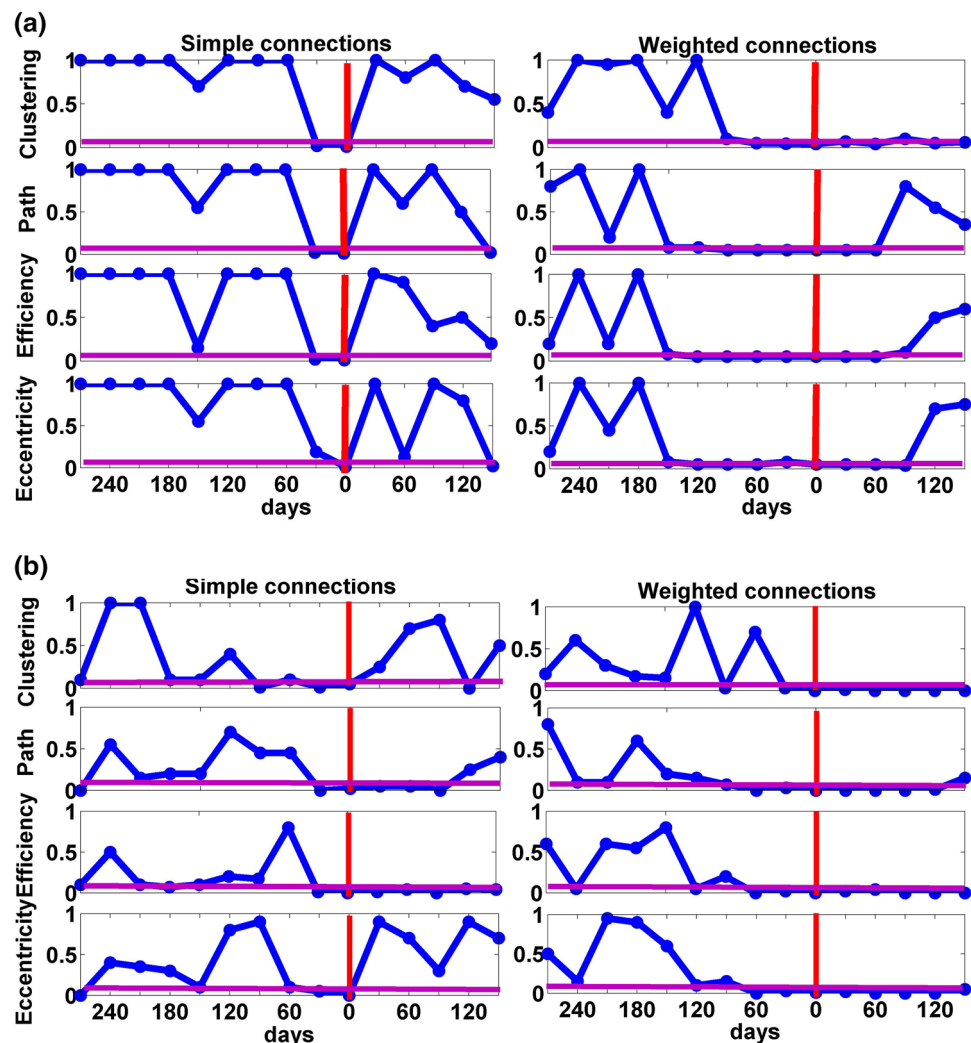
a more clustered and organized seismicity pattern. The characteristic path length and the eccentricity show an inverse behavior in relation with the clustering coefficient, and they tend to decrease before the main event. The high value of clustering coefficient (existence of “clique”) implies a reduction in the distance (number of steps) between two randomly chosen cells. Thus, the increase of clustering coefficient and decrease of the other network measures may reveal that a strong earthquake is anticipated in a few days (60 days). In contrary, a distinct change in the evolution of the global efficiency measure with respect to the main shock is not observed.

Concerning the statistical significance of the network measures, in the first phase (from the beginning of the study period until 2 months before the main shocks), the earthquake networks cannot be differentiated from random graphs, whose structure is characterized by random connections between nodes (the p values are over the threshold of 0.05 in Fig. 4a, b). In the second phase (60 days before the main shocks until their occurrence), a statistically

significant change in the network structure is revealed as the earthquake networks are found to be different than random networks (small p values close to zero in Fig. 4). Thus, the structure of earthquake networks changing 60 days before the main shocks might be related to the foreshock sequence. In the third phase, after the main shocks, the structure of the earthquake networks remains non-random as it is related to the aftershock sequence and after 90 days returns to a random structure (random networks). The results of Figs. 3 and 4 are in agreement. The change in network measures up to 2 months before the main shock is in agreement to the change from random to non-random network at the same period, suggesting that a strong main shock is anticipated during the period of this change.

The change of the structure of the earthquake networks is also confirmed by the evolution of the small-worldness index (S). S is within the expected range of network structure without exhibiting the small-world property until 60 days before the main shock. Then, it increases abruptly

Fig. 4 p value based on statistical test in **a** for the main shock near Kefalonia and in **b** for the main shock near Methoni, where the *horizontal line* denotes the statistically significant level ($\alpha = 0.05$) and the *vertical line* denotes the time of main shock. The seismic measure for introducing the weighted connections is the number of earthquakes

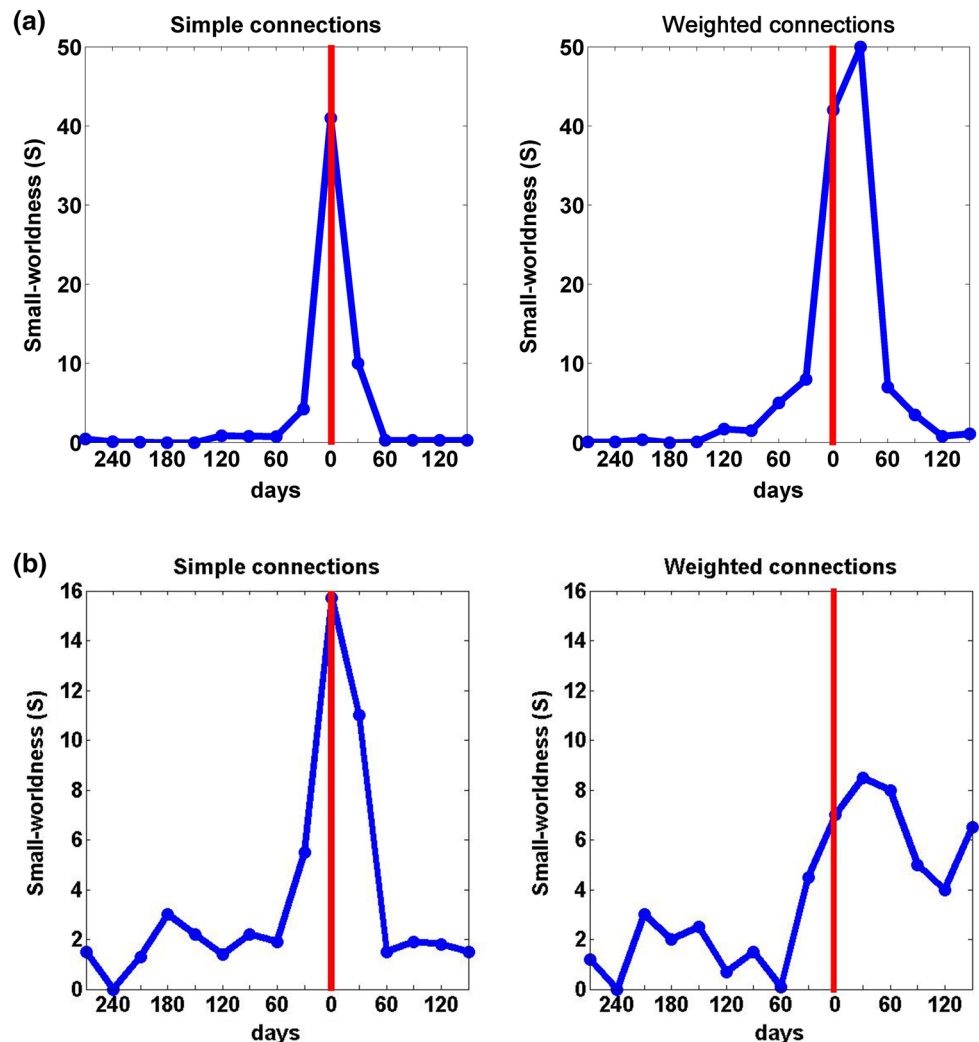


jump for the whole period until the main shock at high levels indicating clearly the small-world property, and then slowly decreases and becomes stable again (Fig. 5). We note that for weighted connections, S tends to stay at the level regarding small-world property also in the third aftershock phase. In conclusion, the topology (structure) of earthquake networks before the main shocks is characterized by statistically significant more clustered networks, per triads of nodes, with profound small-world characteristics.

An important issue concerns the identification of the location of the anticipated main shock. For this purpose, we compute the clustering coefficient for each node, trying to identify the seismicity cells (nodes) that could serve as potential epicentral locations. It is shown that during the period of 60 days before the main shock, the values of clustering coefficient of each node appear randomly dispersed in space, i.e., across the nodes (Fig. 6). Then, about 60 days before the main shock, a different

pattern is emerged. Particularly, at the seismic cell of the main shock epicenter (seismic cell 11), there is a persistent appearance of high values of the clustering coefficient throughout the entire period until the main shock occurrence. Thus, there is a centralization of the clustering coefficient distribution at the seismic cells of epicenters. This behavior is characteristic only for the seismic cells (nodes) that are related to the main shock epicenters. The clustering coefficient of the other nodes does not change significantly. Therefore, the seismicity revolves around this certain space (node), in the seismic cell 11. The results for the weighted connections are referred only in case that we consider the number of earthquakes as seismic measure, because the results are similar to the other seismic measure (seismic moment released). Finally, as regard the computation of local network measures (for each node), we show only the results for clustering coefficient, because the other network measures are not present distinct behavior.

Fig. 5 Evolution of the small-worldness index (S), where the vertical line denotes the time of main shock near Kefalonia in **a** and Methoni in **b**. The seismic measure for introducing the weighted connections is the number of earthquakes



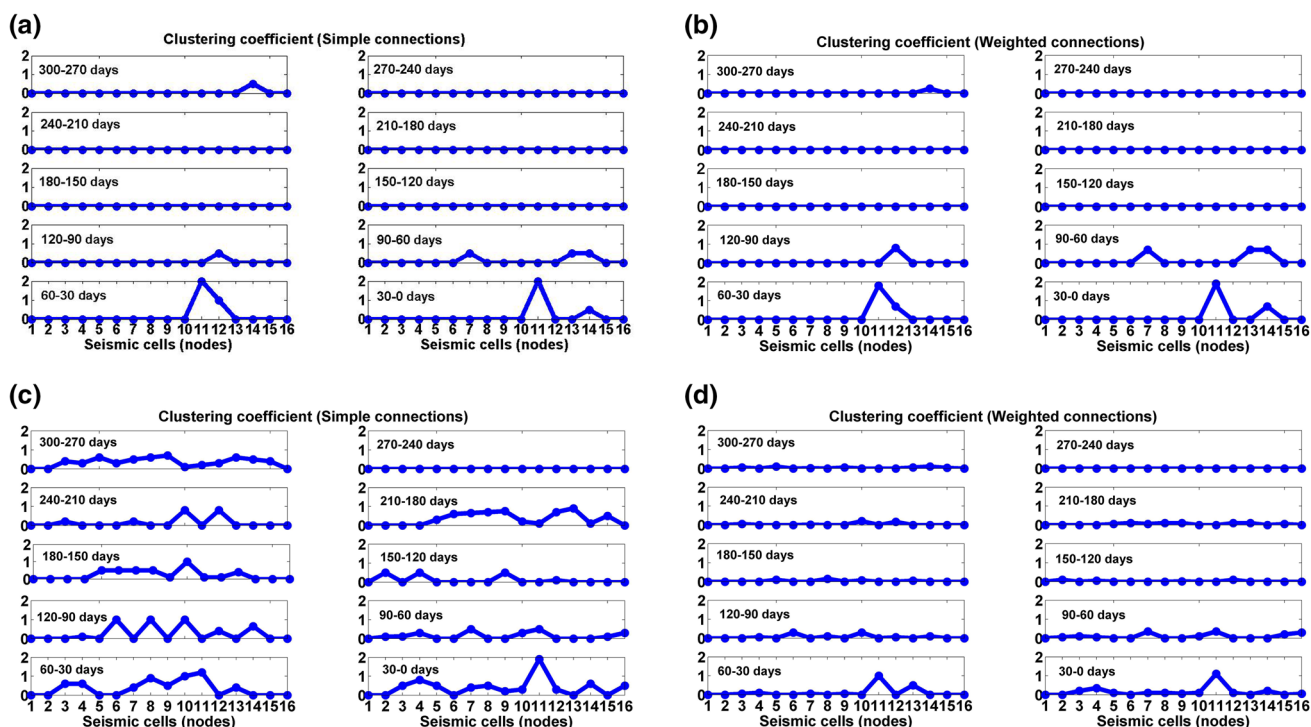


Fig. 6 Clustering coefficient for each node (seismic cell) shown at different time windows as indicated at each panel, before the main shock near Kefalonia in **a** and **b** and Methoni in **c** and **d**. In **a** and **c**,

the connections are simple (binary) while in **b** and **d** are weighted. The seismic measure for introducing the weighted connections is the number of earthquakes

Conclusions

The application of the network theory was found to be a powerful tool that contributes significantly to the investigation of properties of complex phenomena such as seismic activity. Based on the complex network technique, we show that key topological measures, such as the clustering coefficient and the small-world property, may serve as potential indices for short-term seismic hazard assessment. Statistically significant changes in the network structure are shown by certain global measures, such as the clustering coefficient, eccentricity, and small-world index, which are observed simultaneously about 2 months (60 days) before the main shock. It is found that these topological measures can track the changes in the structure evolution of earthquake networks and can be regarded as proxies of the seismicity behavior. The results showed that the topological measures could not discriminate the foreshock from the aftershock activity. For this purpose, there are the classic seismicity statistics that can help for such discrimination beforehand, thanks to the discriminatory power of the b index, where b is the slope of the Gutenberg–Richter relation dropping significantly during foreshocks. Concerning the location of a main shock, a clear centralization of the clustering coefficient close to its epicenter, i.e., in the seismic cell inside which the main shock occurred, is

observed about 2 months before the main shock persisting until the main shock occurrence. The seismic measures (number of earthquakes and seismic moment M_0 release) that introduce the weighted connections provide similar results.

These results suggest the usefulness of network analysis in the study of seismicity in a broader area. The approach of network analysis for the identification of spatio-temporal patterns related to the underlying seismicity is promising and can potentially serve as a complement to well established traditional statistical methods (Markov and semi-Markov model) for the hazard assessment of earthquakes. More evidence needs to be accumulated from the estimation of more network measures and the network evolution before the occurrence of several main shocks. In addition, the construction of the seismic network with other approaches, and particularly the construction of correlated networks from seismic time series, can significantly contribute to seismic hazard assessment. An open issue arising from this work is the application of the same analysis for the two study areas with the above-mentioned settings.

Acknowledgments The authors greatly appreciate the comments of two anonymous reviewers that considerably contributed in the improvement of the manuscript. The editorial assistance of Dr. Console is also acknowledged. Geophysics Department contribution 897.

References

- Abe S, Suzuki N (2004a) Scale-free network of earthquakes. *Europhys Lett* 65:581–586
- Abe S, Suzuki N (2004b) Small-world structure of earthquake network. *Phys A* 337:357–362
- Abe S, Suzuki N (2006) Complex-network description of seismicity. *Nonlinear Process Geophys* 13:145–150
- Abe S, Suzuki N (2007) Dynamical evolution of clustering in complex network of earthquakes. *Eur Phys J B* 59:93–97
- Abe S, Suzuki N (2009) Main shocks and evolution of complex earthquake networks. *Braz J Phys* 39(2A):428–430
- Baiesi M, Paczuski M (2004) Scale-free networks of earthquakes and aftershocks. *Phys Rev E* 69:066106. doi:[10.1103/PhysRevE.69.066106](https://doi.org/10.1103/PhysRevE.69.066106)
- Baiesi M, Paczuski M (2005) Complex networks of earthquakes and aftershocks. *Nonlinear Process Geophys* 12:1–11. doi:[10.5194/npg-12-1](https://doi.org/10.5194/npg-12-1)
- Barrat A, Barthelemy M, Vespignani A (2008) *Dynamical processes on complex networks*. Cambridge University Press, United Kingdom, p 361
- Bath M (1978) Seismic risk in Fennoscandia. *Tectono Phys* 57:285–295
- Brillinger D (1982) Some bounds for seismic risk. *Bull Seismol Soc Am* 72:1403–1410
- Cornell CA (1968) Engineering seismic risk analysis. *Bull Seismol Soc Am* 58:1583–1606
- Daskalaki E, Papadopoulos GA, Spiliotis K, Siettos C (2014) Analysing the topology of seismicity in the Hellenic arc using complex networks. *J Seismol* 18:37–46. doi:[10.1007/s10950-013-9398-8](https://doi.org/10.1007/s10950-013-9398-8)
- Del Genio C, Kim H, Toroczkai Z, Bassler K (2010) Efficient and exact sampling of simple graphs with given arbitrary degree sequence. *PLoS One* 5(4):e10012
- Emmert-Streib F, Dehmer M (2010) Influence of the time scale on the construction of financial networks. *PLoS One* 5(9):e12884
- Hainzl S, Zöller G, Kurths J (1999) Similar power laws for foreshock and aftershock sequences in a spring-block model for earthquakes. *J Geophys Res* 104:7243–7254
- Herrera C, Nava FA, Lomnitz C (2006) Time-dependent earthquake hazard evaluation in seismogenic systems using mixed Markov Chains: an application to the Japan area. *Earth Planets Space* 58:973–979
- Howard RA (1971) *Dynamic probabilistic systems*, 1(2). Wiley, New York
- Jones LM, Molnar P (1979) Some characteristics of foreshocks and their possible relationship to earthquake prediction and premonitory slip on fault. *J Geophys Res* 84:3596–3608
- Kagan Y, Knopoff L (1978) Statistical study of the occurrence of shallow earthquakes. *Geophys J R Astr S* 55:67–86
- Kanamori H, Anderson L (1975) Theoretical basis of some empirical relations in seismology. *Bull Seismol Soc Am* 65(5):1073–1095
- Karakostas V (2009) Seismicity patterns before strong earthquakes in Greece. *Acta Geophys* 57(2):367–386. doi:[10.2478/s11600-009-0004-y](https://doi.org/10.2478/s11600-009-0004-y)
- Karakostas V, Papadimitriou E, Mesimeri M, Gkarlaoui C, Paradisopoulou P (2014) The 2014 Kefalonia Doublet (Mw6.1 and Mw6.0), Central Ionian Islands, Greece: Seismotectonic implications along the Kefalonia Transform fault zone. *Acta Geophysica* 63(1):1–16
- Lomnitz C (1974) *Global tectonics and earthquake risk*. Elsevier Scientific Publishing Co, Amsterdam-London-New York
- Lomnitz C, Nava F (1983) The predictive power of seismic gaps. *Bull Seismol Soc Am* 73:1815–1824
- Maslov S, Sneppen K (2002) Specificity and stability in topology of protein networks. *Science* 296:910–913
- Molloy M, Reed B (1995) A critical point for random graphs with a given degree sequence. *Random Struct Algorithms* 6(2–3):161–180
- Nava FA, Herrera C, Frez J, Glowacka E (2005) Seismic hazard evaluation using Markov chains: application to the Japan area. *Pure Appl Geophys* 162:1347–1366
- Newman M (2010) *Networks: an introduction*. Oxford University Press, New York
- Newman M, Strogatz S, Watts D (2001) Random graphs with arbitrary degree distributions and their applications. *Phys Rev E* 64(2):026118
- Papadopoulos GA, Charalampakis M, Fokaefs A, Minadakis G (2010) Strong foreshock signal preceding the L'Aquila (Italy) earthquake (Mw 6.3) of 6 April 2009. *Nat Hazards Earth Syst Sci* 10:19–24. doi:[10.5194/nhess-10-19](https://doi.org/10.5194/nhess-10-19)
- Papazachos BC (1975) Foreshocks and earthquake prediction. *Tectonophysics* 28:213–226
- Roumelioti Z, Benetatos C, Kiratzi A (2009) The 14 February 2008 earthquake (M6.7) sequence offshore south Peloponnese (Greece): source models of the three strongest events. *Tectonophysics* 471(1):272–284
- Rubinov M, Sporns O (2010) Complex network measures of brain connectivity: uses and interpretations. *NeuroImage* 52(3):1059–1069
- Steeple W, Steeples D (1996) Far-field aftershocks of the 1906 earthquake. *Bull Seismol Soc Am* 86(4):921–924
- Tsapanos TM, Papadopolou AA (1999) A discrete Markov model for earthquake occurrence in Southern Alaska and Aleutian Islands. *Balk Geophys Soc* 2(3):75–83
- Utsu T (2002) A list of deadly earthquakes in the world: 1500–2000, *International Handbook of Earthquake & Engineering Seismology Part A*. Academic Press, San Diego, pp 691–717
- Wang XF, Chen GR (2003) Complex networks: small-world, scale-free and beyond [J]. *IEEE circuits and systems magazine* 3(1):6–20
- Watts DJ, Strogatz SH (1998) Collective dynamics of small-world networks. *Nature* 393:440–442

Non-extensive statistical physics analysis of earthquake magnitude sequences in North Aegean Trough, Greece

Giorgos Papadakis^{1,2} · Filippos Vallianatos^{1,2}

Received: 30 December 2016 / Accepted: 11 May 2017 / Published online: 19 May 2017
© Institute of Geophysics, Polish Academy of Sciences & Polish Academy of Sciences 2017

Abstract In a recent study, Papadakis et al. (*Physica A* 456: 135–144, 2016) investigate seismicity in Greece, using the non-extensive statistical physics formalism. Moreover, these authors examine the spatial distribution of the non-extensive parameter q_M and show that for shallow seismicity, increase of q_M coincides with strong events. However, their study also reveals low q_M values along the North Aegean Trough, despite the presence of strong events during 1976–2009. Consequently, the present study further examines the temporal behaviour of parameters q_M and A , to reveal their relation with the evolution of the earthquake sequence. Through temporal examination of these parameters, we aim to show that the seismogenic system of the North Aegean Trough presents high degree of interactions after strong earthquakes during the studied period. Our findings indicate that increase of q_M signifies the existence of long-range correlations. If its value does not significantly decrease after a strong earthquake (i.e. $M \geq 5$) then the studied area has not reached the state of equilibrium.

Keywords Tsallis entropy · Seismicity · Earthquake magnitude · North Aegean Trough · Greece

Introduction

The concept of non-extensive statistical physics (NESP) (Tsallis 1988, 2009) is a generalisation of Boltzmann–Gibbs entropic functional and refers to typical complex systems exhibiting long-range correlations in space and time (Vallianatos and Telesca 2012). NESP has been applied to a series of dynamical systems and has been successfully used for the investigation of seismicity (Abe and Suzuki 2003, 2005; Efstathiou et al. 2015; Michas et al. 2013; Papadakis 2016; Papadakis et al. 2013, 2015; Silva et al. 2006; Telesca 2010a, b, c, 2011, 2012; Vallianatos and Sammonds 2013; Vallianatos et al. 2012, 2013, 2014; Vilar et al. 2007).

Papadakis et al. (2016) examine the spatial behaviour of parameter q_M in Greece and the surrounding areas. These authors show that high q_M values are consistent with strong events, with the exception of the North Aegean Trough (NAT). Therefore, in the present study, the case of NAT is further examined. The non-extensive parameters q_M and A , which derive from the fragment-asperity model (Sotolongo-Costa and Posadas 2004), are dynamical parameters which change their value with time, reflecting the stability of a tectonically active area. Examination of their temporal behaviour elucidates the disagreement between the estimated q_M value and seismicity.

At this point, it should be noted that the fragment-asperity model uses the NESP formalism to describe the earthquake generation process and enables researchers to study the temporal behaviour of its entropic parameters towards a strong event (Papadakis et al. 2015; Telesca 2010c; Vallianatos et al. 2014). The aforementioned case studies show that increase of q_M is related with the occurrence of moderate-size events prior to the mainshock, indicating the initiation of a preparatory phase leading to a strong event. Papadakis et al. (2015) show that q_M decreases and reaches a minimum value

✉ Giorgos Papadakis
papadakis_giorgos@yahoo.com
Filippos Vallianatos
fvallian@chania.teicrete.gr

¹ Laboratory of Geophysics and Seismology, Technological Educational Institute of Crete, Chania, Greece

² UNESCO Chair on Solid Earth Physics and Geohazards Risk Reduction, Chania, Greece

right after the Kobe earthquake, whereas Vallianatos et al. (2014) reveal a continuous increase of this parameter after the mainshock in the southwest part of Crete.

Tectonic setting and earthquake catalogues

Dextral strike-slip motion is expressed along the North Anatolian Fault (NAF) and along the NAT area in northern Aegean (Kiratzi 2002; Koukouvelas and Aydin 2002; Papanikolaou and Papanikolaou 2007; Papazachos and Kiratzi 1996) (Fig. 1). Kiratzi (1991) determined the rate of deformation in the area of the NAT (15 mm/year) using moment tensor mechanisms. In addition, GPS data indicate that the slip rate of the NAT is ~ 17 mm/year (Hollenstein et al. 2008) and that the dextral slip motion diminishes westwards (Müller et al. 2013).

Furthermore, Kiratzi et al. (2016) used teleseismic data to calculate the source model of the May 24, 2014 earthquake ($M_w = 6.8$) earthquake in NAT and regional catalogues to examine the spatial–temporal characteristics of the sequence. These authors report that the strong earthquake occurred southwest of Samothrace Island (Fig. 6), and that its aftershocks spread along a ~ 200 km zone, activating the entire North Aegean Trough. Moreover, these authors present significant variations in the b-value preceded the occurrence of the strong event that seem to coincide with the results obtained through temporal examination of the parameter A for the period from January 1, 2010 to March 9, 2015 in the present study (see “Results”).

We use the homogeneous earthquake catalogue for Greece and the surrounding areas by Makropoulos et al. (2012). These authors estimated the magnitude of completeness as $M_w \geq 4.1$ for the period 1976–2009. Therefore, in the present study, the threshold magnitude of the catalogue used is $m_0 = 4.1$. Furthermore, earthquake data provided by the Hellenic Unified Seismological Network (HUSN) are used to study the evolution of seismicity along the NAT for the period from January 1, 2010 to March 9, 2015. Mignan and Chouliaras (2014) studied the spatial variation of the completeness magnitude (M_C) of the HUSN catalogue and found that M_C varies between 2.5 and 3.2 during 2008–2011 and between 2 and 2.5 during 2011–2013 in the area of the NAT. Therefore, we adopt the highest computed value of both periods as the threshold magnitude ($m_0 = 3.2$).

Unification of the aforementioned catalogues into a single homogenous catalogue seems of crucial importance for similar studies in the future. Preparation and publication of such a catalogue will allow us to further investigate the evolution of seismicity along the NAT.

Non-extensive statistical physics and the fragment-asperity model

NESP refers to the non-additive entropy S_q (Tsallis 1988, 2009), and it is suggested as an appropriate framework for the description of non-linear systems that violate Boltzmann–Gibbs statistical physics. For the case where the states of the system are discrete, S_q reads as:

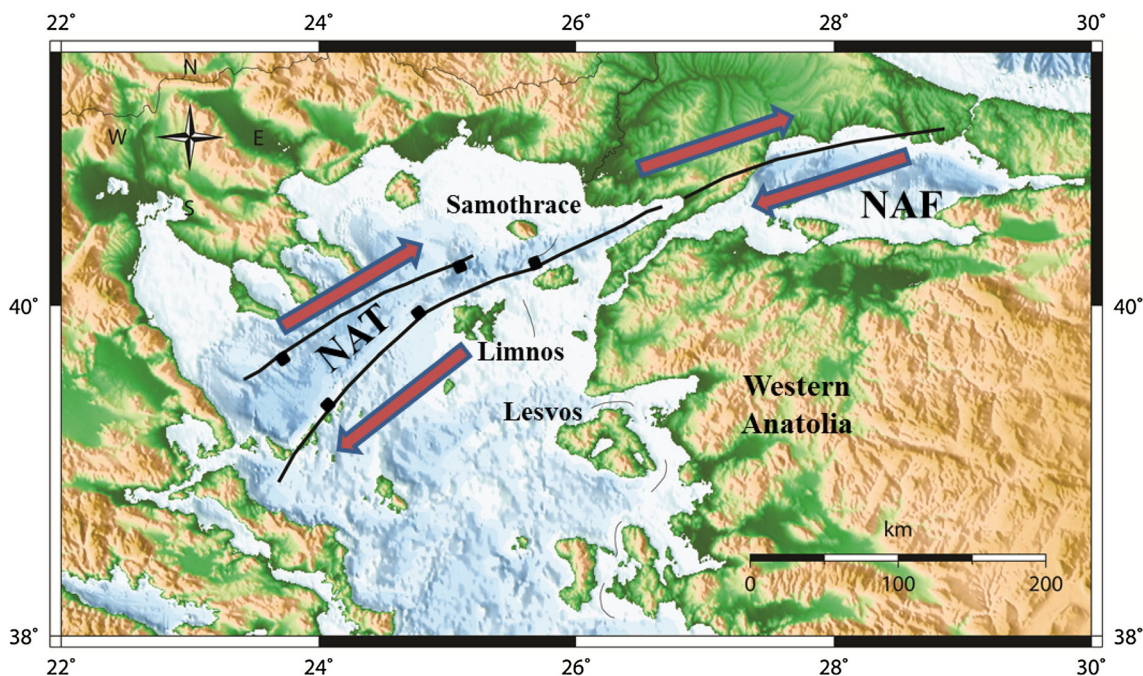


Fig. 1 Tectonic setting of the North Anatolian Fault (NAF) and the North Aegean Trough (NAT) as presented by Royden and Papanikolaou (2011)

$$S_q = k \frac{1 - \sum_{i=1}^W p_i^q}{q - 1}, \quad (q \in \mathbb{R}), \quad (1)$$

with

$$\sum_{i=1}^W p_i = 1, \quad (2)$$

where q is the entropic parameter which characterises the degree of correlations, and k is the positive constant. Expression (1) recovers the Boltzmann–Gibbs entropic function in the limit $q \rightarrow 1$. In the case of two probabilistically independent systems (e.g. A and B), Tsallis entropy (S_q) satisfies:

$$\frac{S_q(A+B)}{k} = \frac{S_q(A)}{k} + \frac{S_q(B)}{k} + (1-q) \frac{S_q(A)S_q(B)}{k^2}. \quad (3)$$

Relation 3 expresses the most important property of NESP. Since in all cases $S_q \geq 0$ (non-negativity), then $q < 1$ corresponds to super-additivity, $q = 1$ to additivity and $q > 1$ to sub-additivity, respectively.

In this study, we use the fragment-asperity model to calculate the non-extensive parameters which are related to the earthquake frequency–magnitude distribution. Sotolongo-Costa and Posadas (2004) introduced the fragment-asperity model, which is consistent with the idea of stick-slip frictional instability in faults. According to this model, earthquakes are triggered when accumulated stress causes strong interactions between the fault blocks and the material filling the gap between them. Furthermore, Sotolongo-Costa and Posadas (2004) proposed a function that relates the size distribution of the filling material with the energy distribution of seismic events. Moreover, Telesca (2011) suggested that the function between the magnitude (M) and the released relative energy (ε) is (Kanamori 1978)

$$M \sim \frac{2}{3} \log(\varepsilon). \quad (4)$$

Telesca (2012) also considered the threshold magnitude m_0 of the earthquake catalogue and proposed a realistic relationship for the earthquake frequency–magnitude distribution, given as:

$$\log\left(\frac{N(>M)}{N}\right) = \frac{2 - q_M}{1 - q_M} \log\left(\frac{1 - \left(\frac{1 - q_M}{2 - q_M}\right) \left(\frac{10^M}{A^{2/3}}\right)}{1 - \left(\frac{1 - q_M}{2 - q_M}\right) \left(\frac{10^{m_0}}{A^{2/3}}\right)}\right), \quad (5)$$

where q_M refers to the q Tsallis parameter.

At this point, it is worth noting that the fragment-asperity model has been used in many studies for the examination of earthquake sequences (Michas et al. 2013; Papadakis et al. 2013, 2015; Silva et al. 2006; Telesca 2010a, b, c, 2011, 2012; Vallianatos et al.

2012, 2013, 2014; Vilar et al. 2007). Many of these studies suggest that high q_M values signify a transition phase away from stability (Matcharashvili et al. 2011; Papadakis 2016; Papadakis et al. 2013, 2015, 2016; Telesca 2010b, c; Vallianatos et al. 2014; Valverde-Esparza et al. 2012).

Results

Examination of the temporal behaviour of the non-extensive parameters q_M and A along the NAT (Fig. 2) is performed to investigate the disagreement of the estimated q_M value with strong earthquakes. Figure 3 shows that the evolution of the seismic activity is consistent with the q_M temporal behaviour (Fig. 4) during 1976–2009. Increase of the q_M parameter is strongly related to four strong earthquakes, occurred on August 6, 1983 ($M_w = 6.7$), March 19, 1989 ($M_w = 5.3$), May 2, 1989 ($M_w = 5.3$) and July 26, 2001 ($M_w = 6.0$), respectively.

We use the maximum likelihood estimation method (Shalizi 2007; Telesca 2012) to calculate the parameters q_M and A , and the bootstrap method (Zoubir and Boashash 1998) (500 bootstrap samples) to estimate the standard deviation and the confidence intervals.

Figure 4 shows that the non-extensive parameter q_M is continuously increasing during 1976–2009. It should be noted that for the detection of possible variations of q_M , calculations are performed using cumulative event-based windows. Calculation is performed adding each time 1 event to the initial window (50-event width). There is a significant increase of q_M due to the occurrence of the two $M_w = 5.3$ earthquakes. Moreover, two recent studies (Papadakis et al. 2015; Vallianatos et al. 2014) also show that the occurrence of events which are not the stronger earthquakes of the examined dataset can cause a remarkable increase of q_M .

Figure 5 shows the temporal variations of the parameter A . Calculations are over increasing (cumulative) windows (per 1 event). This parameter, from 1990 onwards increases or decreases before or right after the occurrence of strong events. However, the most distinct feature of this figure is the decrease of A before the occurrence of the July 26 2001 ($M_w = 6.0$) earthquake. This shows that before a mainshock long-range interactions start occurring reducing the accumulated energy density A . Overall, temporal examination of the non-extensive parameters indicates that despite the occurrence of strong earthquakes, q_M values continue to increase reflecting high degree of interactions.

To validate these observations, temporal examination of the non-extensive parameters is performed for the period, from January 1, 2010 to March 9, 2015 using earthquake data provided by the HUSN (Fig. 6). Figure 7 shows the time distribution of seismicity. The occurrence of two strong earthquakes on January 8, 2013 ($M_L = 5.8$) and on

Fig. 2 Seismicity ($M_w \geq 4.1$) along the NAT (period 1976–2009). Earthquake data are provided by Makropoulos et al. (2012)

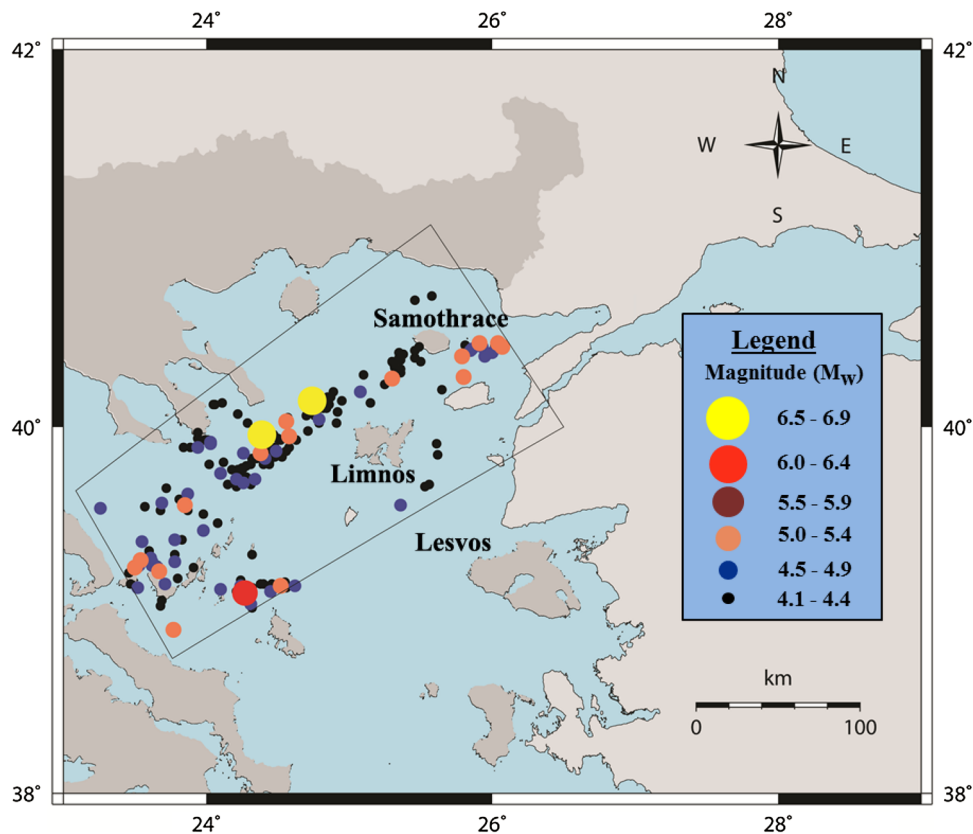
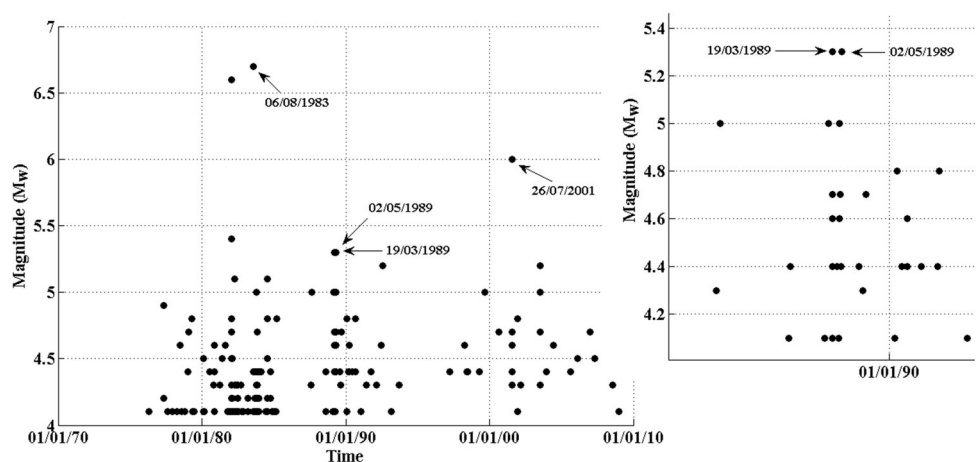


Fig. 3 Time distribution of seismicity. The upper right corner shows the two $M_w = 5.3$ seismic events occurred in 1989



May 24, 2014 ($M_L = 6.3/M_w = 6.8$) validates the hypothesis that the studied area was in a continuous state away from equilibrium. It is worth mentioning that the event which occurred on May 24, 2014 ($M_L = 6.3/M_w = 6.8$) is the strongest earthquake occurred in Greece during the period 2010–2014. Figure 8 presents temporal variations of q_M values over cumulative event-based windows. Calculation is performed adding each time 1 event to the initial window (50-event width).

It is observed that parameter q_M increases constantly despite the occurrence of the strong earthquakes. Figure 9

shows the temporal variations of the A parameter. Calculations are performed over increasing windows (per 1 event). This parameter peaks after the main shock on May 25, 2014 and continues increasing onwards. Moreover, this parameter increases during 2013, a year before the occurrence of the strong event on May 25, 2014 ($M_L = 6.3/M_w = 6.8$) and during the period right after the earthquake on January 8, 2013 ($M_L = 5.8$) indicating stress redistribution. Temporal examination of the non-extensive parameters indicates that despite the occurrence of the main shocks, q_M values continue to increase reflecting a

Fig. 4 Temporal variation of q_M (black line) using cumulative event-based windows. The standard deviation is denoted with the black dashed lines. This figure shows that significant increases of q_M coincide with strong earthquakes ($M_w > 5$)

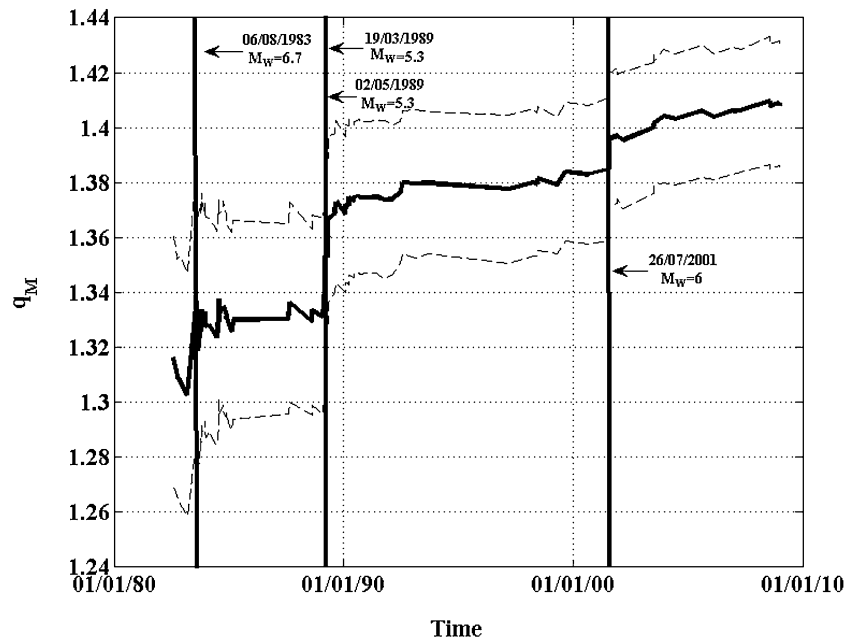
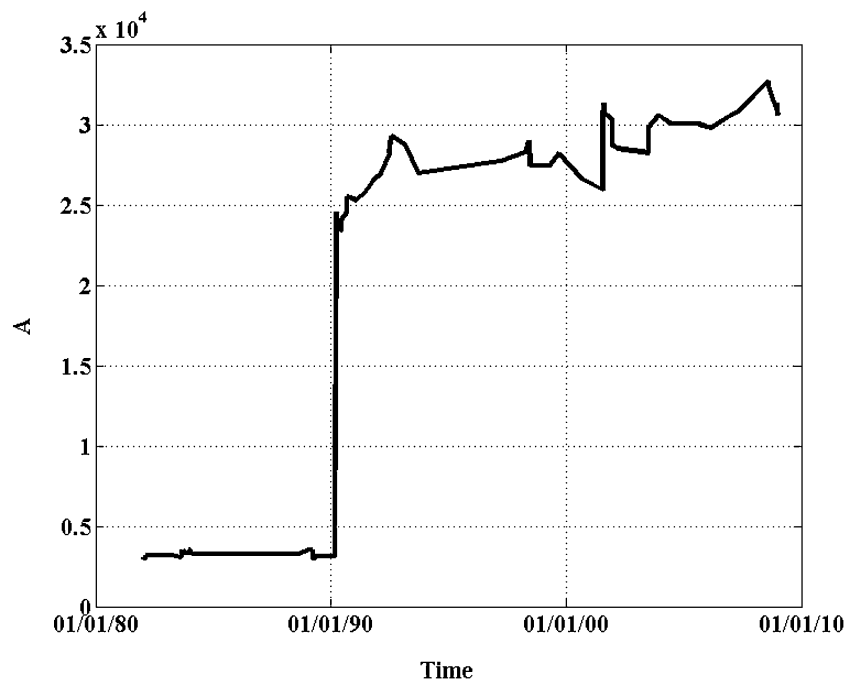


Fig. 5 Temporal variations of A over cumulative event-based windows



high degree of interactions and the increase of the volumetric energy density A manifests accumulated stress energy spreading throughout the seismogenic system. However, examination of A is still at a preliminary stage and further analysis is needed to fully elucidate its behaviour in regard to a strong earthquake.

It is worth mentioning that Kiratzi et al. (2016) also calculate temporal variations of the b-value in respect to the May 24, 2014 earthquake in NAT. These authors observe a continuous increase of the b value from 2008

onwards, followed by a gradual decrease to its background level before the mainshock.

Conclusions

Temporal examination of the non-extensive parameters reveals that the low q_M values estimated for the NAT area for 1976–2009 indicate that the seismogenic system was in a transition phase away from equilibrium. The analysis

Fig. 6 Seismicity ($M_L \geq 3.2$) along the NAT from January 1, 2010 to March 9, 2015. The yellow (biggest) circle denotes the May 24, 2014 earthquake ($M_L = 6.3/M_w = 6.8$) southwest of Samothrace Island

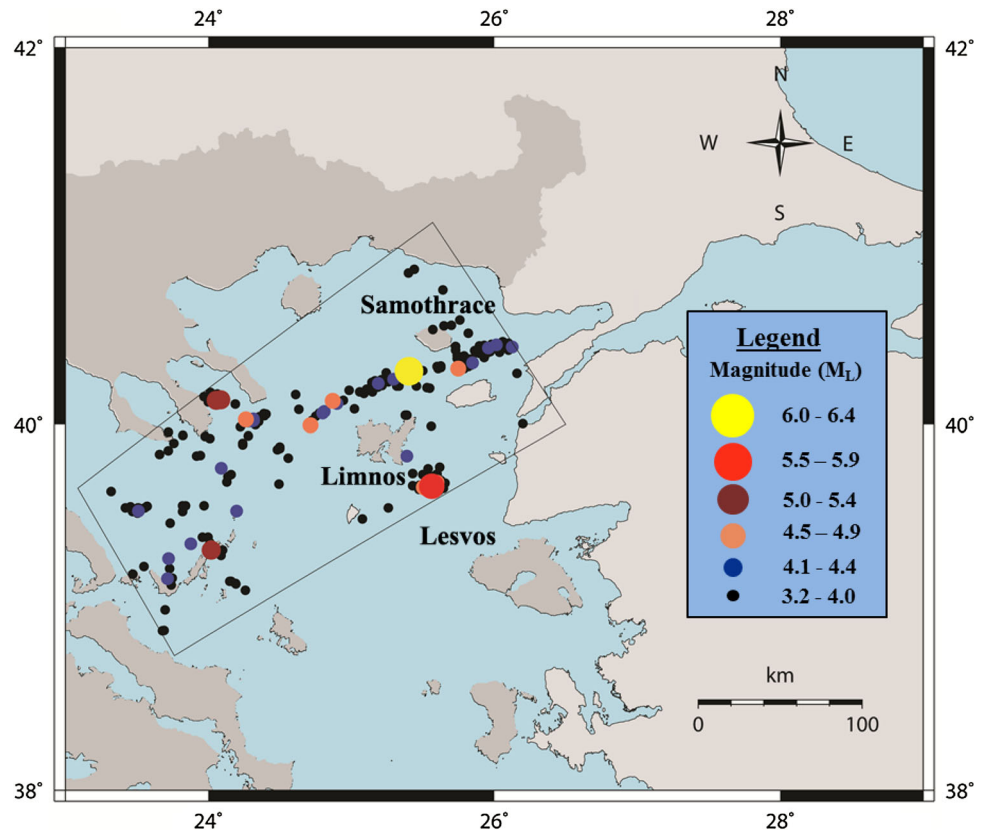
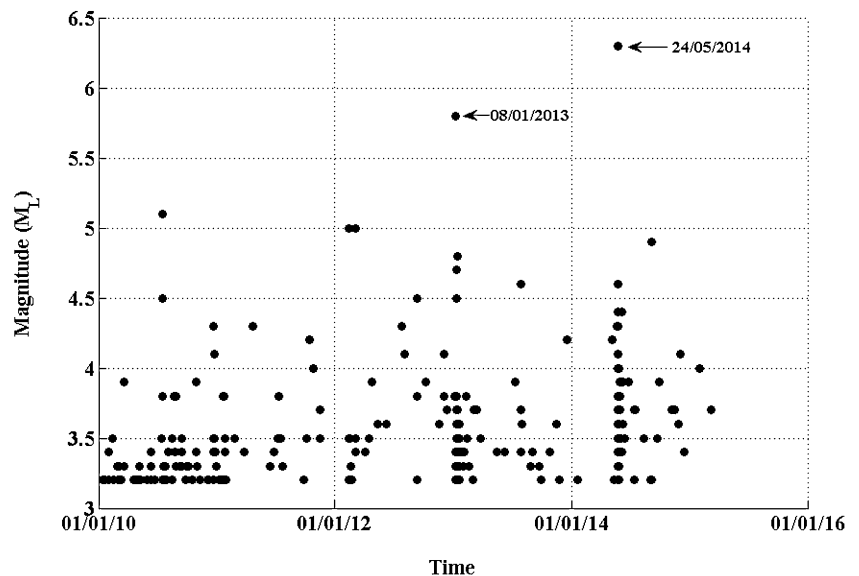


Fig. 7 Time distribution of seismicity for the period, from January 1, 2010 to March 9, 2015



shows that four earthquake events which occurred on August 6, 1983 ($M_w = 6.7$), March 19, 1989 ($M_w = 5.3$), and May 2, 1989 ($M_w = 5.3$) and July 26, 2001 ($M_w = 6.0$), respectively, coincide with significant increase of the q_M parameter, indicating that the seismogenic system was in a continuous pre-earthquake phase that led up to another strong event.

To validate these observations, examination of the non-extensive parameters is performed for the period, from January 1, 2010 to March 9, 2015. The occurrence of two strong earthquakes on January 8, 2013 ($M_L = 5.8$) and on May 24, 2014 ($M_L = 6.3/M_w = 6.8$) validates the hypothesis that the studied area was preparing for energy release. Overall, the temporal examination of the non-

Fig. 8 Temporal variation of q_M (black line) using cumulative event-based windows. The standard deviation is denoted with the black dashed lines

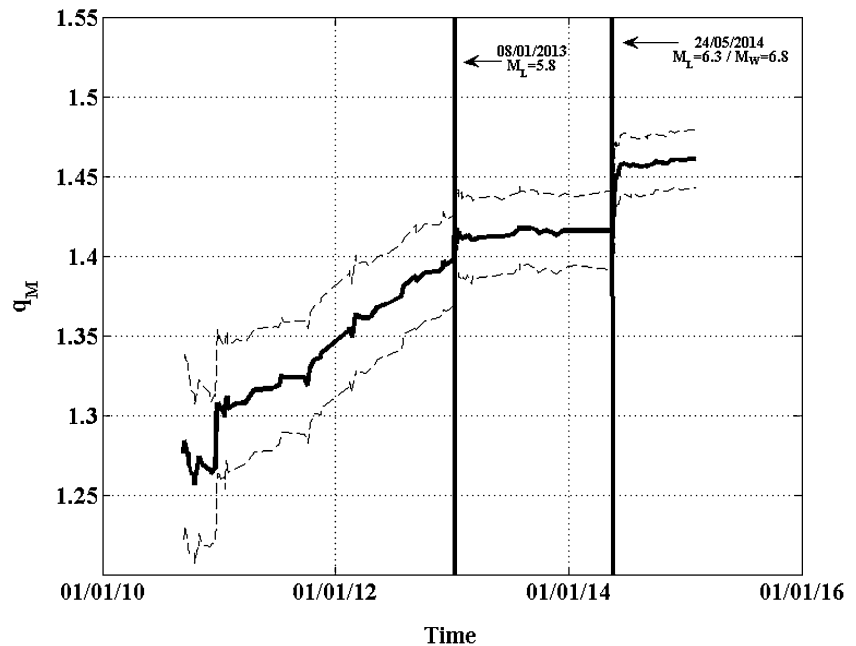
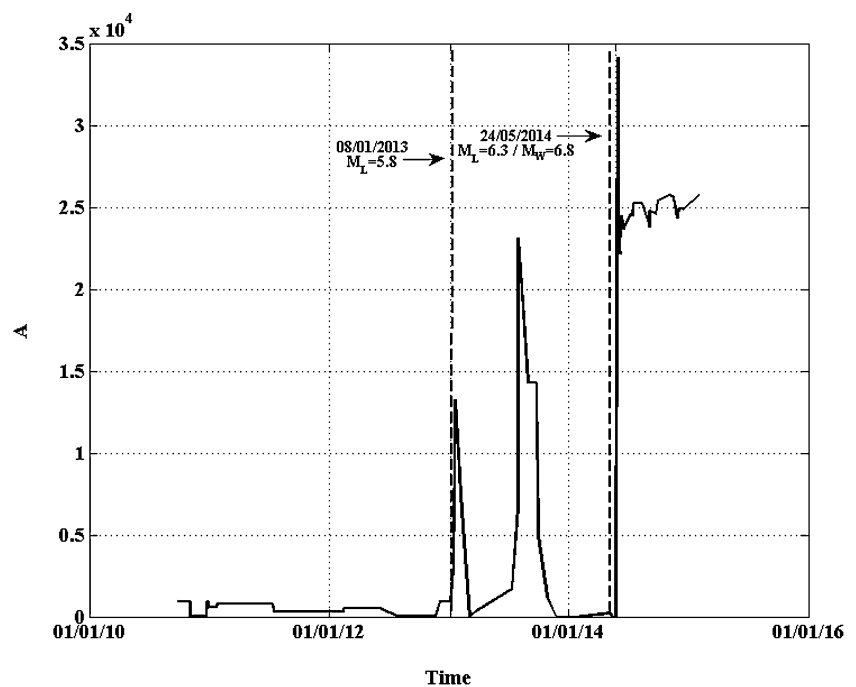


Fig. 9 Temporal variations of A over cumulative event-based windows



extensive parameters indicates that despite the occurrence of various main shocks, q_M values continue to increase reflecting high degree of correlations in the seismogenic system. The volumetric energy density A acquires higher value after the main shock on May 24, 2014 ($M_L = 6.3 / M_W = 6.8$) due to accumulated stress energy.

Concluding, it becomes clear that the consistency of seismicity with the observed non-extensive variations can be used to elucidate different dynamical regimes of

seismicity. However, a systematic attempt to analyse the temporal evolution of these parameters has not been performed yet. Consequently, a model accurately illustrating distinct phases of the earthquake process has not been developed.

Acknowledgements We would like to thank the reviewer for the detailed comments and suggestions that helped us to improve the quality of this study.

References

- Abe S, Suzuki N (2003) Law for the distance between successive earthquakes. *J Geophys Res* 108:2113. doi:[10.1029/2002JB002220](https://doi.org/10.1029/2002JB002220)
- Abe S, Suzuki N (2005) Scale-free statistics of time interval between successive earthquakes. *Phys A* 350:588–596
- Efstathiou A, Tzanis A, Vallianatos F (2015) Evidence of non-extensivity in the evolution of seismicity along the San Andreas Fault, California, USA: an approach based on Tsallis statistical physics. *Phys Chem Earth* 85–86:56–68. doi:[10.1016/j.pce.2015.02.013](https://doi.org/10.1016/j.pce.2015.02.013)
- Hollenstein Ch, Muller MD, Geiger A, Kahle HG (2008) Crustal motion and deformation in Greece from a decade of GPS measurements, 1993–2003. *Tectonophysics* 449:17–40. doi:[10.1016/j.tecto.2007.12.006](https://doi.org/10.1016/j.tecto.2007.12.006)
- Kanamori H (1978) Quantification of earthquakes. *Nature* 271:411–414. doi:[10.1038/271411a0](https://doi.org/10.1038/271411a0)
- Kiratzi AA (1991) Rates of crustal deformation in the North Aegean Trough–North Anatolian Fault deduced from seismicity. *Pure Appl Geophys* 136(4):421–432. doi:[10.1007/BF00878579](https://doi.org/10.1007/BF00878579)
- Kiratzi AA (2002) Stress tensor inversions along the westernmost North Anatolian Fault Zone and its continuation into the North Aegean Sea. *Geophys J Int* 151:360–376. doi:[10.1046/j.1365-246X.2002.01753.x](https://doi.org/10.1046/j.1365-246X.2002.01753.x)
- Kiratzi A, Tsakiroudi E, Benetatos C, Karakaisis G (2016) The May 2014 (M_w 6.8) earthquake (North Aegean Trough): spatiotemporal evolution, source and slip model from teleseismic data. *Phys Chem Earth* 95:85–100. doi:[10.1016/j.pce.2016.08.003](https://doi.org/10.1016/j.pce.2016.08.003)
- Koukouvelas IK, Aydin A (2002) Fault structure and related basins of the North Aegean Sea and its surroundings. *Tectonics* 21(5):1046. doi:[10.1029/2001TC901037](https://doi.org/10.1029/2001TC901037)
- Makropoulos K, Kaviris G, Kouskouna V (2012) An updated and extended earthquake catalogue for Greece and adjacent areas since 1900. *Nat Hazards Earth Syst Sci* 12:1425–1430. doi:[10.5194/nhess-12-1425-2012](https://doi.org/10.5194/nhess-12-1425-2012)
- Matcharashvili T, Chelidze T, Javakishvili Z, Jorjiashvili N, Fra Paleo U (2011) Non-extensive statistical analysis of seismicity in the area of Javakheti, Georgia. *Comput Geosci* 37:1627–1632. doi:[10.1016/j.cageo.2010.12.008](https://doi.org/10.1016/j.cageo.2010.12.008)
- Michas G, Vallianatos F, Sammonds P (2013) Non-extensivity and long-range correlations in the earthquake activity at the West Corinth rift (Greece), *Nonlin. Processes Geophys* 20:713–724. doi:[10.5194/npg-20-713-2013](https://doi.org/10.5194/npg-20-713-2013)
- Mignan A, Chouliaras G (2014) Fifty years of seismic network performance in Greece (1964–2013): spatiotemporal evolution of the completeness magnitude. *Seismol Res Lett* 85:657–667. doi:[10.1785/0220130209](https://doi.org/10.1785/0220130209)
- Müller MD, Geiger A, Kahle HG, Veis G, Billiris H, Paradissis D, Felekis S (2013) Velocity and deformation fields in the North Aegean domain, Greece, and implications for fault kinematics, derived from GPS data 1993–2009. *Tectonophysics* 597–598:34–49. doi:[10.1016/j.tecto.2012.08.003](https://doi.org/10.1016/j.tecto.2012.08.003)
- Papadakis G (2016) A non-extensive statistical physics analysis of seismic sequences: application to the geodynamic system of the Hellenic subduction zone, PhD thesis, University College London
- Papadakis G, Vallianatos F, Sammonds P (2013) Evidence of nonextensive statistical physics behavior of the Hellenic subduction zone seismicity. *Tectonophysics* 608:1037–1048. doi:[10.1016/j.tecto.2013.07.009](https://doi.org/10.1016/j.tecto.2013.07.009)
- Papadakis G, Vallianatos F, Sammonds P (2015) A nonextensive statistical physics analysis of the 1995 Kobe, Japan earthquake. *Pure Appl Geophys* 172:1923–1931. doi:[10.1007/s00024-014-0876-x](https://doi.org/10.1007/s00024-014-0876-x)
- Papadakis G, Vallianatos F, Sammonds P (2016) Non-extensive statistical physics applied to heat flow and the earthquake frequency-magnitude distribution in Greece. *Phys A* 456:135–144. doi:[10.1016/j.physa.2016.03.022](https://doi.org/10.1016/j.physa.2016.03.022)
- Papanikolaou I, Papanikolaou D (2007) Seismic hazard scenarios from the longest geologically constrained active fault of the Aegean. *Quat Int* 171–172:31–44. doi:[10.1016/j.quaint.2007.03.020](https://doi.org/10.1016/j.quaint.2007.03.020)
- Papazachos CB, Kiratzi AA (1996) A detailed study of the active crustal deformation in the Aegean and surrounding area. *Tectonophysics* 253:129–153
- Royden LH, Papanikolaou DJ (2011) Slab segmentation and late Cenozoic disruption of the Hellenic arc. *Geochem Geophys Geosyst* 12(3):Q03010. doi:[10.1029/2010GC003280](https://doi.org/10.1029/2010GC003280)
- Shalizi CR (2007) Maximum likelihood estimation for q-exponential (Tsallis) distribution, [math.ST] 1 February 2007, <http://arxiv.org/pdf/math/0701854v2.pdf>. Accessed September 2016
- Silva R, Franca GS, Vilar CS, Alcaniz JS (2006) Nonextensive models for earthquakes. *Phys Rev E* 73:026102. doi:[10.1103/PhysRevE.73.026102](https://doi.org/10.1103/PhysRevE.73.026102)
- Sotolongo-Costa O, Posadas A (2004) Fragment-asperity interaction model for earthquakes. *Phys Rev Lett* 92(4):048501. doi:[10.1103/PhysRevLett.92.048501](https://doi.org/10.1103/PhysRevLett.92.048501)
- Telesca L (2010a) Analysis of Italian seismicity by using a nonextensive approach. *Tectonophysics* 494:155–162. doi:[10.1016/j.tecto.2010.09.012](https://doi.org/10.1016/j.tecto.2010.09.012)
- Telesca L (2010b) Nonextensive analysis of seismic sequences. *Phys A* 389:1911–1914. doi:[10.1016/j.physa.2010.01.012](https://doi.org/10.1016/j.physa.2010.01.012)
- Telesca L (2010c) A non-extensive approach in investigating the seismicity of L' Aquila area (central Italy), struck by the 6 April 2009 earthquake ($M_L = 5.8$). *Terra Nova* 22(2):87–93. doi:[10.1111/j.1365-3121.2009.00920.x](https://doi.org/10.1111/j.1365-3121.2009.00920.x)
- Telesca L (2011) Tsallis-based nonextensive analysis of the southern California seismicity. *Entropy* 13(7):1267–1280. doi:[10.3390/e13071267](https://doi.org/10.3390/e13071267)
- Telesca L (2012) Maximum likelihood estimation of the nonextensive parameters of the earthquake cumulative magnitude distribution. *Bull Seismol Soc Am* 102(2):886–891. doi:[10.1785/0120110093](https://doi.org/10.1785/0120110093)
- Tsallis C (1988) Possible generalization of Boltzmann–Gibbs statistics. *J Stat Phys* 52:479–487
- Tsallis C (2009) Introduction to nonextensive statistical mechanics: approaching a complex world. Springer, Berlin
- Vallianatos F, Sammonds P (2013) Evidence of non-extensive statistical physics of the lithospheric instability approaching the 2004 Sumatran-Andaman and 2011 Honsu mega-earthquakes. *Tectonophysics* 590:52–58. doi:[10.1016/j.tecto.2013.01.009](https://doi.org/10.1016/j.tecto.2013.01.009)
- Vallianatos F, Telesca T (2012) Statistical mechanics in earth physics and natural hazards. *Acta Geophys* 60(3):499–501. doi:[10.2478/s11600-012-0037-5](https://doi.org/10.2478/s11600-012-0037-5)
- Vallianatos F, Michas G, Papadakis G, Sammonds P (2012) A non-extensive statistical physics view to the spatiotemporal properties of the June 1995, Aigion earthquake ($M_6.2$) aftershock sequence (West Corinth rift, Greece). *Acta Geophys* 60:758–768. doi:[10.2478/s11600-012-0011-2](https://doi.org/10.2478/s11600-012-0011-2)
- Vallianatos F, Michas G, Papadakis G, Tzanis A (2013) Evidence of non-extensivity in the seismicity observed during the 2011–2012 unrest at the Santorini volcanic complex, Greece. *Nat Hazards Earth Syst Sci* 13:177–185. doi:[10.5194/nhess-13-177-2013](https://doi.org/10.5194/nhess-13-177-2013)
- Vallianatos F, Michas G, Papadakis G (2014) Non-extensive and natural time analysis of seismicity before the M_w 6.4, October 12, 2013 earthquake in the south west segment of the Hellenic arc. *Phys A* 414:163–173. doi:[10.1016/j.physa.2014.07.038](https://doi.org/10.1016/j.physa.2014.07.038)
- Valverde-Esparza SM, Ramirez-Rojas A, Flores-Marquez EL, Telesca L (2012) Non-extensivity analysis of seismicity within four

- subduction regions in Mexico. *Acta Geophys* 60:833–845. doi:[10.2478/s11600-012-0012-1](https://doi.org/10.2478/s11600-012-0012-1)
- Vilar CS, Franca GS, Silva R, Alcaniz JS (2007) Nonextensivity in geological faults? *Phys A* 377:285–290. doi:[10.1016/j.physa.2006.11.017](https://doi.org/10.1016/j.physa.2006.11.017)
- Zoubir AM, Boashash B (1998) The bootstrap and its applications in signal processing. *IEEE Signal Process Mag* 15:56–76

Spatio-temporal evolution of aftershock energy release following the 1989, M_w 6.9, LOMA Prieta earthquake in California

Dragomir Gospodinov¹ 

Received: 18 January 2017 / Accepted: 12 April 2017 / Published online: 21 April 2017
© Institute of Geophysics, Polish Academy of Sciences & Polish Academy of Sciences 2017

Abstract We apply a stochastic model to study Benioff strain release after the M_w 6.9 October 18, 1989 Loma Prieta strong earthquake in north California, USA. The model is developed, following a compound Poisson process and contours the evolution of strain release during the aftershock sequence following the main shock occurrence. First, the temporal evolution of the aftershock decay rate was modeled by the Restricted Epidemic Type Aftershock Sequence (RETAS) model and after that the recognized best fit model is integrated into the strain release stochastic analysis. The applied stochastic model of Benioff strain release empowers a more detailed study by detecting possible deviations between observed data and model. Real values of the cumulative Benioff strain release surpass the expected modeled ones, indicating, that large aftershocks cluster at the beginning of the Loma Prieta sequence immediately after the occurrence of the main shock. Strain release spatial analysis reveals release patterns, which change during the aftershock sequence.

Keywords Aftershock sequence · Benioff strain · Stochastic modeling

Introduction

The investigation of large earthquakes is an important objective of seismic studies as they are of major importance in seismic hazard estimation. Nevertheless, the importance of studying in detail aftershock sequences is constantly increasing. Their research allows to study the physical processes of stress relaxation after a main shock and to provide useful information to authorities by making short-term forecasts of the aftershock sequence evolution.

In the present study we examine the seismic activity after the Loma Prieta M_w 6.9 earthquake, that occurred on October 18th, 1989 (Wald et al. 1991). The event was named after the Loma Prieta peak of the Santa Cruz Mountains south of San Jose, it killed 63 people and wounded another 350. The estimated property loss is in the range \$6–10 billion. This event was the largest to impact the Bay Area since the M_w 7.9 San Francisco Earthquake of 1906 (Hansen and Condon 1989; Zoback 2006). Even though the Loma Prieta earthquake took place on the periphery of the Bay Area, it disclosed the exposure of the entire region to forthcoming earthquakes. A M_w 6.0 earthquake reminded this fact on August 24, 2014 (Parsons et al. 2014). It struck about 30 miles of San Francisco in North San Francisco Bay Area and caused economic losses to be at the minimum \$362 million.

All the above facts reveal that future earthquakes could occur in this region and could impact even more populated parts of the Bay Area than the events of 1989 and 2014. This motivates continued research on the available data.

In most cases seismic hazard assessment does not take into account aftershock activity. For that reason different declustering algorithms (Gardner and Knopoff 1974; Reasenber 1985) that exclude aftershocks from the data are implemented. In recent years this tendency has been

Electronic supplementary material The online version of this article (doi:10.1007/s11600-017-0038-5) contains supplementary material, which is available to authorized users.

✉ Dragomir Gospodinov
drago@uni-plovdiv.bg

¹ Plovdiv University “Paisiy Hilendarski”, Tsar Asen str., 24, 4000 Plovdiv, Bulgaria

substituted by the use of different stochastic processes of fitting the clustering features of aftershocks (Ogata 1998; Zhuang 2004; Gospodinov and Rotondi 2006). A similar approach permits the use of all existing information about a sequence, taking into account aftershock statistics to interpret anomalous seismicity variations (Drakatos 2000; Ogata et al. 2003). Aftershocks temporal and spatio-temporal evolution after a strong earthquake is usually analyzed by applying acceptable stochastic models of aftershock occurrences (Ogata 1988, 1998, 2003; Gospodinov and Rotondi 2006).

Certain studies examine the energy distribution of aftershocks, most often by investigating their recurrence law. The aspect of aftershock energy release in space and time is; however, also important. Jaiswal et al. (2010) compared energy to strain release of aftershocks, following the two strong earthquakes of 2004 and 2005 near Sumatra. The first of them is the 2004 Indian Ocean earthquake, which occurred on 26 December with the epicenter off the west coast of Sumatra, Indonesia and had a moment magnitude of 9.1–9.3 (Stein 2007). The 2005 event near Sumatra is the Nias–Simeulue earthquake. It occurred on 28 March off the west coast of northern Sumatra and had a moment magnitude of 8.6 (Konca 2007).

Kagan and Houston (2005) studied the relation between aftershock moment release rate, modeled by a law, similar to Omori's law, and the main shock rupture evolution. They compared the rupture processes (rates of moment release) of three strong California earthquakes (1992 M_w 7.3 Landers 1994 M_w 6.7 Northridge and 1999 M_w 7.1 Hector Mine) and their aftershock seismic moment release rates. The results of this paper revealed that the rate of moment release during an aftershock sequence followed a power-law decay, analogous to the familiar Omori law, applied to depict aftershock frequency.

Tajima and Kanamori (1985) tried to delineate an aftershock area, based upon the amount of the released aftershock energy. They contour areas of different released energy values for the aftershock area.

Another feature of aftershock energy release is examined by Gentili and Bressan (2008). They explored the ratio of the released main shock seismic energy and the summation of the aftershocks seismic energy, released during the sequence.

Gospodinov et al. (2009) surveyed the energy release pattern of three seismic sequences after strong earthquakes in the North Aegean Sea ($M_w = 7.2$ in 1981; $M_w = 7.0$ in 1982 and $M_w = 6.8$ in 1983). The results revealed that at the beginning of the series there were a bigger number of strong aftershocks than expected by their model. Tzanis and Vallianatos (2003) defined the so called seismic release, which, depending on the purpose of the study, can be moment, energy, Benioff strain, defined by the square

root of energy, or event number. When analyzing the energy evolution of weaker events (usually with magnitudes $M_w \leq 5.0$), like aftershocks, the summed Benioff strain is particularly useful. Cumulative moment is controlled by the stronger earthquakes and event count excludes magnitudes.

In the present paper we apply the stochastic process, suggested by Gospodinov et al. (2009) to model Benioff strain in a single aftershock sequence. The model is developed, following a compound Poisson process, based on two main assumptions. The first one suggests that there is no relation between the origin time and the magnitude of an event. The second assumption is that there is no relation between the magnitude of a certain event and magnitudes of previous earthquake. These assumptions seem reasonable in the absence of a physical theory, underlying the relaxation process and considering usual aftershock behavior. The presented stochastic process was implemented to model Benioff strain release of the aftershock sequence, following the M_w 6.9 Loma Prieta earthquake in California, USA. Evaluating the coherence between real data and model, one can identify and interpret eventual deviations, allowing the exploration of the aftershock process in more detail. We also inspected the spatial evolution of Benioff strain, which sheds light on the eventual seismic asperities in the aftershock zone, leading to larger aftershocks.

Methodology

Benioff strain release stochastic model

To elaborate a Benioff strain release model, we apply a marked point process—an analog of a counting process (Taylor and Karlin 1984). It is often named mark accumulator process and is expressed in the following way: consider a Poisson process $\{N(t): t \geq 0\}$, having a rate $\lambda > 0$ and suggest that the time T_i of an event is related to the occurrence of a random variable Y_i , where $\{Y_n: n > 0\}$ is a family of independent random variables with identical distributions of the kind $G(y) = Pr\{Y_i \geq y\}$. Another condition is that these variables will not depend on $\{N(t) : t \geq 0\}$, either. If we define a stochastic process by the formula:

$$Z(t) = \sum_{k=1}^{N(t)} Y_k \text{ for } \geq 0 \quad (1)$$

the process is supposed to be a compound Poisson process (Taylor and Karlin 1984).

If μ and v^2 are the common mean and the variance of the marks Y_1, Y_2, \dots , the moments of $Z(t)$ (mean and variance) are expressed by:

$$E[Z(t)] = \lambda\mu t \quad (2)$$

$$\text{Var}[Z(t)] = \lambda(v^2 + \mu^2)t \quad (3)$$

Taking into account the aforementioned assumptions, performed for the development of the compound Poisson process, we see that they agree with the ones made previously for the aftershocks' magnitudes. This makes the stochastic process suitable to be applied as a model of random events when a sequence of events' magnitudes and their occurrence times is being described.

If a more general consideration of marked point processes is addressed, $\{N(t) : t \geq 0\}$ can be an inhomogeneous Poisson process with an intensity, depending on time $\lambda = \lambda(t) : t \geq 0$ and it is not obligatory that the marks $\{Y_n : n > 0\}$ create an independent series of random variables. Also, it is not necessary for the marks not to depend on the counting process or the occurrence times (Snyder and Miller 1991).

Let us survey a compound Poisson process of rate $\lambda = \lambda(t)$, which is inhomogeneous. In that case, following Snyder and Miller (1991), formulae (2) and (3) would be transformed into:

$$E[Z(t)] = \int_{t_0}^t \lambda(t) dt \quad (4)$$

$$\text{Var}[Z(t)] = (v^2 + \mu^2) \int_{t_0}^t \lambda(t) dt \quad (5)$$

We may use the common mean, provided by formula (4), to model the aggregate Benioff strain release, whereas the variance (its square root) stands for the error bounds.

Examining formulae (4) and (5), one can see that the intensity function $\lambda = \lambda(t)$ is required to employ the Benioff strain release model. That is why we first evaluate the intensity function parameters by modeling it by the RETAS model.

Restricted epidemic type aftershock sequence (RETAS) model

When the intensity function of aftershock decay is examined, the Modified Omori Formula (MOF) model is usually the first to be applied (Formula 6)

$$\lambda(t) = \frac{K}{(t+c)^p} \quad (6)$$

where t is the time elapsed from the occurrence of the main shock, K is a parameter related to the total number of aftershocks in the sequence, p is a coefficient of attenuation and c is a constant, thought to be linked to the time delay before the onset of the power-law aftershock decay rate.

The MOF model follows the idea of aftershocks conditional independency and that the events follow a non-stationary Poisson process (Utsu 1970). More complex aftershock sequences of multiple strong events led Ogata (1988) to propose the formulation of the Epidemic Type Aftershock Sequence (ETAS) model. According to ETAS, each aftershock can trigger its own secondary events.

Other authors (Gospodinov and Rotondi 2006) elaborated the RETAS model, based on the supposition that only aftershocks, whose magnitudes are larger than or equal to a threshold M_{th} can trigger secondary activity. This model has the advantage to include both versions, MOF and the ETAS, as limited cases, verifying at the same time all in-between cases. Its conditional intensity function is:

$$\lambda(t|H_t) = \mu + \sum_{\substack{t_i < t \\ M_i \geq M_{th}}} \frac{K_0 e^{\alpha(M_i - M_0)}}{(t - t_i + c)^p} \quad (7)$$

The formula is quite similar to the ETAS model intensity function (Ogata 1988) with the restriction that not all aftershocks but only events stronger than a certain limit can induce new shocks and hence the name RETAS. Here K_0 is a multiplier, common to all triggering aftershocks, which has an impact on the total aftershock productivity. The coefficients c and p are characterized as the ones in the MOF model, and the summation is taken over every i th aftershock with a magnitude stronger than or equal to the triggering threshold M_{th} . By H_t , we denote the history of the process before time t , which for RETAS is the set of origin times and magnitudes of all events with magnitudes $M \geq M_{th}$. The parameter μ stands for the background seismicity rate, t_i is the i th event occurrence time and α accounts for the influence of magnitude on the triggering of aftershocks.

Considering the conditional intensity function parameters, a Fortran program was developed to calculate the maximum log-likelihood function:

$$\log L(\theta) = \sum_{i=1}^N \log \lambda_{\theta}(t_i|H_{t_i}) - \int_S^T \lambda_{\theta}(t|H_t) dt \quad (8)$$

Formula (8) was used to acquire the model parameters estimates by the maximum likelihood method. Here S is the occurrence time of the main shock, the symbol Θ denotes the model parameters K_0 , μ , α , c and p , $\lambda_{\theta}(t|H_t)$ is the intensity function of the RETAS model, conditioned on the history, H_t the history being defined as for Formula 7. The triggering magnitude M_{th} was not included as a parameter for estimation in the model. Instead, obtaining the maximum likelihood estimates (MLE) for different M_{th} , we may choose the value of M_{th} , for which we get minimum value of the Akaike Information Criterion (AIC) and this value defines the best fit RETAS model (Akaike 1974).

Table 1 MLEs of the best fit RETAS model parameters [see formula (6)]

Model	M_{th}	AIC	μ	K	α	C	p
ETAS (best fit)	2	-5137.16	0	0.015	1.511	0.019	1.12

$$AIC = -2\max \log L + 2k \quad (9)$$

In formula (9) L stands for the likelihood function while k represents the number of model parameters.

Benioff strain

The aftershock intensity of the analyzed Loma Prieta aftershock sequence was estimated by the method of Gospodinov et al. (2007). The RETAS model (formula 7.) was applied and the estimated model parameters are presented in Table 1. Following, in the present paper we use the latter results to model the strain release rate in the aftershock sequence. Gutenberg and Richter (1956) provided the following formula, relating the total energy of seismic waves and its surface-wave magnitude:

$$\log E = 1.5M + 11.8 \quad (10)$$

which we applied to turn magnitude into energy. We have chosen Benioff strain, ε , as a measure of seismic energy release, which is given by the square root of each aftershock's energy. The cumulative Benioff strain is:

$$\varepsilon(t) = \sum_{i=1}^N \varepsilon_i = \sum_{i=1}^N \sqrt{E_i(t)} \quad (11)$$

This measure is the most appropriate to use, compared to seismic energy, when smaller events are considered, as in the current case (Tzanis and Vallianatos 2003). In this formula $E_i(t)$ is the i th event seismic energy and the summation is for all N events, that occurred before time t . To incorporate smaller energy values, we normalized the energy of each aftershock to the one with the smallest magnitude in the data sample.

Using Benioff strain rate instead of the number of aftershocks, we also evade the problem of omitting weak aftershocks, given that the bigger part of strain release is contained in the strongest aftershocks.

Data and results

Data

A huge amount of data has been compiled for the study of the relaxation process after the Loma Prieta earthquake. A special Data Archive was established to gather, organize,

and archive raw data related to this strong event (Dietz and Ellsworth 1991).

The main goal was to complement the National Earthquake Hazards Program (NEHRP). Twenty-four data sets are included in the archive. There are different datasets for strong motion, aftershocks, geotechnical, structural and social survey data.

All recorded earthquakes (10,373 events) from Oct 18, 1989 to Oct 17, 1991 are included in the file lp8910.zip from the Loma Prieta Data Archive (Dietz and Ellsworth 1991) with primary coda magnitudes FMAG1 (Eaton 1992). The aftershocks are located in the polygon defined by these corners:

Lat (°N)	Long (°E)
37.33	-122.17
37.33	-122.03
36.95	-121.49
36.75	-121.49
36.75	-121.72
37.06	-122.17
37.33	-122.17

The magnitude of completeness for the events, occurring within several hours after the main shock, is $\sim M1.5$. We analyzed data of the Loma Prieta aftershock sequence, containing $N = 1024$ events with magnitude $M \geq 2.0$ in the period, covering the first year after the strong earthquake (see Fig. 1).

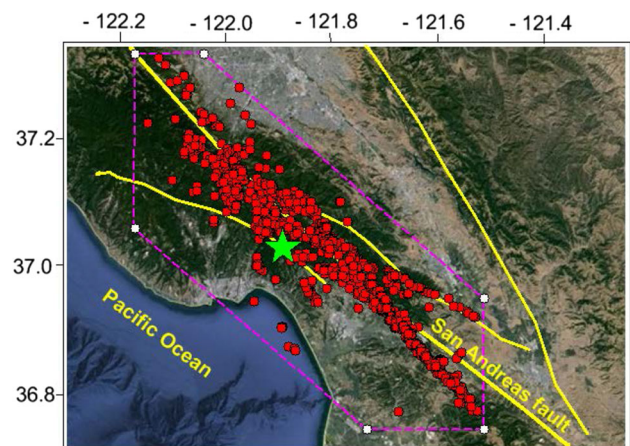


Fig. 1 Epical map of the aftershocks, following the 1989, $M_w 6.9$, Loma Prieta earthquake. Green star indicates the main shock epicenter and circles denote epicenters (circles radii are not scaled with magnitudes). The thick line stands for the San Andreas fault and the thinner lines reveal nearby faults (faults locations are by Plafker and Galloway 1989). The polygon, covering the locations of the examined events, is delineated by the dashed line

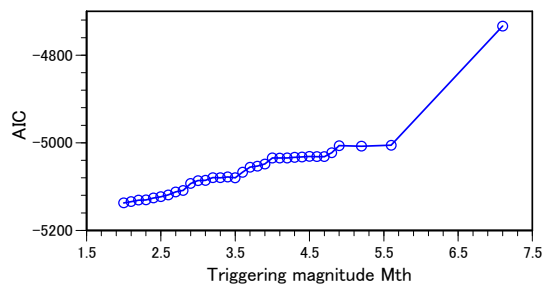


Fig. 2 The AIC values versus the triggering magnitude values. The minimum value of AIC is when M_{th} equals the lowest cutoff magnitude of the sample

Temporal evolution of Benioff strain

Our first task was to apply the RETAS model to fit the temporal decay of aftershocks rate. The calculated smallest value of AIC is for M_{th} equal to the lowest cutoff

magnitude of the sample (see Fig. 2). Thus, the identified best fit RETAS version corresponds to the ETAS model.

Table 1 contains the MLEs of the best fit model parameters. The identified clustering pattern reveals that events are grouped temporally not only to stronger aftershocks and can also form clusters of weaker ones.

The detected temporal model of rate decay allowed to calculate the aggregate number of events in time and to plot it along with the real cumulative number (Fig. 3a). The identified best fit model provided the necessary conditional intensity $\lambda_{\theta}(t|H_t)$, which was later integrated into Formulae 4 and 5 to model the Benioff strain release of the studied sequence. The results from the observed and modeled strain release were plotted on Fig. 3b.

We examined the compatibility between the ETAS model and real data by comparing the observed number of events in time with the one calculated by the MLEs. Standard deviation was used as an error estimate (Fig. 3a).

Fig. 3 Temporal Benioff strain evolution and cumulative number of events for a 1-year period: **a** Cumulative number—circles denote the real cumulative number, the thick line represents the expected cumulative number and dashed lines are the error bounds. Vertical lines signify events' magnitudes; **b** Benioff strain—circles denote real strain released, thick line indicates the expected released strain values, calculated after Formula 4, and the dashed lines are the error bounds, represented by the standard deviation

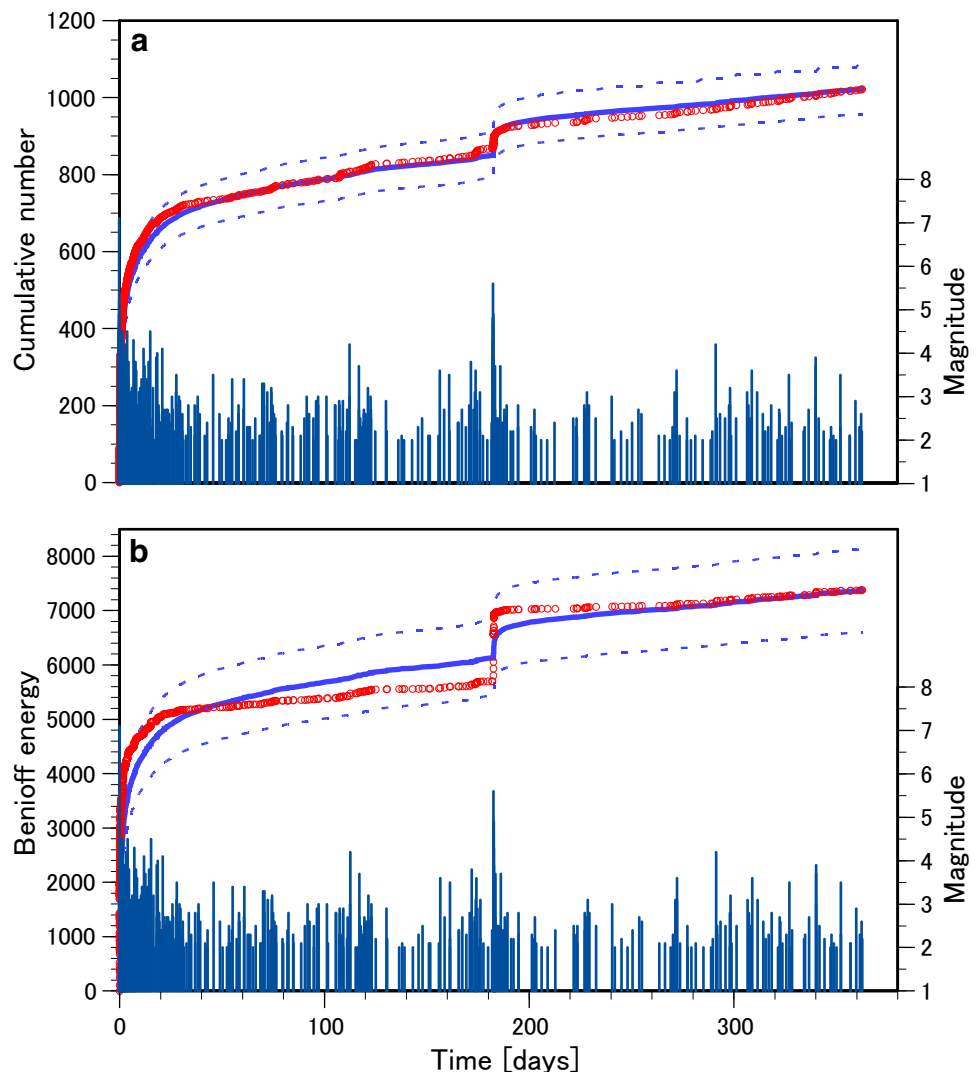
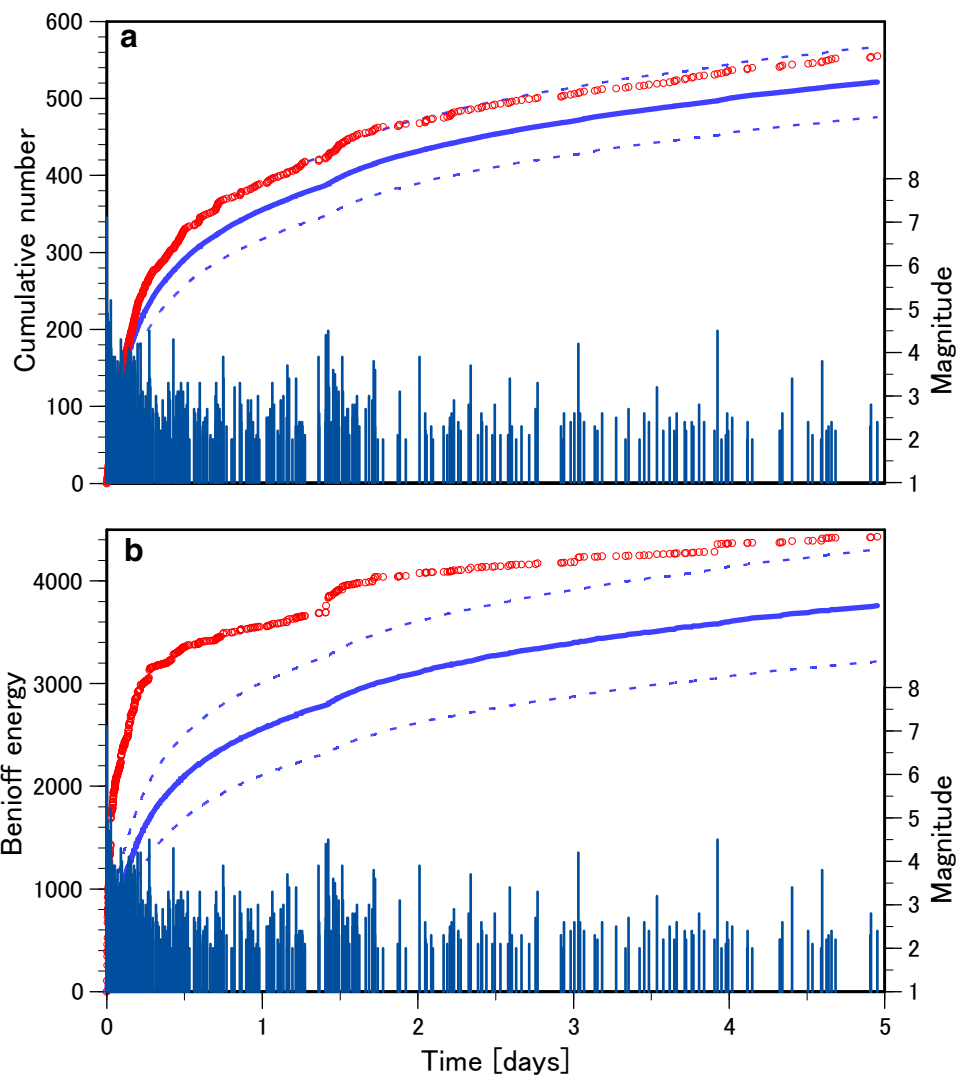


Fig. 4 Benioff strain evolution and cumulative number in time for a 5-days period immediately after the occurrence of the main shock. Notation as in Fig. 3



Concerning the aftershock decay rate (Fig. 3a) it can be observed that the applied model fits the real data quite well. Although there is some exceedance of the real cumulative number over the modeled one at the beginning of the sequence, both curves remain in-between the error bounds for the entire one-year period.

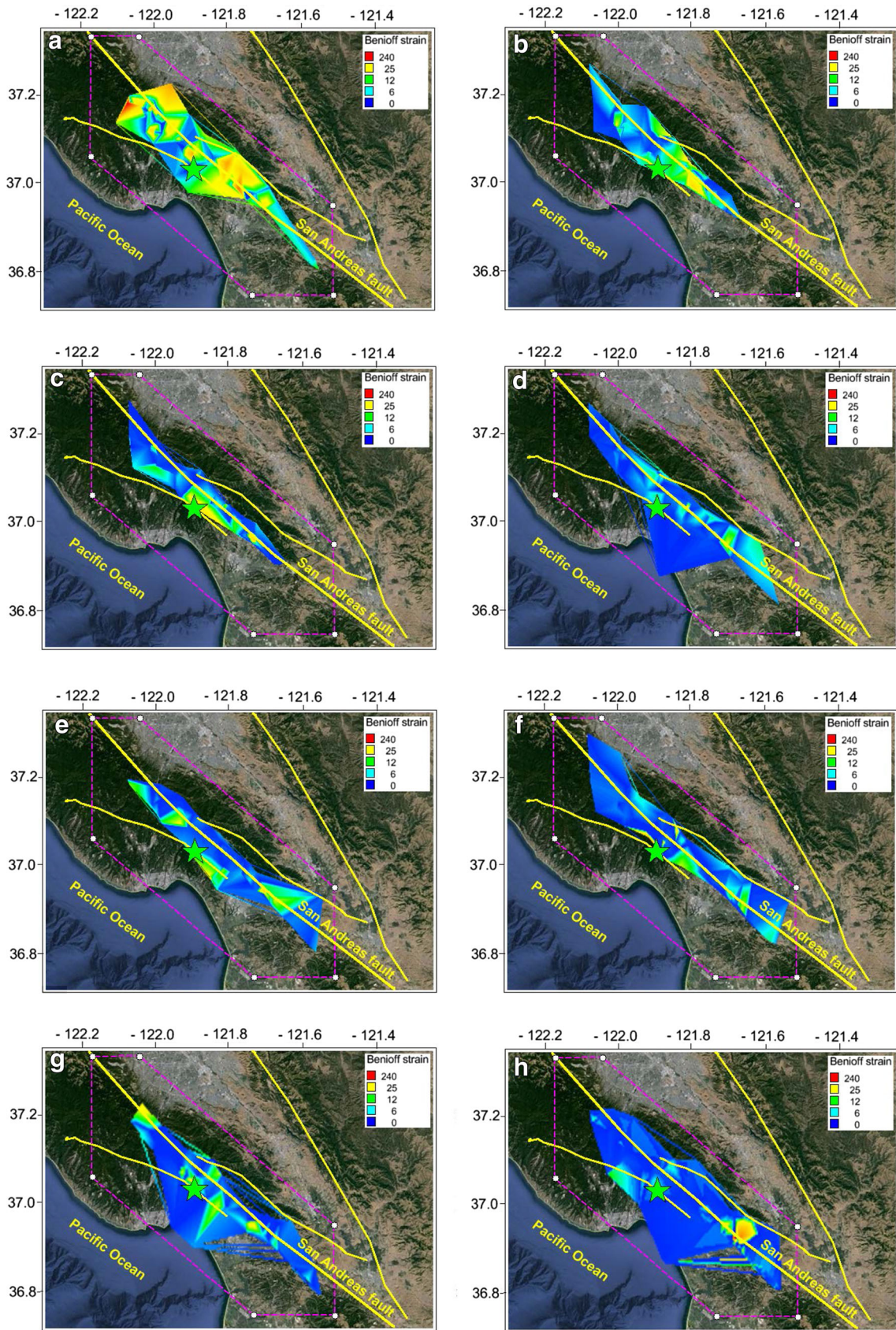
On Fig. 3b the Benioff strain temporal evolution of the aftershock sequence is presented. Circles represent the observed released strain, thick line corresponds to the expected released strain values, calculated after Formula 4 and the dashed lines reveal the error bounds, according to the standard deviation (see Formula 5).

Certain differences between modeled and observed values are seen on Fig. 3b. The long time period (1 year); however, does not allow capturing details of the observed discrepancy at the beginning of the sequence right after the occurrence of the main shock. That motivated us to execute another comparison of observed and modeled Benioff

Fig. 5 Spatial evolution of the Benioff strain on consecutive times intervals after the main shock occurrence: **a** 0–1.3 h, **b** 1.3–3.8 h, **c** 3.8–9.5 h, **d** 9.5–26.4 h, **e** 26.4 h–2.67 days; **f** 2.67–7.54 days, **g** 7.54–23.02 days, **h** 23.02–362.66 days. See more details in text

strain release, for a period of only 5 days. The results are plotted on Fig. 4.

In Fig. 4a real and expected cumulative numbers remain within the error bounds although there is a discrepancy between them, concerning the first 12 h after the occurrence of the main shock occurrence, during which the observed cumulative number surpasses the modeled one. On the other hand, an important deviation is observed for the strain release, presented in Fig. 4b. The discrepancy between the modeled and real values is significant, given that the real rate of strain release substantially surpasses the modeled rate. This is particularly the case for the first 6 h of the first day after the main shock, proving that a cluster



of stronger aftershocks occurred at the beginning of the sequence, not anticipated by the model.

Spatial evolution of the Benioff strain

To explore the spatio-temporal evolution of the Benioff strain of the sequence, we analyze a series of consecutive time intervals (see Fig. 5). We examine $N = 100$ aftershocks in each time interval except the last one, where the events number is equal to $N = 324$. For each data sample we calculate Benioff strain of the different aftershocks and normalize it to the one of the weakest event in the sequence. Then we use different colors to plot the spatial variation of the calculated Benioff strain for each time period (see legends on Fig. 5).

As it can be observed, the entire aftershock zone is activated immediately after the occurrence of the main shock and we could not identify any process of expansion. In addition, the biggest values of the Benioff strain were obtained for the first time interval with duration of approximately 1 hour (Fig. 5a), a fact, which is also supported by the results from the Benioff strain stochastic modeling in time (Fig. 4b), which revealed an excess of observed strain release values, compared to the modeled ones. The areas of increased strain release are situated E-SE of the main shock and in the NW edge of the aftershock area, encompassing the San Andreas fault and some nearby faults.

A different pattern is detected for the next time periods. During these intervals the activated zone narrows around the San Andreas fault and this strain release pattern continues until the last period, in which the release zone again broadens to cover almost the entire aftershock zone. We suppose this second activation of a larger aftershock area is related to the impact by the largest $M = 5.6$ aftershock in the sequence, that occurred on April, 18, 1990 in the SE part of the aftershock zone (see Fig. 5h).

Discussion

In this study we examined the spatio-temporal evolution of the Benioff strain during the Loma Prieta aftershock sequence. We offered a stochastic model for modeling strain release in time. Aftershock rate decay in time was initially modeled by the RETAS model and the identified version, best fitting the data, successfully disclosed the temporal evolution of the number of events. The recognized model turned out to be a RETAS version, for which the triggering magnitude coincided with the magnitude of completeness, i.e., the model proved to be ETAS. Following, the best fit temporal model was implemented in the strain release analysis. Whereas the temporal model of

aftershock rate decay follows the actual data quite closely, a certain disagreement is observed between the model and the data, concerning the Benioff strain evolution. Cumulative Benioff strain values significantly exceed the modeled ones for the first day after the main shock occurrence, which is a clear sign of increased strong aftershocks clustering during the beginning of the sequence. The clustering is stronger than suggested by the model for independent events and this result unveils that one of the criteria for the elaboration of the Benioff strain stochastic model, performed at the beginning, which is the independence between event time and magnitude, is not fulfilled.

The results from the strain release stochastic modeling in time demonstrate that the applied stochastic model empowers the detection of specific features of the Benioff strain temporal evolution. The proposed stochastic pattern can be used as a benchmark model, elaborated after some assumptions of aftershock independence in the sequence.

Strain release spatial evolution was also analyzed by studying released strain of the entire zone for eight subsequent time intervals. Dietz and Ellsworth (1990) examined the evolution of the aftershock spatial distribution of the same Loma Prieta sequence and they concluded that immediately after the main shock most aftershocks cluster near the border of the aftershock zone, framing a comparatively aseismic center, close to the of main shock epicentral region. We obtained slightly different results, by which strain release in the main event zone remains active (Fig. 5) nearly for the entire first half of the 1 year period, excluding the fourth time interval, overing the period 9.5–26.4 h after the main shock.

Both spatial and temporal analysis of strain release reveal that stronger aftershocks are clustered predominantly right after the occurrence of the main shock, when observed release values surpass significantly the expected modeled ones. Our results reveal no gradual expansion of the aftershock zone as suggested by the results of Dietz and Ellsworth (1990). Quite on the contrary, we observe only two time intervals of entire zone activation, related, on our opinion, to the impact of the main shock (0–1.3 h after its occurrence) and of the strongest aftershock. For the remaining periods the aftershock zone narrows along the San Andreas fault.

The main result of this study, the fact that strong aftershocks tend to cluster in time immediately after the occurrence of the main earthquake, concerns also the simulation of the selected model, best fitting the data and from there is related to short-term forecasting of the aftershock rate. The simulation technique of the RETAS (ETAS) model is presented by Gospodinov and Rotondi (2006). Another study analyzed the details of the simulation procedure if we simulate an entire aftershock sequence, immediately after the occurrence of a strong

earthquake (Gospodinov et al. 2007). The results from the latter investigation revealed that if magnitudes of future aftershocks were randomly generated to follow the recurrence law of actual events, the ETAS model could not provide satisfactory simulation of real seismicity, as it implies arbitrary dimension values in the simulation procedure. The results from the present examination unclosed that in real sequences strong aftershocks are often more likely to occur early in the process and it is advisable to incorporate this fact in the stochastic models of the aftershock activity by introducing time-dependence of the generated magnitudes.

Acknowledgements This research was supported by the University of Plovdiv "Paisii Hilendarski", under contract N^o NII5-FFIT-005/23.04.2015.

References

- Akaike H (1974) A new look at the statistical model identification. *IEEE Trans Autom Control* 19:716–723
- Dietz L, Ellsworth W (1990) The October 17, 1989 Loma Prieta, California, earthquake and its aftershocks: geometry of the sequence from high resolution locations. *Geophys Res Lett* 17(9):1417–1420A
- Dietz L, Ellsworth W (1991) Loma Prieta data archive, National Information Service for Earthquake Engineering (NISEE)
- Drakatos G (2000) Relative seismic quiescence before large aftershocks. *Pure Appl Geophys* 157:1407–1421
- Eaton JP (1992) Determination of amplitude and duration magnitudes and site residuals from short-period seismographs in Northern California. *Bull Seis Soc Am* 82(2):533–579
- Gardner JK, Knopoff L (1974) Is the sequence of earthquakes in Southern California, with aftershocks removed, Poissonian? *Bull Seis Soc Am* 64(5):1363–1367
- Gentili S, Bressan G (2008) The partitioning of radiated energy and the largest aftershock of seismic sequences occurred in the northeastern Italy and western Slovenia. *Journal of Seismology* 3:343–354
- Gospodinov D, Rotondi R (2006) Statistical analysis of triggered seismicity in the Kresna Region of SW Bulgaria (1904) and the Umbria–Marche Region of Central Italy (1997). *Pure Appl Geophys* 163:1597–1615
- Gospodinov D, Papadimitriou E, Karakostas V, Ranguelov B (2007) Analysis of relaxation temporal patterns in Greece through the RETAS model approach. *Phys Earth Planet Inter* 165(3–4):158–175. doi:10.1016/j.pepi.2007.09.001
- Gospodinov D, Papadimitriou E, Karakostas V, Ranguelov B (2009) Energy release patterns in aftershock sequences of North Aegean Sea (Greece) through stochastic modelling. *Cashiers du Centre Europeen de Geodynamique et de Seismologie*, North Carolina
- Gutenberg B, Richter C (1956) Earthquake magnitude, intensity, energy and acceleration. *Bull Seis Soc Am* 46:105–145
- Hansen G, Condon E (1989) Denial of disaster: the untold story and photographs of the San Francisco earthquake and fire of 1906. *Cameron & Co.*, San Francisco
- Jaiswal R, Naswa H, Singh A (2010) Seismic Characteristics and Energy Release of Aftershock Sequences of Two Giant Sumatran Earthquakes of 2004 and 2005. In *Proceedings of the 8th Biennial International Conference & Exposition on Petroleum Geophysics*, 2010, Hyderabad, Pakistan
- Kagan Y, Houston H (2005) 2005, Relation between mainshock rupture process and Omori's law for aftershock moment release rate. *Geophys J Int* 163:1039–1048. doi:10.1111/j.1365-246X.2005.02772.x
- Konca O, Hjorleifsdottir V, Song T, Avouac J, Helmberger D, Chen J, Sieh K, Briggs R, Meltzner A (2007) Rupture Kinematics of the 2005 Mw 8.6 Nias-Simeulue Earthquake from the Joint Inversion of Seismic and Geodetic Data. *Bull Seismol Soc Am* 97:S307–S322. doi:10.1785/0120050632
- Ogata Y (1988) Statistical models for earthquake occurrences and residual analysis for point processes. *J Am Stat Assoc* 83:9–27
- Ogata Y (1998) Space–time point–process models for earthquake occurrences. *Ann Inst Stat Math* 50:379–402
- Ogata Y, Jones LM, Toda S (2003) When and where the aftershock activity was depressed: contrasting decay patterns of the proximate large earthquakes in southern California. *J Geophys Res* 108:2318. doi:10.1029/2002JB002009
- Parsons T, Segou M, Sevilgen V, Milner K, Field E, Toda S, Stein RS (2014) Stress-based aftershock forecasts made within 24 hours post-mainshock: expected north San Francisco Bay area seismicity changes after the 2014 M = 6.0 West Napa earthquake. *Geophys Res Lett* 41(24):8792–8799. doi:10.1002/2014GL062379
- Plafker G, Galloway J (1989) Lessons learned from the Loma Prieta, California, earthquake of October 17, 1989, Circular 1045. U.S. Geological Survey, Reston, p 48
- Reasenber P (1985) Second-order moment of central California seismicity, 1969–82. *J Geophys Res* 90:5479–5495
- Snyder D, Miller M (1991) Random point processes in time and space. Springer, Verlag
- Stein S, Okal E (2007) Ultralong period seismic study of the december 2004 Indian ocean earthquake and implications for regional tectonics and the subduction process. *Bull Seismol Soc Am* 97:S279–S295. doi:10.1785/0120050617
- Tajima F, Kanamori H (1985) Aftershock area expansion and mechanical heterogeneity of fault zone within subduction zones. *Geophys Res Lett* 12(6):345–348
- Taylor H, Karlin S (1984) An introduction to stochastic modeling. Academic Press, Cambridge
- Tzanis A, Vallianatos F (2003) Distributed power-law seismicity changes and crustal deformation in the SW Hellenic arc. *Nat Haz Earth System Sci* 3:179–198
- Utsu T (1970) Aftershocks and earthquake statistics (II): further investigation of aftershocks and other earthquake sequences based on a new classification of earthquake sequences. *J Fac Sci* 3:198–266
- Wald DJ, Helmberger D, Heaton TH (1991) Rupture model of the 1989 Loma Prieta earthquake from the inversion of strong ground motion and broadband teleseismic data. *Bull Seism Soc Am* 81:1540–1572
- Zhuang J, Ogata Y, Vere-Jones D (2004) Analyzing earthquake clustering features by using stochastic reconstruction. *J Geophys Res* 109:B05301. doi:10.1029/2003JB002879
- Zoback ML (2006) The 1906 earthquake and a century of progress in understanding earthquakes and their hazards. *GSA Today* 16:4–11

Erratum to: A physics-based earthquake simulator and its application to seismic hazard assessment in Calabria (Southern Italy) region

Rodolfo Console^{1,2} · Anna Nardi² · Roberto Carluccio² · Maura Murru² · Giuseppe Falcone² · Tom Parsons³

Published online: 16 May 2017

© Institute of Geophysics, Polish Academy of Sciences & Polish Academy of Sciences 2017

Erratum to: *Acta Geophys.* (2017) 65:243–257 DOI 10.1007/s11600-017-0020-2

Unfortunately this article was published in the wrong issue. Correctly it should have been published in the special issue “Statistical Seismology”. The abstract of the article is given below.

Abstract The use of a newly developed earthquake simulator has allowed the production of catalogs lasting 100 kyr and containing more than 100,000 events of magnitudes ≥ 4.5 . The model of the fault system upon which we applied the simulator code was obtained from the DISS 3.2.0 database, selecting all the faults that are recognized

on the Calabria region, for a total of 22 fault segments. The application of our simulation algorithm provides typical features in time, space and magnitude behavior of the seismicity, which can be compared with those of the real observations. The results of the physics-based simulator algorithm were compared with those obtained by an alternative method using a slip-rate balanced technique. Finally, as an example of a possible use of synthetic catalogs, an attenuation law has been applied to all the events reported in the synthetic catalog for the production of maps showing the exceedance probability of given values of PGA on the territory under investigation.

The online version of the original article can be found under doi:[10.1007/s11600-017-0020-2](https://doi.org/10.1007/s11600-017-0020-2).

✉ Rodolfo Console
rodolfo.console@ingv.it

¹ Center of Integrated Geomorphology for the Mediterranean Area (CGIAM), Potenza, Italy

² Istituto Nazionale di Geofisica e Vulcanologia (INGV), Rome, Italy

³ United States Geological Survey, USGS, Menlo Park, CA, USA

Statistical seismology: preface to the topical issue

Rodolfo Console^{1,2} · Vassilios G. Karakostas³ · Eleftheria E. Papadimitriou³ · Georgios M. Tsaklidis⁴

Received: 16 May 2017 / Accepted: 16 May 2017 / Published online: 29 May 2017
© Institute of Geophysics, Polish Academy of Sciences & Polish Academy of Sciences 2017

From the Editors,

It is widely recognized that Seismology, the quantitative study of which started in the 19th century, has not yet achieved the ambitious target of predicting time, place and intensity of strong earthquakes in such a way as to allow concrete actions to mitigate their disastrous effects. This is mainly due to the intrinsic non-linear and chaotic nature of the earthquake process. In lack of any kind of physics-based and deterministic prediction, seismologists have applied statistical models for seismic hazard assessment that could be useful for earthquake mitigation measures of prevention.

A special session on Statistical Seismology was organized in the program of the Fourteenth International Congress of the Geological Society of Greece, held at the Aristotle University Campus of Thessaloniki, Greece on 25–27 May 2016. The aim of this session was to bring together and foster collaboration among seismologists and

mathematicians in order to reduce the gap that may exist between their different methodologies. In the course of this special session it was decided for a topical issue to be published where the presentations would be put together. Invitation was also extended to colleagues dealing with and interested in statistical seismology aspects.

The contributions cover a broad range of approaches to the study of non-randomness of the seismic processes.

One of these contributions (Abe and Suzuki) reports a comparative study on volcanic seismicity at Icelandic volcano, Eyjafjallajökull, and Mt. Etna in Sicily from the viewpoint of complex systems science, and discovers remarkable similarities between them.

Two papers (Leptokaropoulos et al., Olszewska et al.) consider time-dependent seismic hazard and other statistical features of mining-induced seismic events, a problem of great concern for mining industry in Poland.

The Group of the Geophysics Department of the University of Thessaloniki has provided three papers dealing with three different kinds of statistical analysis of seismicity in Central Ionian Islands and Corinth Gulf. They adopted respectively the Linked Stress Release Model (Mangira et al.), the Semi-Markov Model (Pertsinidou et al.) and the Complex Network Theory (Chorozoglou et al.).

Papadakis and Vallianatos have applied a non-extensive statistical physics analysis to the study of earthquake magnitude sequences in North Aegean Trough, Greece.

Different methods of modeling seismic processes applied to different countries are introduced by Gospodinov for the spatio-temporal evolution of aftershock energy release in California, and by Console et al. with a physics-based earthquake simulator and applied to seismic hazard assessment in Calabria, Southern Italy.

✉ Rodolfo Console
r.console@cigiam.org; rodolfo.console@ingv.it

Vassilios G. Karakostas
vkarak@geo.auth.gr

Eleftheria E. Papadimitriou
ritsa@geo.auth.gr

Georgios M. Tsaklidis
tsaklidi@math.auth.gr

¹ Center of Integrated Geomorfology for the Mediterranean Area, Potenza, Italy

² Istituto Nazionale di Geofisica e Vulcanologia, Rome, Italy

³ Department of Geophysics, School of Geology, University of Thessaloniki, Thessaloniki, Greece

⁴ School of Mathematics, University of Thessaloniki, Thessaloniki, Greece